Dancing on the Devil's Staircase: The Synchronization of the Quasi-Biennial Oscillation in the Tropical Stratosphere

Kylash Rajendran

Wolfson College

University of Oxford

A thesis submitted for the degree of

Doctor of Philosophy

Hilary Term 2017

For my parents

Acknowledgements

First and foremost, I would like to thank my three indefatigable supervisors: Irene Moroz, Scott Osprey, and Peter Read, for many years of patient guidance, support, ideas and inspiration.

I am grateful to Axel Gabriel, Scott Osprey, Will Seviour, and Shingo Watanabe for graciously providing me with datasets for my analysis.

For many insightful discussions and useful criticism, I thank James Anstey, Alfonso Castrejón-Pita, Andrew Fowler, Lesley Gray, John Norbury, Tim Palmer, Alan Plumb, Adam Scaife, John Scinocca, Will Seviour, and John Wettlaufer. Special thanks to Lesley Gray for showing me much kindness, and for being so generous with your time, knowledge, and encouragement. Thanks also to the members of both the Geophysical Fluid Dynamics Group and Stratospheric Processes Group in AOPP, for providing me with numerous opportunities to present, discuss, and clarify my work.

The wonderful community at Wolfson College, Oxford, provided me with a warm and welcoming environment within which to pursue my research.

Raquel Canadilia Tumimbang cheerfully and tirelessly looked after me over the long months spent writing up this thesis. You have been a source of great strength, thank you for being such a wellspring of positivity.

To my friends, I give special thanks to Chethan Anil, Santhy Balachandran, Amogh Chakravarti, Janet Dunkelbarger, Aaron Eldridge, Leanne Johansson & Alan Molenaar, Nina Klein, Parvin Kumar, Din-Houn Lau, Jae Lee, Christina Lienen, Garlen Lo, Danna & Luka Lukic, Gabriela Pavarini, Ravin Periasamy, Pravin Prakash, Sarah Puello Alfonso, Moritz Riede, Marc Sarazin, Ilenia Scerra, Desmond Tan, and Gemma Tidman. Thank you for the many years of music, laughter, repartee, joy, support and love; you have helped to carry me through.

To my family - uncles, aunts, cousins, Asia, Kaushika, and especially my siblings Giri and Gowri - thank you for always supporting me and encouraging me to pursue my interests, and for helping me to grow. To Basheerah, my partner-in-crime: thank you for your love, for keeping my feet on the ground, and for helping me to remember what is truly important.

Final thanks, of course, are to my parents; the great mountains down which this little stream has flowed. Thank you for your infinite patience, financial largesse, excellent advice, and moral and emotional support. This thesis is dedicated to you.

Abstract

In this thesis we investigate the variability of the Quasi-Biennial Oscillation (QBO), which is the dominant mode of variability in the tropical stratosphere. In particular, we study the susceptibility of the QBO to the phenomenon of synchronization; that is, the adjustment of the rhythms of the QBO under the influence of a periodic external force. We approach the problem using a combination of theoretical analysis, numerical modelling, and observational study. The dynamics of the QBO are studied in detail using the Holton-Lindzen partial differential equation. We introduce various forcing terms to this equation, to simulate the effects of the Brewer-Dobson circulation, the Semi-Annual Oscillation, the Inter-Tropical Convergence Zone, and tropical wave forcing variations on the QBO. We find that the QBO enters a state of synchronization in its interactions with all of the above forcing terms, with the exception of the Semi-Annual Oscillation. The general structure of QBO synchronization takes the form of either exact frequency locking, discrete multi-cycle periods, or quasiperiodic behaviour. By recasting the Holton-Lindzen equation into the form of a descent rate model, we demonstrate that the dynamics of the QBO period can be described using a simple one-dimensional ordinary differential equation, which is shown to be closely related to the circle map. This simplification greatly reduces the complexity of the model, whilst retaining all the key observed features of synchronization.

We study the dynamics of the QBO in reanalysis and general circulation model datasets, using a combination of Extended Empirical Orthogonal Function analysis and analytic phase techniques. We show that the descent rate of the QBO correlates with the strength of tropical upwelling. Further, by defining a statistical measure for QBO synchronization based on the evolution of QBO periods, we demonstrate that both the observed and modelled QBOs behave in a way that is consistent with synchronization to the annual cycle. The observed QBO is found to be phase synchronized with the Brewer-Dobson circulation, and we find that it jumps irregularly between the $2:1$, $5:2$, and $3:1$ synchronization ratios. We find evidence that the phase slips of the observed QBO tend to occur during periods when the El Niño Southern Oscillation is in a strong positive phase.

Our results make a robust case in favour of the proposition that the QBO is synchronized to the annual cycle via seasonal and inter-annual variations in tropical upwelling strength and tropical wave activity.

Contents

List of Figures

Chapter 1

Introduction

1.1 Background

The variability of the zonal wind field in the tropical stratosphere is dominated by oscillations on both intra-seasonal and inter-annual timescales. The Quasi-Biennial Oscillation, or QBO, is a zonally symmetric wind system that is the most prominent feature of the lower and middle stratosphere between 5 and 100 hPa (roughly 17–40 km). It consists of alternating bands of westerly[1] and easterly winds that form in the tropical upper stratosphere and descend to the tropical tropopause at an average rate of approximately 1km per month. The period of the QBO varies from cycle to cycle, with a mean period of 28.5 months - hence the quasi-biennial appellation. An excellent review of the basic properties and dynamics of the QBO is given in Baldwin et al. [2001].

The cycle to cycle variability of the QBO period is quite substantial, with individual QBO cycles varying in length between 20–35 months. The aim of this thesis is to achieve a better understanding of this observed variability of the QBO period. In essence, we intend to explain the 'Quasi' of the Quasi-Biennial Oscillation. What are the various factors that affect the period of the QBO? How does the QBO respond

[1]The terms 'westerly' and 'easterly' denote winds blowing *from* the west and east respectively.

to external periodic drivers in the atmosphere? And does the evolution of the QBO period conform to any kind of structure? These are the key questions that we will attempt to address in this thesis.

This chapter serves as an introduction and motivation for the remainder of the thesis. In section 1.2, we give some further background to the QBO and describe its basic kinematic and dynamical properties. The relevance of the QBO to the meteorological community is highlighted in section 1.3, where we give an overview of its influence on other parts of the atmosphere via atmospheric teleconnections. In section 1.4, we introduce the concept of *synchronization*, which is crucial to understanding the dynamics of the QBO period. We also review studies in the literature that have investigated the variability of the QBO period. Finally, in section 1.5, we describe our approach to the problem, and give an outline of the remainder of the thesis.

1.2 Dynamics of the QBO

Figure 1.1 depicts contours of zonal wind velocities between 17 and 35 km as compiled from radiosonde data from three different near-equatorial stations: Kanton Island in Kiribati (2°S, 171°W), Gan in the Maldives (1°S, 73°E), and Singapore (1°N, 103°E) between January 1956 and December 2015. The data was provided by the Free University of Berlin[2] (Naujokat [1986]), and gives a good idea of wind variability in the tropical stratosphere. Yellow/orange regions denote westerlies, while blue regions represent easterlies. There is a clear pattern in the data, of alternating westerly and easterly wind regimes that originate from above 35 km and propagate down to the tropopause at 17 km; this wind structure is known as the QBO.

The QBO has been found to be approximately zonally symmetric (Belmont and Dartt [1968]), and so data from a single equatorial station may be used to approxi-

[2] `http://www.geo.fu-berlin.de/en/met/ag/strat/produkte/qbo/index.html`. Accessed 12/11/2016.

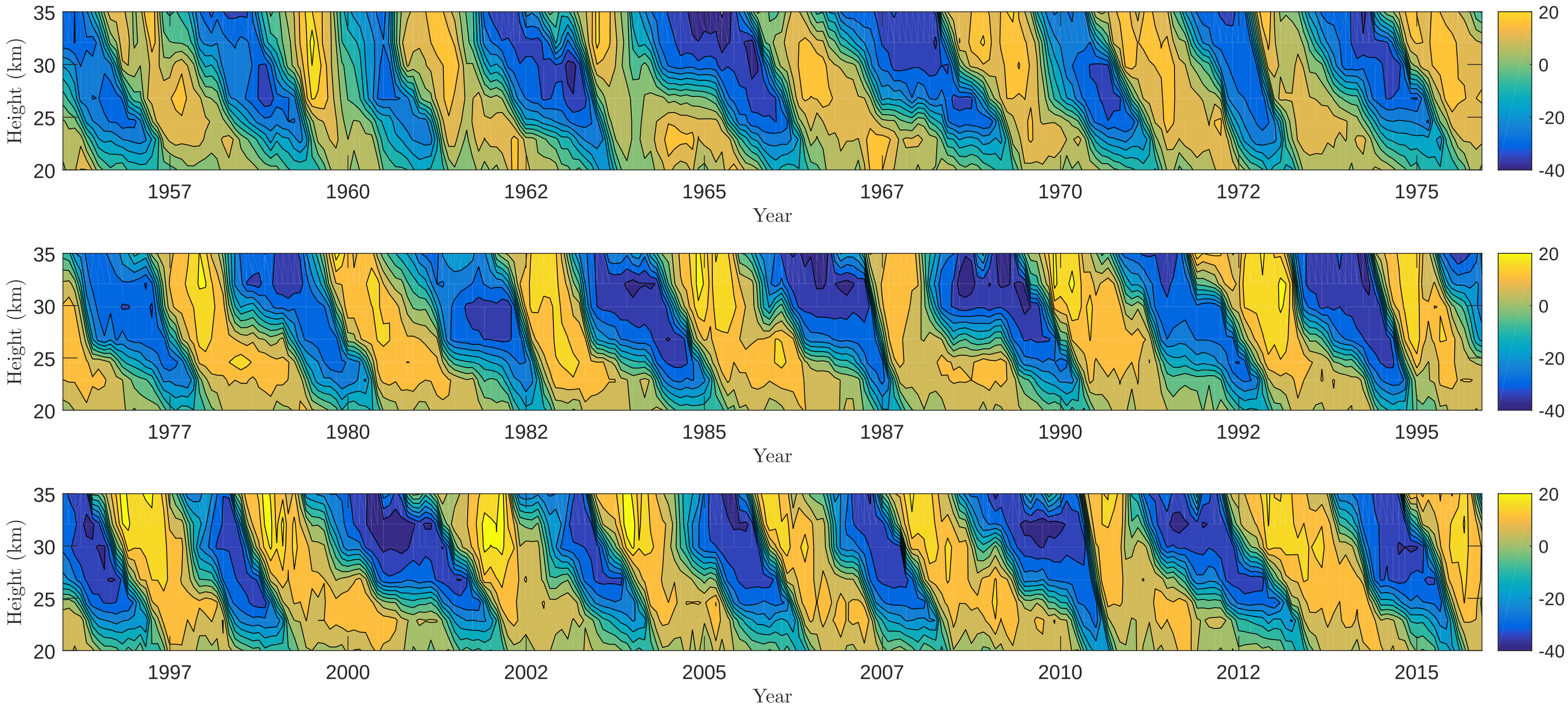

Figure 1.1: Evolution of the zonal-mean zonal winds in the tropical stratosphere between January 1956 and December 2015. Taken from Free University of Berlin data (Naujokat [1986]).

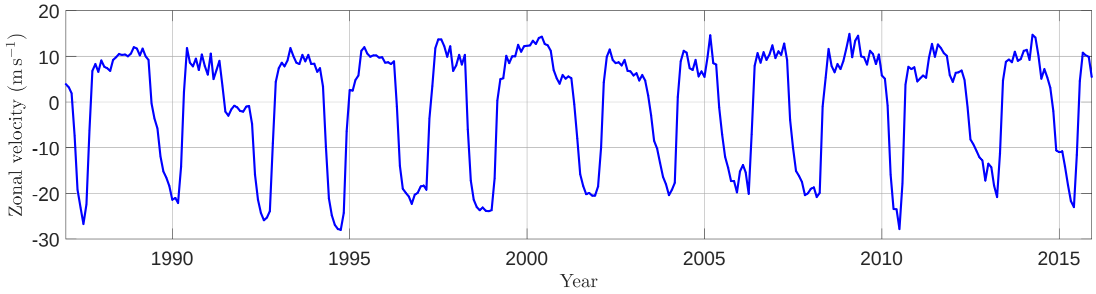

Figure 1.2: Monthly time series of zonal winds over Singapore at 50 hPa between January 1987 and January 2016 (Naujokat [1986]).

mately represent the phenomenon across all longitudes. The oscillation is strongest at the equator, and decays polewards with a latitudinal half-width of 15 degrees (Dunkerton and Delisi [1985]).

Figure 1.2 shows the time series of zonal winds at 50 hPa (roughly 23 km), as measured at the Singapore station between January 1987 and December 2015. Note the strong asymmetry between easterly and westerly wind regimes. QBO easterlies tend to be around twice as strong as QBO westerlies, with average amplitudes of around $23\,\mathrm{m\,s^{-1}}$. In contrast, westerly amplitudes are closer to $13\,\mathrm{m\,s^{-1}}$. The mean descent rate of the westerly shear zone is 4 hPa per month, while the descent rate of easterlies is slower at 2 hPa per month (Pascoe et al. [2005]). The discrepancy in descent rate can be attributed to the occasional stalling of the easterly phase around 30 hPa - this stalling is considered to have a dominant influence on the variability of the QBO period (Dunkerton [1990]).

The QBO was discovered in the early 1960s by Reed et al. [1961] and Ebdon [1960], from analysis of radiosonde data recorded at Kanton Island. A theory explaining the existence of such an oscillation remained elusive for several years until the work of Lindzen and Holton [1968]. Lindzen and Holton adapted ideas from the paper by Booker and Bretherton [1967], on gravity wave absorption at critical levels in a fluid, to show that the QBO could be generated by a *wave-mean flow interaction*. They later refined their theory in a subsequent paper (Holton and Lindzen [1972], or HL72 hereafter). To this day the HL72 theory, with minor modifications, remains the paradigm through which we understand the dynamics of the QBO.

Wave-mean flow theory considers the question of active interaction between propagating waves and the background medium through which they propagate. In the HL72 theory of the QBO, the background mean flow of the stratosphere is modified as a result of the dissipation of vertically propagating waves originating from the troposphere. As these waves move through the stratosphere, they dissipate due to thermal damping, and thereby deposit momentum into the background flow. Booker and Bretherton showed that the dissipation rate of an internal gravity wave at a given height is dependent on the Doppler shifted frequency $\bar{u} - c$ of the wave at that height; that is, the difference between the velocity of the background flow $\bar{u}$ and the horizontal phase speed c of the wave. When the Doppler shifted frequency is small at a given point in the flow, the relative velocity of the wave through the fluid is small and hence the net dissipation of the wave at that point is greater. The implication of this interaction is that wave momentum tends to be preferentially deposited near to so-called critical levels in the mean flow, where the Doppler-shifted frequency of the wave is equal to zero. The mean flow will be preferentially accelerated at these levels, and thereby evolve to a new state which subsequent waves can then interact with. Conversely, waves with large Doppler-shifted frequencies at a given height level experience relatively little dissipation at that level, and so continue to propagate to higher levels of the stratosphere.

The HL72 theory invokes this nonlinear mechanism to elegantly explain the formation of the QBO. The fundamental features of the theory were elucidated by Plumb [1977]. Consider a stratosphere that is continually forced at the lower boundary by two types of gravity wave, of identical amplitude and opposite horizontal phase speeds (Figure 1.3, adapted from Plumb [1984]). As each wave travels upward it dissipates and deposits zonal momentum into the background flow. This dissipation is maximal

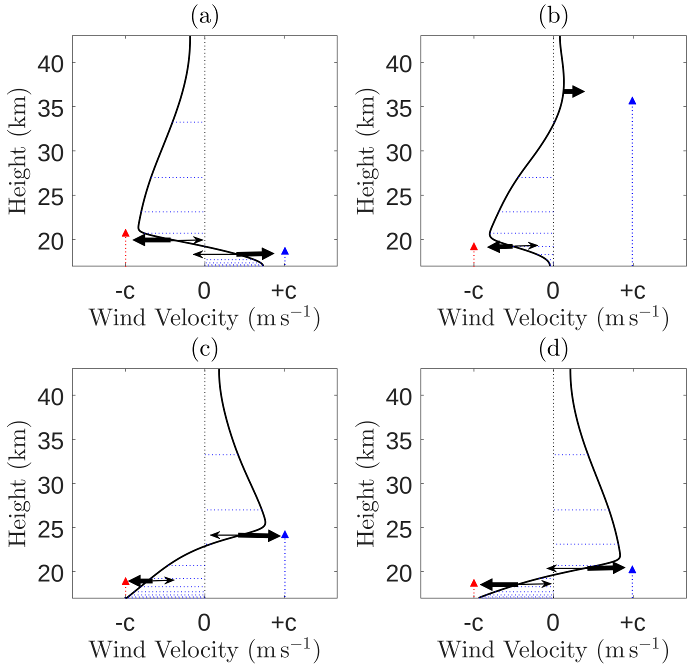

Figure 1.3: The generation of an oscillation via wave-mean flow interaction. Dotted arrows represent the depth of propagation of each wave. Large arrows denote acceleration due to wave momentum deposition. Thin arrows represent the direction of viscous forces. Adapted from Plumb [1984].

just below a *critical* level, where the wave speed is equal to the mean flow velocity. This results in the formation and descent of westerly and easterly shear zones (Figure 1.3a). As the easterly shear zone approaches the tropopause (which is the bottom of the model and the source of the waves), viscous diffusion acts to destroy the westerly shear zone below it. The westerly wave is now free to propagate through to higher levels of the stratosphere (Figure 1.3b), where it forms a new westerly shear zone. Meanwhile, the easterly shear zone continues to propagate down to the tropopause. As the westerly shear zone descends the easterly shear zone is then eventually destroyed, and the process repeats. This succession of descending westerly and easterly regimes thus forms the QBO.

In the original HL72 paper, the authors forced a QBO in a one-dimensional model by using just two waves: a westerly Kelvin wave, and an easterly mixed Rossby-gravity (MRG) wave. Gray and Pyle [1989] used the same set of waves to simulate a QBO in a 2d dynamical/radiative/chemistry model that included a realistic representation of the seasonal cycle. They found that the strengths of Kelvin and MRG wave forcings required by the model were around three times larger than the fluxes of these waves observed in reality. Similarly, the observational study of Bergman and Salby [1994] estimated the theoretical net wave flux in the stratosphere, and found it to be around 2.5 times the amount contributed by Kelvin and MRG waves alone. Dunkerton [1991] attributed the need for greater wave forcing to the effect of vertical upwelling in the equatorial stratosphere due to the Brewer-Dobson circulation. As the QBO has to propagate downward through rising air, the wave forcing would have to be correspondingly larger in order for the net descent of the QBO regimes to be simulated. Using a 2-D simulation of the QBO, Dunkerton [1997] showed that the required extra wave forcing could be provided by a broad spectrum of gravity waves. Current knowledge suggests that the QBO is driven by a broad spectrum of waves, including Kelvin, gravity, inertia-gravity and Rossby-gravity waves. Equatorward propagating waves from the extratropics, such as Rossby waves from the winter hemisphere, may also contribute to the QBO at higher levels. Although it was thought that the lower stratosphere is generally shielded from such effects (Baldwin et al. [2001]), a recent disruption to the QBO (Newman et al. [2016], Osprey et al. [2016]) has re-emphasised the possible significance of these extratropical waves.

The QBO in zonal wind also induces a corresponding temperature oscillation, via the approximate thermal wind relationship that has been observed to hold at the equator (Andrews et al. [1987]):

$$\frac{\partial \bar{u}}{\partial z} = -\frac{R}{H\beta}\frac{\partial^2 T}{\partial y^2}. \tag{1.2.1}$$

Here $\bar{u}$ is the zonal wind, T is temperature, y is latitude, and z is log-pressure height. Also, R is the gas constant for dry air, H is the log-pressure scale height, and β is the rate of change of the Coriolis parameter with latitude.

From Equation (1.2.1), we expect a positive temperature anomaly to develop below a westerly shear zone. Conversely easterly wind shears should have an associated negative temperature anomaly. The source of these temperature anomalies is diabatic heating and cooling by an induced residual mean meridional circulation. Under suitable approximations, Plumb and Bell [1982] have shown that the vertical component of this meridional circulation takes the form

$$\bar{w}^L = -\mu \frac{\bar{\theta}}{N^2}, \tag{1.2.2}$$

where $\bar{w}^L$ is the Lagrangian-mean vertical upwelling, μ is the thermal dissipation rate ($\sim (10\,\mathrm{day})^{-1}$), $\bar{\theta}$ is the potential temperature, and N is the buoyancy frequency. Equation (1.2.2) implies the presence of an upward vertical circulation around easterly shear zones, and a downward circulation around westerly shear zones. Plumb and Bell [1982] showed that this circulation is partly responsible for the observed difference in descent rates of the easterly and westerly shear zones: easterlies tend to descend at a slower rate due to the upward motion of the background flow induced by the meridional circulation.

Although the dynamics of the QBO are fairly well-understood, its simulation still poses significant challenges to the climate modelling community. The accurate simulation of a QBO is a demanding requirement on General Circulation Models (GCMs), given the wave-driven nature of the QBO. The QBO is also very sensitive to the configuration of the model, and as such there are very few state of the art models at present that can successfully generate the oscillation (Takahashi [1999], Scaife et al. [2000], Giorgetta et al. [2002]). Thus, the accurate simulation of the QBO remains an ongoing challenge (Schenzinger et al. [2016]).

1.3 Influence of the QBO

The QBO displays significant interactions and teleconnections with many other elements of the atmosphere-ocean system in both the tropics and the extratropics. For example, the phase of the QBO has been found to affect the strength of the stratospheric vortices that form over the winter poles; this is known as the Holton-Tan effect (after Holton and Tan [1980]). The strength of the polar vortex is significantly affected by vertical propagation of planetary Rossby waves (Matsuno [1971]). The zonal mean zonal wind is in a westerly state in the extratropical winter stratosphere, allowing Rossby waves to propagate vertically into the stratosphere (Charney and Drazin [1961]). These waves eventually break and deposit easterly momentum into the mean flow via a similar wave-mean flow interaction process to the one that drives the QBO (Holton et al. [1995]). The net result is that the zonal westerlies bounding the stratospheric vortex weaken, and there is a concurrent temperature increase by the thermal wind relation. If the wave forcing is strong enough, the vortex may even break down completely in what is known as a Sudden Stratospheric Warming (SSW) (Charlton and Polvani [2007]).

The QBO modulates the location of the zero-wind line in latitude that marks the transition between easterly and westerly winds as one travels from the equator to the winter pole. Holton and Tan [1980] hypothesised that Rossby wave activity will be confined to high latitudes to a greater extent when the zero wind line is at a higher latitude (as would happen when the QBO is in its easterly phase). This concentration of wave forcing near the pole increases the likelihood of a disturbed polar vortex, and possible breakdown of the vortex in a warming event. This is indeed what they found in the observational record: on average, when the QBO is in its westerly phase the polar vortex tends to be colder, and warming events are more likely to happen when the QBO is in its easterly phase.

SSWs are known to impact the climate of the troposphere (Thompson et al.

[2002]). For example, major warmings in January 2009 and February 2010 are known to have caused the anomalously cold temperatures in Britain in those periods. Consideration that the QBO phase might influence the frequency of such events has led to increasing interest in using the QBO as a diagnostic tool in numerical weather prediction on seasonal timescales (Marshall and Scaife [2009], Scaife et al. [2014]).

Although observations support this picture of QBO-vortex coupling, it should be noted that many details of the wave-mean flow interaction underlying this mechanism are as yet unknown. There are also other competing interactions that affect the polar vortex - the El Niño Southern Oscillation, for example - and it is difficult to isolate the effect of the QBO alone on the state of the vortex. For a review of these issues, see Anstey and Shepherd [2013].

Recent research has also revealed that the QBO exerts a sizeable influence on tropical tropospheric conditions. The phase of the QBO affects seasonal tropical convection, as has been observed in analyses of Outgoing Longwave Radiation (Collimore et al. [2003]) and tropical precipitation (Liess and Geller [2012]). These effects have been simulated in a cloud-resolving model (Nie and Sobel [2015]), where it was shown that the strength and direction of precipitation changes due to the QBO depend in a nonlinear way on the strength of Sea Surface Temperature (SST) anomalies. The QBO also significantly modulates the strength of the Madden-Julian Oscillation (MJO) during boreal winter (Yoo and Son [2016]); the strength of Indian monsoon precipitation (Kane [1995], Giorgetta et al. [1999]); and the intensity of the hurricane season and positioning of tropical cyclone tracks (Gray [1984], Ho et al. [2009]). Furthermore, it plays a key role in the distribution of ozone and other trace species throughout the atmosphere (Gray and Pyle [1989], O'Sullivan and Dunkerton [1997]), and it modulates the impact of the 11-year solar cycle on the extratropics (Labitzke and Loon [1988], Salby and Callaghan [2006]).

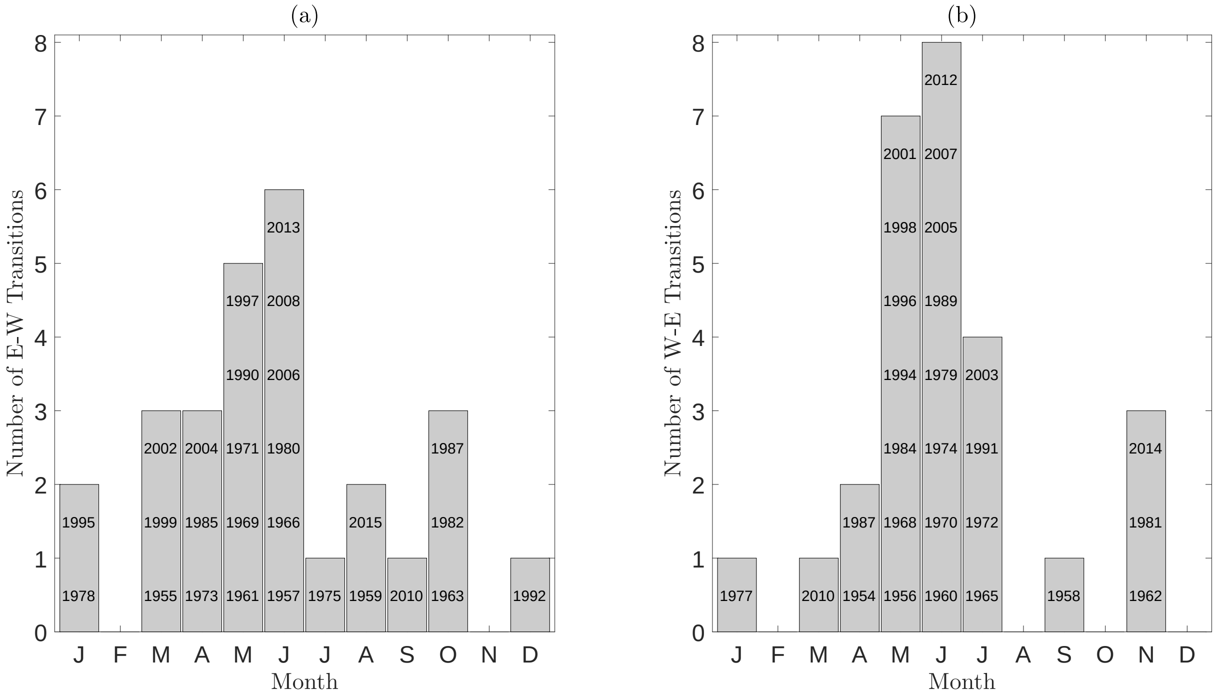

Figure 1.4: Histograms of the number of QBO transitions at 50 hPa for each month of the year, over the time period of January 1953–December 2015. (a) Easterly to Westerly transitions, (b) Westerly to Easterly transitions.

1.4 Synchronization of the QBO

The previous section has highlighted the key role played by the QBO in the climate system. Given its significant influence, it would be desirable to understand the causes of variability in the phase evolution of the QBO from cycle to cycle.

Observational studies of the QBO (Dunkerton and Delisi [1985], Dunkerton [1990], Gabis [2015]) have highlighted that the annual cycle is a key influence on the QBO. Figures 1.4(a) and (b) show histograms of the onset months of QBO westerlies and easterlies respectively, at a height of 50 hPa. We see that easterly and westerly transitions at 50 hPa have a strong preference to cluster during Northern Hemisphere spring and summer, with relatively few transitions in winter. Similar behaviour has also been simulated in QBO models, ranging from simple low-dimensional models with parameterised wave forcings (Hampson and Haynes [2004], Kinnersley and Pawson [1996]) to a full GCM (Krismer et al. [2013]).

The above observations imply a strong connection between QBO evolution and the annual cycle. Indeed, they suggest that the QBO may in fact be *synchronized* to the annual cycle. Synchronization is a dynamical phenomenon that refers to the mutual adjustment and possible entrainment of the frequencies of self-sustaining oscillators due to weak coupling (Pikovsky et al. [2003]). It has been observed in a variety of physical and biological systems, among which are fireflies (Mirollo and Strogatz [1990]), lasers (Simonet et al. [1994]), and atrial pacemaker cells (Glass and Mackey [1988]). Two oscillators, A and B, are said to be in $m : n$ synchronization if their average periods, $\bar{\tau}_A$ and $\bar{\tau}_B$, satisfy

$$\frac{\bar{\tau}_A}{m} = \frac{\bar{\tau}_B}{n}, \tag{1.4.1}$$

where m and n are positive integers. In the context of the QBO, we are interested in synchronization due to an external periodic influence; in this instance, the coupling between the oscillators is one-way.

The critical behaviour that defines synchronization is the adjustment of the *average* period of the forced oscillator in response to an external influence. We note that this is not the same as a *frequency modulation*, in which the cycle to cycle period of the oscillator is modulated by the external forcing, without necessarily any change to the mean period of the forced oscillation. Both synchronization and frequency modulation are often present in forced systems; however, the presence of one does not necessarily imply the other.

There are several candidate external forces that could potentially induce synchronization of the QBO. One possibility is that synchronization of the QBO is achieved via interactions with the annual cycle in the upwelling strength of the Brewer-Dobson circulation. The annual cycle in tropical upwelling is due to hemispheric asymmetries in the strength of the breaking planetary waves that drive this circulation (Yulaeva et al. [1994]). Since the descent of the QBO is affected by upwelling, it is plausible that the periodic upwelling could synchronize the QBO. This possibility was first investigated by Hampson and Haynes [2004], who studied phase alignment of the QBO as a result of the annual cycle in upwelling in a 3-D mechanistic model of the QBO.

A subset of annual cycle influence on the QBO occurs through the interaction of the QBO with the stratopause semi-annual oscillation (SAO) (Garcia et al. [1997], Pascoe et al. [2005]). The SAO is a different wind system that also lives in the tropical stratosphere; it dominates variability above 5 hPa ($\sim$ 35 km) and upwards to the stratopause at 1 hPa ($\sim$ 50 km). In the original QBO theory of Lindzen and Holton [1968] it was thought that the SAO was crucial to the generation of the QBO by providing a high-altitude seed for the westerly QBO phase. Although further studies (Holton and Lindzen [1972], Plumb [1977]) have shown that this seeding mechanism is not necessary to generate a QBO, recent results (Kuai et al. [2009], Read and Castrejón-Pita [2012], Krismer et al. [2013]) indicate the the SAO may still have a role to play in modulating the phase of the QBO.

A third possibility is the effect of seasonal variations in the strength of the waves that force the QBO. The strength of the wave forcing affects the rate of descent of the QBO; therefore, periodicities in the wave forcing strength could carry forward to affect the period of the oscillation. This possibility was first studied by Geller et al. [1997], in the context of the impact of the El Niño Southern Oscillation (ENSO) on the QBO.

1.5 Thesis Outline

The aim of this thesis is to carry out a detailed investigation of QBO synchronization via the three mechanisms stated in the previous section. We will approach the question of QBO synchronization using a combination of theoretical, modelling, and observational studies. A summary of our investigations - as well as our findings - is stated below.

We begin with the modelling approach. In Chapters 2–5, we study the influence of periodic external forces on the QBO using the Holton-Lindzen (HL) equation first introduced by Holton and Lindzen [1972]. This is the simplest model that generates a reasonably realistic oscillation, and so forms the bedrock of our modelling studies.

In Chapter 2, we provide a theoretical review of the HL equation, and derive it from first principles from the governing equations. We then study the basic properties of the equation, and investigate its sensitivity to changes in model parameters such as the strength of wave forcing, diffusion, and the wave numbers and wave speeds of the forcing waves. We discover a new bifurcation of the QBO amplitude at high values of wave forcing, and briefly discuss its properties.

In Chapter 3, we begin the first of three synchronization studies using the HL equation. We investigate the influence of the annual cycle of tropical upwelling on the QBO in the HL equation. We find that the QBO does indeed become synchronized to the annual cycle, and also that it exhibits frequency modulation for a large range of wave forcing amplitudes. We explore the synchronization properties in detail, and show how the interaction can generate significant variability in the period of the QBO. The robustness of the results are tested by adding stochasticity to the system, and we find that the qualitative structure of synchronization is preserved even in the presence of noise. Finally, we study the evolution of the QBO period in the context of a warming climate, in which the strength of the Brewer-Dobson circulation is expected to gradually increase.

Chapter 4 takes up the question of the interaction of the QBO with direct zonal semi-annual forcings. We consider the influence of both the upper stratospheric SAO discussed in the previous section, as well as semi-annual winds at the tropopause due to the migration of the Inter-Tropical Convergence Zone (ITCZ) across the equator twice a year. In line with the predictions of Plumb [1977], we find that the SAO cannot synchronize the QBO, although we do find that it modulates the frequency of QBO winds in the mid-stratosphere. In contrast, we find that the ITCZ winds imposed at the bottom of the model have a significant synchronizing effect on the QBO. We then repeat the SAO and ITCZ studies using imposed advective forcings rather than direct zonal forcings, and obtain similar results.

Chapter 5 is the final modelling chapter and it investigates synchronization of the QBO due to periodic variations in the strength of the waves that force the QBO. We consider wave forcings with semi-annual, annual, and multi-annual periodicities; in all cases, we find that wave periodicity induces robust synchronization of the QBO. In the inter-annual case, the variability of the QBO is very large, and approximates observed variability of the QBO quite well. We also briefly investigate the effects of wave filtering by the semi-annual ITCZ winds on the QBO. This mechanism also generates synchronization, although the strength of tropopause winds required to generate synchronization are too large to be of physical relevance.

Chapter 6 presents some theoretical considerations to help understand and interpret the findings of the previous chapters. We investigate a class of equations that we call *descent rate* models, and show that they capture the basic set of synchronization behaviours seen in Chapters 3–5. We then show that the HL equation itself can be converted into the form of a descent rate model. This simplification reduces the complexity of the model equation from that of a 1-D Partial Differential Equation (PDE) to that of an essentially 1-D Ordinary Differential Equation (ODE). The descent rate models provide a robust framework to interpret all of the synchronization behaviour of the QBO, and we show how they are closely related to the circle map. This connection provides a secure mathematical foundation for understanding QBO synchronization.

In Chapter 7, we study synchronization of the QBO in data from an atmospheric reanalysis, as well as from the output of two general circulation models. We show that the descent rate of the QBO shows significant correlation to the strength of tropical upwelling, and that the observed QBO periods are consistent with synchronization to the annual cycle. We utilise a combination of Extended Empirical Orthogonal Function analysis and analytic phase techniques to define the phase evolutions of the QBO, SAO, and Brewer-Dobson (BD) circulation in the data sets. In all three data sets we find statistically significant phase synchronization between the QBO and the BD circulation at 2 : 1, 5 : 2, and 3 : 1 synchronization ratios. The observed synchronization ratio is found to jump sporadically between these three values over time. The QBO and SAO are also found to be synchronized at ratios of 4 : 1, 5 : 1, and 6 : 1; however, this may be attributable to the exact 2 : 1 synchronization of the BD and SAO due to their shared entrainment to the underlying annual cycle. We also find hints of a relationship to the El Niño Southern Oscillation (ENSO), which suggests that the phase evolution of the QBO accelerates during large El Niño events.

Finally, in Chapter 8 we summarise our findings and their implications, and we point out directions for further research.

Chapter 2

The Holton-Lindzen model

2.1 Introduction

The Holton-Lindzen (HL) equation is one of the simplest mathematical models that captures the essential dynamics of the QBO. First developed by Holton and Lindzen [1972], it is the foundation stone around which much of this thesis is built. The model equation represents the acceleration of the equatorial zonal wind field due to dissipation of vertically propagating equatorial waves. The wave-induced modification of the background wind affects subsequent wave propagation, and it is this mechanism of wave-mean flow interaction that is the fundamental driver of the QBO phenomenon.

In this chapter we motivate and derive the HL equation, and explore some of its basic properties. This will set the stage for later work in subsequent chapters, where various mechanistic extensions of the basic HL model will be used to model the interaction and possible synchronisation of the QBO by candidate external drivers.

We use a version of the HL equation that is closely related to one described by Plumb [1977]. In Plumb's model, the forcing waves are taken to be two identical gravity waves with equal and opposite phase speeds. This is in contrast to the original formulation of Holton and Lindzen [1972], where westerly forcing is provided by a

Kelvin wave and easterly forcing by a mixed Rossby-gravity (MRG) wave. The benefits of the Plumb formulation are that it is simpler than the full HL equation, whilst still capturing the essential mechanism of the QBO. In particular, the symmetry of the wave forcing profiles is a useful simplification that helps to analyse cleanly the synchronization of the QBO in later chapters.

We follow the setup of Plumb [1977], using an equivalent description in which the westerly forcing is provided by a Kelvin wave and the easterly forcing by an 'anti-Kelvin' wave, as described in Dunkerton [1991] and Kinnersley and Pawson [1996]. The anti-Kelvin wave is a fictitious Kelvin wave with an easterly wave speed and is not physically realisable. However, in the one-dimensional context of the HL model the behaviour of Kelvin waves in height is identical to gravity waves (Andrews et al. [1987]), and so the formulation is entirely equivalent to Plumb [1977]. In the remainder of the thesis we will use the term 'Holton-Lindzen equation' to generically refer to this particular formulation.

The remainder of the chapter is set out as follows. In Sections 2.2–2.4 we formulate the HL equation from first principles. After introducing the governing equations for the mean flow and perturbations in Section 2.2, in Sections 2.3 and 2.4 we study equatorial wave solutions in the presence of either a constant or vertically sheared background zonal wind, focusing on the Kelvin wave. The wave solutions allow us to formulate the wave stresses on the mean flow, leading to the HL equation. All of the material in these sections is well known, and has been compiled from Lindzen [1970, 1971], Holton and Lindzen [1972], Holton [1975], Andrews and McIntyre [1976a,b] and Andrews et al. [1987].

Having derived the HL equation, in Section 2.5 we solve it numerically in the case of two forcing waves, and describe some of the properties of the QBO it generates. (We will generically refer to any oscillating solution of the HL equation as a 'QBO', regardless of the actual oscillation period). Finally, we conduct a parameter study to investigate the influence that various model parameters - wave amplitude, wavenumber, wave speed, and the strength of diffusion - have on the appearance and characteristics of the QBO generated by the HL equation.

2.2 Fundamental equations

As we are interested in equatorially trapped wave disturbances, it is sufficient to consider the dynamics of the tropical stratosphere on an equatorial beta plane. We assume that the stratosphere consists of a Boussinesq fluid, which is to say that density perturbations will be taken to be small except when coupled to gravity. Waves will be considered as linear disturbances to a background geostrophic zonal wind that varies only in height. Both waves and zonal wind are assumed to be in hydrostatic balance.

Under the Boussinesq assumption, the equations governing the motion of the fluid are (Lindzen [1970], Andrews and McIntyre [1976a]):

$$u_t + uu_x + vu_y + wu_z - \beta yv + \bar{\rho}^{-1}p_x = -X, \tag{2.2.1}$$

$$v_t + uv_x + vv_y + wv_z + \beta yu + \bar{\rho}^{-1}p_y = -Y, \tag{2.2.2}$$

$$p_z = -g(\bar{\rho} + \rho'), \tag{2.2.3}$$

$$\rho_t + u\rho_x + v\rho_y + w\rho_z = -Q, \tag{2.2.4}$$

$$u_x + v_y + w_z = 0. \tag{2.2.5}$$

Equations (2.2.1) and (2.2.2) represent force balances in the zonal (east-west) and meridional (north-south) directions respectively, in accordance with Newton's Second Law. Equation (2.2.3) is the vertical force balance, which is assumed to reflect hydrostatic balance. Equation (2.2.4) is the thermodynamic equation, and equation (2.2.5) is the continuity equation. Subscripts represent derivatives. x, y, and z are the eastward, northward and upward directions, u, v, and w are the corresponding directional wind fields, p and ρ are the fluid pressure and density, and X, Y, and Q are unspecified dissipation terms. $\beta = 2\Omega a^{-1}$ represents the linear variation of the Coriolis force with latitude at the equator, with the Earth's radius and angular speed of rotation given by $a = 6{,}370\,\mathrm{km}$ and $\Omega = 7.292 \times 10^{-5}\,\mathrm{rad\,s^{-1}}$ respectively. Each field ψ can be expressed as the sum of a zonal mean part and a perturbation about that mean, as represented by quantities with overbars and primes respectively: $\psi(x, y, z, t) = \overline{\psi}(y, z, t) + \psi'(x, y, z, t)$. Here the zonal mean is defined as

$$\overline{\psi}(y, z, t) = \frac{1}{2\pi a} \int_0^{2\pi a} \psi(x, y, z, t) dx, \tag{2.2.6}$$

and $2\pi a$ is the length of the latitude circle at the equator.

2.2.1 The zonal mean flow

We assume that the mean zonal wind varies in altitude only, $\bar{u} = \bar{u}(z, t)$. Applying the zonal averaging operator (2.2.6) to (2.2.1)–(2.2.5) and performing some standard manipulations (Holton and Hakim [2012], p. 329) yields the following zonally averaged equations:

$$\bar{u}_t - \beta y \bar{v} + \overline{w} \bar{u}_z = -(\overline{u'v'})_y - (\overline{u'w'})_z - \overline{X}, \tag{2.2.7}$$

$$\bar{v}_t + \bar{v}\bar{v}_y + \overline{w}\bar{v}_z + \beta y \bar{u} + \bar{\rho}^{-1}\bar{p}_y = -(\overline{v'^2})_y - (\overline{v'w'})_z - \overline{Y}, \tag{2.2.8}$$

$$\bar{p}_z + g\bar{\rho} = 0, \tag{2.2.9}$$

$$\bar{\rho}_t + \bar{v}\bar{\rho}_y + \overline{w}\bar{\rho}_z = -(\overline{v'\rho'})_y - (\overline{w'\rho'})_z - \overline{Q}, \tag{2.2.10}$$

$$\bar{v}_y + \overline{w}_z = 0. \tag{2.2.11}$$

If the right hand sides are zero we get a steady solution representing a purely zonal flow $\bar{u}(z)$ in geostrophic and hydrostatic balance, with $\partial/\partial t = \bar{v} = \overline{w} = 0$. The basic state equations are given by

$$\beta y\bar{u} = -\bar{\rho}^{-1}\bar{p}_y, \tag{2.2.12}$$

$$\bar{p}_z = -g\bar{\rho}. \tag{2.2.13}$$

Substituting $\frac{\partial}{\partial y}$(2.2.13) into $\frac{\partial}{\partial z}$(2.2.12), using the Boussinesq approximation and integrating in y, we get the basic density in terms of the zonal wind:

$$\ln\bar{\rho} = \frac{\beta y^2}{2g}\frac{d\bar{u}}{dz} + F(z), \tag{2.2.14}$$

where $F(z)$ is some arbitrary function of height. We choose

$$F(z) = -\frac{N^2 z}{g}, \tag{2.2.15}$$

where $N^2 = 4.41 \times 10^{-4}\,\mathrm{s}^{-1}$ is the Brunt-Väisälä frequency, a measure of static stability. By choosing the basic state such that

$$\left|\frac{N^2}{g}\right| \gg \left|\frac{\beta y^2}{2g}\frac{d^2\bar{u}}{dz^2}\right|, \tag{2.2.16}$$

we can approximate

$$\begin{aligned} -g\frac{\partial\ln\bar{\rho}}{\partial z} &\approx N^2, \\ -g\frac{\partial\ln\bar{\rho}}{\partial y} &\approx -\beta y\bar{u}_z. \end{aligned} \tag{2.2.17}$$

In section 2.2.3 we will use $\bar{u}$, $\bar{p}$ and $\bar{\rho}$ defined above as the quasi-stationary basic state about which the wave perturbations are excited.

2.2.2 The Holton-Lindzen equation

As detailed in equations (2.2.7)–(2.2.11), the evolution of the zonal mean state is modified by converging wave fluxes, advection due to wave-induced meridional circulations, and dissipation. Direct physical interpretation of these equations is not straightforward, however, as the effects of the wave drag and meridional circulations often act in concert and mitigation of each other. In order to derive a physically coherent and consistent interpretation of the interaction between the waves and the zonal mean flow, it is advantageous to recast the zonal mean evolution equation into Transformed Eulerian Mean (TEM) form (Andrews and McIntyre [1976a, 1978]). To do this we introduce a residual mean meridional circulation $(0, \bar{v}^*, \overline{w}^*)$ defined by

$$
\begin{aligned}
\bar{v}^* &= \bar{v} - \bar{\rho}^{-1} \left(\overline{v'\rho'}/\bar{\rho}_z \right)_z , \\
\overline{w}^* &= \overline{w} + \left(\overline{v'\rho'}/\bar{\rho}_z \right)_y .
\end{aligned}
\tag{2.2.18}
$$

Substituting into (2.2.7) and rearranging gives the TEM form of the zonal mean zonal wind evolution:

$$
\bar{u}_t - \beta y \bar{v}^* + \overline{w}^* \bar{u}_z = -\frac{1}{\bar{\rho}} \nabla \cdot \boldsymbol{F} - \overline{X}. \tag{2.2.19}
$$

Here we have reintroduced density variations in a way that is compatible with the Boussinesq approximation. The vector $\boldsymbol{F} = (0, \mathcal{F}^{(y)}, \mathcal{F}^{(z)})$ is known as the Eliassen-Palm (EP) flux, and its components are given by

$$
\begin{aligned}
\mathcal{F}^{(y)} &= \bar{\rho}_c \left[\overline{u'v'} - \bar{u}_z \overline{v'\rho'}/\bar{\rho}_z \right] , \\
\mathcal{F}^{(z)} &= \bar{\rho}_c \left[\overline{u'w'} - \beta y \overline{v'\rho'}/\bar{\rho}_z \right] .
\end{aligned}
\tag{2.2.20}
$$

Here $\bar{\rho}_c$ is the (constant) density at the tropopause. For waves in the equatorial stratosphere, the meridional circulation terms in (2.2.19) can be neglected to a first approximation (Andrews and McIntyre [1976a]). We define a meridional average as

$$\langle \phi \rangle = \frac{1}{L} \int_{-\infty}^{\infty} \phi \, dy, \tag{2.2.21}$$

where $L \approx 1200\,\mathrm{km}$ is the meridional scale of the mean flow. Applying the above to (2.2.19), and recalling that disturbances vanish as $y \to \pm\infty$, we get:

$$\frac{\partial \langle \bar{u} \rangle}{\partial t} = -\frac{1}{\bar{\rho}} \frac{\partial \langle \mathcal{F}^{(z)} \rangle}{\partial z} + \Lambda(z) \frac{\partial^2 \langle \bar{u} \rangle}{\partial z^2}, \tag{2.2.22}$$

where we have further assumed that $-\bar{X}$ takes the form of a diffusion term. The above equation is known as the Holton-Lindzen (HL) equation. In essence, it states that the acceleration of the zonal wind is given by the sum of diffusion and the vertical component of the EP fluxes of the wave quantities of interest.

2.2.3 Perturbation equations

We derive the equations for the perturbed quantities, assuming that the dissipation terms are given by Rayleigh friction and Newtonian cooling, with the forms

$$(X', Y', Q') = -\alpha(u', v', \rho'). \tag{2.2.23}$$

Here α is a constant. We also introduce a geopotential $\Phi' = \frac{p'}{\bar{\rho}}$, so that approximately

$$\frac{\partial \Phi'}{\partial y} \approx \frac{1}{\bar{\rho}} \frac{\partial p'}{\partial y}, \tag{2.2.24}$$

$$\frac{\partial \Phi'}{\partial z} \approx \frac{1}{\bar{\rho}} \frac{\partial p'}{\partial z}, \tag{2.2.25}$$

which is consistent with the Boussinesq approximation. By expressing each field in equations (2.2.1)–(2.2.5) as the sum of a zonal mean part and wave part, substituting for the basic state fields using (2.2.12), (2.2.13), and (2.2.17), neglecting products of wave quantities, and replacing pressure with geopotential using (2.2.24)–(2.2.25), we get the following linearized equations for the perturbed quantities:

$$u'_t + \bar{u}u'_x + w'\bar{u}_z - \beta y v' = -\Phi'_x - \alpha u', \tag{2.2.26}$$

$$v'_t + \bar{u}v'_x + +\beta y u' = -\Phi'_y - \alpha v', \tag{2.2.27}$$

$$\Phi'_z = -g\frac{\rho'}{\bar{\rho}}, \tag{2.2.28}$$

$$\Phi'_{zt} + \bar{u}\Phi'_{zx} - \beta y v'\bar{u}_z + w'N^2 = -\alpha\Phi'_z, \tag{2.2.29}$$

$$u'_x + v'_y + w'_z = 0. \tag{2.2.30}$$

We assume that the perturbations exhibit wave-like behaviour in x and t, and so introduce

$$u'(x, y, z, t) = \mathrm{Re}\left(\hat{u}(y, z)e^{i(kx-\omega t)}\right), \tag{2.2.31}$$

and similarly for v', w', ρ' and Φ'. Here k and ω are the (real) wavenumber and angular frequency respectively. Substitution into (2.2.26)–(2.2.30) yields:

$$i\hat{\omega}\hat{u} + \hat{w}\bar{u}_z - \beta y\hat{v} = -ik\hat{\Phi}, \tag{2.2.32}$$

$$i\hat{\omega}\hat{v} + \beta y\hat{u} = -\hat{\Phi}_y, \tag{2.2.33}$$

$$\hat{\Phi}_z = -g\frac{\hat{\rho}}{\bar{\rho}}, \tag{2.2.34}$$

$$i\hat{\omega}\hat{\Phi}_z - \beta y\bar{u}_z\hat{v} + \hat{w}N^2 = 0, \tag{2.2.35}$$

$$ik\hat{u} + \hat{v}_y + \hat{w}_z = 0, \tag{2.2.36}$$

where we have introduced

$$\hat{\omega} = -\omega + k\bar{u} - i\alpha. \tag{2.2.37}$$

2.3 Equatorial waves in a constant mean flow

We review the simplest case where $\bar{u}$ = constant, and $\alpha = 0$. For comparison with later results it proves convenient to introduce re-scaled variables $Y = \frac{y}{l}$ and $\hat{z} = fz$, where l and f are constant scaling factors to be chosen later. Substituting into equations (2.2.32)–(2.2.36) and setting $\bar{u}_z = 0$ yields:

$$i\hat{\omega}\hat{u} - \beta lY\hat{v} = -ik\hat{\Phi}, \tag{2.3.1}$$

$$i\hat{\omega}\hat{v} + \beta lY\hat{u} = -\frac{1}{l}\hat{\Phi}_Y, \tag{2.3.2}$$

$$f\hat{\Phi}_{\hat{z}} = -\frac{g\rho'}{\bar{\rho}}, \tag{2.3.3}$$

$$i\hat{\omega}f\hat{\Phi}_{\hat{z}} + \hat{w}N^2 = 0, \tag{2.3.4}$$

$$ik\hat{u} + \frac{1}{l}\hat{v}_Y + f\hat{w}_{\hat{z}} = 0. \tag{2.3.5}$$

Using (2.3.4) to eliminate $\hat{w}$ from (2.3.5), we get:

$$ik\hat{u} + \frac{1}{l}\hat{v}_Y - i\hat{\omega}\frac{f^2}{N^2}\hat{\Phi}_{\hat{z}\hat{z}}. \tag{2.3.6}$$

From (2.3.1) and (2.3.2) we see that both $\hat{u}$ and $\hat{v}$ can be expressed as linear combinations of $\hat{\Phi}$ and $\hat{\Phi}_Y$; this implies that $\hat{\Phi}$, $\hat{u}$, and $\hat{v}$ must all share the same vertical structure. By defining

$$\left[\hat{u}(Y,\hat{z}), \hat{v}(Y,\hat{z}), \hat{\Phi}(Y,\hat{z})\right] = G(\hat{z})\left[\tilde{u}(Y), \tilde{v}(Y), \tilde{\Phi}(Y)\right] \tag{2.3.7}$$

and substituting into (2.3.1), (2.3.2), and (2.3.6), we can separate the variables. Both (2.3.1) and (2.3.2) lose a factor of $G(\hat{z})$, while (2.3.6) becomes

$$\underbrace{\frac{ik\tilde{u} + \tilde{v}_Y/l}{i\hat{\omega}\tilde{\Phi}}}_{\text{function of } Y \text{ only}} = \underbrace{\frac{f^2}{N^2}\frac{G''}{G}}_{\text{function of } \hat{z} \text{ only}} = -\frac{1}{gh}, \tag{2.3.8}$$

where h is a separation constant.

To summarize, we have a set of four equations consisting of a vertical structure equation:

$$G'' + \frac{N^2}{f^2 gh} G = 0, \tag{2.3.9}$$

and three horizontal structure equations:

$$i\hat{\omega}\tilde{u} - \beta l Y \tilde{v} = -ik\tilde{\Phi}, \tag{2.3.10}$$

$$i\hat{\omega}\tilde{v} + \beta l Y \tilde{u} = -\frac{1}{l}\tilde{\Phi}_Y, \tag{2.3.11}$$

$$ik\tilde{u} + \frac{1}{l}\tilde{v}_Y = -\frac{i\hat{\omega}}{gh}\tilde{\Phi}. \tag{2.3.12}$$

Picking $f = \frac{N}{\sqrt{gh}}$, the vertical structure equation can be solved immediately to yield

$$\begin{aligned} G(\hat{z}) &= A\exp(i\hat{z}) + B\exp(-i\hat{z}) \\ &= A\exp(i|m|z) + B\exp(-i|m|z), \end{aligned} \tag{2.3.13}$$

where $|m| = f = \frac{N}{\sqrt{gh}}$ is the absolute vertical wavenumber.

2.3.1 The Kelvin wave

We now turn to the horizontal structure equations, and consider first the special case of a wave for which $\tilde{v} = 0$ - this is known as the Kelvin wave. For this special case we can divide (2.3.10) by (2.3.12) to give:

$$\frac{\hat{\omega}^2}{k^2} = gh = \frac{N^2}{m^2} \implies \hat{\omega} = \pm\frac{Nk}{|m|}. \tag{2.3.14}$$

The corresponding group velocity is

$$c_g^{(z)} = \frac{\partial\omega}{\partial m} = -\frac{\partial\hat{\omega}}{\partial|m|}\frac{\partial|m|}{\partial m} = \pm\,\mathrm{sgn}\,(m)\frac{Nk}{m^2}. \tag{2.3.15}$$

As we are interested in waves that propagate energy upwards through the stratosphere we want the group velocity to be positive, which for $k > 0$ corresponds to

$$\hat{\omega} = \frac{Nk}{m}. \tag{2.3.16}$$

Hence $\hat{\omega}$ and m must share the same sign for the wave to propagate energy upward. We note from (2.3.16) that the Kelvin wave has the same dispersion relation as a pure internal gravity wave with no meridional component (Andrews et al. [1987]).

The latitudinal structure of the Kelvin wave can be deduced from (2.3.11) by substituting for $\tilde{u}$ using (2.3.10) and integrating immediately to give

$$\begin{aligned} \tilde{\Phi} &= A_0 \exp\left(\frac{\beta l^2 Y^2}{2}\frac{k}{\hat{\omega}}\right) \\ &= A_0 \exp\left(-\frac{Y^2}{2}\right). \end{aligned} \tag{2.3.17}$$

Here A_0 is a constant, and we have chosen l such that $\beta l^2 = -\hat{\omega}/k$. Since we want the perturbations to decay away from the equator, it is necessary to impose the condition

$$\frac{\hat{\omega}}{k} < 0, \tag{2.3.18}$$

which for $k > 0$ implies that the wave phase speed $c = \omega/k > \bar{u}$, so that the Kelvin wave is always westerly (i.e. eastward) with respect to the background wind. Further, $\hat{\omega} < 0 \implies m < 0$ by (2.3.16), and so $f = -m$ and we set $A = 0$ in (2.3.13) as it is the amplitude of a wave mode with downward energy propagation.

2.3.2 Waves with non-zero meridional velocities

For the general case where $\tilde{v} \neq 0$, it is necessary to solve the full horizontal structure equations (2.3.10)–(2.3.12). These may be combined and re-expressed as a single differential equation in either $\tilde{v}$ or $\tilde{\Phi}$. In the former case this is achieved by using

(2.3.10) and (2.3.12) to express $\tilde{u}$ and $\tilde{\Phi}$ as functions of $\tilde{v}$ and $\tilde{v}_Y$:

$$\begin{pmatrix} i\hat{\omega} & ik \\ ik & \frac{i\hat{\omega}}{gh} \end{pmatrix} \begin{pmatrix} \tilde{u} \\ \tilde{\Phi} \end{pmatrix} = \begin{pmatrix} \beta l Y \tilde{v} \\ -\frac{1}{l}\tilde{v}_Y \end{pmatrix} \implies \begin{pmatrix} \tilde{u} \\ \tilde{\Phi} \end{pmatrix} = \frac{1}{\frac{\hat{\omega}^2}{gh} - k^2} \begin{pmatrix} \frac{\hat{\omega}}{gh} & -k \\ -k & \hat{\omega} \end{pmatrix} \begin{pmatrix} -i\beta l Y \tilde{v} \\ \frac{i}{l}\tilde{v}_Y \end{pmatrix}. \tag{2.3.19}$$

Taking derivatives as appropriate and substituting into (2.3.11), we get a single equation for $\tilde{v}$:

$$\tilde{v}_{YY} + \left[\left(\frac{\hat{\omega}^2 l^2}{gh} + \frac{k\beta l^2}{\hat{\omega}} - l^2 k^2\right) - \left(\frac{\beta^2 l^4}{gh}\right) Y^2\right] \tilde{v} = 0. \tag{2.3.20}$$

Alternatively, one could express $\tilde{u}$ and $\tilde{v}$ as functions of $\tilde{\Phi}$ and $\tilde{\Phi}_Y$ in a similar manner, in which case the resulting equation is

$$\frac{1}{l^2}\tilde{\Phi}_{YY} - \frac{2\beta^2 Y}{\beta^2 l^2 Y^2 - \hat{\omega}^2}\tilde{\Phi}_Y + \left[\frac{k\beta}{\hat{\omega}} \frac{\beta^2 l^2 Y^2 + \hat{\omega}^2}{\beta^2 l^2 Y^2 - \hat{\omega}^2} - k^2 - \frac{\beta^2 l^2 Y^2 - \hat{\omega}^2}{gh}\right] \tilde{\Phi} = 0. \tag{2.3.21}$$

This form will be used in the general case when the zonal wind varies with altitude. For now, however, we focus on equation (2.3.20). By defining

$$\hat{a} = \frac{\hat{\omega}^2 l^2}{gh} + \frac{k\beta l^2}{\hat{\omega}} - l^2 k^2, \tag{2.3.22}$$

$$\hat{b}^2 = \frac{\beta^2 l^4}{gh}, \tag{2.3.23}$$

(2.3.20) takes the form

$$\tilde{v}_{YY} + \left[\hat{a} - \hat{b}^2 Y^2\right] \tilde{v} = 0. \tag{2.3.24}$$

Together with the boundary conditions $\tilde{v} \to 0$ as $Y \to \pm\infty$, this is the same equation as appears in studies of the quantum harmonic oscillator. Choosing l such that

$$\beta^2 l^4 = gh = \frac{N^2}{m^2}, \tag{2.3.25}$$

we get an infinite set of solutions to (2.3.24) of the form

$$\begin{aligned}\tilde{v} &= A_0 H_n (Y) \exp\left(-\frac{Y^2}{2}\right) \\ &= A_0 H_n \left(\left(\frac{\beta|m|}{N}\right)^{\frac{1}{2}} y\right) \exp\left(-\frac{\beta|m|}{2N} y^2\right),\end{aligned} \tag{2.3.26}$$

for $n = 0, 1, 2, \ldots$. Here A_0 is a constant, and H_n is the Hermite polynomial of order n. The dispersion relation is given for each n as $\hat{a} = (2n+1)\hat{b}$, which in this case is

$$\frac{N}{\beta|m|}\left[\frac{\hat{\omega}^2 m^2}{N^2} + \frac{k\beta}{\hat{\omega}} - k^2\right] = 2n + 1. \tag{2.3.27}$$

For each $n \geq 1$ the various roots $m(\hat{\omega})$ of (2.3.27) correspond to wave modes that are classified as either equatorial inertia-gravity waves or equatorial Rossby waves. The $n = 0$ mode constitutes a special case and is known as a mixed Rossby-gravity (MRG) wave; it is a key component of the easterly forcing of the QBO (Baldwin et al. [2001]).

As our simple model utilises only the equatorial Kelvin wave discussed in the previous section, we will not discuss the properties of these waves any further. Interested readers are directed to Andrews et al. [1987] for details.

2.4 Equatorial waves in vertical shear $\bar{u}(z)$

We consider the case of equatorial wave propagation through a height-varying background wind $\bar{u}(z)$, with a focus on the equatorial Kelvin wave. Our discussion in this section closely follows that of Lindzen [1970, 1971]. To aid in our analysis we assume that the Richardson number is large in the stratosphere, which means that

$$\mathrm{Ri}^{-1} = \frac{\bar{u}_z^2}{N^2} \ll 1. \tag{2.4.1}$$

This condition holds true so long as the basic zonal wind shear is weak relative to the background density stratification, which is generally the case in the equatorial stratosphere away from wave critical levels. By neglecting terms that are $\mathcal{O}(\mathrm{Ri}^{-1})$, it is possible to combine equations (2.2.32)–(2.2.36) into a single equation for the dynamics of $\hat{\Phi}$:

$$\begin{aligned}(\beta^2y^2-\hat{\omega}^2)\hat{\Phi}_{zz} \quad &+ \quad 2\beta y\bar{u}_z\hat{\Phi}_{zy}+N^2\hat{\Phi}_{yy}+\beta\bar{u}_z\left[\frac{\beta y^2}{N^2}\bar{u}_{zz}-\frac{\beta^2y^2+\hat{\omega}^2}{\beta^2y^2-\hat{\omega}^2}\right]\hat{\Phi}_z \\ &- \quad \frac{2N^2\beta^2y}{\beta^2y^2-\hat{\omega}^2}\hat{\Phi}_y+\frac{N^2k}{\hat{\omega}}\left[\beta\frac{\beta^2y^2+\hat{\omega}^2}{\beta^2y^2-\hat{\omega}^2}-k\hat{\omega}\right]\hat{\Phi}=0. \qquad (2.4.2)\end{aligned}$$

The derivation of this equation is outlined in Appendix A. The boundary conditions are (Lindzen [1970, 1971]):

$$\begin{cases}\hat{\Phi}\to 0, & y^2\to\infty,\\ \hat{\Phi}=f(y), & z=17\,\mathrm{km},\\ \hat{\Phi}\to 0, & z\to\infty.\end{cases} \qquad (2.4.3)$$

Other perturbed variables may then be derived from $\hat{\Phi}$ via:

$$\frac{\hat{\rho}}{\bar{\rho}}=-\frac{1}{g}\hat{\Phi}_z, \qquad (2.4.4)$$

$$\hat{v}=\frac{1}{\beta^2y^2-\hat{\omega}^2}\left[ik\beta y\hat{\Phi}-i\hat{\omega}\left(\frac{\beta y}{N^2}\bar{u}_z\hat{\Phi}_z+\hat{\Phi}_y\right)\right], \qquad (2.4.5)$$

$$\hat{u}=-\frac{1}{\beta y}\left(\hat{\Phi}_y+i\hat{\omega}\hat{v}\right), \qquad (2.4.6)$$

$$\hat{w}=\frac{1}{N^2}\left(-i\hat{\omega}\hat{\Phi}_z+\beta y\bar{u}_z\hat{v}\right). \qquad (2.4.7)$$

The partial differential equation (2.4.2) is hyperbolic near the equator, thus admitting wave-like solutions. Beyond the critical latitudes where $y=\pm\beta\hat{\omega}$, the equation is elliptic and perturbations decay with latitude. Lindzen [1970] has argued that the wave solutions are continuous through the critical latitudes, and this claim has been verified in numerical simulations. Thus, (2.4.2) is a good model for equatorially trapped waves.

In order to make analytical progress with (2.4.2) we adopt a WKB approximation (Lindzen [1971]). The key assumption in this approach is that the characteristic vertical scale for variations of the zonal mean flow is much larger than the characteristic vertical scale of the waves. Since the latter quantity is generally quite small (around 1-2 km), this assumption is justifiable. We then introduce so-called 'short' and 'tall' height-scales $\hat{z}$ and τ as follows:

$$\hat{z} = \int_{z_0}^{z} f(\tau) dz, \tag{2.4.8}$$

$$\tau = \epsilon z, \tag{2.4.9}$$

where $\epsilon \ll 1$, $z_0 = 17\,\text{km}$ is height of the tropopause, and f is to be chosen later. We also re-scale the latitude variable by introducing

$$y = lY, \tag{2.4.10}$$

where $l(\tau) = l_0(\tau) + \epsilon l_1(\tau) + \dots$, and the l_i are also to be set over the course of the solution.

Following Lindzen [1971], we will assume that the zonal wind variation is solely a function of the tall scale, i.e. $\bar{u} = \bar{u}(\tau)$ only. The wave variables, however, are assumed to depend on both the short and tall scales, e.g. $\hat{\Phi} = \hat{\Phi}(\tau, \hat{z}, Y)$. We can re-express y and z derivatives in terms of the new variables, for example:

$$\begin{aligned}
\bar{u}_z &= \epsilon \bar{u}_\tau, \\
\hat{\Phi}_y &= \frac{1}{l}\hat{\Phi}_Y, \\
\hat{\Phi}_z &= \epsilon\hat{\Phi}_\tau + f(\tau)\hat{\Phi}_{\hat{z}} - \epsilon Y \frac{d\ln l}{d\tau}\hat{\Phi}_Y.
\end{aligned} \tag{2.4.11}$$

Similar expressions can be derived for the higher derivatives (see Lindzen [1971] equations 20(a)-(e) for details). Substitution into (2.4.2) then yields

$$\begin{aligned}
&(\beta^2 l^2 Y^2 - \hat{\omega}^2)^2 \left[f^2 \hat{\Phi}_{\hat{z}\hat{z}} + \epsilon\left(2f\hat{\Phi}_{\hat{z}\tau} + f'\hat{\Phi}_{\hat{z}} - 2fY\frac{d\ln l}{d\tau}\hat{\Phi}_{\hat{z}Y}\right) + \mathcal{O}(\epsilon^2)\right] \\
&\quad + 2\beta Y l(\beta^2 l^2 Y^2 - \hat{\omega}^2)\epsilon\bar{u}_\tau \left[\frac{f}{l}\hat{\Phi}_{\hat{z}Y} + \mathcal{O}(\epsilon)\right] + N^2(\beta^2 l^2 Y^2 - \hat{\omega}^2)\frac{1}{l^2}\hat{\Phi}_{YY} \\
&\quad + \beta\bar{u}_\tau\epsilon\left[-(\beta^2 l^2 Y^2 + \hat{\omega}^2) + \mathcal{O}(\epsilon^2)\right]\left[f\hat{\Phi}_{\hat{z}} + \mathcal{O}(\epsilon)\right] - 2N^2\beta^2 Y\hat{\Phi}_Y \\
&\quad + \frac{N^2 k}{\hat{\omega}}\left[\beta(\beta^2 l^2 Y^2 + \hat{\omega}^2) - k\hat{\omega}(\beta^2 l^2 Y^2 - \hat{\omega}^2)\right]\hat{\Phi} = 0.
\end{aligned} \tag{2.4.12}$$

2.4.1 Zeroth order solution

We substitute $\hat{\Phi} = \hat{\Phi}_0 + \epsilon\hat{\Phi}_1 + \ldots$ and $l = l_0(\tau) + \epsilon l_1(\tau) + \ldots$ into (2.4.12) and group accordingly to obtain a differential equation for $\hat{\Phi}_i$ at each order of ϵ. The zeroth order equation is:

$$\begin{aligned}
f^2\hat{\Phi}_{0\hat{z}\hat{z}} + \frac{N^2}{l_0^2}\frac{1}{\beta^2 l_0^2 Y^2 - \hat{\omega}^2}\hat{\Phi}_{0YY} - \frac{N^2}{l_0^2}\frac{2\beta^2 l_0^2 Y}{(\beta^2 l_0^2 Y^2 - \hat{\omega}^2)^2}\hat{\Phi}_{0Y} \\
+ \frac{N^2 k}{\hat{\omega}}\left[\beta\frac{\beta^2 l_0^2 Y^2 + \hat{\omega}^2}{(\beta^2 l_0^2 Y^2 - \hat{\omega}^2)^2} - \frac{k\hat{\omega}}{\beta^2 l_0^2 Y^2 - \hat{\omega}^2}\right]\hat{\Phi}_0 = 0.
\end{aligned} \tag{2.4.13}$$

This equation is separable by introducing $\hat{\Phi}_0(\tau, \hat{z}, Y) = \varphi(\tau, Y)L(\hat{z})$. If we express the separation constant as $-{}^1\!/_{gh}$ as in (2.3.8), we then get the vertical structure equation in the form

$$\frac{d^2L}{d\hat{z}^2} + \frac{N^2}{f^2gh}L = 0. \tag{2.4.14}$$

The corresponding horizontal structure equation is

$$\frac{1}{l_0^2}\varphi_{YY} - \frac{2\beta^2 Y}{\beta^2 l_0^2 Y^2 - \hat{\omega}^2}\varphi_Y + \left[\frac{k\beta}{\hat{\omega}}\frac{\beta^2 l_0^2 Y^2 + \hat{\omega}^2}{\beta^2 l_0^2 Y^2 - \hat{\omega}^2} - k^2 - \frac{\beta^2 l_0^2 Y^2 - \hat{\omega}^2}{gh}\right]\varphi = 0. \tag{2.4.15}$$

Note that these equations are identical to equations (2.3.9) and (2.3.21), except that now φ is a function of both the tall variable τ and latitude Y. Hence, the zeroth order solutions are the same as the solutions in the $\bar{u}$ =constant case discussed in section 2.3, with $\beta^2 l_0^4 = N^2/f^2 = gh$. The integration 'constant', however, is now a function of τ: $A_0 = A_0(\tau)$. For example, the geopotential of the Kelvin wave, (2.3.17) is given by

$$\hat{\Phi}_0 = A_0(\tau)\exp\left(-\frac{1}{2}Y^2\right)\exp\left(-i\hat{z}\right). \tag{2.4.16}$$

2.4.2 $\mathcal{O}(\epsilon)$ Analysis

To complete the zeroth order solutions we must determine $A_0(\tau)$, and therefore it is necessary to study the next order in ϵ. The $\mathcal{O}(\epsilon)$ balance of (2.4.12) yields the following equation for $\hat{\Phi}_1$:

$$\begin{aligned} f^2\hat{\Phi}_{1\hat{z}\hat{z}} + \frac{N^2}{l_0^2}\frac{1}{\beta^2 l_0^2 Y^2 - \hat{\omega}^2}\hat{\Phi}_{1YY} - \frac{N^2}{l_0^2}\frac{2\beta^2 l_0^2 Y}{(\beta^2 l_0^2 Y^2 - \hat{\omega}^2)^2}\hat{\Phi}_{1Y} \\ + \frac{N^2 k}{\hat{\omega}}\left[\beta\frac{\beta^2 l_0^2 Y^2 + \hat{\omega}^2}{(\beta^2 l_0^2 Y^2 - \hat{\omega}^2)^2} - \frac{k\hat{\omega}}{\beta^2 l_0^2 Y^2 - \hat{\omega}^2}\right]\hat{\Phi}_1 \\ = -I_1 - \frac{I_2}{\beta^2 l_0^2 Y^2 - \hat{\omega}^2} - \frac{I_3}{(\beta^2 l_0^2 Y^2 - \hat{\omega}^2)^2}, \end{aligned} \tag{2.4.17}$$

where I_1, I_2, and I_3 are given by

$$I_1 = 2f\hat{\Phi}_{0\hat{z}\tau} + f'\hat{\Phi}_{0\hat{z}} - 2fY\frac{d\ln l_0}{d\tau}\hat{\Phi}_{0Y\hat{z}}, \tag{2.4.18}$$

$$I_2 = 4l_0l_1\beta^2Y^2f^2\hat{\Phi}_{0\hat{z}\hat{z}} + 2\beta Y\bar{u}_\tau f\hat{\Phi}_{0\hat{z}Y} - 2N^2\frac{l_1}{l_0^3}\hat{\Phi}_{0YY}, \tag{2.4.19}$$

$$I_3 = 2N^2\beta^2Y^2\frac{l_1}{l_0}\hat{\Phi}_{0YY} - \beta\bar{u}_\tau f(\beta^2l_0^2Y^2 + \hat{\omega}^2)\hat{\Phi}_{0\hat{z}} + \frac{N^2k}{\hat{\omega}}(2l_0l_1\beta^2Y^2)(\beta - k\hat{\omega})\hat{\Phi}_0. \tag{2.4.20}$$

Note that the LHS of (2.4.17) is the same as equation (2.4.13) for $\hat{\Phi}_0$. Therefore, if any of the terms on the RHS of (2.4.17) have non-zero projections onto $\hat{\Phi}_0$, there will be an unbounded resonant response in $\hat{\Phi}_1$. Our strategy, therefore, is to choose A_0 and l_1 in such a way as to suppress the projection of the RHS terms onto $\hat{\Phi}_0$. (Recall that the projection of a function $\hat{\phi}(Y)$ onto another function $\hat{\psi}(y)$ is given by

$$\int_{-\infty}^{\infty}\hat{\phi}(y)\hat{\psi}(y)dy, \tag{2.4.21}$$

where both $\hat{\phi}$ and $\hat{\psi}$ are square-integrable functions of latitude y).

In his original analysis of this problem, Lindzen [1971] demonstrated that for the Kelvin wave solution, choosing l_1 such that

$$l_1 = -\frac{il_0\bar{u}_\tau}{N} \tag{2.4.22}$$

results in

$$\frac{I_2}{(\beta^2l_0^2Y^2 - \hat{\omega}^2)} + \frac{I_3}{(\beta^2l_0^2Y^2 - \hat{\omega}^2)^2} = 0. \tag{2.4.23}$$

Therefore, with this choice of l_1 it is only necessary to ensure that the projection of I_1 onto $\hat{\Phi}_0$ is zero. Substituting the zero-order solution (2.4.16) for the Kelvin wave geopotential into I_1 gives

$$
\begin{aligned}
I_1 = &-2if\frac{dA_0}{d\tau}\exp\left(-\frac{Y^2}{2}\right)\exp\left(-i\hat{z}\right) \\
&- i\frac{df}{d\tau}A_0\exp\left(-\frac{Y^2}{2}\right)\exp\left(-i\hat{z}\right) \\
&+ 2if\frac{d\ln l_0}{d\tau}Y\hat{\Phi}_{0Y}.
\end{aligned}
\tag{2.4.24}
$$

The first two terms in the above expression are immediately proportional to $\hat{\Phi}_0$; the projection of the third term onto $\hat{\Phi}_0$ is given by

$$
\begin{aligned}
\frac{\int_{-\infty}^{\infty}\left(2if\frac{d\ln l_0}{d\tau}\right)Y\hat{\Phi}_{0Y}\hat{\Phi}_0 dY}{\int_{-\infty}^{\infty}\hat{\Phi}_0^2 dY}\hat{\Phi}_0 &= \left(2if\frac{d\ln l_0}{d\tau}\right)\frac{\int_{-\infty}^{\infty}Y\hat{\Phi}_{0Y}\hat{\Phi}_0 dY}{\int_{-\infty}^{\infty}\hat{\Phi}_0^2 dY}\hat{\Phi}_0 \\
&= -if\frac{d\ln l_0}{d\tau}A_0\exp\left(-\frac{Y^2}{2}\right)\exp\left(-i\hat{z}\right),
\end{aligned}
\tag{2.4.25}
$$

where the integral $J = \int_{-\infty}^{\infty}Y\hat{\Phi}_{0Y}\hat{\Phi}_0 dY$ is evaluated by parts as follows:

$$
\begin{aligned}
J &= \int_{-\infty}^{\infty}Y\hat{\Phi}_{0Y}\hat{\Phi}_0 dY \\
&= \left[Y\hat{\Phi}_0^2\right]_{-\infty}^{\infty} - J - \int_{-\infty}^{\infty}\hat{\Phi}_0^2 dY \\
\implies J &= -\frac{1}{2}\int_{-\infty}^{\infty}\hat{\Phi}_0^2 dY.
\end{aligned}
\tag{2.4.26}
$$

Thus, in order that the projection of I_1 onto $\hat{\Phi}_0$ be equal to zero we set

$$
\begin{aligned}
&-2if\frac{dA_0}{d\tau} - i\frac{df}{d\tau}A_0 - if\frac{d\ln l_0}{d\tau}A_0 = 0 \\
\implies &\frac{d\ln A_0}{d\tau} + \frac{1}{2}\left(\frac{d\ln f}{d\tau} + \frac{d\ln l_0}{d\tau}\right) = 0.
\end{aligned}
\tag{2.4.27}
$$

This last equation can be integrated to give the required expression for $A_0(\tau)$:

$$
A_0 = \frac{C_\Phi}{\sqrt{fl_0}},
\tag{2.4.28}
$$

where C_Φ is a constant of integration.

2.4.3 The HL equation revisited

With (2.4.28) we have completed the derivation of the zeroth order solutions. For the Kelvin wave geopotential, this is:

$$\hat{\Phi}_0 = \frac{C_\Phi}{\sqrt{f l_0}} \exp\left(-i\int_{z_0}^{z} f dz\right) \exp\left(-\frac{1}{2}Y^2\right). \tag{2.4.29}$$

The introduction of non-zero dissipation α introduces a small perturbation to $\hat{\omega} = -\omega + k\bar{u} - i\alpha$, which can be ignored in most of our calculations. Thus we generally approximate

$$-\hat{\omega}/k \approx c - \bar{u}, \tag{2.4.30}$$

where c is the phase speed of the wave. The crucial effect of the dissipation perturbation is to introduce an imaginary part to f, which results in the exponential decrease of wave forcing with height (cf. the first exponential in equation (2.4.29)). Thus for this term only we consider the dissipation-perturbed value of f, which is approximately

$$f = -\frac{Nk}{\hat{\omega}} \approx \frac{N}{c-\bar{u}}\left[1 - \frac{i\alpha}{k(c-\bar{u})}\right]. \tag{2.4.31}$$

The full set of solutions for the Kelvin wave can then be reconstructed using (2.4.4)–(2.4.7) and (2.2.31), giving:

$$\begin{aligned}\left\{\Phi_0', u_0', v_0', w_0', \frac{\rho_0'}{\bar{\rho}}\right\} &= \left\{(c-\bar{u})^{1/4}, (c-\bar{u})^{-3/4}, 0, \frac{k}{N}(c-\bar{u})^{1/4}, \frac{iN}{g}(c-\bar{u})^{-3/4}\right\} \\ &\quad \times C_\Phi \left(\frac{\beta}{N^2}\right)^{1/4} \times \exp\left(\int_{z_0}^{z} \operatorname{Im} f dz\right) \times \exp\left(-\frac{1}{2}Y^2\right) \\ &\quad \times \exp\left(i\left(kx + \omega t - \int_{z_0}^{z} \operatorname{Re} f dz\right)\right).\end{aligned} \tag{2.4.32}$$

We can use the above wave solutions to calculate the vertical component of the Kelvin wave Eliassen-Palm flux (2.2.20). For any wave fields $\phi'_{1,2}$ of the form $\phi'_{1,2} = \hat{\phi}_{1,2} \exp\left(i\left(kx + \chi\right)\right)$, we can calculate $\overline{\phi'_1 \phi'_2}$ using

$$\overline{\phi'_1 \phi'_2} = \frac{1}{2}\left[\mathrm{Re}(\hat{\phi}_1)\,\mathrm{Re}(\hat{\phi}_2) + \mathrm{Im}(\hat{\phi}_1)\,\mathrm{Im}(\hat{\phi}_2)\right]. \tag{2.4.33}$$

Applying (2.2.21) to (2.2.20), substituting for the perturbations from (2.4.32) and finally using (2.4.33), we get

$$\begin{aligned}
\langle \mathcal{F}^{(z)} \rangle &= \rho_c \langle \overline{u'w'} \rangle \\
&= \rho_c \frac{C_\Phi^2}{2L}\frac{k}{N}\left(\frac{\beta}{N^2}\right)^{1/2} (c-\bar{u})^{-1/2} \exp\left(2\int_{z_0}^{z} \mathrm{Im}\, f dz\right)\left(\int_{-\infty}^{\infty} \exp\left(-\frac{Y^2}{2}\right) dy\right) \\
&= \rho_c \frac{C_\Phi^2}{2L}\frac{k}{N^2} \exp\left(2\int_{z_0}^{z} \mathrm{Im}\, f dz\right)\left(\int_{-\infty}^{\infty} \exp\left(-\frac{Y^2}{2}\right) dY\right) \\
&= \rho_c \left(\frac{\sqrt{\pi} C_\Phi^2 k}{2LN^2}\right) \exp\left(-\int_{z_0}^{z} \frac{N(2\alpha)}{k(\bar{u}-c)^2} dz\right) \\
&= \rho_c F \exp\left(-\int_{z_0}^{z} \frac{N\mu}{k(\bar{u}-c)^2} dz\right),
\end{aligned} \tag{2.4.34}$$

where we have defined the amplitude of wave forcing $F = \sqrt{\pi} C_\Phi^2 k / 2LN^2$ and $\mu = 2\alpha$. In the third line we have used that $dy = l_0 dY$, with

$$l_0 = \left(-\frac{\hat{\omega}}{k\beta}\right)^{1/2} = \left(\frac{c-\bar{u}}{\beta}\right)^{1/2}. \tag{2.4.35}$$

Armed with the above expression for $\langle \mathcal{F}^{(z)} \rangle$, we return to the Holton-Lindzen equation (2.2.22). Assuming that the zonal wind is forced by n waves - each defined by a particular wavenumber k_n, wave speed c_n and wave forcing amplitude F_n - we can express $\langle \mathcal{F}^{(z)} \rangle$ as the sum of the n wave contributions $\langle \mathcal{F}_i^{(z)} \rangle$, and then substitute into (2.2.22) to get the zonal mean evolution. Dropping the latitudinal average notation, we have:

$$\frac{\partial \bar{u}}{\partial t} = -\frac{1}{\rho_0}\sum_{i=1}^{n}\frac{\partial \tilde{\mathcal{F}}_i^{(z)}}{\partial z} + \Lambda\frac{\partial^2 \bar{u}}{\partial z^2}, \tag{2.4.36}$$

where $\rho_0 = \bar{\rho}(z)/\rho_c$ and

$$\tilde{\mathcal{F}}_i^{(z)} = F_i \exp\left(-\int_{z_0}^{z}\frac{N\mu}{k_i(\bar{u}-c_i)^2}dz\right). \tag{2.4.37}$$

Following Plumb [1977], we restrict our consideration to the simplest case wherein the zonal wind is forced by just two identical Kelvin/gravity waves travelling in opposite directions. Thus $n = 2$, and we set $k_1 = k_2 = k$, $c_1 = -c_2 = c$, and $F_1 = -F_2 = F$. We also introduce a scale height H_ρ for the density, that is:

$$\rho_0(z) = e^{-\frac{z}{H_\rho}}. \tag{2.4.38}$$

Substituting these into (2.4.37) and (2.4.36) and evaluating the z derivative, we get:

$$\begin{aligned}\frac{\partial \bar{u}}{\partial t} &= Fe^{z/H_\rho}\frac{N\mu}{k(\bar{u}-c)^2}\exp\left\{-\int_{z_0}^{z}\frac{N\mu}{k(\bar{u}-c)^2}dz\right\}\\ &- Fe^{z/H_\rho}\frac{N\mu}{k(\bar{u}+c)^2}\exp\left\{-\int_{z_0}^{z}\frac{N\mu}{k(\bar{u}+c)^2}dz\right\}\\ &+ \Lambda\frac{\partial^2 \bar{u}}{\partial z^2}.\end{aligned} \tag{2.4.39}$$

This is the version of the Holton-Lindzen equation that we will be using throughout the thesis. It describes the evolution of the zonal mean wind as a result of acceleration due to momentum deposition by vertically propagating equatorial waves. The model is based on the following assumptions: (a) the fluid is Boussinesq; (b) the Richardson number is large; (c) the dynamics can be confined on an equatorial beta plane; (d) the waves are dissipated by Rayleigh friction and Newtonian cooling; and (e) the vertical scale of the waves is short compared to the vertical scale of the mean flow.

We take the boundary conditions to be no shear conditions; that is,

$$\frac{\partial \bar{u}}{\partial z}(z_t) = \frac{\partial \bar{u}}{\partial z}(z_b) = 0, \tag{2.4.40}$$

where $z_t = 43\,\mathrm{km}$ and $z_b = 17\,\mathrm{km}$ are the respective upper and lower boundaries of the model domain. In the QBO literature it is more common to choose a no slip condition for the lower boundary, that is, $\bar{u}(z_b) = 0$ (Holton and Lindzen [1972], Plumb [1977], Saravanan [1990], Hampson and Haynes [2004]). However, this is neither a necessary condition for a QBO to form, nor is it a particularly realistic condition, as there is no physical kinematic constraint in the lower stratosphere that so constrains the zonal winds. (The observed weakening of the QBO winds near the tropopause is likely to be a dynamical phenomenon brought about by the increased density at lower levels, which reduces the net acceleration due to the waves). Thus in many respects the no slip condition is too strong a constraint. We have chosen to adopt the more flexible no shear boundary condition at the lower boundary. This mitigates one of the unphysical aspects of the no slip condition by precluding the formation of thin shear zones at the lower boundary. This approach is not without problems, however; notably, the QBO winds descend too low, resulting in the formation of strong QBO jets at the tropopause. However, the overall dynamical behaviour still matches that of the QBO quite well. We tested the model behaviour using both no slip and no shear conditions, and found that the QBO evolution was comparable in both instances.

The version of the Holton-Lindzen equation given by (2.4.39) and (2.4.40) is one of the simplest known models of the QBO. The equation effectively captures the fundamental dynamical mechanism of the QBO phenomenon, despite the fact that that, in practice, the solutions to (2.4.39) do not always satisfy the assumption of weak shear that went into its derivation. As such, it serves as an excellent testing ground for our exploration of QBO synchronization, and we shall make extensive use

Parameter	Description	Value
z_t	Model upper boundary	$43\,\mathrm{km}$
z_b	Model lower boundary	$17\,\mathrm{km}$
F	Wave forcing	$5.4 \times 10^{-3}\ \mathrm{m}^2\,\mathrm{s}^{-2}$
k_0	Wave number	$2\pi/40,000\ \mathrm{km}^{-1}$
c	Wave speed	$30\,\mathrm{m\,s}^{-1}$
μ_0	Dissipation	$10^{-6}\,\mathrm{s}^{-1}$
Λ_0	Diffusion	$0.3\,\mathrm{m}^2\,\mathrm{s}^{-1}$
N	Buoyancy frequency	$2.1 \times 10^{-2}\,\mathrm{s}^{-1}$
H_ρ	Density scale height	$7.64\ \mathrm{km}$

Table 2.1: Standard reference parameters used in the Holton-Lindzen equation (2.4.39). Taken from Holton and Lindzen [1972] and Plumb [1977].

of it in the following chapters.

2.5 Basic properties of the HL equation

2.5.1 Standard parameters and numerical solution

Table 2.1 lists the default set of values used for the different model parameters. Both diffusion and dissipation are assumed to vary with height, and their respective profiles are given by

$$\Lambda(z) = \Lambda_0 P_\Lambda(z) = \Lambda_0 \left[1 + \exp\left(-\frac{z - z_b}{0.1\,\mathrm{km}}\right)\right] \tag{2.5.1}$$

and

$$\mu(z) = \mu_0 P_\mu(z) = \mu_0 \begin{cases} \frac{1}{3} + \frac{1}{3}\left(\frac{z-z_b}{6.5}\right), & z \leq 30\,\mathrm{km}, \\ 1, & z > 30\,\mathrm{km}. \end{cases} \tag{2.5.2}$$

The normalised profiles P_Λ and P_μ are depicted in Figures 2.1(a) and 2.1(b) respectively. The diffusion profile is effectively constant throughout the model except near the bottom boundary, where it rapidly increases to twice the prescribed Λ_0 value.

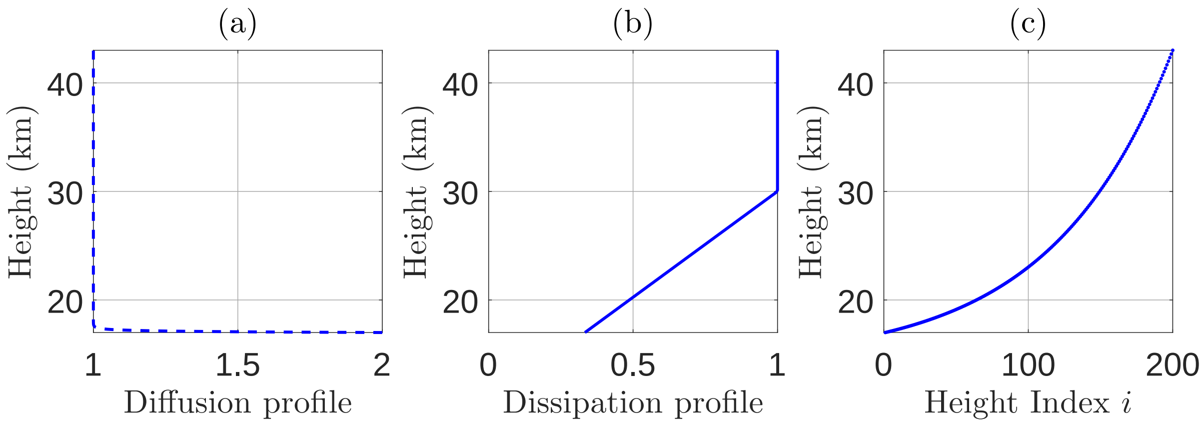

Figure 2.1: (a) Normalised diffusion profile $P_\Lambda(z)$, chosen such that diffusion is effectively constant everywhere except near the lower boundary. (b) Normalised dissipation profile $P_\mu(z)$, which increases linearly from 17 km to 30 km, and is constant above 30 km. (c) Distribution of the height points z_i used in the variable mesh discretization of the HL equation. A shallow gradient indicates a greater local concentration of points.

This increased diffusion was found to be necessary in order to assist in the destruction of QBO wind regimes at the lower boundary of the model. The dissipation profile $\mu(z)$ was taken from Holton and Lindzen [1972].

We solved the HL equation numerically for the given parameters by discretizing (2.4.39) in time with a time step of $\Delta t = 0.25$ days, and in height using a vertical grid with non-uniform spacing such that the height of the i$^{\text{th}}$ grid point z_i is given by

$$z_i = z_b + \left[\frac{r^{i-1} - 1}{r^{n-1} - 1}\right](z_t - z_b). \tag{2.5.3}$$

Here $n = 200$ is the number of grid points, and $r = 1.012$ is the rate of widening of the interval between successive grid points. The distribution of these grid points in height is displayed in Figure 2.1(c); note the non-uniform spread, with more points clustered near the lower boundary and fewer at the upper boundary. This distribution was chosen to provide the best resolution of the shear zones that form near the bottom of the stratosphere in the model.

The discretized equation (2.4.39), together with its boundary conditions (2.4.40),

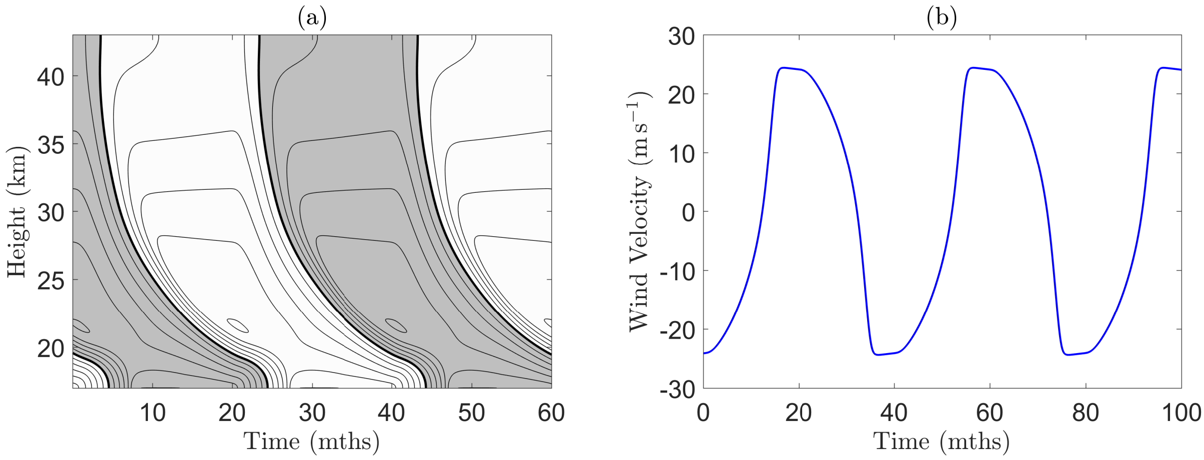

Figure 2.2: Sample solution of the HL equation using the parameters stated in Table 2.1. (a) Contour plot of zonal wind velocities. Easterly winds have been shaded, and the contour interval is $5\,\mathrm{m\,s^{-1}}$. The zero wind line has been darkened. (b) Time series of the zonal wind at 23.5 km.

is solved using an implicit Crank-Nicolson method (Crank and Nicolson [1947]). Results of a test simulation are plotted in Figure 2.2 for the set of parameters listed in Table 2.1, using a parabolic zonal wind configuration as the initial condition. The equation generates a solution that rapidly converges onto a limit cycle closely resembling the QBO. The oscillating solution consists of descending bands of westerly and easterly winds (Figure 2.2(a)), and has a period of 39.7 months. Both westerly and easterly wind regimes descend at the same rate, however, as a consequence of the use of identical wave sources to provide the forcing. The prominent asymmetry between easterly and westerly winds in the real stratosphere (Figure 1.2) is also absent; the amplitude of the oscillation is the same in both easterly and westerly phases at $24.4\,\mathrm{m\,s^{-1}}$, as can be seen from the zonal wind time series at 23.5 km (Figure 2.2(b)).

Figures 2.3(a)–(f) display the evolution of the zonal wind profile over the course of a full oscillation cycle. The dotted horizontal lines in each plot depict the distribution of grid points along the vertical column; note the concentration of points near the lower boundary.

The QBO cycle starts with the onset of an easterly flow regime at the lower boundary (Figure 2.3(a)), which confines the easterly wave to the lower stratosphere and allows the westerly wave to propagate deep into the stratosphere, where it accelerates the upper level winds in an eastward direction. This results in the creation of a westerly shear zone (Figure 2.3(b)) which slowly propagates downward in time. As the westerly shear zone reaches the lower stratosphere (Figure 2.3(c)), it enhances the curvature of the flow, thereby augmenting the strength of diffusion. This results in the collapse of the easterly shear zone (Figure 2.3(d)), and the establishment of a westerly flow regime at the lower boundary which now traps the westerly wave and frees the easterly wave for deep propagation. The same dynamics seen in Figures 2.3(b)–(c) then pertain to the formation (Figure 2.3(e)) and descent (Figure 2.3(f)) of a new easterly shear zone driven by the easterly wave. When this easterly shear approaches the lower boundary, diffusion kicks in again and collapses the prevailing westerly winds - returning us to the situation seen in Figure 2.3(a), and the cycle repeats.

2.5.2 Parameter studies

Having established that the HL equation creates a reasonably realistic QBO, we now investigate how the form of the oscillation depends on the choice of model parameters. In particular, we shall investigate the influence of four parameters on the QBO: wave amplitude (F), diffusion (Λ_0), wave number (k) and wave speed (c). Changes to these parameters will generally affect the period and amplitude of the QBO, as well as the extent of its vertical penetration into the stratosphere. While a single parameter is varied, the values of all the others are fixed at the default values given in Table 2.1.

2.5.2.1 Wave amplitude

Figures 2.4(a) and 2.4(b) demonstrate how variations of the strength of the wave amplitude F affect the QBO amplitude and period. Each plot shows results for 300

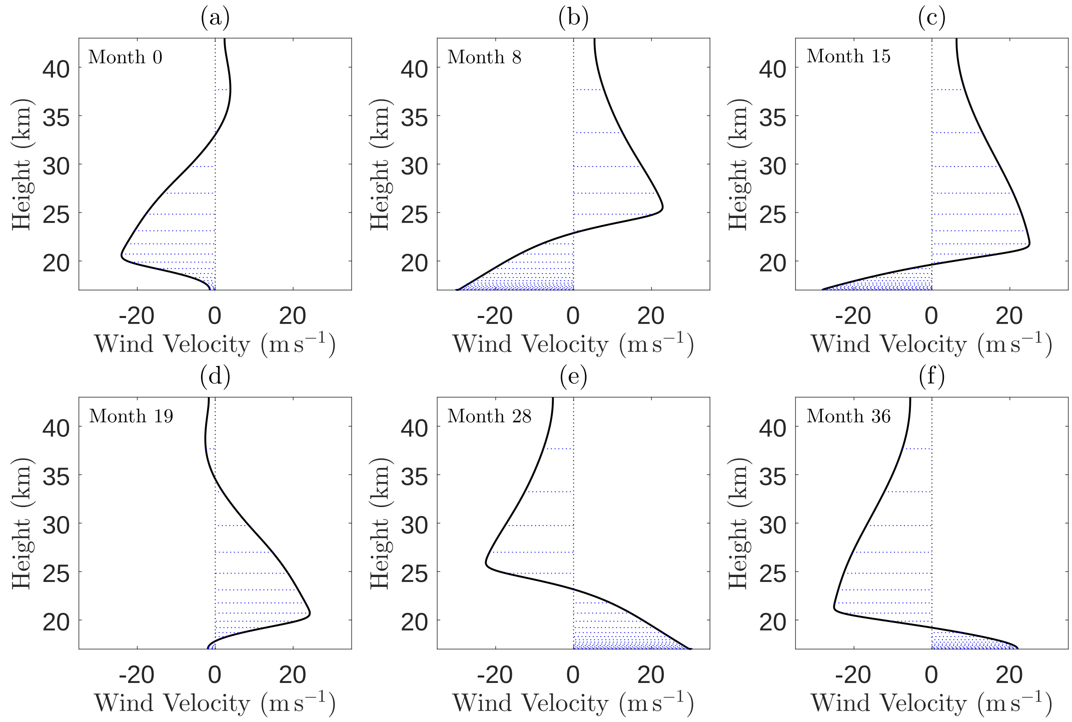

Figure 2.3: Life cycle of a sample QBO generated by the HL equation. Parameters are given in Table 2.1. Refer to text for details.

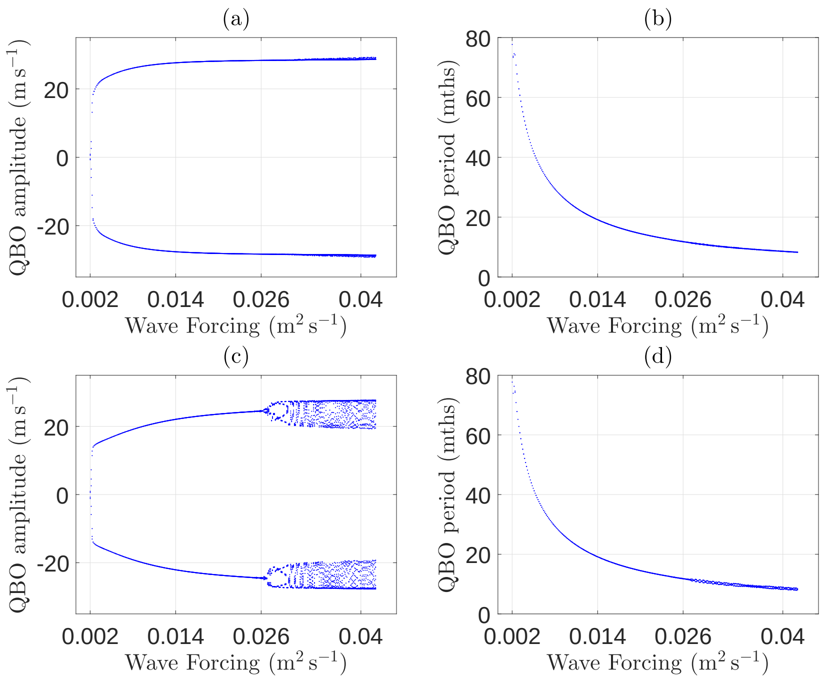

Figure 2.4: Systematic changes to the QBO amplitude and period as wave amplitude F is varied, with all other parameters fixed as in Table 2.1. Plots (a) and (b) present the QBO amplitude maxima and periods as observed at a height of 23.5 km. Corresponding plots for observations at 30 km are presented in (c) and (d).

different values of F, ranging uniformly between $F = 1.0 - 42.1 \times 10^{-3}\mathrm{m}^2\,\mathrm{s}^{-2}$. The amplitudes and periods are both measured at 23.5 km. Amplitudes are recorded as the set of absolute local maxima of the wind time series at that height, and cycle periods are defined as the times between onsets of successive westerly wind regimes.

For small values of F, the wave amplitude is not sufficient to overcome the effects of diffusion (Figure 2.4(a)). As such, the only stable solution is the state of no motion, $\bar{u} = 0$, and so there are no oscillations. As F increases beyond a certain threshold value - approximately $2.0 \times 10^{-3}\,\mathrm{m}^2\,\mathrm{s}^{-2}$ - a limit cycle is born out of a supercritical Hopf bifurcation (Yoden and Holton [1988]), representing the onset of the QBO. As F increases further, the amplitude of the oscillation increases until it saturates at around $28\,\mathrm{m}s^{-1}$, which is close to the wave critical level at $c = 30\,\mathrm{m}s^{-1}$. The wave-forced mean flow cannot accelerate beyond the critical level, at which the wave breaks down and deposits all of its remaining momentum into the mean flow.

After an initial transition period at the start of the simulation, the period of each oscillation cycle is found to remain constant for fixed F. As F increases, the period of the QBO generally decreases (Figure 2.4(b)). The range of F for which the QBO displays periods that are close to observed values of 20–35 months is roughly $F = 6 - 15 \times 10^{-3}\,\mathrm{m}^2\,\mathrm{s}^{-2}$, with the extremal values in this range generating oscillations with periods of 36 and 18 months respectively.

Figures 2.4(c) and 2.4(d) present the same amplitude and period measurements from the experiments discussed in the previous paragraph, but with measurements made at $z = 30\,\mathrm{km}$ rather than $z = 23.5\,\mathrm{km}$. For values of F below about $26 \times 10^{-3}\mathrm{m}^2\,\mathrm{s}^{-2}$, there is no qualitative difference between Figures 2.4(a) and 2.4(c) apart from a general weakening of QBO amplitudes at the higher level. However, significantly different amplitude behaviour is observed at 30 km for $F \geq 26 \times 10^{-3}\mathrm{m}^2\,\mathrm{s}^{-2}$. The amplitude variations are plotted in detail in Figure 2.5 for the positive amplitude branch. The amplitude of the QBO undergoes a bifurcation at $F = 26 \times 10^{-3}\mathrm{m}^2\,\mathrm{s}^{-2}$,

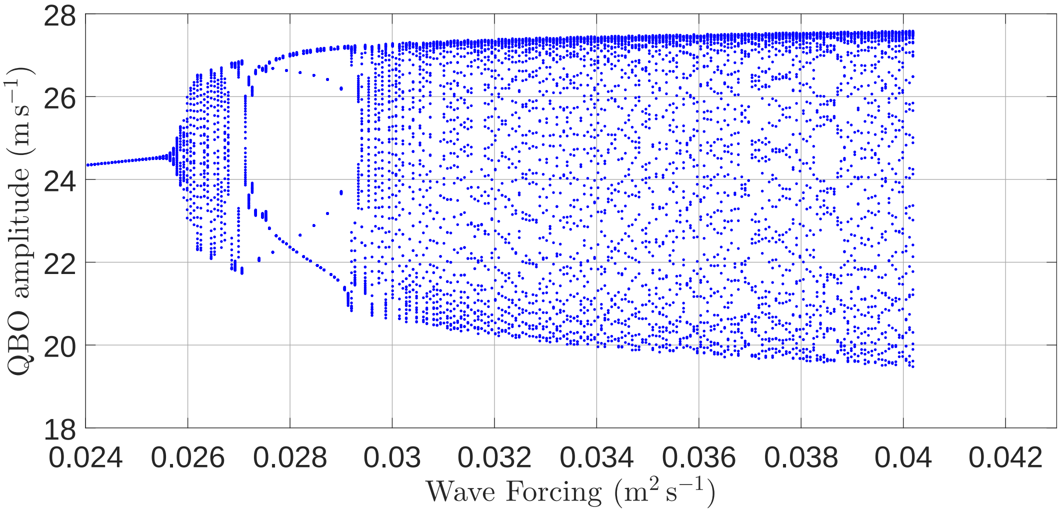

Figure 2.5: Detailed view of the upper branch of the second amplitude bifurcation in Figure 2.4(c).

adopting two different values. As the wave amplitude increases further the amplitude bifurcates again at $F = 28 \times 10^{-3}\mathrm{m}^2\,\mathrm{s}^{-2}$. Further increases in F see the amplitude varying between multiple values within a bounded envelope. There appear to be bands and patterns within the envelope, although exact structures are difficult to identify. It is likely that the picture is at least partially confused by small amounts of numerical noise in the model. The QBO period also displays small variations within the new regime (Figure 2.4(d)); however, these are relatively small in comparison to the magnitude of the amplitude variations.

Figure 2.6(a) and (b) show the evolution of a QBO for which $F = 35.4 \times 10^{-3}\,\mathrm{m}^2\,\mathrm{s}^{-2}$, which is within the regime of the second bifurcation. The time series in Figure 2.6(b) was measured at a height of 30 km. The average QBO period is just 9.3 months, indicative of the extreme wave amplitude. From Figures 2.6(a) and (b) we see that the QBO amplitude in the upper levels of the model is highly variable compared to the amplitude at lower levels. Despite this variation of amplitude, the period of the QBO is scarcely changed over the course of the model run, as can be deduced from the regular spacing between the westerly and easterly flow regimes in Figure 2.6(a).

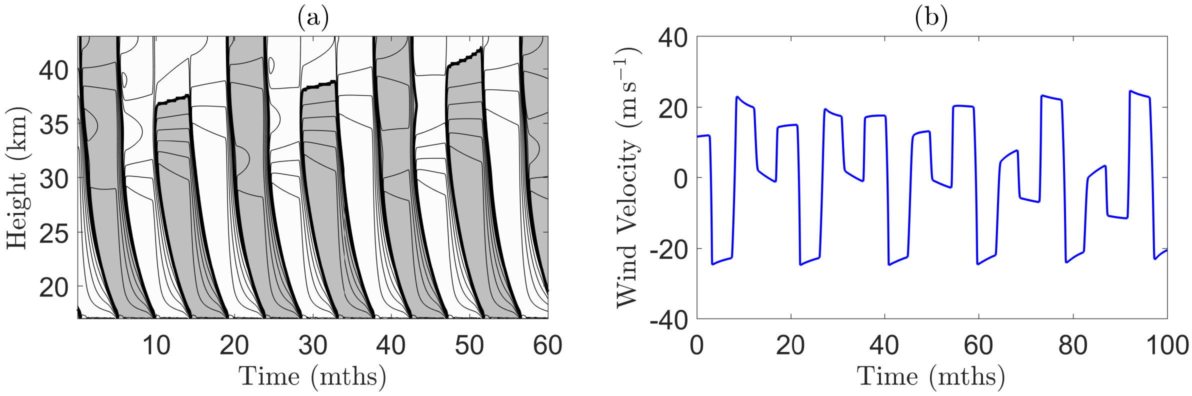

Figure 2.6: Evolution of the QBO for $F = 35.4 \times 10^{-3}\mathrm{m}^2\,\mathrm{s}^{-2}$, exemplifying model behaviour in the attendant flow regime after the second amplitude bifurcation. Contour plot formatting in (a) is the same as in Figure 2.2. The zonal wind time series presented in (b) is at a height of 30 km.

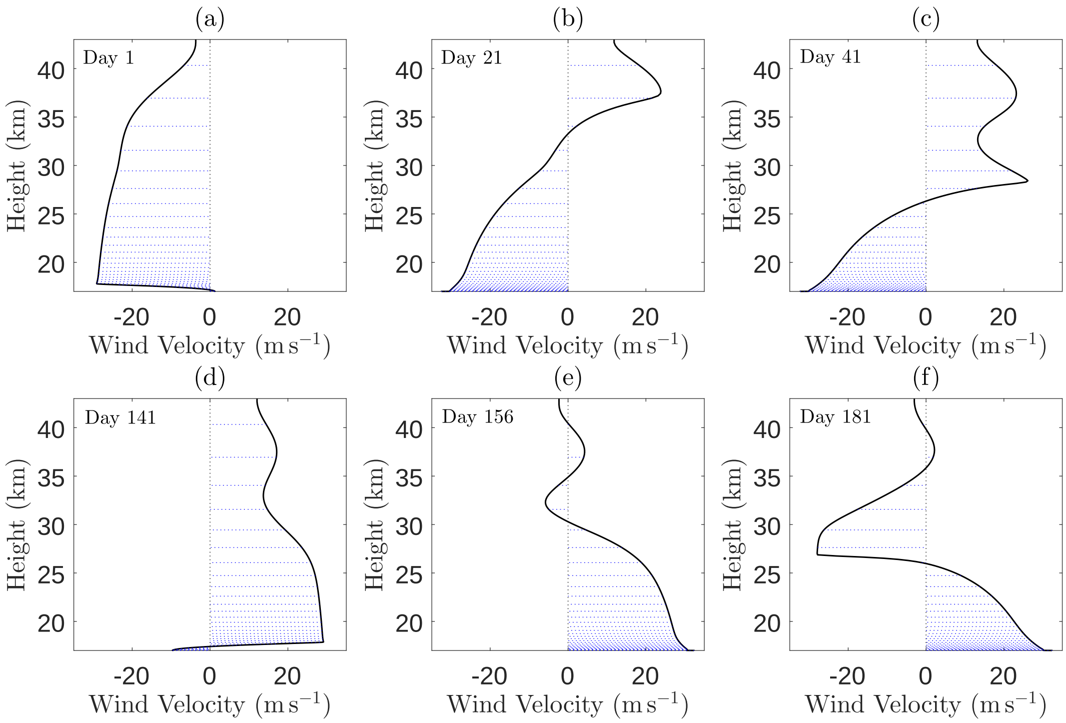

Figure 2.7: Evolution of the QBO wind profile over the course of one cycle, for $F = 35.4 \times 10^{-3}\mathrm{m}^2\,\mathrm{s}^{-2}$. See text for details.

We can qualitatively understand the source of the amplitude variations by studying the evolution of the QBO profile in a test case. We consider the case where $F = 35.4 \times 10^{-3} \mathrm{m}^2\,\mathrm{s}^{-2}$ (Figures 2.7(a)–(f)). In Figure 2.7(a), a new easterly regime takes hold at the lower boundary of the model, which releases the westerly wave to accelerate upper levels. Now, the acceleration at a given upper level is determined by three quantities: 1.) the balance of wave forcing at that level, 2.) the balance of wave forcing *below* that level, and 3.) the strength of diffusion. Whilst the first quantity generally increases in magnitude higher up in the model domain (due to the decrease of density with height), it can be strongly suppressed if any of the lower levels are accelerated relatively quickly enough. For example, in Figure 2.7(a) there is a small kink in the velocity profile at 30 km, due to the change in the dissipation profile at that height (cf. Figure 2.1(b)). Since the acceleration of the forcing wave is inversely proportional to the square of the Doppler shifted wave speed $(\bar{u} - c)^2$ (see (2.4.39)), the kink provides a focal point for acceleration of the winds in that region (Figure 2.7(b)). Thus, even though the larger wave forcing at high levels creates an upper level shear zone, over time the lower level kink absorbs more and more of the incoming wave momentum, thus choking off the supply of wave energy to higher levels (Figure 2.7(c)). As the lower shear zone descends the vestigial upper level shear zone is slowly destroyed by diffusion, but not completely. As a result, when the QBO switching occurs at the lower boundary, there is a non-negligible imprint of the upper shear zone remaining in the flow (Figure 2.7(d)). This 'memory' serves as a seed for non-uniform wave accelerations in the next round of shear zone formation (Figure 2.7(e)). The location of the new 'kink' is at a height level between the previous upper and lower level shear zones, and this is the level at which the new easterly shear zone forms and descends (Figure 2.7(f)). Thus, the continual alternation of wind maxima across these height levels leads to the amplitude variations seen in Figure 2.4(c).

The reason that this behaviour is only seen at large F is because for smaller values

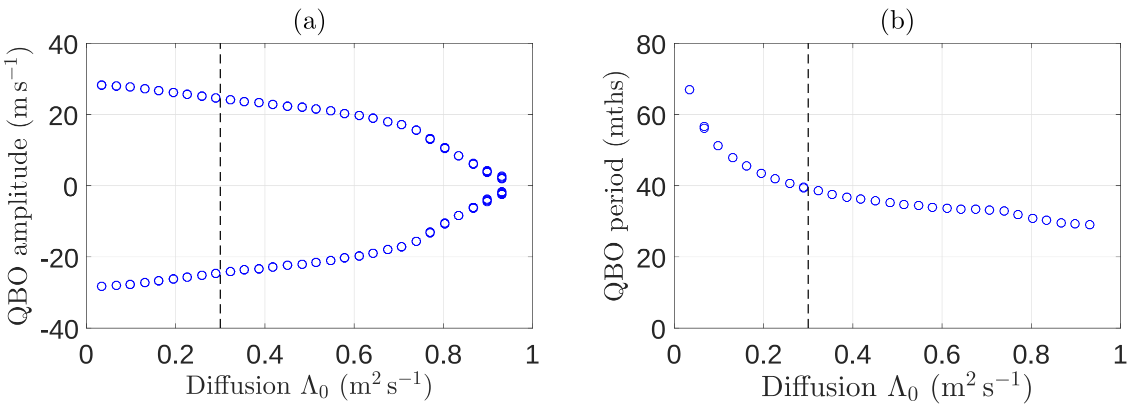

Figure 2.8: Variation of QBO amplitude (a) and QBO period (b) as the strength of diffusion Λ is increased. All other parameters are as stated in Table 2.1. The location of the standard value of $\Lambda_0 = 0.3\,\mathrm{m^2\,s^{-1}}$ is highlighted by the vertical dashed line in each plot.

of F, the time scale of wave-induced acceleration at lower levels is slow enough that the higher level shear zone - aided by diffusion - can descend to the level of the kink before the kink induces any sizeable change in the flow state at its level. Thus, there is a smooth descent of the upper level shear zone all the way through to the bottom of the model (cf. Figure 2.3).

2.5.2.2 Diffusion

We now consider the effect of varying the value of diffusion Λ_0 in the model, whilst keeping other parameters constant as defined in Table 2.1.

Figures 2.8(a) and (b) depict variations in the QBO amplitude and period respectively, as Λ_0 is varied over 30 values in uniform increments between $\Lambda_0 = 0.003\,\mathrm{m^2\,s^{-1}}$ to $\Lambda_0 = 0.93\,\mathrm{m^2\,s^{-1}}$. The period of the QBO increases for decreasing values of Λ_0, and seems to tend to infinity as $\Lambda_0 \to 0$. The phase space trajectory of the oscillator seems to be approaching a pair of heteroclinic orbits between two fixed points, which is similar to the dynamics of a simple pendulum as it approaches the 'overhead' fixed point.

For slightly larger values of Λ_0, the QBO forms as normal. The period of the

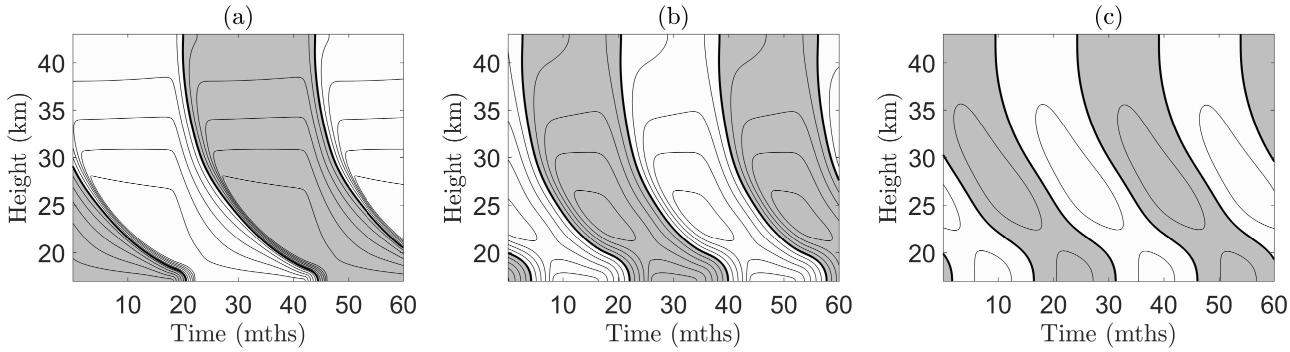

Figure 2.9: Changes to the QBO structure as Λ_0 varies between (a) $0.13\,\mathrm{m^2\,s^{-2}}$, (b) $0.45\,\mathrm{m^2\,s^{-2}}$, and (c) $0.87\,\mathrm{m^2\,s^{-2}}$ respectively. Contour plot formatting is the same as in Figure 2.2.

oscillation is long for weak diffusion (Figure 2.8(b)), for two reasons. Firstly, the descent of QBO shear zones will be slower with less downward diffusion of velocities. Secondly, the shear zones will have to descend very close to the lower boundary in order to generate enough curvature for diffusive switching to occur. As diffusion increases, so the period of the oscillation shortens for the same reasons.

For small values of Λ_0 the QBO amplitude is large, and it slowly weakens with increasing Λ_0 and therefore increased momentum diffusion of the QBO jet (Figure 2.8(a)). Eventually, when diffusion becomes large enough (at around $\Lambda_0 = 0.7\,\mathrm{m^2\,s^{-1}}$), the QBO amplitude begins to reduce significantly. This behaviour reflects the same Hopf bifurcation observed in Figure 2.4(a), with the limit cycle now being destroyed by increased diffusion at around $\Lambda_0 = 0.9\,\mathrm{m^2\,s^{-1}}$ (Figure 2.8(a)).

Figure 2.9 depicts contour plots for three sample cases that reflect the above observations. When diffusion is weak (Figure 2.9(a)), the oscillation has a long period and a large amplitude. As diffusion increases, both the period and amplitude of the oscillation decrease (Figure 2.9(b)), and there is significant weakening of the oscillation amplitude for large diffusion (Figure 2.9(c)).

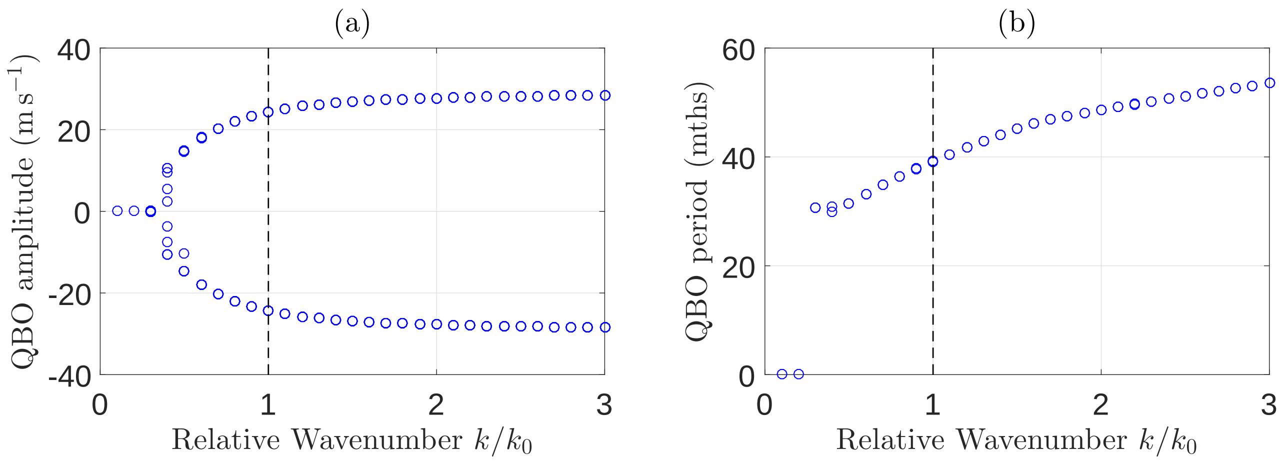

Figure 2.10: Variation of QBO amplitude (a) and QBO period (b) as the wave number k is increased. Values of k on the abscissa have been scaled relative to $k_0 = 2\pi/40,000$, where k_0 is the standard value of the wave number given in Table 2.1.

2.5.2.3 Wave number and wave speed

In this final section we consider the effect of different values of the wave number k and wave speed c, the two parameters that inform the structure of the waves that force the QBO. Unlike wave amplitude and diffusion, changes to k and c affect the exponential decay term in (2.4.39). As a result, changes to these quantities modify the vertical penetration of the waves into the stratosphere.

Figures 2.10 and 2.11 display the variation of the QBO amplitude and period as k and c are varied. Values of k have been scaled relative to $k_0 = 2\pi/40,000$, where k_0 is the standard value of the wave number given in Table 2.1. We note that values of k less than k_0 are not physically realisable on the Earth.

For small values of both parameters, the exponential term dominates in the expression for wave forcing, and as a result the wave forcing becomes effectively zero, thus preventing any kind of oscillation. As the parameter values increase, the wave forcing term strengthens. It eventually becomes large enough to compete with diffusion, at which point a Hopf bifurcation occurs, generating the QBO limit cycle. As the amplitude of the QBO oscillation scales with wave speed, the amplitude curves (Figures 2.10(a) and 2.11(a)) look quite different in the wave number and wave speed

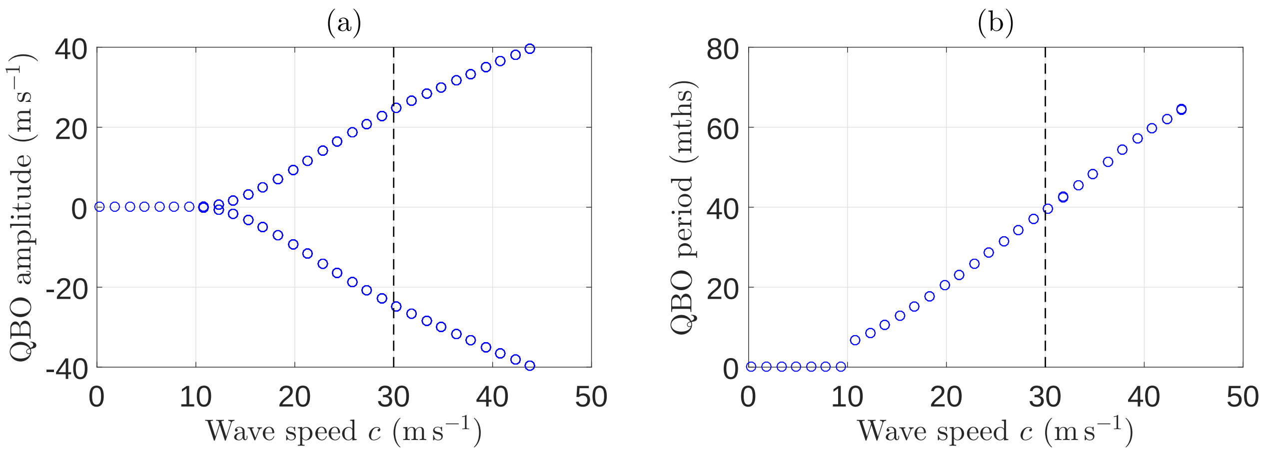

Figure 2.11: Variation of QBO amplitude (a) and QBO period (b) as the wave speed c is increased. Other parameters are as stated in Table 2.1. The standard value of $c = 30\,\mathrm{m\,s^{-1}}$ has been highlighted by a vertical dashed line.

cases. The wave number diagram (Figure 2.10(a)) is quite similar to that of the wave amplitude diagram (Figure 2.4(a)), with a sudden onset of the oscillation as the parameter increases through the bifurcation point. In the case of the wave speed (Figure 2.11(a)) the transition is much smoother, since c itself controls the amplitude of the oscillation.

The oscillation period is short for weak values of k and c (Figures 2.10(b) and 2.11(b)). This is because the penetration depth of the QBO is small for small k and c, and so the shear zones do not have to descend very far before reaching the lower boundary of the model. As the parameter values increase, so does the oscillation depth, as well as the oscillation period (Figures 2.10(b) and 2.11(b)). Furthermore, as k and c increase the strength of the $1/\left[k(\bar{u}-c)^2\right]$ term in (2.4.39) decreases, and so wave-induced accelerations get weaker, resulting in slower descent and a longer period QBO.

Figure 2.12 presents contour plots of QBO evolution for three different values of c, in order to illustrate some of the points raised in the preceding paragraphs. For small c (Figure 2.12(a)), the penetration of the QBO into the stratosphere is quite weak, as is the QBO amplitude. The period is short, as the shear zones form lower

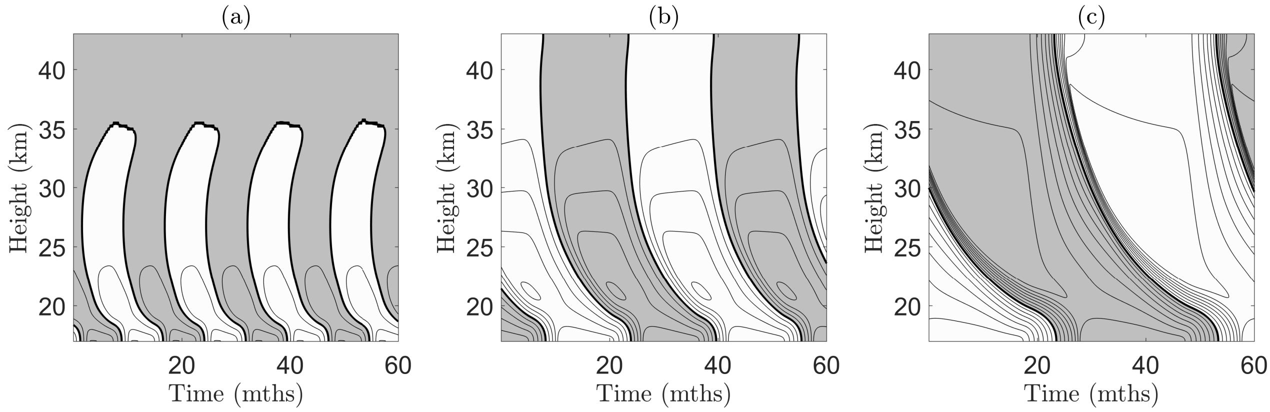

Figure 2.12: Changes in QBO structure as the wave speed c varies between (a) $16.8\,\mathrm{m\,s^{-1}}$, (b) $25.8\,\mathrm{m\,s^{-1}}$, and (c) $40.8\,\mathrm{m\,s^{-1}}$ respectively.

down in the model domain. As c increases (Figures 2.12(b)–(c)), the penetration depth, amplitude, and period of the QBO all increase. Similar results hold in the wave number case, except that the amplitude of the QBO would only increase weakly along with the increasing wave number.

2.6 Summary

In this chapter we have derived the Holton-Lindzen equation (2.4.39) that is the major focus of study in this thesis. We have also investigated the basic properties of the HL equation, and have analysed the sensitivities of the model to changes in various parameters. These results are summarised in Table 2.2.

In the case of wave amplitude variations, we found a significant qualitative change in the behaviour of the upper level winds in our model for large values of F. In particular, we showed that the QBO amplitude undergoes a second bifurcation for large F, and we linked this to a change in the balance of forces acting on upper level winds on account of the faster acceleration at lower levels. This particular phenomenon has not been reported in the literature before, although Yoden and Holton [1988] briefly allude to it in their investigation of the bifurcation properties of

Parameter	QBO amplitude	QBO period	QBO penetration
F	weak increase	decrease	no effect
Λ_0	weak decrease	decrease	no effect
k_0	weak increase	increase	increase
c	increase	increase	increase

Table 2.2: Summary of the changes to QBO properties as a result of increasing various parameter values.

the Plumb [1977] model. The wave amplitude at which the bifurcation occurs is quite large, however, and so it is not clear whether the mechanism plays a role in the real atmosphere. This would be an interesting object of further work. For the purposes of this work we will not discuss the bifurcation further, seeing as it has little effect on the period of the QBO.

The following three chapters of the thesis will focus on the behaviour of various extensions of HL equation, in order to understand how the period of the QBO is influenced by periodic external forces.

Chapter 3

Synchronization I: Annual cycle in tropical upwelling

3.1 Introduction

The global scale meridional circulation of the Earth's stratosphere is known as the Brewer-Dobson circulation, or BD circulation hereafter (Butchart [2014]). First described by Brewer [1949] and Dobson [1956] to account for the latitudinal distribution of ozone and water vapour, the circulation consists of rising air in the tropical stratosphere that migrates poleward and downward into the extratropics on a seasonal timescale. As a result it is a significant dynamical determinant of the global distribution of long-lived trace gases in the atmosphere (Plumb [2002]). The BD circulation is driven by the vertical propagation and breaking of Rossby waves in the extratropical stratosphere of the winter hemisphere. The resulting wave drag on the zonal mean winds at these high latitudes acts as a non-local 'Rossby wave pump' (Haynes et al. [1991], Holton et al. [1995]) that drives the poleward circulation.

This vertical advection induced by the BD circulation at the equator acts as an impediment to the descent of QBO wind regimes, resulting in an increase in its oscillation period (Saravanan [1990], Dunkerton [1991]). Due to the hemispheric asymmetry of land distribution on the Earth there is greater extratropical wave driving during boreal (i.e. Northern Hemisphere) winter compared to austral (Southern Hemisphere) winter, resulting in an annual cycle in the strength of the tropical upwelling branch of the BD circulation (Yulaeva et al. [1994]). It has been suggested that the resultant annual modulation of the descent rate of the QBO may be responsible for the observed seasonal synchronisation of the QBO (Kinnersley and Pawson [1996], Hampson and Haynes [2004]).

There is general agreement amongst climate models that the strength of tropical upwelling will increase at a rate of between 2 and 3.2% per decade as a result of increased greenhouse gas emissions (Butchart [2014]). The overall effect that the emissions increase might have on the period of the QBO, however, is still unclear (Schirber et al. [2014]). Although one would naturally expect increased upwelling of tropical air to delay further the descent of QBO winds, increased convective wave activity in the tropics - due to changes in sea surface temperatures in a warming climate, as well as to the increase of the depth and area coverage of convection during ENSO events - might simultaneously enhance tropical wave activity, which generally tends to increase the descent rate and decrease the period of the QBO (Liess and Geller [2012]). Nevertheless, it would be instructive to study how the QBO period would change as a result of an increase in upwelling, if one assumes that this is the dominant forcing in a future climate.

In this chapter we will investigate the relationship between the QBO and the Brewer-Dobson circulation using the idealised HL model. Since comprehensive climate models still encounter difficulties in generating realistic QBOs (e.g. Yao and Jablonowski [2015], Schenzinger et al. [2016]), there is some utility to be gained from studying this question in the context of a simple low-dimensional model. Such a model offers the obvious advantage of being computationally inexpensive, thus allowing for a much more detailed exploration of the model parameter space. It is also easier to tease out the chain of causality in a simple model, where there are far fewer variables to consider. Insights gained through such studies may then be used to inform future investigations using larger, more comprehensive models.

In Section 3.2 we describe the modifications made to the Holton-Lindzen model to account for tropical upwelling. Results are described in Section 3.3. A thorough examination of the parameter space of the model is conducted with regards to the effect of wave forcing and both the constant and annually varying components of tropical upwelling. We demonstrate that the addition of tropical upwelling creates broad regions of frequency locking where the QBO period remains an integer multiple of the annual cycle period. Outside of these locking regions it is shown that the QBO period no longer remains constant in time, but instead exhibits a frequency modulation in which it cycles through a set of periods of varying structure and complexity. If the set of unique periods is discrete (as it often is), then the sum of the set of unique periods always adds to a multiple of the annual forcing period, indicating that the QBO is synchronized to the annual cycle in these cases as well. The robustness of these structures to stochasticity is tested, and we further demonstrate that the addition of the annual cycle in tropical upwelling can actually help to generate a QBO in particular cases. In the context of increasing tropical upwelling, we investigate the evolution of the QBO period and suggest the possibility that the QBO period may adjust toward a 36 month period in a warming climate. Finally, in Section 3.4, we discuss our results in the context of related work, and briefly provide some observational evidence for cyclical behaviour of QBO periods in the real atmosphere.

The bulk of the material in this chapter has been published as a research article (Rajendran et al. [2016]).

3.2 Model description

We use the one-dimensional QBO model of Holton and Lindzen [1972] with the addition of tropical upwelling (Saravanan [1990], Hampson and Haynes [2004]). Two equatorial waves, travelling in opposing directions but identical in every other respect, propagate vertically through the stratosphere and dissipate, depositing zonal momentum into the background flow. The resultant evolution of the zonal mean zonal wind, $\bar{u}(z,t)$, is given by the Holton-Lindzen equation

$$\frac{\partial \bar{u}}{\partial t} + w\frac{\partial \bar{u}}{\partial z} = -\frac{1}{\rho_0}\sum_i \frac{\partial \mathcal{F}_i}{\partial z} + \Lambda(z)\frac{\partial^2 \bar{u}}{\partial z^2}, \tag{3.2.1}$$

where the various terms in the equation are as discussed in Chapter 2. The second term on the left hand side of the equation represents the vertical advection of zonal winds by tropical upwelling, as first introduced by (Saravanan [1990]). The upwelling velocity w is partitioned into the sum of constant and annually varying components as follows, following Hampson and Haynes [2004]:

$$w(z,t) = \left[w_c + w_a \cos\left(\frac{2\pi t}{360}\right)\right]\left\{0.2 + 0.8\exp\left(\frac{z - z_t}{z_t - z_l}\right)\right\}. \tag{3.2.2}$$

Here $z_t = 17\,\text{km}$ and $z_l = 43\,\text{km}$ are the top and bottom boundaries of the model respectively, time t is measured in days, and for simplicity we have taken an annual cycle period of exactly 360 days. We will refer to w_c and w_a as the *constant* and *annually varying* components of tropical upwelling respectively.

As described in Chapter 2, the equation of motion (3.2.1) is discretised over a non-uniform vertical grid of 200 points and solved for various choices of F, w_c and w_a, using an implicit Crank-Nicholson scheme with a time step of $dt = 0.2$ days.

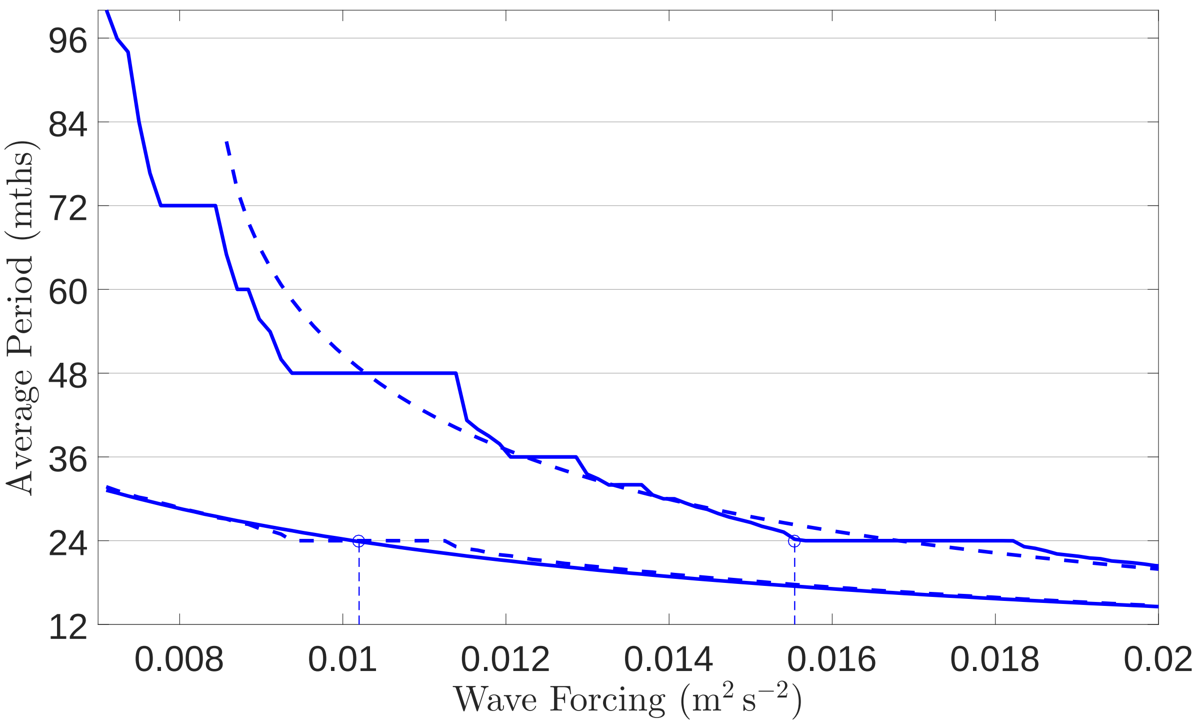

Figure 3.1: Average QBO period as wave forcing F is varied in two sets of 100 simulations with (top, solid line) and without (bottom, solid line) tropical upwelling. In the upwelling runs we set $w_c = 0.3$ mm s^{-1} and $w_a = 0.2$ mm s^{-1}; in the no-upwelling comparisons we set both to zero. The two dashed curves correspond to upwelling simulations where just one of w_a (top, dashed line) or w_c (bottom, dashed line) are set to zero (with the other parameter retaining its non-zero value). The points on the solid curves where the QBO period is 24 months have been marked.

3.3 Results

3.3.1 Influence of tropical upwelling on QBO period

The response of the model QBO to increased wave forcing in the presence of tropical upwelling was considered. We ran a series of one hundred simulations of the QBO, with tropical upwelling parameters set at $w_c = 0.3$ mm s^{-1} and $w_a = 0.2$ mm s^{-1}. These numbers were chosen to represent approximately the strength of the present day Brewer-Dobson circulation (Seviour et al. [2012]). Wave forcing was varied uniformly between $F = 7.0 \times 10^{-3}$ m^2 s^{-2} and $F = 20.0 \times 10^{-3}$ m^2 s^{-2}. The simulations were run in series from low to high values of F, such that the final condition of a simulation run at lower wave forcing was used as the initial condition for the next simulation at higher wave forcing. The average period of the resulting QBO was then calculated by measuring the average time between westerly QBO onsets at $z = 24$ km.

The variation of the QBO period with wave forcing in the presence of tropical upwelling is plotted in Figure 3.1 (solid line, top). This is compared with the QBO response in the absence of upwelling (that is, with $w_c = w_a = 0$), which is also plotted (solid line, bottom).

The inclusion of upwelling results in a significant increase in the QBO period compared to the case with no upwelling. The relative increase in period is greatest under conditions of weak forcing, and the gap in period reduces as wave forcing increases. We see that significant increases in wave forcing are required to maintain the QBO at a particular period under upwelling conditions. For example, a 24 month QBO requires that the wave forcing be around 50% larger in the presence of upwelling ($F = 15.7 \times 10^{-3}$ m^2 s^{-2}, as compared to $F = 10.2 \times 10^{-3}$ m^2 s^{-2} in the no-upwelling scenario; these points have been marked on Figure 3.1).

Furthermore, we see that the period of the QBO, though still monotonic, is no longer strictly decreasing as wave forcing increases. Instead, there are several plateau regions where the QBO period remains unchanged over a range of wave forcing, forming a structure reminiscent of the devil's staircase well-known from dynamical systems theory (Jensen et al. [1984], Ott [2002]). Each plateau interval represents a set of simulated QBOs that have an average period that is a rational multiple of the annual forcing period. The broadest plateaus represent integer multiples of 12 months, with plateaus at 24, 36, 48, 60 and 72 months. Regions corresponding to even-integer locking ratios tend to be broader than regions with odd-integer locking ratios. There is also a noticeable 30 month plateau, corresponding to a rational ratio of 5/2 times the forcing period. We presume that other locking intervals exist as well, but are too narrow to be resolved here.

The dashed curves in Figure 3.1 represent two sets of simulations in which either the constant or the annually-varying component of the annual cycle was set to zero, with the other component set to its usual value ($w_a = 0.2$ mm s^{-1} and $w_c = 0.3$ mm s^{-1} respectively). In the case where $w_c = 0$ (bottom dashed curve), the period of the QBO returns to values that are comparable to the case where there is no upwelling at all, except for a small interval near the 24 month locking region. In the other case when $w_a = 0$ (top dashed curve), the period of the QBO becomes much longer due to the effect of the nonzero w_c. However, there are no plateaus corresponding to locking regions. Further, there is a minimum value of F below which the strength of the wave forcing is insufficient to overcome the effect of upwelling, resulting in the QBO being unable to form at all. For this reason, the curve has been truncated at small values of F.

3.3.2 Quasi-periodic modulation of QBO periods

We re-evaluate the results in 3.3.1 by investigating the cycle-to-cycle variation in the period of the QBO in the presence of upwelling. Figure 3.2 shows individual QBO cycle lengths over the same range of wave forcing, with (blue dots) and without (red dots) upwelling. Each data point represents the period of an individual QBO cycle; taking the mean of the set of periods at each wave forcing returns the corresponding solid curves presented earlier in Figure 3.1. From the plots we see that there is in fact a great deal of variation in the length of individual periods. In the set of runs without upwelling - marked by red dots on Figure 3.2 - there is no temporal variation in QBO period. The QBO adopts exactly one period throughout each simulation run at a given wave forcing, once transients have died away. In contrast, when tropical upwelling is included in the simulations (blue dots on Figure 3.2), the only regions of wave forcing space where the QBO takes a single period are the locking regions at integer multiples of the annual cycle discussed in the previous subsection. Outside

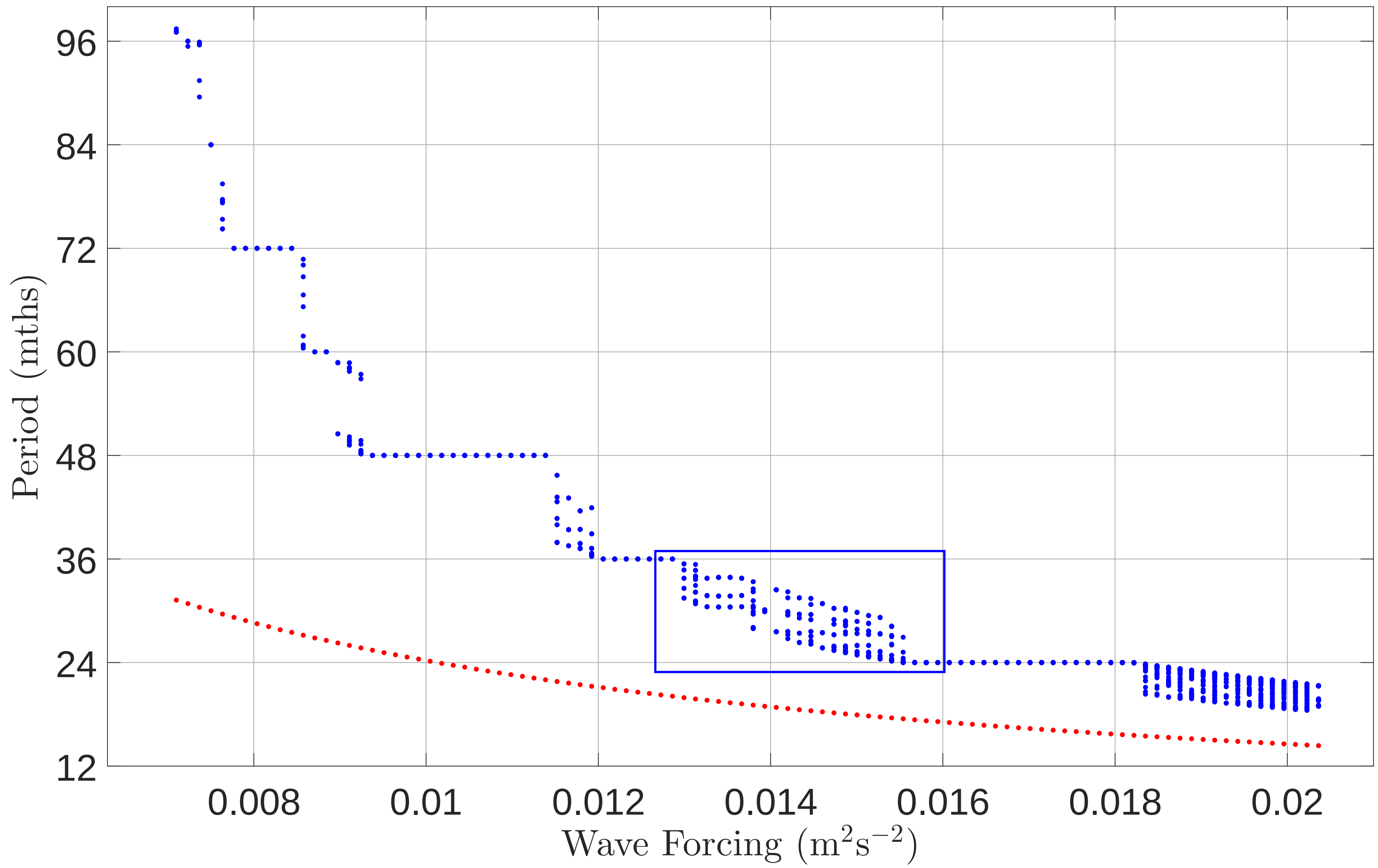

Figure 3.2: Individual QBO cycle lengths plotted against wave forcing, in the presence and absence of tropical upwelling. Each cycle length is defined by the time between the onset of westerly wind regimes at $z = 24$ km. Data points from the simulations with and without upwelling are plotted as blue and dots respectively. The region enclosed within the blue box is explored in greater detail in Figure 3.3.

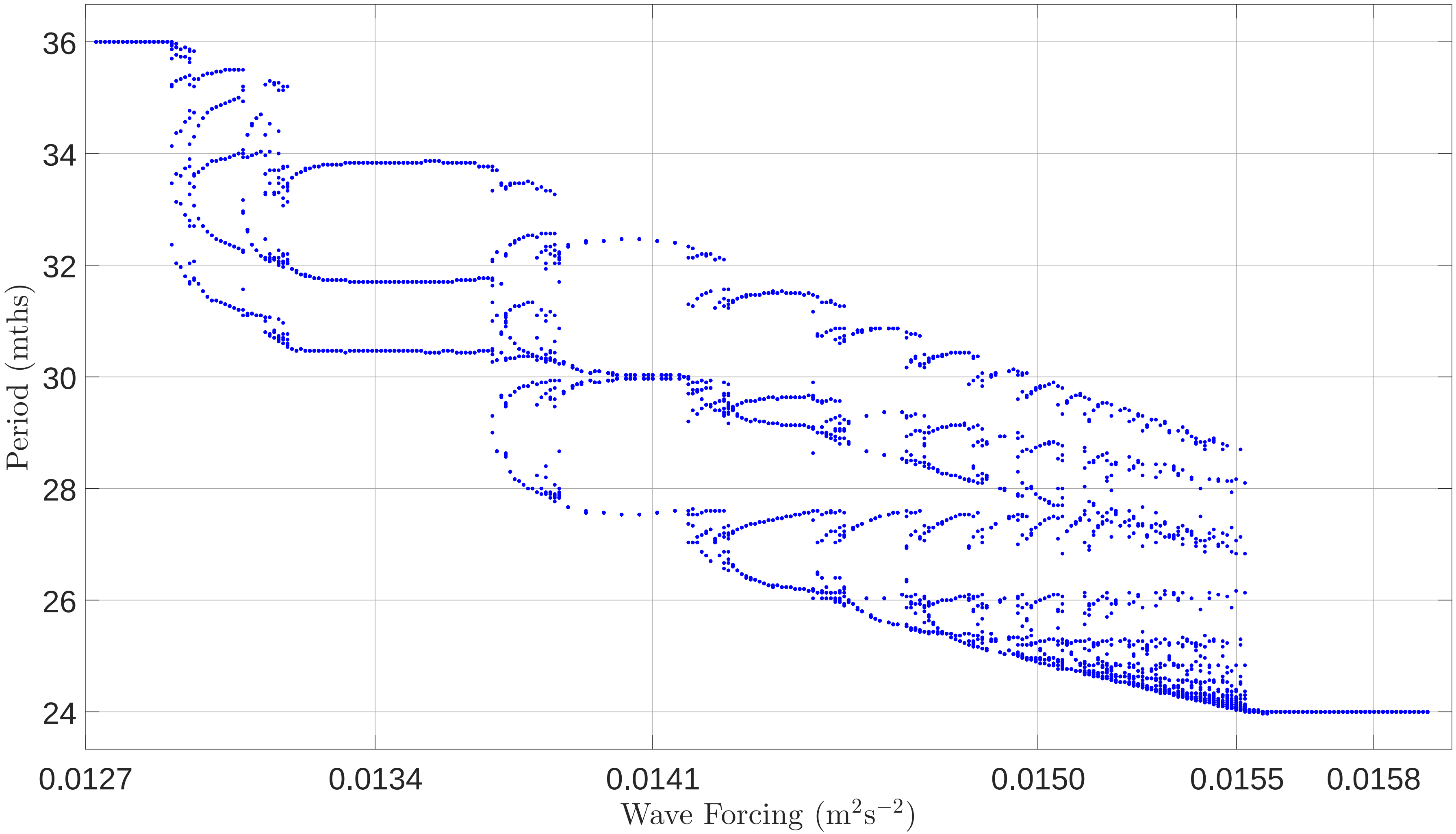

Figure 3.3: Recalculation of the QBO cycle periods for the region contained within the blue box in Figure 3.2. The resolution along the wave forcing axis has been increased by 12 times over the resolution in Figure 3.2. See text for details.

of these intervals, the QBO cycle length changes dynamically in time, and exhibits a complex pattern of variations that follows the general trend of the average QBO period shown in Figure 3.1 but with much more cycle-to-cycle variability.

In light of these findings we performed a second calculation to investigate the behaviour of QBOs with wave forcings in the region between the 36 month and 24 month locking regions (denoted by the dotted box in Figure 3.2). The number of simulations within this region was increased by a factor of twelve, with a view to tease out the sensitivity of the QBO period to small changes to the wave forcing. The resulting QBO periods of each simulation were plotted against the corresponding value of wave forcing, and are presented in Figure 3.3. We see that the QBO period undergoes a complicated series of bifurcations as wave forcing increases. These are reminiscent of the period-doubling bifurcations observed in one-dimensional iterative maps such as the logistic map. Furthermore, we note that relatively small increases in wave forcing can generate significant qualitative changes in the behaviour of the QBO period.

To illustrate some of the details of the observed behaviour, we consider four representative simulation runs, corresponding to wave forcing values of $F = 13.4 \times 10^{-3}$, 14.1×10^{-3}, 15.5×10^{-3}, and 15.8×10^{-3} $\mathrm{m^2\,s^{-2}}$ respectively. (These have been marked on the horizontal axis of Figure 3.3). For each simulation, the periods of the individual QBO cycles are plotted sequentially across time in Figure 3.4. Histograms of the frequency of different QBO cycle lengths are then computed (Figure 3.5), as well as the frequency of westerly QBO regime onsets at 24 km for different phases of the annual cycle (Figure 3.6). Finally, we use delay embedding plots of the zonal wind time series at $z = 24\,\mathrm{km}$ to reconstruct the geometry of phase space (Takens [1981]). These are presented in Figure 3.7, using an embedding dimension $d = 2$ and a delay time of 300 days.

It is clear from Figure 3.4 that variations in the QBO period are a robust feature of

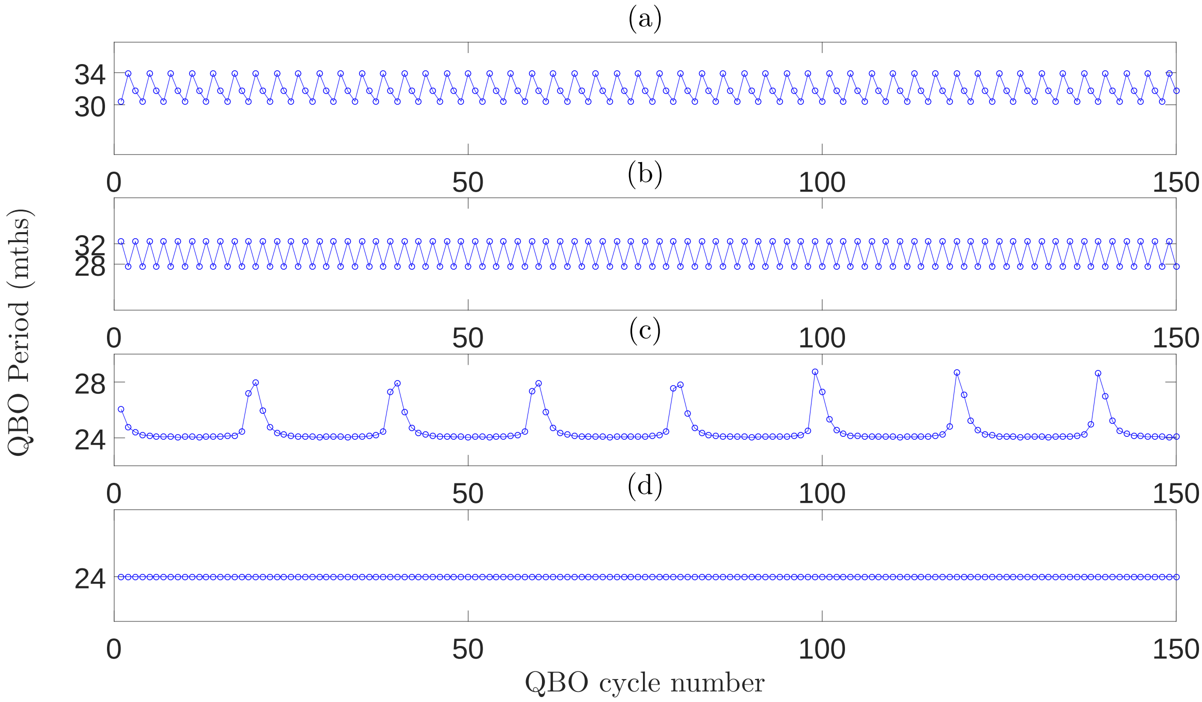

Figure 3.4: Evolution of QBO cycle length in the presence of tropical upwelling for four selected values of the wave forcing. Cycle length is measured by the time between onset of westerly QBO regimes at $z = 24\,\text{km}$. The plots (a) - (d) correspond to wave forcing values of $F = 13.4 \times 10^{-3}$ m^2 s^{-2}, 14.1×10^{-3} m^2 s^{-2}, 15.5×10^{-3} m^2 s^{-2}, and 15.8×10^{-3} m^2 s^{-2} respectively; their locations have been marked on Figure 3.3.

the simulations, and that they do not decay even after hundreds of years. Of the four simulations considered, only one obtains a regular period (Figures 3.4(d), 3.5(d)). In this case ($F = 15.8 \times 10^{-3}$ m^2 s^{-2}), the intrinsic QBO period is suitably close to an integer multiple of 12 months, allowing the period of the QBO to adjust to an exact $2:1$ synchronisation ratio with the annual cycle. As a result, the onset of westerlies at 24 km always occurs in the same month (Figure 3.6(d)). In general, we found that the onset month of QBO westerlies at a given height shifts to earlier months as wave forcing increases within a locking region (not shown).

In contrast, Figure 3.4(a) shows a QBO with a period that does not settle on a single value, but rather adopts a period-3 cycle in which it consistently alternates between periods of 913, 951, and 1016 days (Figure 3.5(a)). The sum of these periods is 2880 days, or exactly 8 times the forcing period of 360 days. This highlights a

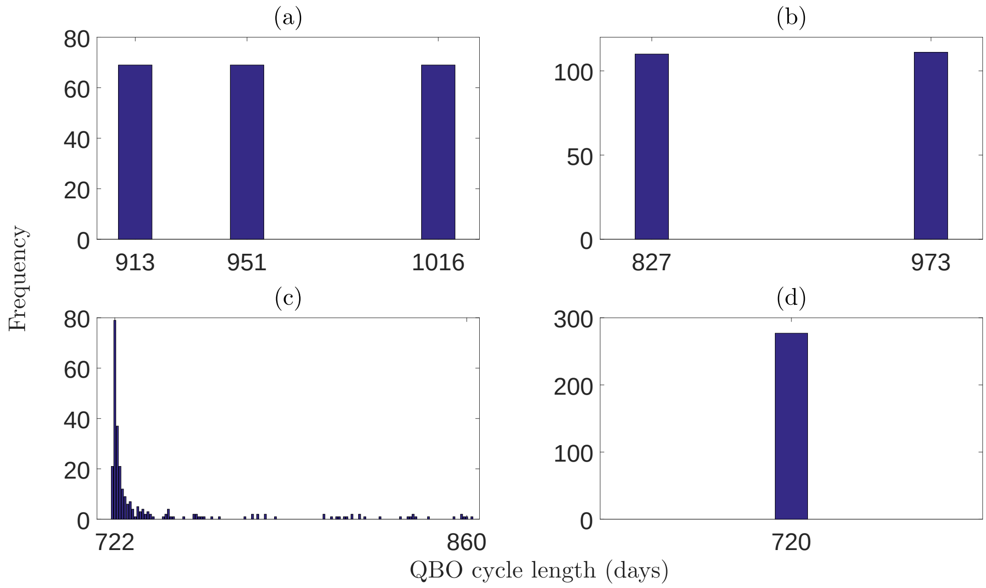

Figure 3.5: Histograms of the frequency of occurrence of different QBO cycle lengths in days, for each of the four cases considered in Figure 3.4.

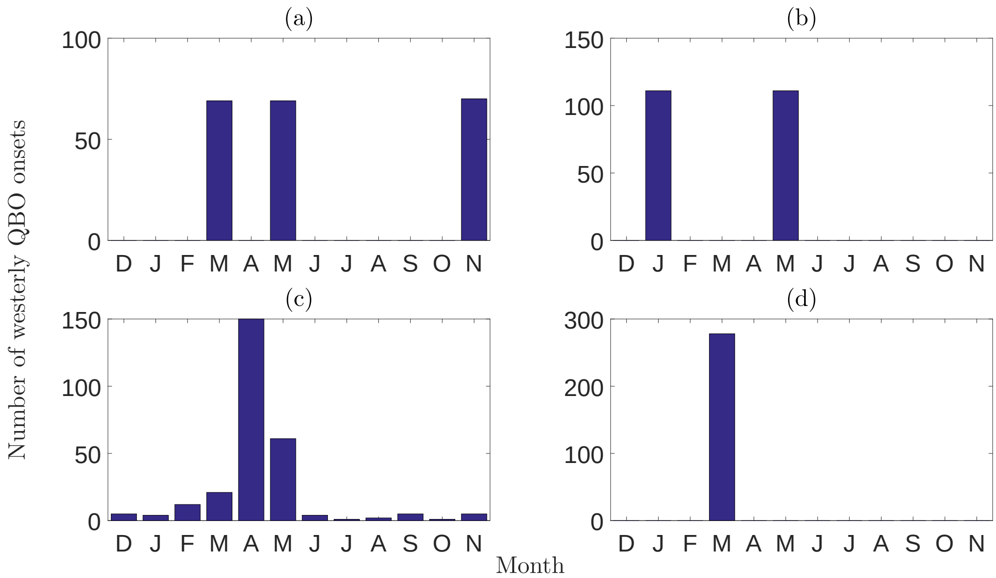

Figure 3.6: Number of QBO westerly onsets during different phases of the annual cycle, for each of the four cases from Figure 3.4.

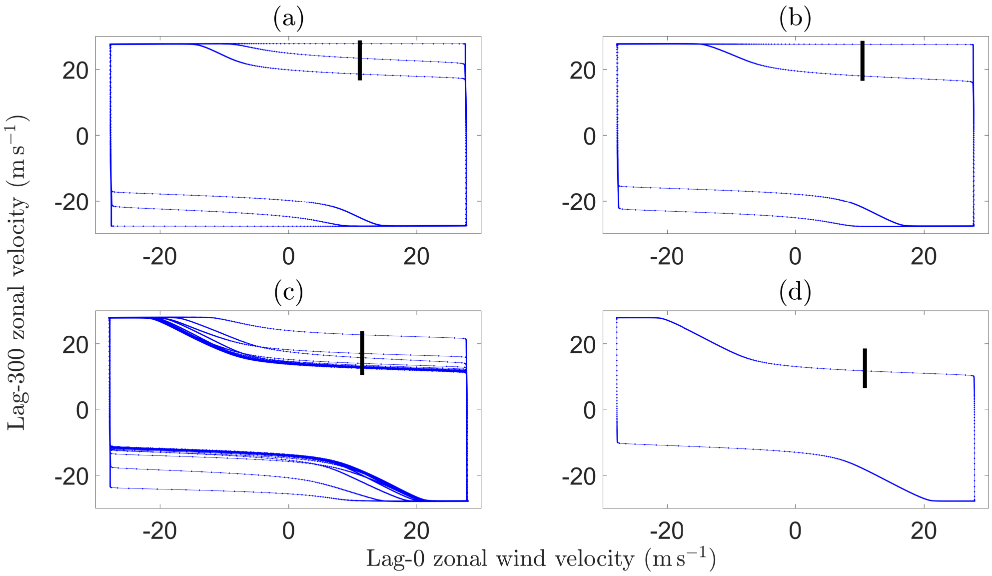

Figure 3.7: Delay embedding plots for each of the four cases from Figure 3.4, using zonal wind time series at $z = 24\,\mathrm{km}$ and a time delay of 300 days. The short, dark, vertical lines illustrate the locations at which Poincaré sections are taken. The number of different QBO periods in each case can be inferred by counting the number of distinct lines intersecting the corresponding Poincaré section.

different type of synchronisation of the QBO with the annual cycle. The QBO period itself undergoes a frequency modulation, whereby several QBO cycles of different lengths combine in such a way that the sum of the periods is always a multiple of the annual cycle period. The number of cycles in the set can be deduced by counting the number of lines that would intersect a surface perpendicular to the reconstructed phase portrait of the oscillation (i.e. a Poincaré section). In this case there are 3 intersections (Figure 3.7(a)), reflecting the 3 discrete QBO periods. The average QBO period in this simulation - 960 days - represents a 8 : 3 synchronization ratio with respect to the 360 day annual cycle.

Figure 3.4(b) shows a simulated QBO with very similar behaviour to the one discussed in the preceding paragraph. The major difference is that this QBO adopts a period-2 cycle instead of a period-3 cycle (Figure 3.5(b)). The period lengths are 827 and 973 days respectively, which add to 1800 days, or exactly 5 years. Thus the QBO is in 5 : 2 synchronization with the annual cycle.

The final example (Figure 3.4(c)) shows a QBO realisation that is near the end of the bifurcation sequence depicted in Figure 3.3 ($F = 15.5 \times 10^{-3}$ m^2 s^{-2}). In this case, the period of the QBO remains very close to 24 months for around 16 to 17 cycles, but after a long period of quiescence of over 30 years, the QBO period suddenly jumps up to around 28 months. Over the next 2-3 cycles the period then relaxes back down to the vicinity of a 24 month oscillation. The largest jump happens at regular intervals of 20 QBO cycles, but the set of periods is not a discrete set as in the previous examples. This can be seen from consideration of the frequency histogram (Figure 3.5(c)), where we see that the QBO period now has an irregular distribution with a strong peak around 722 days, but with a long tail of periods going out to around 860 days. The delay embedding plot (Figure 3.7(c)) has thicker lines in this case as compared to the other examples, suggesting that the simulated QBO possesses a broad-banded set of periods. The QBO periods do not form a closed set even after 500 years. This suggests an irrational synchronization ratio between the QBO and the annual cycle; the evolution of the QBO is quasi-periodic in this instance. Westerly onsets occur throughout the year (Figure 3.6(c)), although there is a marked preference for onsets around April and May with relatively few onsets occurring in the second half of the year.

3.3.3 QBO response to changes in w_c and w_a

We considered the effect on QBO period of changes to both the wave forcing F and the constant component of tropical upwelling, w_c. Ten different values of w_c were considered, starting with the present-day value of $w_c = 0.3$ mm s^{-1} and increasing in 5% increments to $w_c = 0.43$ mm s^{-1}. As in 3.3.1 the wave forcing F took one hundred uniformly spaced values between $F = 7.1 \times 10^{-3}$ m^2 s^{-2} and $F = 20.4 \times 10^{-3}$ m^2 s^{-2}. The amplitude of the annual component in upwelling was held constant at $w_a = 0.2$ mm s^{-1}. Hence, a total of one thousand simulations were run.

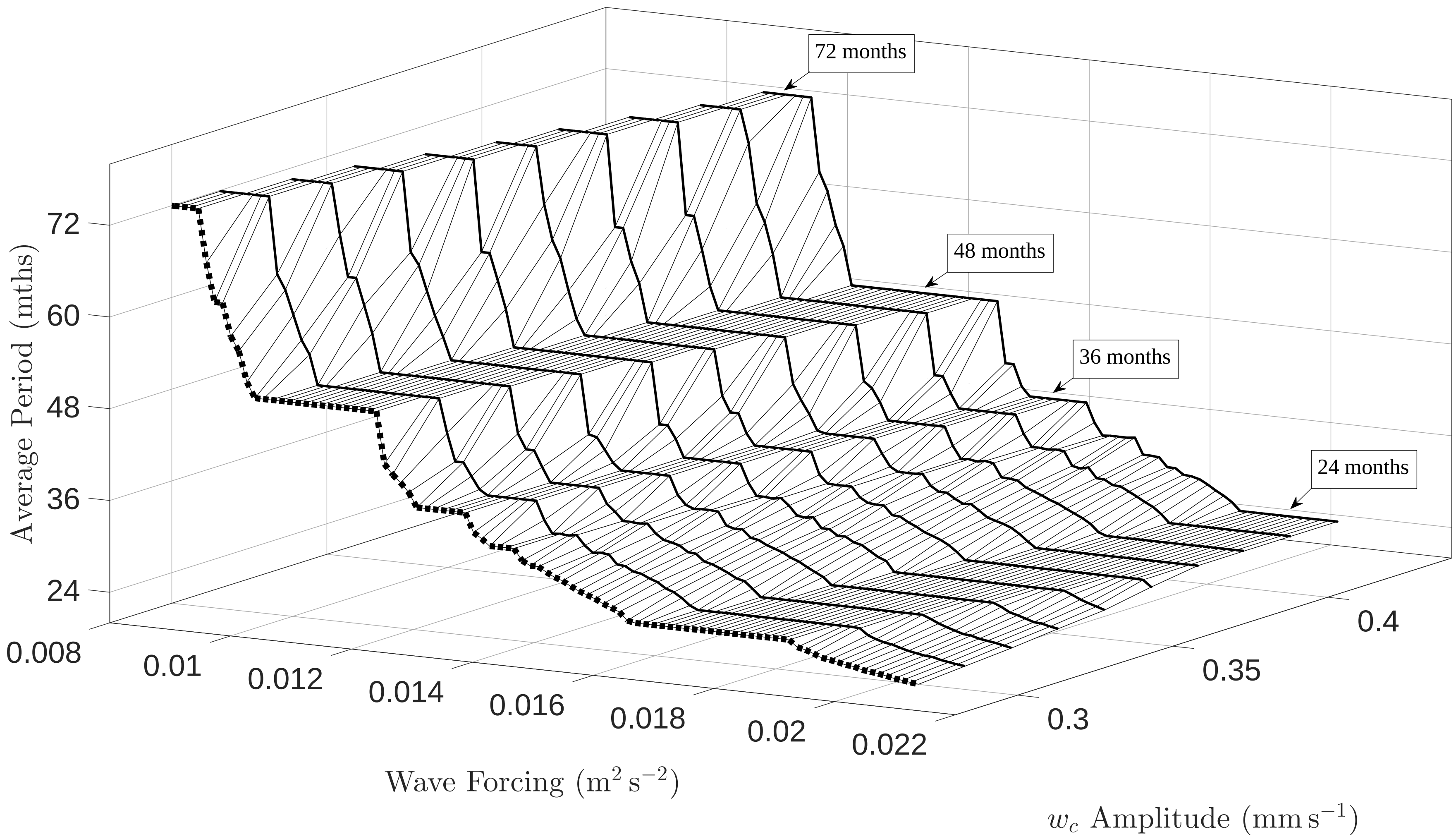

Figure 3.8: Surface plot of the variation of average QBO period with wave forcing (left axis) and the strength of the constant component of tropical upwelling (right axis). Plateaus in the surface - corresponding to integer year QBO periods - have been labelled. The bold dotted line is equivalent to the upper solid curve in Figure 3.1.

Results of the runs described above are summarised in Figure 3.8, where the average QBO period is plotted as a surface whose height depends on the values of F and w_c. The cross-section of this surface along $w_c = 0.3$ mm s^{-1} can be identified as the upper solid curve in Figure 3.1; it is marked by a dotted line in Figure 3.8.

In general we find that the QBO period increases as w_c increases, in line with our understanding of how increased upwelling impedes the descent of QBO shear zones (Dunkerton [1991]). A striking feature of Figure 3.8 is the presence of several shelves or plateaus on the period surface which clearly correspond to the locking regions discussed in 3.3.1. Significant regions of annual synchronization occur at periods of 24, 36, 48 and 72 months. Within each locking region, increasing the strength of w_c at fixed values of F has the effect of delaying the onset of QBO westerlies at 24 km to later months (not shown). As w_c is increased we see that the width of the locking regions remain unchanged, but also that they shift horizontally and sit over higher values of wave forcing.

We also ran a separate set of experiments, very similar to the ones just described, but with w_c kept fixed at the present-day value of $w_c = 0.3$ mm s^{-1}, while the strength of the annual component of upwelling w_a was varied uniformly over ten values between $w_a = 0$ and $w_a = 0.36$ mm s^{-1}. Wave forcing variations are as described previously.

Results of the simulations are displayed in Figure 3.9; we confirm the presence of the same locking regions discussed earlier. In sensitivity tests (not shown), we find that increases in w_a at fixed F had a minimal impact on the onset month of the westerly QBO within a locking region. As the strength of w_a is increased, the sizes of the locking regions become progressively larger. Away from locking regions, we find that the QBO period generally decreases as w_a is increased. (This can be best seen by noticing that most of the lines linking the different locking regions in Figure 3.9 slant downwards rather than upwards). This suggests that w_a reduces the impact that w_c has on the descent rate of QBO shear zones, and that sufficiently strong values of w_a

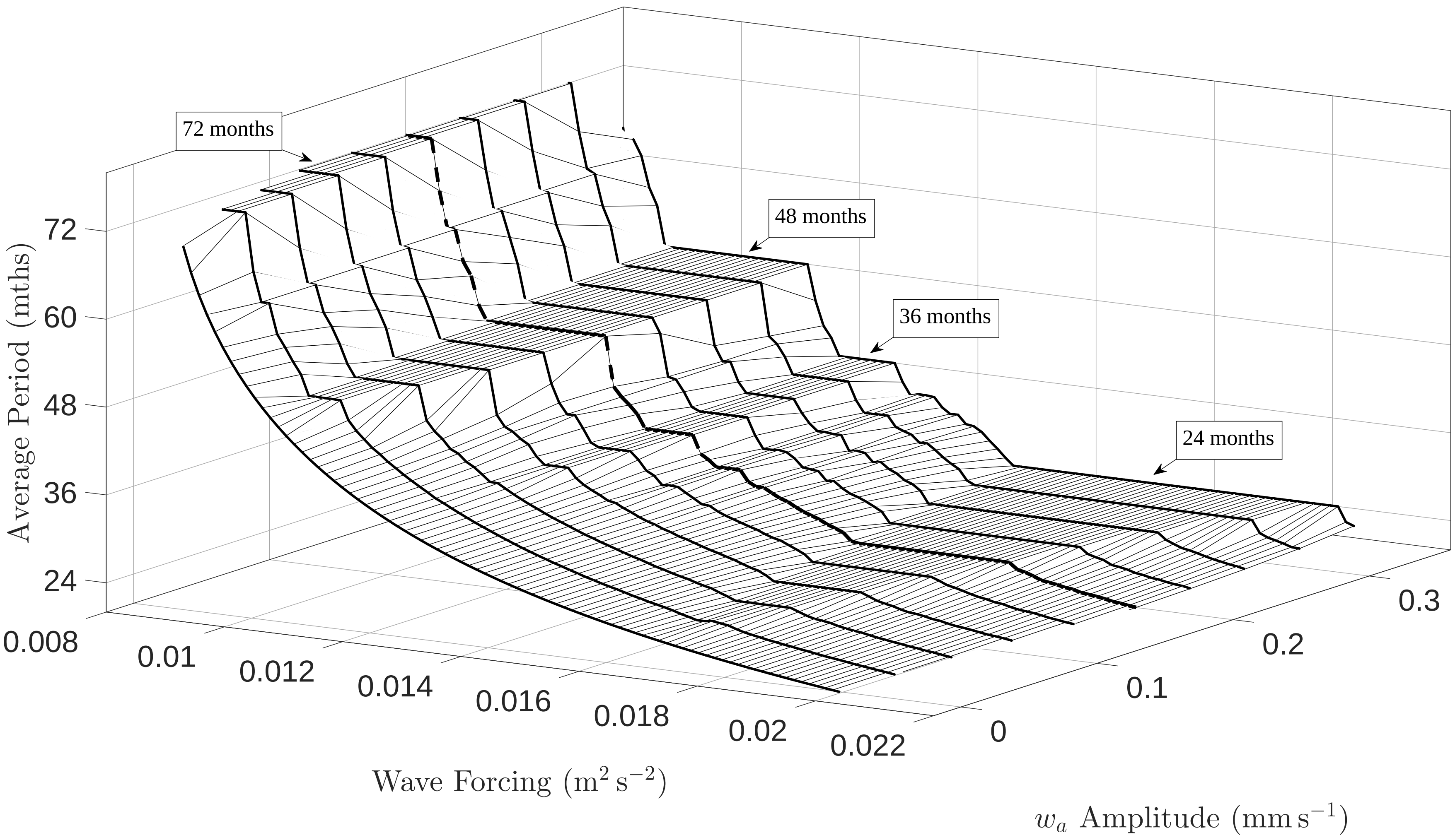

Figure 3.9: Surface plot of the variation of average QBO period with wave forcing (left axis) and the strength of the annually varying component of tropical upwelling (right axis). Plateaus in the surface - corresponding to integer year QBO periods - have been labelled.

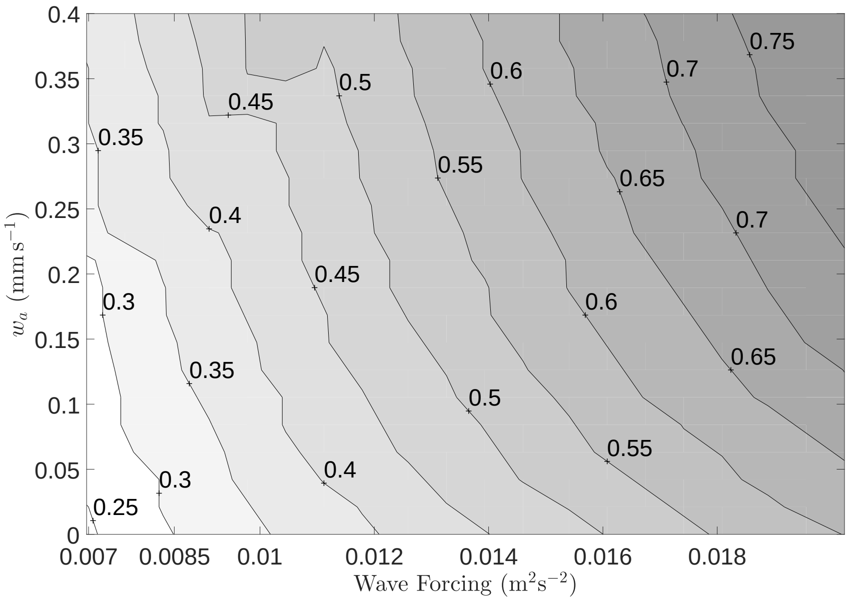

Figure 3.10: Contour map depicting the largest possible value of w_c (in mm s^{-1}) at which a QBO can still form (for given values of F and w_a). Contour lines are drawn at intervals of 0.05 mm s^{-1}; darker shades represent higher values of w_c.

may be able to assist in QBO formation by mitigating the effect of w_c.

To investigate this possibility, we ran a series of 441 experiments, comprising permutations of 21 different values for each of F and w_a. In each simulation, the value of w_c was incrementally increased until just before the strength of the upwelling became large enough to prevent the formation of a QBO. A contour plot of this 'maximal-w_c' is presented in Figure 3.10. We see that there is a clear tradeoff between F and w_a at a fixed maximal w_c. In other words, if the wave forcing is too weak to overcome the effect of a fixed mean upwelling, it may still be possible to generate a QBO by increasing the value of w_a to compensate, without having to increase the amount of parameterised wave forcing in the model.

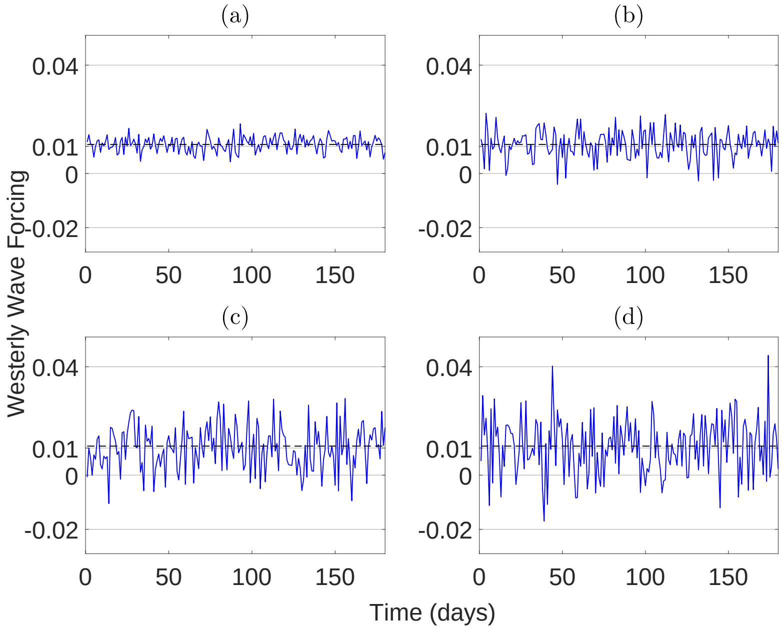

Figure 3.11: Sample time series of stochastic westerly wave forcing at the tropopause over 6 months. Each series is the sum of a fixed mean wave forcing component of $\bar{F}_1 = 11.0 \times 10^{-3}\text{m}^2\,\text{s}^{-2}$, and a stochastic component modelled as Gaussian white noise. The standard deviations of the noise processes are set at $\sigma_1 =$ (a) 2.7×10^{-3}, (b) 5.4×10^{-3}, (c) 8.1×10^{-3}, and (d) $10.8 \times 10^{-3}\,\text{m}^2\,\text{s}^{-2}$ respectively.

3.3.4 Stochasticity effects

In order to test whether the preceding results are robust to random perturbations, we introduce noise terms to the prescribed wave forcing at the tropopause:

$$F_i(t) = \bar{F}_i + \eta_i(t), \tag{3.3.1}$$

where $i = 1, 2$.

Here $\bar{F}_i$ is the fixed or mean component of wave forcing for the i^{th} wave, and $\eta_i(t)$ is the stochastic addition consisting of Gaussian white noise with mean zero and standard deviation σ_i. The noise contributions to the different waves are independent of each other.

Figure 3.11 shows sample time series of the tropopause wave forcing over the course of 6 months for a westerly wave with mean component $\bar{F}_1 = 11.0 \times 10^{-3}\text{m}^2\,\text{s}^{-2}$, with

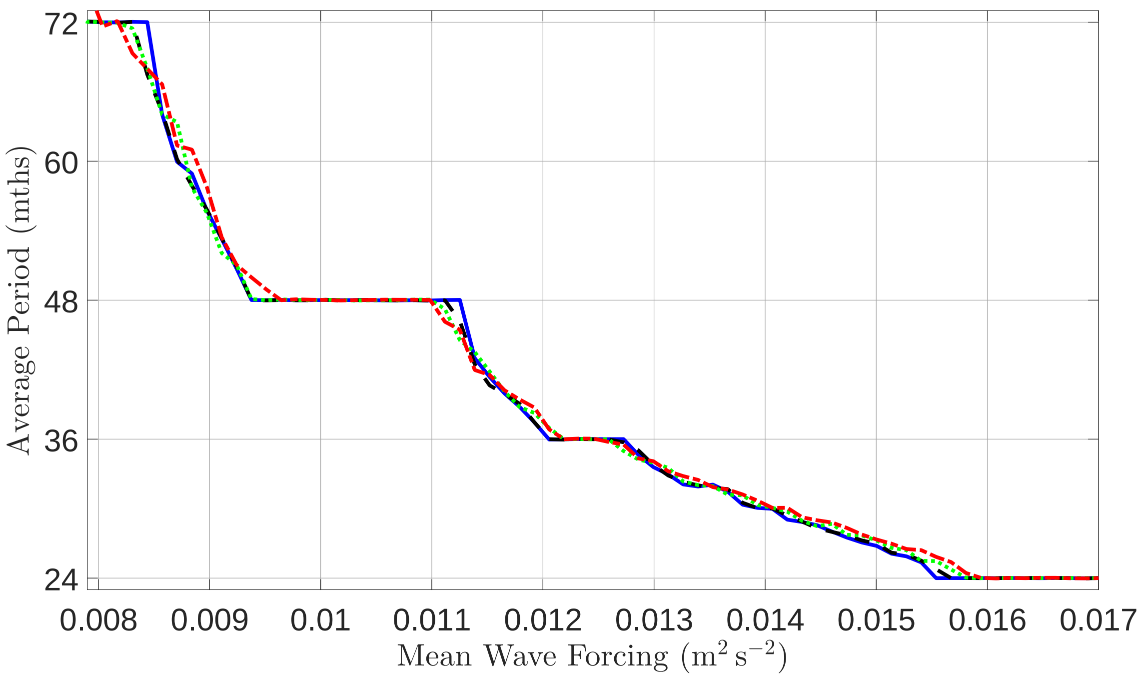

Figure 3.12: Mean QBO period with the addition of Gaussian white noise to the wave forcing with standard deviations of $\sigma_{1,2} = 2.7 \times 10^{-3}\,\mathrm{m^2\,s^{-2}}$ (solid blue line), (b) $5.4 \times 10^{-3}\,\mathrm{m^2\,s^{-2}}$ (dashed black line), (c) $8.1 \times 10^{-3}\,\mathrm{m^2\,s^{-2}}$ (dotted green line), and (d) $10.8 \times 10^{-3}\,\mathrm{m^2\,s^{-2}}$ (dash-dotted red line) respectively.

four different values of standard deviation: $\sigma_1 = 2.7 \times 10^{-3}\ \mathrm{m^2\,s^{-2}}$, $5.4 \times 10^{-3}\ \mathrm{m^2\,s^{-2}}$, $8.1 \times 10^{-3}\ \mathrm{m^2\,s^{-2}}$, and $10.8 \times 10^{-3}\,\mathrm{m^2\,s^{-2}}$ respectively. As a result of the stochastic terms the total momentum flux F_1 displays significant fluctuations about the mean forcing value. Large values of the standard deviation σ_1 result in correspondingly large deviations of the wave forcing away from this mean value, with the total wave forcing quadrupling relative to the mean forcing at some points in the case of the strongest deviation (Figure 3.11(d)).

In order to investigate the effect of stochastic forcing on the period of the QBO we ran four sets of 100 runs, with the mean wave forcings $\bar{F}_1 = -\bar{F}_2$ varying uniformly between $7.9 - 17.0 \times 10^{-3}\,\mathrm{m^2\,s^{-2}}$ in each set, and with each set of runs using one of the four values of σ mentioned in the preceding paragraph. The mean periods of the resulting simulated QBOs were computed as described in earlier sections of the chapter; these are plotted against mean wave forcing in Figure 3.12. The solid blue, dashed black, dotted green and dash-dotted red lines trace the mean periods of simulated QBOs with stochastic wave forcings with standard deviations $\sigma_{1,2} = (2.7, 15.4, 8.1, 10.8) \times 10^{-3}$ $\mathrm{m}^2\,\mathrm{s}^{-2}$ respectively. All four lines have a similar structure to the case with no stochastic forcing (top solid line in Figure 3.1); the overall shape of the curve is not significantly changed. Thus it would seem that the stochasticity does not have a significant effect on the mean period of the QBO, presumably because the relatively long period of the QBO allows for the short timescale stochastic variations in wave forcing to be largely smoothed out. We note, however, that the widths of the locking regions do get narrower as the standard deviation of the noise is increased; therefore, narrower rational ratio locking regions are likely to become lost with increasing noise.

Figure 3.13 displays individual QBO cycles for different values of the fixed wave forcing in the case when $\sigma = 5.4 \times 10^{-3}\,\mathrm{m}^2\,\mathrm{s}^{-2}$. The discrete QBO cycles that were so prominent in the non-stochastic case (Figure 3.3) have now largely disappeared, replaced by a general 'smudging' or spreading of the QBO periods due to the addition of the noise. There is, however, little change in the range of QBO periods; the upper and lower bounds of the QBO period for a given mean forcing are largely unchanged.

A similar picture holds in the section bounded by the rectangular box in Figure 3.13 - this region was rerun, as before, at 12 times the resolution in wave forcing. Results are displayed in Figure 3.14. As before, we see that very little of the fine structure observed in the non-stochastic case (Figure 3.3) has been preserved. Although the QBO periods have been smeared out by the noise, we see that the general structure of the bifurcations are still visible, and that the QBO periods in the stochastic case are still organised into bands corresponding to n-cycle QBOs. This is most obvious at lower values of the wave forcing, where the QBO period bifurcates through the 2-cycle and 3-cycle regimes. As wave forcing increases, the regimes begin to overlap and details are blurred by the noise. Nevertheless, the qualitative behaviour of the QBO

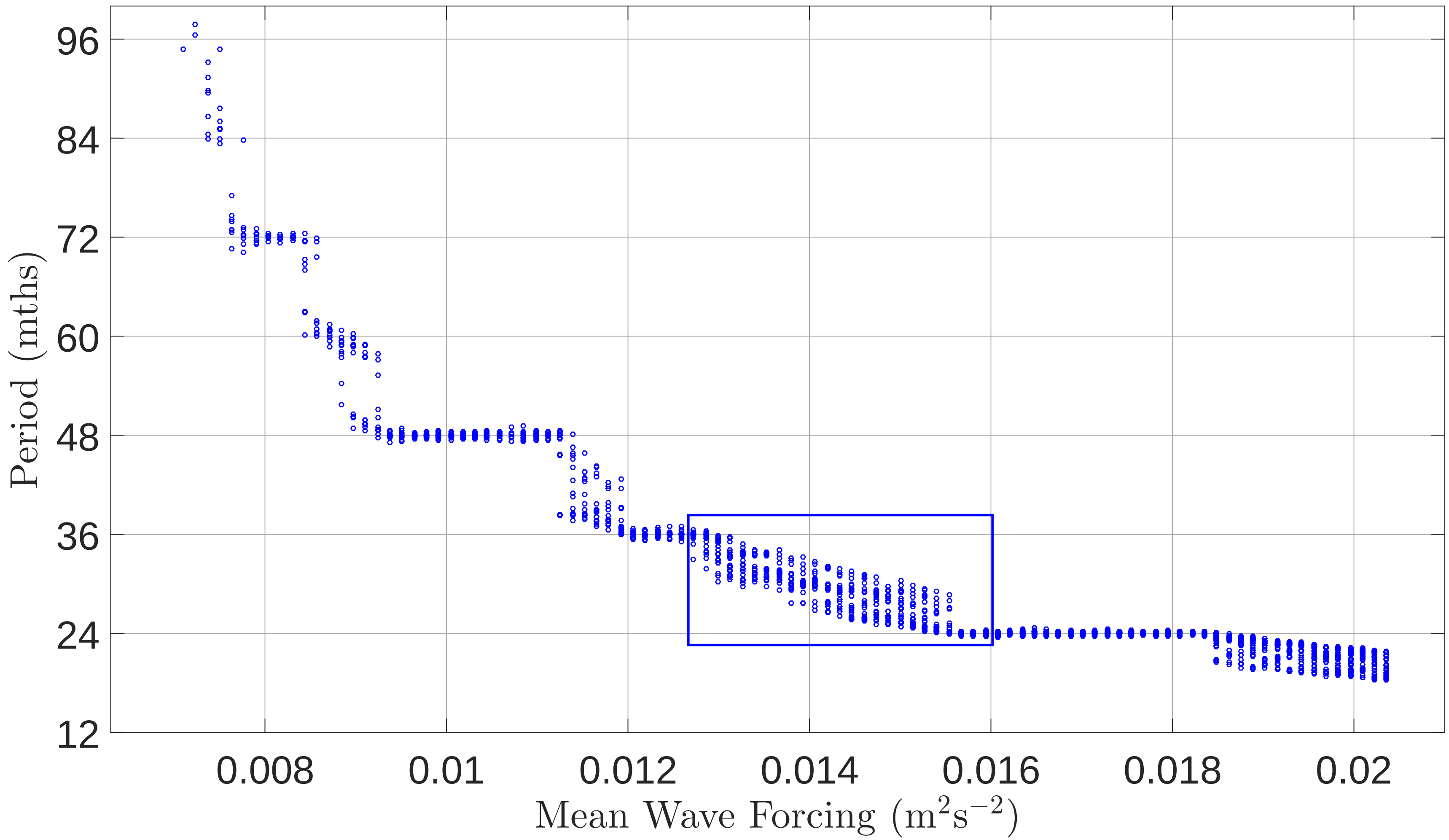

Figure 3.13: Individual QBO cycle lengths for simulations with stochastic wave forcing with standard deviation $\sigma = 5.4 \times 10^{-3}\,\mathrm{m}^2\,\mathrm{s}^{-2}$. The boxed region is explored in greater detail in Figure 3.14.

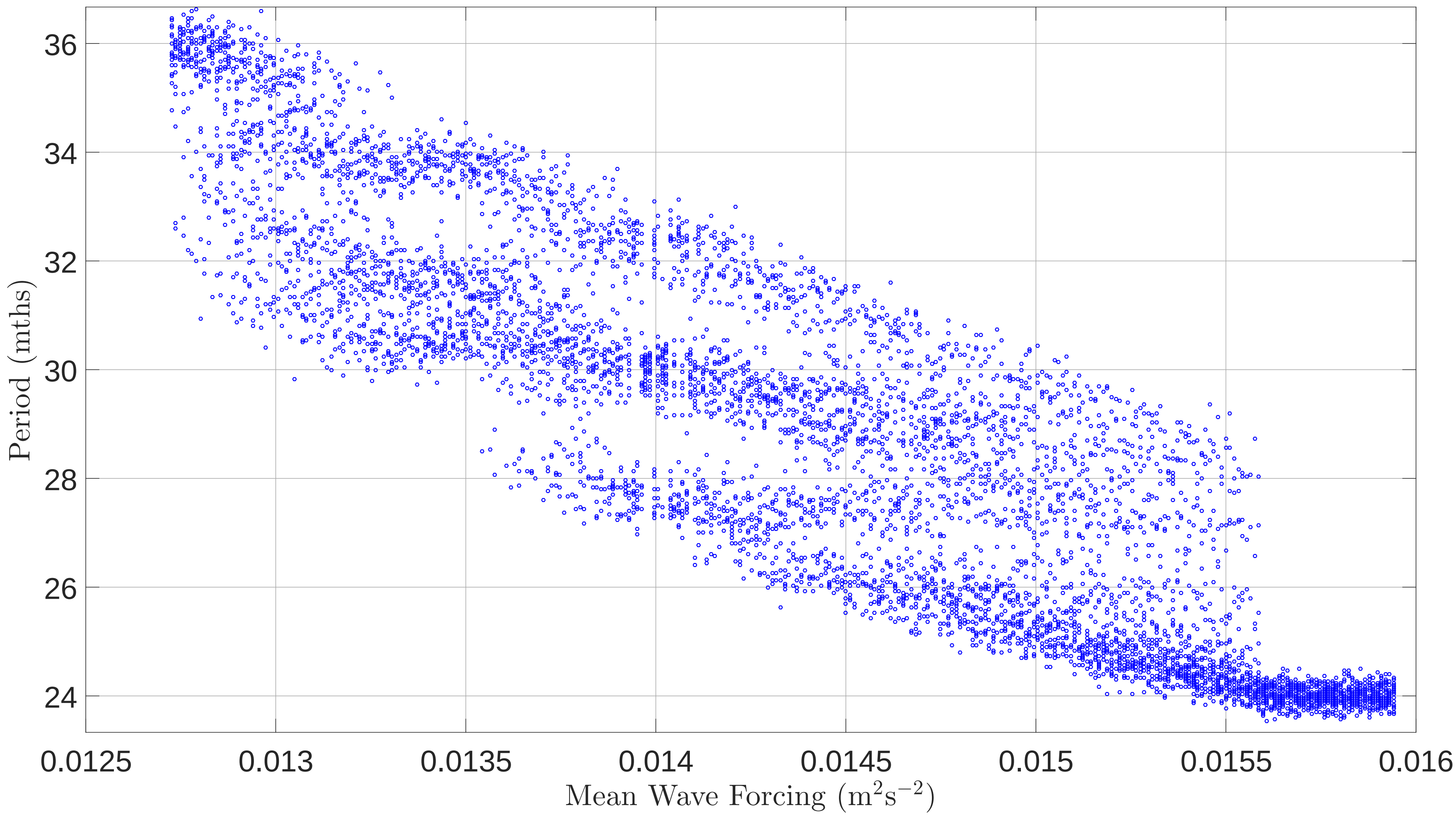

Figure 3.14: Recalculation of the QBO cycle periods for the region contained within the rectangular box in Figure 3.13, for simulations with stochastic wave forcing with standard deviation $\sigma = 5.4 \times 10^{-3}\,m^2\,s^{-2}$. The resolution along the wave forcing axis has been increased by 12 times over the resolution in Figure 3.13.

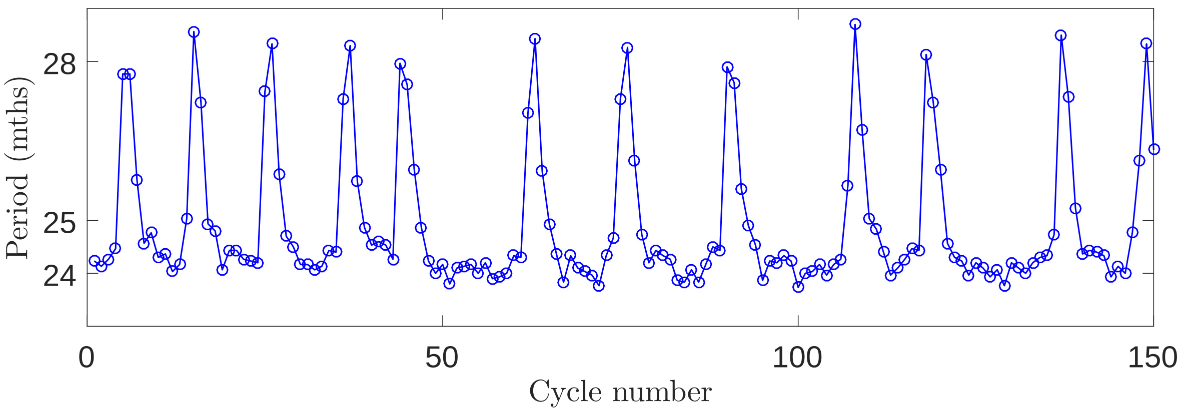

Figure 3.15: Evolution of QBO cycle period for a simulation with stochastic wave forcing consisting of a mean component of $\bar{F} = 15.5 \times 10^{-3}\mathrm{m}^2\,\mathrm{s}^{-2}$ and a stochastic component consisting of white noise with standard deviation $\sigma = 5.4 \times 10^{-3}\,\mathrm{m}^2\,\mathrm{s}^{-2}$. The evolution can be contrasted with the non-stochastic case presented in Figure 3.4(c).

periods is not that different. As an example, Figure 3.15 shows the evolution of the QBO period in the case when the mean wave forcing is equal to $\bar{F} = 15.5\times10^{-3}\mathrm{m}^2\,\mathrm{s}^{-2}$; contrast this with the non-stochastic version of this simulation which is displayed in Figure 3.4(c). The general behaviour of the QBO periods are clearly similar - the QBO spends a relatively long time at a period close to 24 months, before suddenly jumping to a longer period of around 28 months. The addition of noise has not fundamentally changed the basic mechanism of interaction between the QBO and the annual cycle in upwelling. However, the frequency of the jumps has changed - they are more common and more irregular in the stochastic case with 12 jumps in 150 cycles as opposed to 7 jumps in 150 cycles in the non-stochastic case. Furthermore, the number of cycles between jumps is much more variable in the stochastic case, varying from as few as 7 to as many as 22 full QBO cycles between jumps.

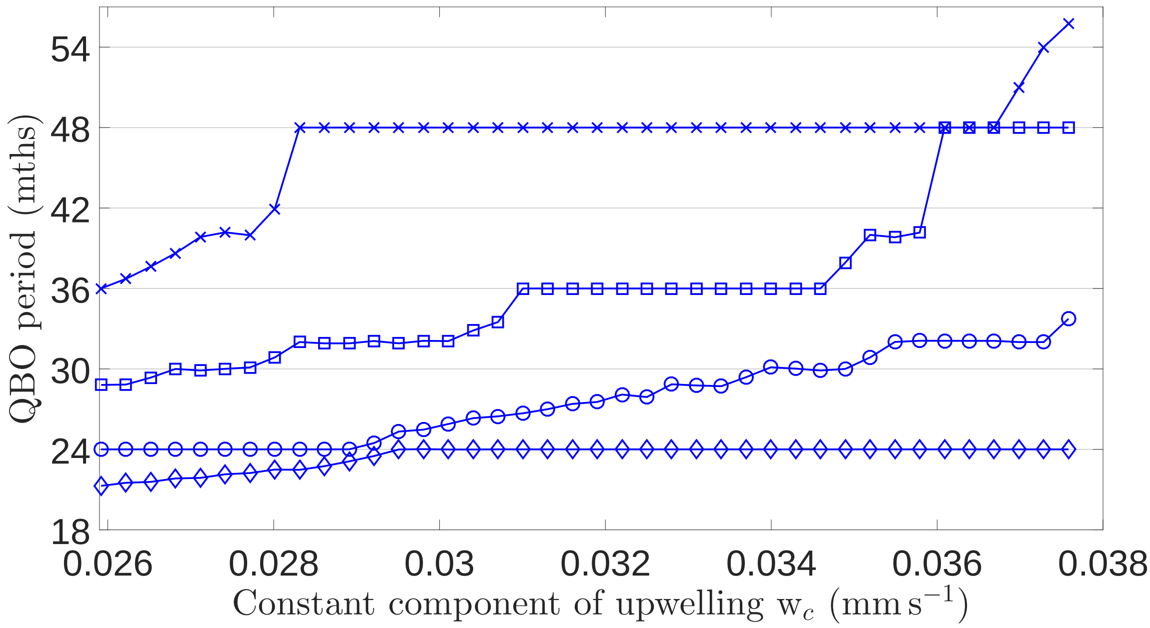

Figure 3.16: Increase in the average QBO period with increasing w_c. The amplitude of the annual cycle component of upwelling is kept constant at $w_a = 0.2$ mm s^{-1}. The four plots correspond to wave forcings of $F = 12.1 \times 10^{-3}$ (crosses), $F = 14.3 \times 10^{-3}$ (squares), $F = 16.3 \times 10^{-3}$ (circles), and $F = 19.3 \times 10^{-3}$ (diamonds).

3.3.5 QBO response to increased tropical upwelling in a warming climate

To study the effect of increased upwelling on the QBO at constant wave forcing, we considered four representative wave forcings, $F = (12.1, 14.3, 16.3, 19.3) \times 10^{-3}$ m^2 s^{-2}, and fixed $w_a = 0.2$ mm s^{-1} while letting w_c vary uniformly between $w_c = 0.2 - 0.7$ mm s^{-1}. We ran the simulations sequentially in w_c and computed the QBO periods is the usual way.

Results of the average QBO period at each value of w_c are plotted in Figure 3.16 for each run. In all four cases, the QBO period tends to increase with increased upwelling over long periods. As the period increases, the QBO enters into frequency locked states with the annual cycle, and sometimes remains in these states even with significant increases in the upwelling strength.

In light of the previous findings presented in section 3.3.2 on the quasi-periodic behaviour of the QBO cycles, however, we would expect that the QBO period would adopt a complicated set of frequency modulated oscillation cycles as upwelling increases, rather than the smooth period changes of Figure 3.16 . To investigate this dynamical evolution of the QBO period, we took the simulation for $F = 16.1 \times 10^{-3}$ $\mathrm{m}^2\,\mathrm{s}^{-2}$ and ran it again. This time, as the model evolved, we set the value of w_c to increase *dynamically* at a rate of 3% per decade, in line with the predictions of GCM studies (Butchart [2014]). The model QBO was simulated for 300 years, and the evolution of the QBO period was calculated using the time between westerly onsets at 24 km. The results are plotted in Figure 3.17. As anticipated, the QBO period fluctuated quite considerably. For the first 24 years it remained in the 24 month locking region, fully locked to the annual cycle and unaffected by the increase in upwelling. When it finally drifted out of the locked state, it then entered into a series of 5-, 4-, 3-, and 2-cycles similar to those discussed in section 3.3.2. After around 100 years, the period had drifted close enough to the 36 month locking region, and once again the QBO became locked to the annual cycle for 48 years. After clearing the 36 month locking region, it spent a short 15 years in transition before once again becoming entrained to the annual cycle. For the final 100 years or so until the end of the simulation, the QBO remained trapped in a 48 month oscillation.

3.4 Discussion

In this chapter we have demonstrated the possibility of synchronization of the QBO by the annual cycle in tropical upwelling, albeit in a highly idealised model. Frequency locking between the QBO and the annual cycle has not generally been reported in the real stratosphere (Dunkerton [1990]), although a recent paper has presented observational evidence arguing in favour of this (Gabis [2015]).

The identification of discrete jumps in the QBO period at fixed values of the wave

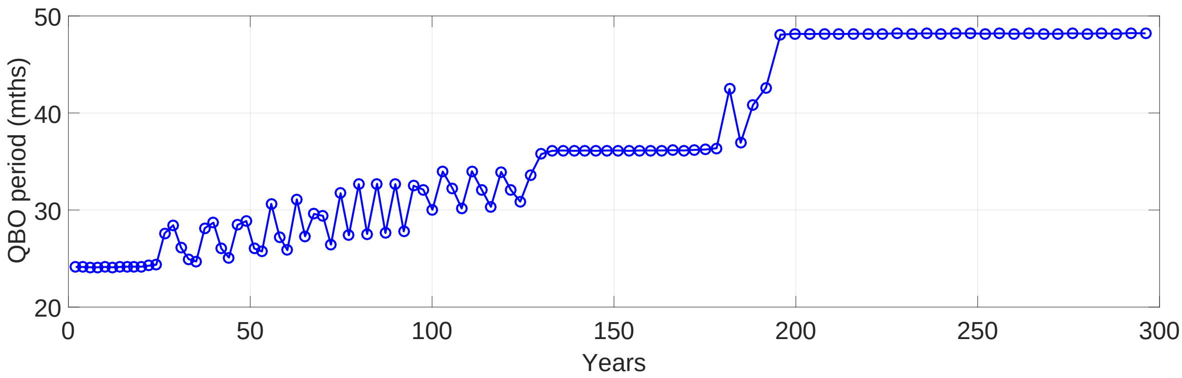

Figure 3.17: The changing length of individual QBO cycles over a span of 300 years as a result of continuously increasing upwelling. Wave forcing is fixed at $F = 16.1 \times 10^{-3}$ $\mathrm{m^2\,s^{-2}}$, and $w_a = 0.2$ $\mathrm{mm\,s^{-1}}$. The constant component of upwelling w_c is allowed to change dynamically during the model run, increasing over present-day values at a rate of 3% per decade.

forcing has not been observed by previous authors in the context of a one-dimensional QBO model. Our model results show that the QBO can adopt different periods from cycle to cycle that are not multiples of the annual cycle period, and yet are still influenced by the annual cycle in the sense that the set of unique periods at a given wave forcing sums to a multiple of 12 months. The model behaviour seems to be an example of synchronization under the influence of a periodic external force (eg. Pikovsky et al. [2003]); this point will be discussed in more detail in Chapter 6.

As a simple test of whether the multiply-periodic behaviour found in our model is seen in the real atmosphere, we considered the duration of westerly phases of the QBO in 50 hPa wind from 1953-2001 (Table 3.1). (This data was taken from Figure 1 of Hamilton [2002]). We considered westerly regimes in isolation, as they are not affected by the stalling that sometimes impedes the regular descent of easterly regimes (Baldwin et al. [2001]). In Table 3.1 the individual westerly periods have been listed in order of occurrence, but have been separated into seven sets. The sum of the periods of each set is given in the second column of the table. Under this partitioning of the data, we see that the sum of periods in each set is either exactly or very close to a multiple of 12 months. This is consistent with the predictions of our model.

Table 3.1: Duration of westerly phases of the QBO at 50 hPa from 1951-2001, taken from Figure 1 of Hamilton [2002]. The phases are listed in order of appearance (left to right, top to bottom), and have been separated into seven sets. The second column entries are the sum of phase durations in each row.

Westerly phase duration (mths)	Row Sum
15, 14, 15, 10, 18,	72
21, 23, 13, 14,	71
14, 18, 17,	49
17, 19,	36
24,	24
20, 14,	34
17, 16, 13, 26,	72

It has been suggested that the long-term cycle in the observed periods of the QBO are due to a 'multi-decadal oscillation' caused by an interaction between the QBO and the solar cycle (Salby and Callaghan [2000]). The results of our (admittedly idealised) modeling study suggest a possible alternative explanation to this phenomenon: the multi-decadal oscillation of the QBO period is the result of the periodic adjustment of the QBO phase due to its interaction with the annual cycle in tropical upwelling. However, much more work would be required before making such a definitive statement either way as to the cause of the multi-decadal oscillation.

Recently there has been a heightened interest in the dynamics of the QBO, after the oscillation underwent an unprecedented 'disruption' in the 2015–2016 winter season (Newman et al. [2016], Osprey et al. [2016]). An anomalous easterly jet, possibly due to forcing by an extratropical Rossby wave, formed in the lower stratosphere and disrupted the existing westerly shear zone at 40 hPa. This behaviour was not seen before in the 60 year observational record, and has renewed the question of the accuracy of the statistics of the QBO based on a relatively short observational record. Indeed, the results of this chapter reinforce the point that the QBO is quite capable of displaying unusual long-term variations in its period, simply through its interaction with the annual cycle. For example, in Figure 3.4(c) the QBO spends almost 30 years at an approximately constant 24 month period, before jumping to a long period regime for 3 cycles. Understanding how and when such behaviour might occur in a comprehensive climate model is therefore of some urgency if we are to make sense of the intrinsic variability of the QBO and predict future disruptions with any confidence.

We have shown that the frequency locking between the QBO and the annual cycle in tropical upwelling allows for the creation of 24, 30, and 36 month synchronization regions (although the 30 month locking region is somewhat narrow). These are the same QBO periods identified by Read and Castrejón-Pita [2012] in their study of the QBO period in the ERA-40 and ERA-Interim reanalysis data sets. Our findings reinforce the notion that the observed synchronization between the QBO and the stratopause semi-annual oscillation (SAO) (Dunkerton and Delisi [1997], Kuai et al. [2009], Read and Castrejón-Pita [2012], Krismer et al. [2013]) does not necessarily imply a causal dynamical link between the two oscillations, but may in fact simply be due to the independent synchronization of both wind systems to the underlying annual cycle. We will revisit these issues again in Chapter 7 when we explore synchronization of the QBO in reanalysis and GCM data.

In the real atmosphere the QBO is thought to be generated by a wave spectrum made up of Kelvin waves, mixed Rossby-gravity waves, and gravity waves. The exact make-up of this wave spectrum, and the relative importance of the large-scale and small-scale components, is still poorly understood (Baldwin et al. [2001]. We have not considered any of these issues, and have chosen to focus on a highly idealised wave spectrum that is constant in time and only has two wave components. This constrains the direct applicability of our results to the real atmosphere. Nevertheless, even in this simple setting, our findings highlight that the pattern of QBO periods under the influence of the annual cycle is very rich (Figure 3.2). Further, relatively small variations in the wave forcing lead to quite dramatic qualitative variations in the dynamics of the QBO period (Figure 3.3). This implies that our ability to predict the long-term QBO period (Scaife et al. [2014]) may be quite limited due to the sensitivity of the QBO period to variations in the strength of upwelling and wave forcing as a result of both natural variability and anthropogenic climate forcing.

In the context of a warming climate, Kawatani and Hamilton [2013] presented evidence of a weakening trend in the amplitude of the QBO winds in the lower stratosphere, and used this to infer a strengthening of the Brewer-Dobson circulation. In our study of the QBO response to increased tropical upwelling we did not consider changes to the QBO amplitude as our prescription of the wave forcing is too simplistic. Instead, we focused on the resulting changes to the QBO period. Our results suggest that the period of the QBO will increase in line with the strengthening of the mean amplitude of the Brewer-Dobson circulation that is predicted by most GCMs (Butchart [2014]). The current QBO-resolving GCMs, however, are not consistent in their predictions of the future trend of the QBO period in a warming climate. Indeed, two models (MPI-ESM-MR and HadGEM2-CC) actually predict a *decrease* in the period of the QBO (see Figure S8 in the Supplementary Information of Kawatani and Hamilton [2013]). This decrease could be due to an increase in the annual component of tropical upwelling, which has been shown to reduce the period of the QBO in our model (see Figure 3.9). This would be consistent with the predicted increase in mean tropical upwelling if the future increasing trend in upwelling varies with season, so that the northern hemisphere winter trend is stronger than the southern hemisphere winter trend.

The QBO period in our model undergoes a series of oscillations as the strength of tropical upwelling increases, and it eventually enters the 36 month locking region (Figure 3.17). A firm prediction as to whether or not increased upwelling will eventually lead to exact frequency locking of the QBO at 36 months sometime in the next century cannot be made with any precision from this simplified model. However, our findings do underscore the crucial role that the annual cycle in the Brewer-Dobson circulation plays in determining the evolution of the QBO period in future decades. The importance of realising a robust representation of this feature in GCMs should be emphasised.

Chapter 4

Synchronization II: Semi-annual forcings

4.1 Introduction

In this chapter we consider the relationship between the QBO and different semi-annual winds in the tropics. Chiefly we study the stratopause Semi-Annual Oscillation (SAO), a zonal wind oscillation with a precise six month period that spans the upper stratosphere and peaks near the stratopause. The existence of the SAO was first reported in observational studies by Reed [1962, 1966], and its presence has been further confirmed using a variety of radiosonde, rocketsonde, and satellite observations (for a review, see Garcia et al. [1997]). The SAO actually consists of two oscillations, with the second oscillation confined to the mesosphere with a peak at the mesopause (Hirota [1978]). The phase of the SAO varies smoothly throughout the upper stratosphere and mesosphere, with the stratopause and mesopause winds approximately out of phase with each other (Hirota [1978], Hamilton [1982]). The easterly phase of the SAO is driven by the cross-equatorial advection of easterly winds by the seasonal cycle (Dunkerton [1991]), whereas the westerly phase is primarily wave-driven, by a mixture of fast Kelvin and gravity waves (Dunkerton [1979]).

The SAO and the QBO have long been considered to be coupled or synchronized (Baldwin et al. [2001], Dunkerton and Delisi [1997]). Observations strongly suggest a smooth transition between descending westerly SAO shear zones aloft and the formation of new QBO westerly shear zones (Dunkerton and Delisi [1997]). This observation was a key component of the first successful theory that recognised the wave-driven nature of the QBO (Lindzen and Holton [1968]). The authors supposed that the presence of semi-annual winds in the upper stratosphere would provide a 'seed' for the formation and subsequent descent of QBO wind regimes in the mid-stratosphere via the triggering of critical level absorption of equatorial waves. A subsequent refinement of this theory (Holton and Lindzen [1972]) induced wave-mean flow interaction via the dissipation of waves by Newtonian cooling rather than critical level wave breaking. Although the Holton-Lindzen theory retained a semi-annual forcing term in the model equation, it was found that the SAO was no longer strictly necessary in order to produce a wave-driven oscillation. A few years later, Plumb [1977] proved that wave momentum forcing at any given height in the Holton-Lindzen model equation was only dependent on zonal mean winds *at or below that height*, at least in the absence of diffusion. In other words, a semi-annual oscillation in the upper stratosphere could not affect wave deposition in the middle and lower stratosphere in the absence of diffusion. This result implied that the SAO was not crucial to the mechanism of the QBO and was likely unable to synchronise it either, at least in the Holton-Lindzen model.

The above result, whilst valid for the Holton-Lindzen theory, does not necessarily preclude the possibility of QBO-SAO synchronization in general. Indeed, Dunkerton [1997] showed that the wave parameterisation of the 1968 Lindzen-Holton model of the QBO - based on critical level absorption of a gravity wave spectrum - could, in principle, exert a downward influence via wave driving alone, thus allowing for

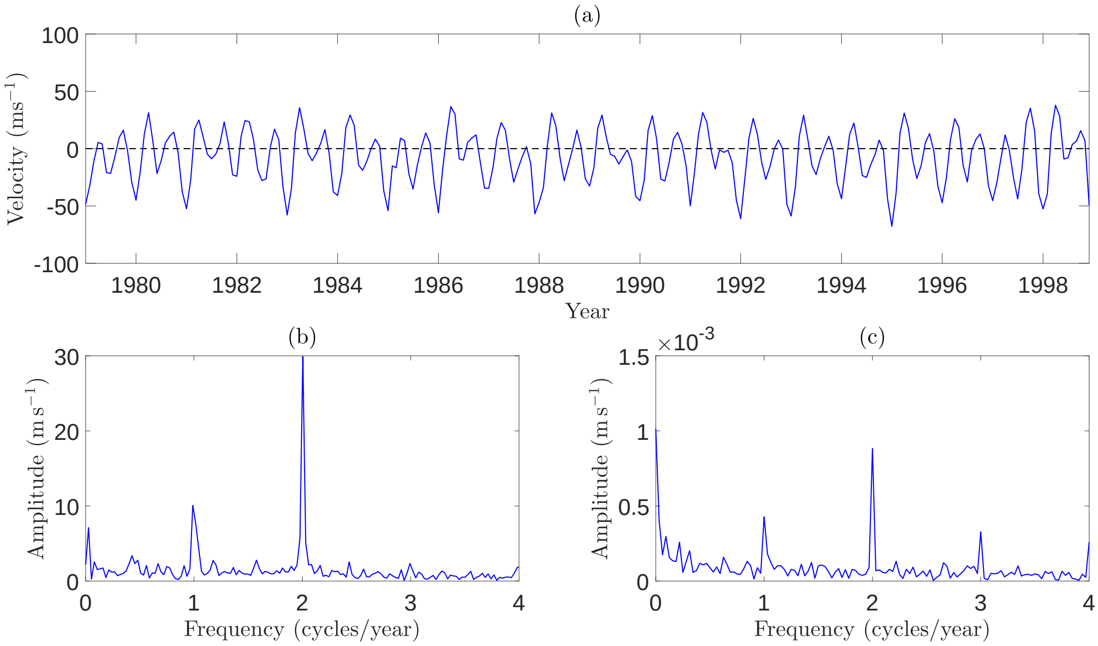

Figure 4.1: Semi-annual winds over the equator at 1hPa. (a) Zonal mean zonal wind velocities at 1hPa, from ERA-Interim data. (b) Fourier spectrum of the 1hPa zonal mean zonal wind. (c) Residual vertical upwelling w^* at 1hPa, as diagnosed from ERA data by Seviour et al. [2012]. Note the strong semi-annual peak in both the $\bar{u}$ and w^* spectra due to the SAO.

synchronization of the QBO by the SAO. Thus the interaction between the QBO and SAO is quite sensitive to the wave parameterisation used. Read and Castrejón-Pita [2012] studied the QBO and SAO in ERA-40 and ERA-Interim reanalysis data sets using singular systems analysis and analytic phase techniques, and found coherent synchronization of the wind systems at SAO:QBO frequency ratios of 4:1, 5:1, and occasionally 6:1. Similarly Kuai et al. [2009] found robust synchronization between the SAO and QBO at upper stratospheric levels in ERA-40 data and, furthermore, found that the QBO periods in their model simulation followed a bimodal distribution centered around multiples of four and five times the period of the SAO.

From a slightly different perspective, Hampson and Haynes [2004] investigated the relationship between the QBO and the annual cycle in upwelling in a 3-D mechanistic model and found evidence of phase alignment of the QBO due to the annual cycle in upwelling. Since there is a strong semiannual cycle in upwelling in the mid-

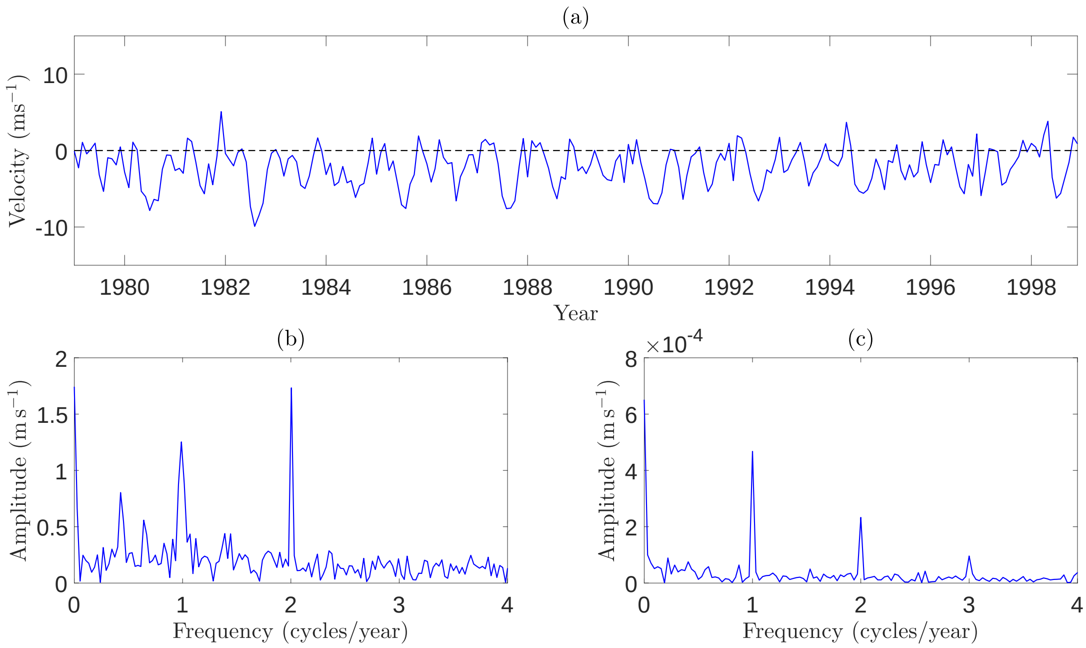

Figure 4.2: As in Figure 4.1, but for winds measured at 100hPa. Note the strong annual and semi-annual peaks in both Fourier spectra.

stratosphere (Rosenlof [1995]), they postulated that perhaps the semiannual cycle in *upwelling* might be the proximate cause of the observed QBO-SAO synchronization, rather than it being a direct zonal wind effect.

Furthermore, the stratopause SAO is not the only semi-annual cycle present in the Tropics. Figures 4.1 and 4.2 show two sets of wind velocities and Fourier spectra as measured on the equator at 1hPa and 100hPa (approximately 48 km and 17 km respectively). Plot (a) in each figure presents time series of zonal mean zonal wind velocities extracted from the ERA-Interim reanalysis data set (Dee et al. [2011]). Corresponding Fourier spectra of the time series are shown in plot (b) of each figure. The signature of the stratopause SAO can be seen clearly from the prominent semi-annual peak in Figure 4.1(b). We note, however, the presence of a significant semi-annual signal in the 100hPa winds as well (Figure 4.2(b)). The associated velocity profile has a strong easterly bias and has a much smaller amplitude as compared to the stratopause SAO. The source of this oscillation is thought to be due to the twice-yearly equatorial crossing of the Inter-Tropical Convergence Zone (ITCZ) as it tracks the latitude of the subsolar point[1] (Van Loon and Jenne [1970]).

Plot (c) in each figure depicts the Fourier spectrum of the vertical component of the residual mean meridional circulation at the relevant height, as calculated by Seviour et al. [2012] (see Chapter 7 for more details). Again we see the presence of a significant semi-annual peak at both heights, although the annual cycle clearly dominates at 100hPa.

In the rest of this chapter we will explore the influence of these semi-annual signals on the period of the QBO, using the Holton-Lindzen model with various additional forcing terms. In Section 4.2 we introduce the relevant modifications to the Holton-Lindzen model, and outline the argument put forward by Plumb [1977] for no downward propagation of influence. Semi-annual forcing due to the SAO and the ITCZ are then considered in turn. As expected, we find that the SAO modulates the period of the QBO in the upper stratosphere, but is unable to propagate that influence downward. In contrast, by acting in the lower stratosphere the ITCZ forcing is able to influence the period of the QBO throughout the stratosphere. The possibility of synchronization via upwelling suggested by Hampson and Haynes [2004] is taken up in Section 4.3; once again, it is shown that the SAO is unable to influence the period of the QBO via this mechanism. The ITCZ upwelling, in contrast, does synchronize the QBO, and produces very similar results to the annual cycle in upwelling that was considered in detail in Chapter 3. Finally, we discuss our findings in Section 4.4.

4.2 Synchronization via direct forcing

4.2.1 Model description

We consider the dynamics of the Holton-Lindzen (HL) model in the presence of external periodic forcing terms. The evolution of the zonal wind $\bar{u}(z)$ is given by

[1]The point on the surface of the Earth where the Sun is perceived to be directly overhead.

$$\frac{\partial \bar{u}}{\partial t} = -\frac{1}{\rho_0}\sum_i \frac{\partial \mathcal{F}_i}{\partial z} + \Lambda(z)\frac{\partial^2 \bar{u}}{\partial z^2} + \frac{\partial}{\partial t}\left(G(z,t)\right). \tag{4.2.1}$$

The first three terms are the usual acceleration, wave forcing and diffusion terms in the Holton-Lindzen equation, and have been discussed previously. Recall from Chapter 2 that the wave forcing due to each wave in the HL72 model at height z is given by

$$\begin{aligned} -\frac{1}{\rho_0}\frac{\partial \mathcal{F}_i(z)}{\partial z} &= -\frac{1}{\rho_0}\frac{\partial}{\partial z}\left(F_i \exp\left\{-\int_{z_l}^{z} \frac{N\mu(z')}{k_i(\bar{u}(z',t)-c_i)^2}dz'\right\}\right) \\ &= \frac{F_i}{\rho_0}\left(\frac{N\mu(z)}{k_i(\bar{u}(z,t)-c_i)^2}\right)\exp\left\{-\int_{z_l}^{z} \frac{N\mu(z')}{k_i(\bar{u}(z',t)-c_i)^2}dz'\right\}. \end{aligned} \tag{4.2.2}$$

Plumb [1977] noted that the final expression on the right hand side depends only on the velocity profile at heights $z' \leq z$, and that it is also independent of spatial derivatives of $\bar{u}$. Therefore, it follows that the wave forcing at height z must be independent of the wind profile at heights $z' > z$, and so an imposed semi-annual forcing at higher levels cannot affect the wave forcing at lower levels except through the diffusion term in equation (4.2.1). This is the principle of *no downward influence* outlined in Plumb [1977].

We have extended the Holton-Lindzen equation (4.2.1) to include an extra forcing term $\partial G/\partial t$, which represents acceleration due to the SAO/ITCZ winds. Such a term was first introduced in Holton and Lindzen [1972] to simulate the influence of the SAO; it was later found to be non-essential to the generation of the QBO. Here we introduce two different versions of the forcing term, in order to consider both the influence of the SAO (which we expect to be minimal from the considerations of the previous paragraph) as well as the influence of ITCZ-induced semi-annual winds at the tropopause. The function $G(z,t)$ is defined as

$$G(z,t) = u_F P(z) Q(t), \tag{4.2.3}$$

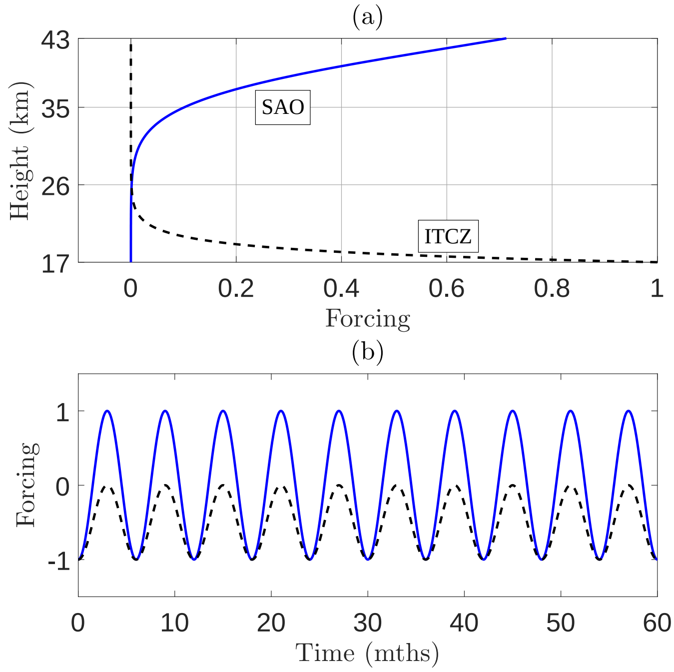

Figure 4.3: Normalised forcing profiles of the SAO and ITCZ. (a) Height profiles $P(z)$ for the SAO (solid line) and ITCZ (dashed line) respectively. (b) Time series profiles $Q(t)$ for the SAO (solid line) and ITCZ (dashed line) respectively.

where $P(z)$ and $Q(t)$ are normalised height and time profiles appropriate for the wind system being simulated, and u_F is a tunable parameter representing the maximal amplitude of the forced winds. $P(z)$ and $Q(t)$ profiles for the two wind systems are shown in Figure 4.3(a) and (b) respectively. The SAO is modelled as having a Gaussian profile in height with a peak at 48 km (above the upper boundary of the model) and a standard deviation of 6 km. It is represented by the solid line in Figure 4.3(a). The ITCZ height profile is represented by the dashed line in Figure 4.3(a). It attains its maximum value at the tropopause, and decreases exponentially with height with a scale height $H_F = 1.3\,\text{km}$.

Time dependencies of the forcings are shown in Figure 4.3(b). The SAO time profile is a pure semi-annual harmonic given by

$$Q(t) = -\cos({}^{2\pi t}/{}_{180}), \tag{4.2.4}$$

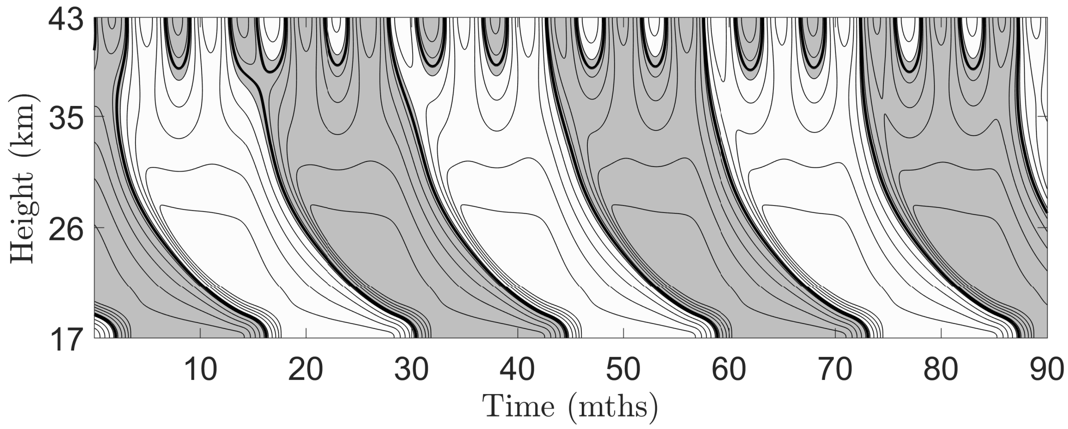

Figure 4.4: Sample simulation of equation (4.2.1) for the SAO forcing configuration, with $u_F = 24\,\mathrm{m\,s^{-1}}$ and $F = 8.0 \times 10^{-3}\,\mathrm{m^2\,s^{-2}}$. Easterly winds are shaded, and contours are drawn at intervals of $5\,\mathrm{m\,s^{-1}}$. The zero wind contour has been darkened.

and is drawn as a solid line in Fig.4.3(b)). The ITCZ time profile takes into account the easterly bias of the 100hPa winds (cf. Figure 4.2), and is given by

$$Q(t) = -\cos^2(2\pi t/360) = -1/2 - 1/2\cos(2\pi t/180). \tag{4.2.5}$$

It is plotted as the dashed line in Figure 4.2(b).

In the following subsections we will investigate the influence of the above forcing profiles on the evolution of the QBO for different values of the wave forcing F and the maximal amplitude of the forced winds, u_F.

4.2.2 Top-down: Impact of the SAO forcing

We first focus attention on the relationship between the QBO and the SAO. We fix $P(z)$ and $Q(t)$ to reflect the SAO profiles described in the preceding subsection, and consider ten different values for the maximum SAO amplitude u_F, ranging between 0–27 $\mathrm{m\,s^{-1}}$. The Holton-Lindzen equation with additional forcing (4.2.1) is then solved in the usual way over a range of values of the wave forcing F, for each choice of u_F.

Figure 4.4 shows a sample numerical simulation of the system in the case when

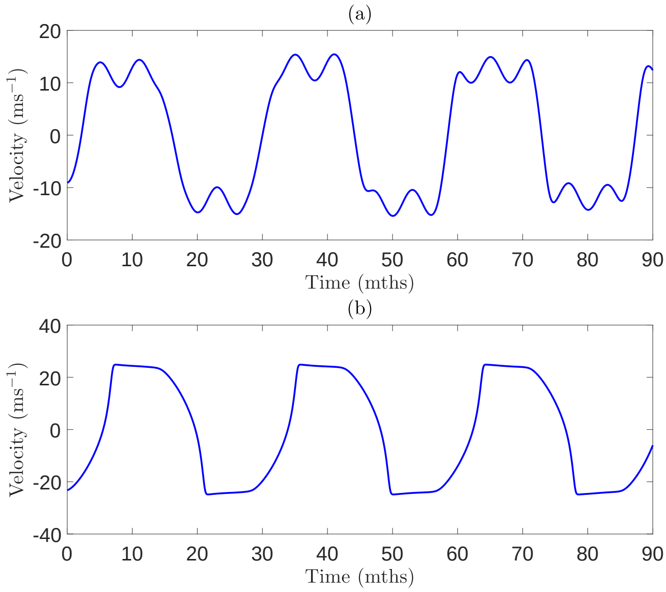

Figure 4.5: Zonal wind time series extracted from Figure 4.4, at heights of (a) 35 km and (b) 26 km.

$u_F = 24\,\mathrm{m\,s^{-1}}$ and $F = 8.0 \times 10^{-3}\,\mathrm{m^2\,s^{-2}}$. The SAO forcing creates a corresponding semi-annual wind oscillation in the upper levels of the model. The influence of the forcing weakens at lower levels, as can be seen from consideration of zonal wind time series at 35 km and 26 km, presented in Figure 4.5. At 35 km, the influence of the semi-annual forcing is clearly visible as periodic small amplitude modulations of the underlying QBO wind. By 26 km, however, these amplitude modulations have essentially disappeared.

In order to systematically study the effect of the SAO on the period of the QBO, we ran 1000 simulations of the combined QBO-SAO system, ranging over ten values of u_F and one hundred values of F. The mean QBO period in each simulation was calculated by measuring the average time between westerly QBO onsets at 26 km. The resultant periods are presented as a surface plot in Figure 4.6. Unsurprisingly, perhaps, there are no indications of synchronization on the surface plot. As wave forcing increases, the period of the QBO decreases monotonically without evidence of locking regions. The mean period is also independent of the strength of the SAO amplitude u_F. The

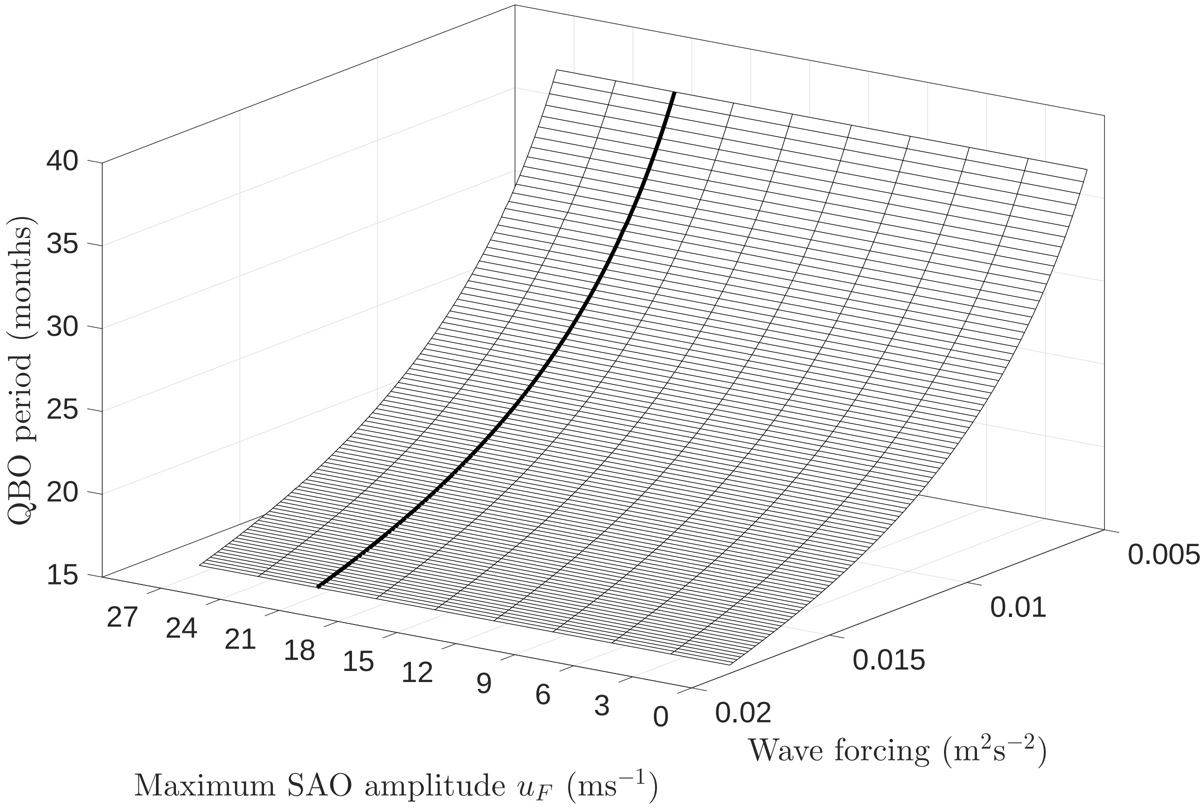

Figure 4.6: Average QBO period in the combined QBO-SAO system as wave forcing F and the maximum SAO amplitude u_F are varied. The period is measured averaging the times between westerly wind onsets at 26 km. The bold line highlights the set of simulations for which $u_F = 21\,\mathrm{m\,s^{-1}}$.

QBO period was also measured at 35 km to check for any variation in the mean QBO period in height (not shown); we found that the results were identical to the 26 km case.

Although the mean period of the QBO is unaffected by the presence of the SAO forcing, individual QBO cycles might display some variability around this value as a result of the semiannual forcing. To investigate this we plotted individual QBO cycle length variations across the usual range of wave forcings and for a fixed SAO amplitude of $u_F = 21\,\mathrm{m\,s^{-1}}$. The simulations in question have been highlighted by the bold line in Figure 4.6.

Figure 4.7 presents the results, for QBO periods measured at 26 km (Figure 4.7(a)) and 35 km (Figure 4.7(b)). We see that QBO periods measured at 26 km display very

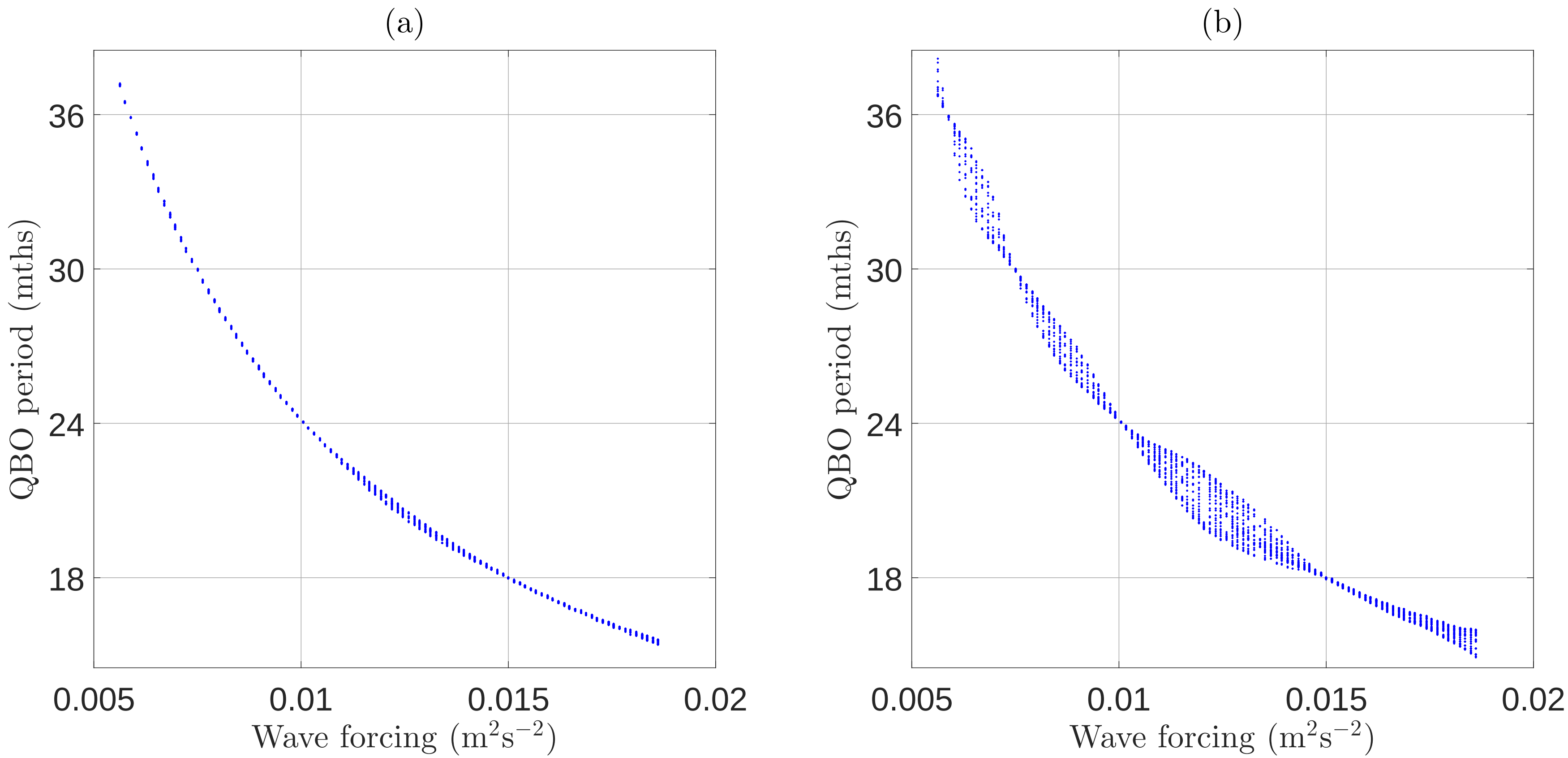

Figure 4.7: Individual QBO cycle lengths as wave forcing is increased in the combined QBO-SAO system for a fixed SAO amplitude of $u_F = 21\,\mathrm{m\,s^{-1}}$. The QBO cycle lengths in the plots are measured as the times between westerly onsets at (a) 26 km, and (b) 35 km respectively.

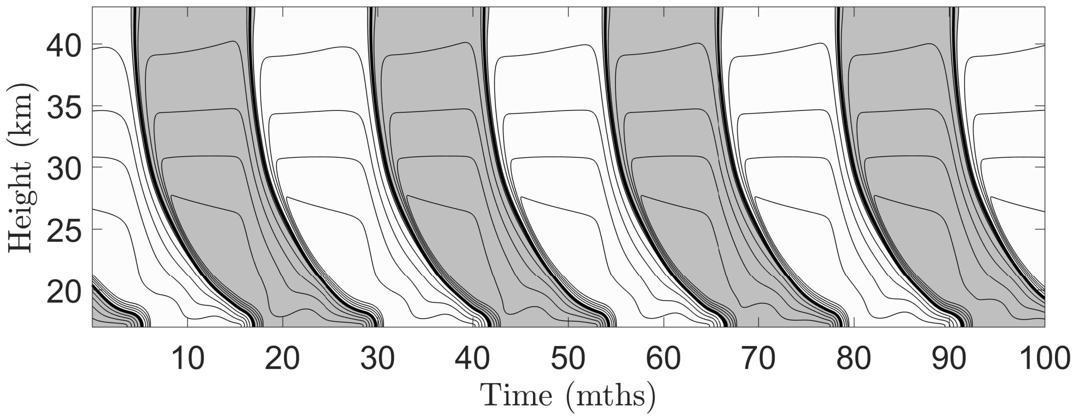

Figure 4.8: Sample simulation of equation (4.2.1) for the ITCZ forcing configuration, with $u_F = 12\,\mathrm{m\,s^{-1}}$ and $F = 10.7 \times 10^{-3}\,\mathrm{m^2\,s^{-2}}$. Easterly winds are shaded, and contours are drawn at intervals of $5\,\mathrm{m\,s^{-1}}$. The zero wind contour has been darkened.

little variation about their mean values. The variation is very slightly more prominent in the range of QBO periods between 24 and 18 months, although even there the range of variability is no greater than half a month at maximum. Thus the influence of the SAO on the QBO - here induced by diffusion, which is the only term in the equation capable of propagating downward influence - is largely negligible at and below 26 km.

There is much more variability, however, in the QBO periods measured at 35 km (Figure 4.7(b)). At this height the QBO is embedded in a background wind that is directly accelerated by the SAO forcing, and as a result there is a definite modulation of the QBO periods by the SAO. The variability is lowest at fixed points corresponding to QBO periods that are multiples of the SAO forcing period, that is 18, 24, 30 and 36 months. In between these values the variability waxes and wanes, with maximal variability of just over two months occurring between the 18 and 24 month fixed points. However, we note that the frequency modulation of the QBO induced by the SAO winds does not change the average period of the QBO in any way; thus, this is an example of a pure frequency modulation, without any synchronization (Pikovsky et al. [2003]).

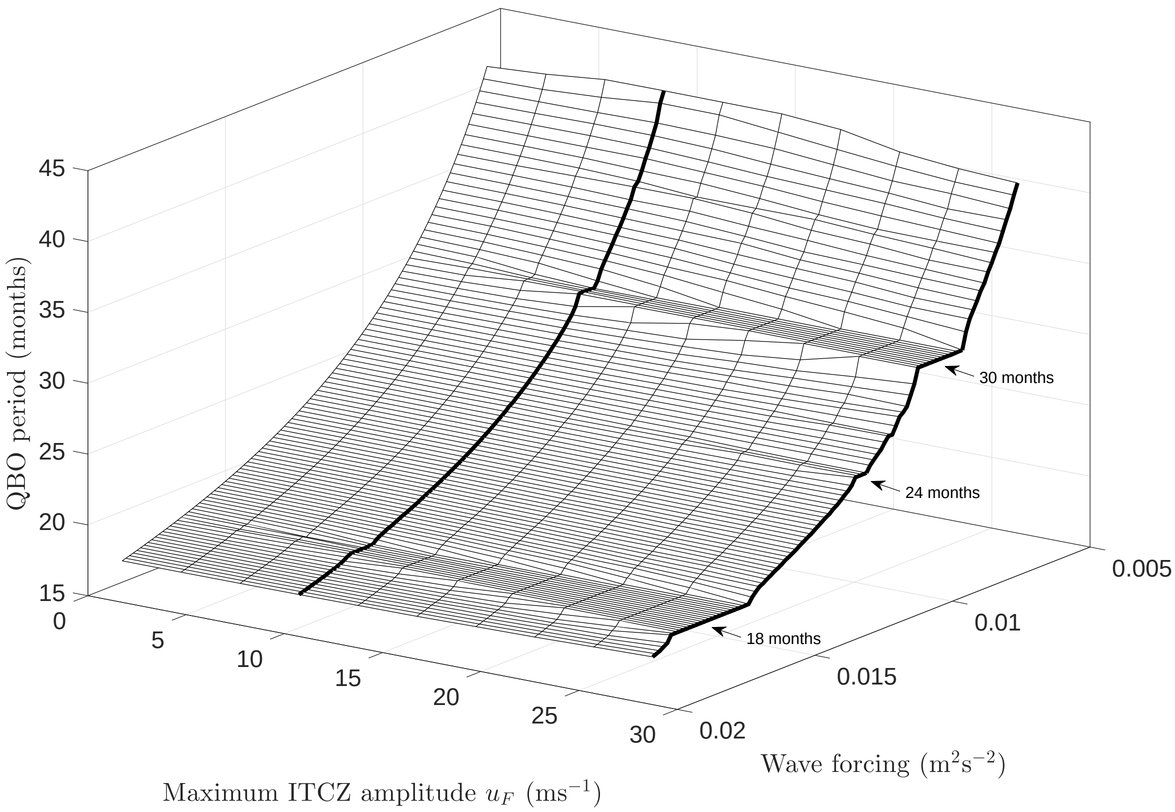

Figure 4.9: Average QBO period in the combined QBO-ITCZ system as wave forcing F and the maximum ITCZ amplitude u_F are varied. QBO cycle variation along the bold lines are considered in greater detail in Figure 4.10.

4.2.3 Bottom-up: Impact of ITCZ forcing

We now consider the case of ITCZ forcing, wherein a semi-annual forcing is imposed that is strongest at the lower boundary of the model and decreases in strength with altitude with a scale height of 1.3 km. A sample run of the combined QBO-ITCZ system is shown in Figure 4.8, with $u_F = 12\,\mathrm{m\,s^{-1}}$ and $F = 10.7 \times 10^{-3}\,\mathrm{m^2\,s^{-2}}$ respectively. The influence of the ITCZ forcing can be seen in the curved contour lines just above the lower boundary of the model.

As before, we consider ten different values of the ITCZ amplitude ranging between 0–27 $\mathrm{m\,s^{-1}}$, and 100 different values of the wave forcing for each value of u_F, giving a total of 1000 simulations. The mean QBO period at 26 km is measured for each simulation, and the resulting surface plot is depicted in Figure 4.9. In contrast to

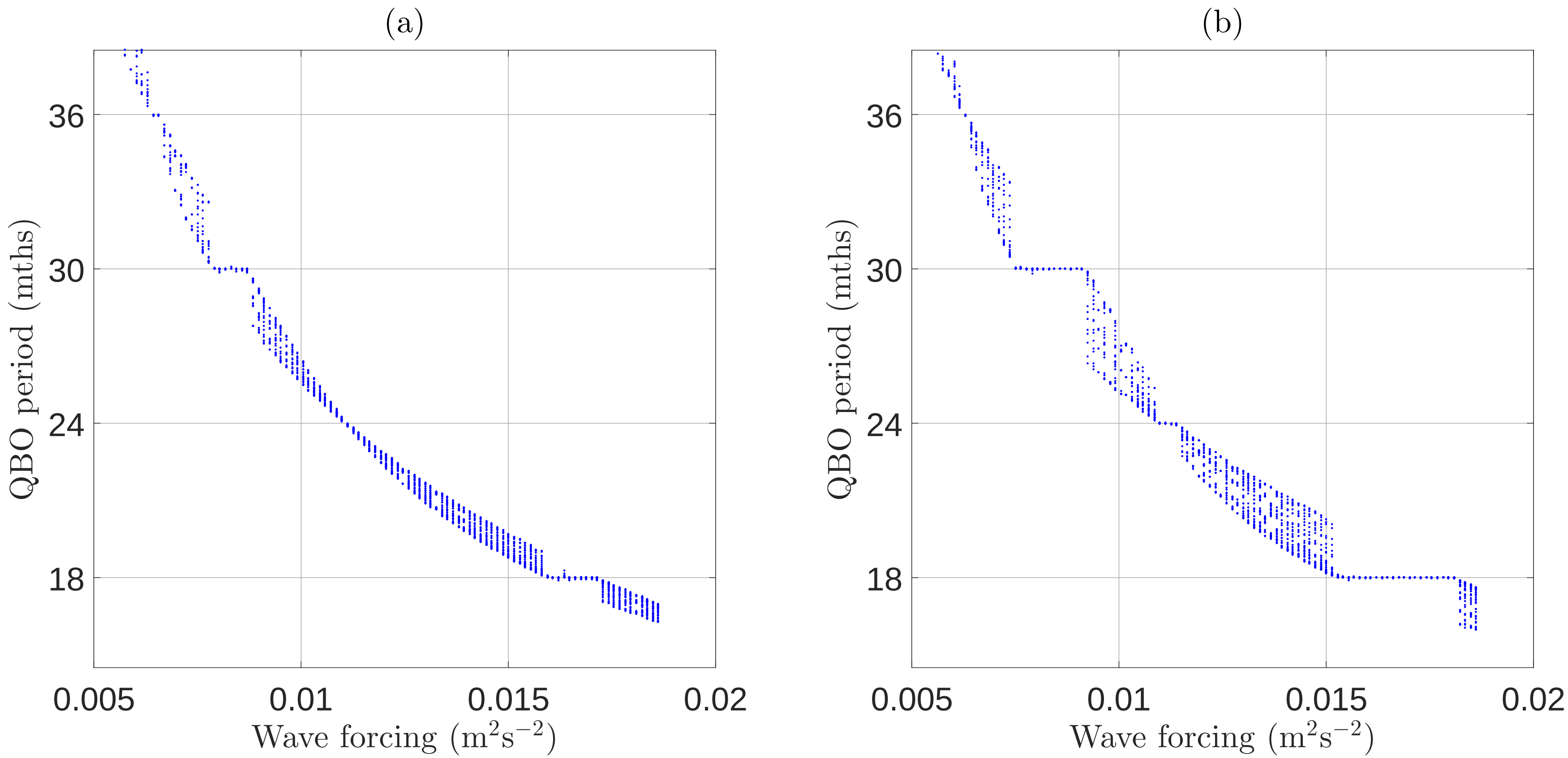

Figure 4.10: Individual QBO cycle lengths as wave forcing is increased in the combined QBO-ITCZ system. The values of the ITCZ amplitude are (a) $u_F = 9\,\mathrm{m\,s^{-1}}$ and (b) $u_F = 27\,\mathrm{m\,s^{-1}}$ respectively.

the SAO case (Figure 4.6), there are clear locking regions at 18 and 30 months, that increase in width as u_F increases. There is also a much narrower 24 month locking region present at large values of u_F. The locked QBO periods are clearly multiples of the semi-annual forcing period, with locking at odd multiples of the forcing period preferred over locking at even multiples.

Figures 4.10(a) and (b) plot individual QBO cycle lengths for the ITCZ amplitudes of $9\,\mathrm{m\,s^{-1}}$ and $27\,\mathrm{m\,s^{-1}}$ respectively (highlighted by the dark lines in Figure 4.9). The $9\,\mathrm{m\,s^{-1}}$ case is a more reasonable approximation of the magnitude of the observed 100hPa winds. From Figure 4.10(a) we see that the QBO period varies from cycle to cycle as a result of the semi-annual forcing, with a maximum variation of around 1.5 months. As in the case of the SAO results at 35 km (cf. Figure 4.7(b)), there are fixed points of the QBO period at 24 and 36 months. However, in contrast to the SAO results, there are also frequency locking regions present at 18 and 30 months. The range of variation between QBO cycles is largest just before entering these locking regions, and then reduces precipitously to zero upon entering the locking region. The behaviour of the cycle variation approaching locking regions is thus qualitatively different from the behaviour approaching an individual fixed point, where the range of variation reduces smoothly to zero.

The results described above carry over and are augmented in magnitude in the case when $u_F = 27\,\mathrm{m\,s^{-1}}$ (Figure 4.10(b)). The maximum range of period variation just prior to entering a locking region has now increased to over 3.5 months. A qualitative difference in this case is that the 24 month fixed point has expanded into a locking region. There is also evidence of multi-cycle and quasiperiodic QBO cycle behaviour, very similar to the behaviour described in Chapter 3 in the context of the relationship between the QBO and the annual cycle in tropical upwelling.

We tested the sensitivity of the above results to the rate at which the ITCZ forcing decays with height. The decay rate of the forcing is specified by a scale height

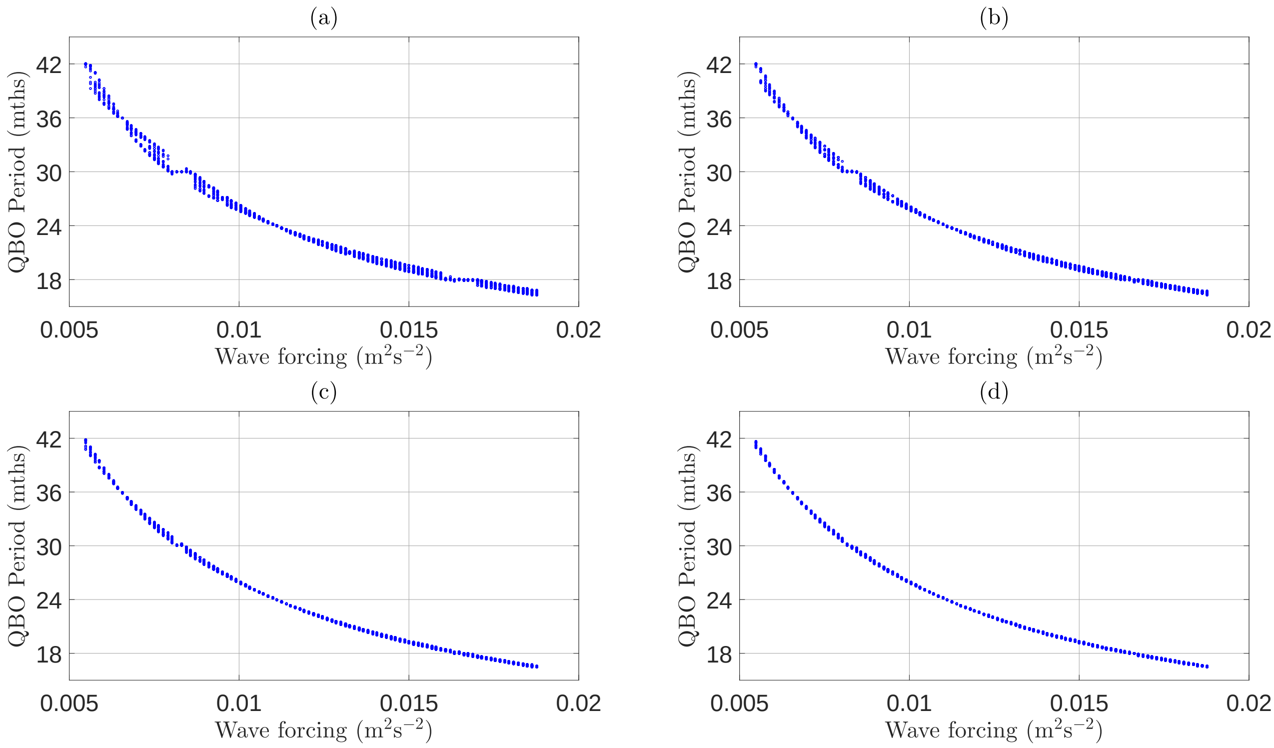

Figure 4.11: Variability of individual QBO cycle lengths as wave forcing increases for four different ITCZ scale heights with $u_F = 9\,\mathrm{m\,s^{-1}}$. The profile scale heights H_F are: (a) 1.3 km, (b) 650 m, (c) 330 m, and (d) 220 m respectively.

parameter H_F; thus far we have focused on the case of $H_F = 1.3\,\mathrm{km}$. Figure 4.11(a)–(d) shows the variation of the QBO period for four different values of the scale height: $H_F = 1.3\,\mathrm{km}$, 650 m, 330 m, and 220 m respectively. The ITCZ amplitude is fixed at $u_F = 9\,\mathrm{m\,s^{-1}}$ in all cases. As the scale height decreases we see that the impact of the ITCZ forcing on the QBO period reduces. The range of variability of the QBO cycles decreases and the variable periods converge toward the single, unforced periods. The locking regions at 18 and 24 months shrink and become fixed points, and the extent of the 30 month locking region is greatly reduced, although it does not entirely disappear even when $H_F = 220\,\mathrm{m}$.

4.3 Synchronization via semi-annual upwelling

We consider the possible role of semi-annual upwelling associated with the SAO and the ITCZ in the synchronization of the QBO. Upwelling was discussed in detail in Chapter 3 in the context of the annual cycle of the Brewer-Dobson circulation. In this section we revisit those results, but now considering a semi-annual upwelling period, as well as different upwelling profiles as would be appropriate to the SAO and ITCZ. The governing equation is

$$\frac{\partial \bar{u}}{\partial t} + w\frac{\partial \bar{u}}{\partial z} = -\frac{1}{\rho_0}\sum_i \frac{\partial \mathcal{F}_i}{\partial z} + \Lambda(z)\frac{\partial^2 \bar{u}}{\partial z^2}. \tag{4.3.1}$$

We have removed the direct forcing term and have reintroduced the upwelling term (second term from the left). The remaining acceleration, wave forcing and diffusion terms are unchanged. The vertical velocity in the upwelling term is modified to

$$w(z,t) = w_c\left[0.2 + 0.8\exp\left(\frac{z - z_t}{z_t - z_l}\right)\right] + w_s P(z)\cos\left(\frac{2\pi t}{180}\right). \tag{4.3.2}$$

Here we have maintained a constant upwelling value fixed at $w_c = 0.3\,\mathrm{mm\,s^{-1}}$, with the same vertical profile used in Chapter 3. For the semi-annual upwelling velocity we use a standard semi-annual harmonic coupled with the appropriate vertical profile $P(z)$ as defined for the SAO or the ITCZ in Section 4.2 (see also Figure 4.3(a)). The overall strength of the semi-annual upwelling is set by the parameter w_s.

4.3.1 SAO Upwelling

Figure 4.12 depicts the surface plot of the variation of the mean QBO period in the case when we use the SAO profile to represent semi-annual upwelling. The strength of this upwelling is varied between 0–0.36 $\mathrm{mm\,s^{-1}}$, and wave forcing is also varied in the usual way. Just as in the case of the direct SAO forcing, we see that the imposition

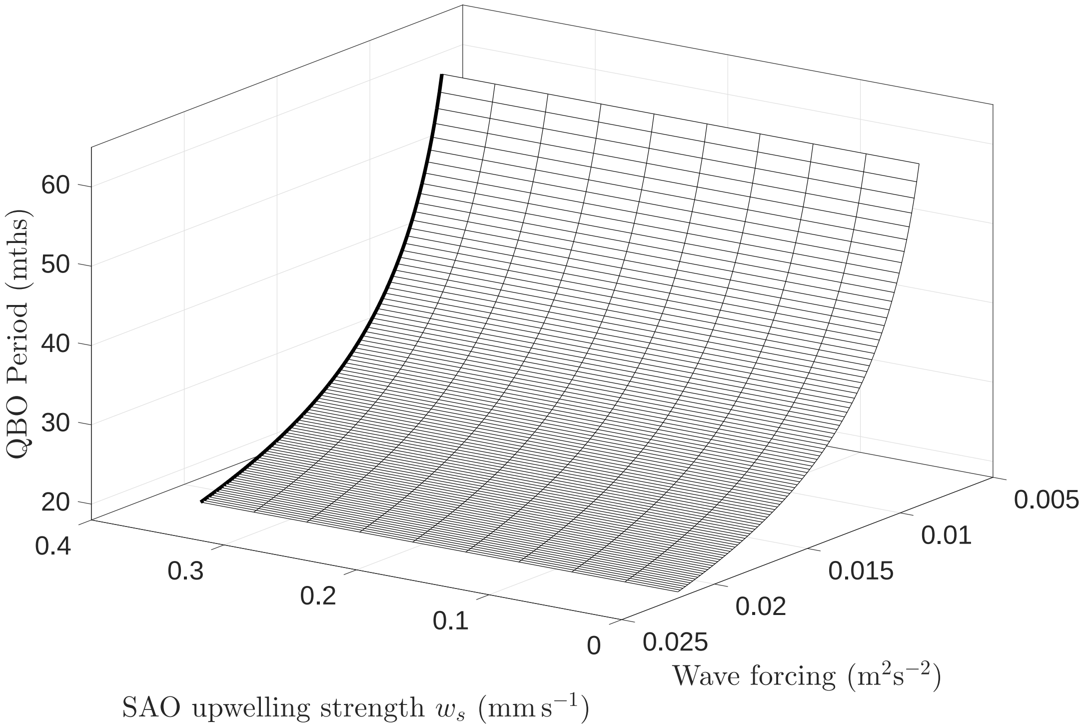

Figure 4.12: Surface plot of the variation of mean QBO period as a function of wave forcing and the strength of the semi-annual upwelling due to the SAO, w_s.

of upwelling in the upper levels of the model has no effect on the mean period of the QBO; the period for fixed wave forcing is clearly independent of w_s.

The cycle to cycle variability of the QBO is plotted in Figure 4.13 for the case when $w_s = 0.36\,\mathrm{mm\,s^{-1}}$. Here too, the QBO period shows almost no variation as a result of the semi-annual upwelling. This is in spite of the fact that the QBO periods for these plots have been measured at 35 km, where the influence of the SAO upwelling term is expected to be more significant. It is clear, then, that a semi-annual upwelling due to the SAO cannot induce synchronization of the QBO in the Holton-Lindzen model, at least for the parameter range tested here.

4.3.2 ITCZ upwelling

Figure 4.14 shows the corresponding surface plot for the case when the ITCZ profile is used to model the semi-annual upwelling. In contrast to the SAO profile results, here

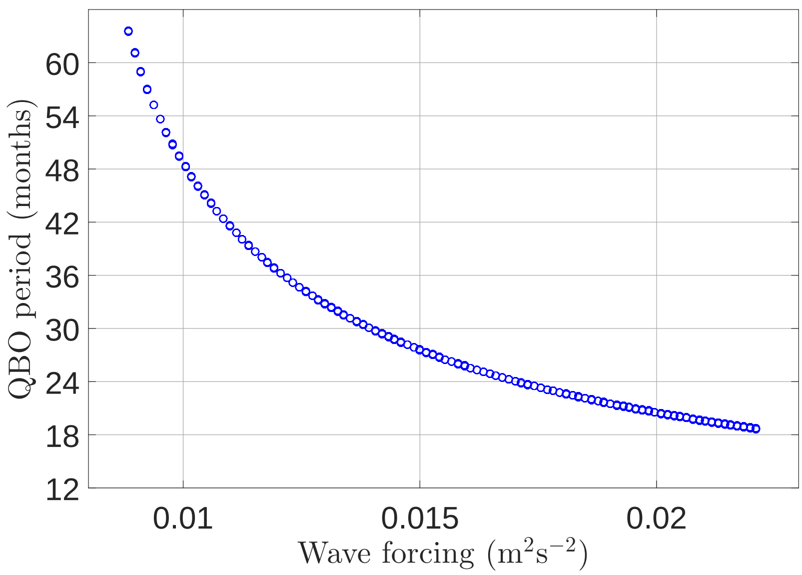

Figure 4.13: Cycle to cycle variation of the QBO period under the influence of a semi-annual upwelling due to the SAO. The value of w_s is set at $0.36\,\mathrm{mm\,s^{-1}}$, and QBO periods are measured at a height of 35 km.

there is evidence of significant synchronization as evidenced by substantial locking regions corresponding to QBO periods of 24, 36 and 48 months. There are also locking regions at 30 and 42 months, but these are much weaker. Thus it would seem that synchronization is preferred at even number multiples of the forcing period rather than odd number multiples. As usual, the width of the locking regions increases along with increased w_s.

Figure 4.15 shows the cycle to cycle variation of QBO periods in the case when $w_s = 0.21\,\mathrm{mm\,s^{-1}}$. The plot is strongly reminiscent of Figure 3.2 in Chapter 3, and Figure 4.10(b) from earlier in this chapter. Multiples of the forcing period create locking regions within which the QBO period is essentially fixed; outside of these regions the period is more variable and demonstrates multi-cycle and quasiperiodic behaviour (for example there are clear 5-cycles and 3-cycles that occur just after leaving the 48 month locking region on the high wave forcing side).

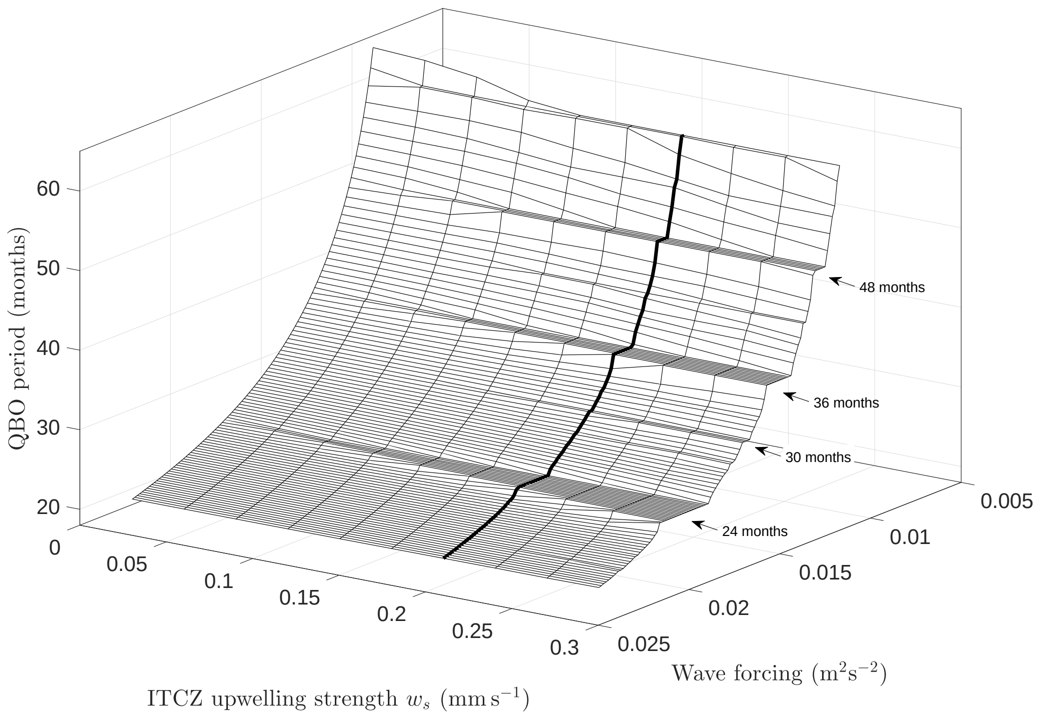

Figure 4.14: Surface plot of the variation of mean QBO period as a function of wave forcing and the strength of the semi-annual upwelling due to the ITCZ, w_s. Cycle to cycle period variation is considered along the dark line; see Figure 4.15.

4.4 Discussion

In this chapter we have considered the influence of semi-annual forcings on the period of the QBO. We considered two different types of forcing and two different forcing profiles. The forcing profiles were chosen to simulate the observed distribution of zonal winds due to the stratopause Semi-Annual Oscillation (SAO) and the Inter-Tropical Convergence Zone (ITCZ). The two types of forcing were: (a) direct acceleration of the zonal wind, and (b) acceleration via upwelling.

For both classes of forcing we found that the SAO was unable to influence the period of the QBO in any significant way. The SAO only influenced the model via direct forcing at high altitudes; however, this forcing had no bearing on the evolution of the zonal wind at lower levels, in line with Plumb's principle of no downward influence. It would seem, then, that the influence of the SAO on the QBO is one

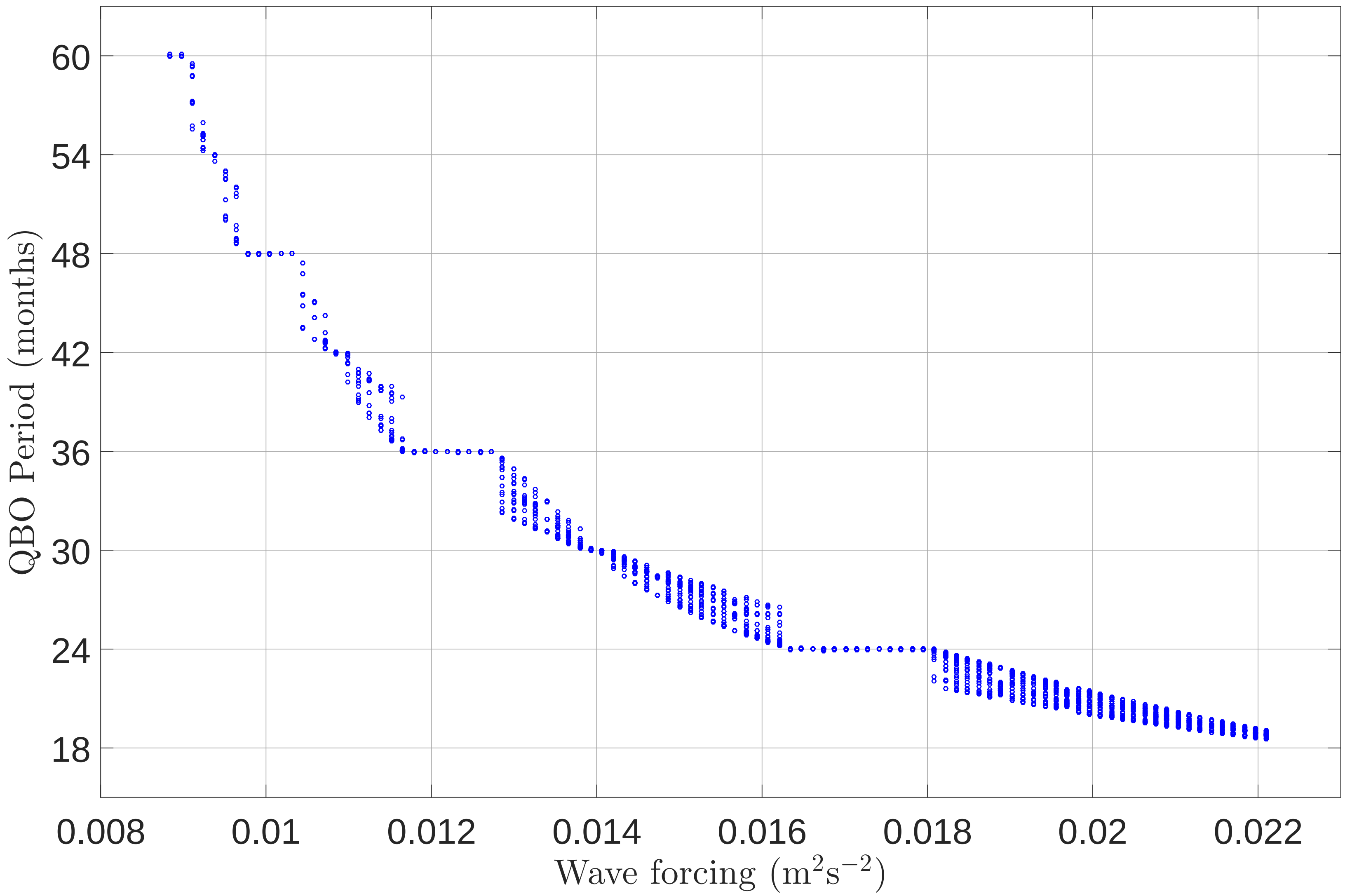

Figure 4.15: Cycle to cycle variation of the QBO period under the influence of a semi-annual upwelling due to the ITCZ. The value of w_s is set at $0.21\,\mathrm{mm\,s^{-1}}$, and QBO periods are measured at a height of 26 km.

of a pure frequency modulation, without synchronization. In contrast, the ITCZ forcing - which is strongest at the tropopause / lower stratosphere - is able to exert a robust synchronizing influence on the QBO. These findings suggest that in general, periodic upwelling and zonal wind forcings can indeed synchronize the QBO in the Holton-Lindzen model, *but only if the forcing is applied near the bottom of the model.*

The mechanism of ITCZ synchronization suggested here is novel and has not been considered before in the literature. The imposition of semi-annual upwelling allows for robust synchronization of the QBO at 30 months, which was not found in the annual upwelling case studied in Chapter 3. We note the possibility that the mechanism of influence of the ITCZ wind is not via direct forcing, as was considered here, but rather through the periodic filtering of vertically propagating equatorial waves. This mechanism will be considered in the next chapter, when we investigate the effects of periodicity in the waves driving the QBO.

We note the similarities in the cycle-to-cycle variations of the QBO period whenever synchronization is found to be present; for example, comparing Figure 4.15 with Figure 3.3 from the previous chapter (pg. 63). The dynamic of the QBO variation seems to be quite universal in this regard. It is also puzzling that different synchronization mechanisms engender different preferences for locking region width. Whilst the upwelling mechanisms (annual or semi-annual) seem to favour even multiple synchronization regions over odd multiples, the exact opposite is true for the direct forcing mechanism! The reasons for this disparity are not presently clear.

Lastly, we should note that the absence of QBO-SAO synchronization found in the Holton-Lindzen model does not preclude the possibility of synchronization between these wind systems in the real atmosphere. Much of the discussion of the influence of the SAO on the QBO has focussed on the 'no-downward-influence' principle elucidated by Plumb [1977]. In that work he showed that wave dissipation at a given height in the stratosphere depends only on the value of the zonal winds at and below the height in question; crucially, the wave dissipation does not depend on derivatives of $\bar{u}$. As a result, it is not possible for SAO winds in the upper stratosphere to directly influence wave dissipation at lower levels. While this reasoning is not disputed, one could argue that the evolution of the zonal wind *is itself* dependent on vertical derivatives of $\bar{u}$ via the vertical advection term. So long as the stratospheric wave-mean flow structure is such that new shear zones form most easily in the upper stratosphere, it is in principle possible that the SAO will affect the initial descent of the QBO shear zones by modulating the strength of vertical advection term -$\overline{w}^*\frac{\partial\bar{u}}{\partial z}$, either via the semiannual signal in the upwelling $\overline{w}^*$ or via the semiannual cycle in the vertical shear $\frac{\partial\bar{u}}{\partial z}$. This height dependence of wave dissipation may be more pronounced in a QBO model that uses a continuous spectrum of waves; it does not seem to be significant for the discrete wave spectrum used in the Holton-Lindzen model.

Our main objective here has been to demonstrate conclusively that QBO-SAO synchronization is not possible in the Holton-Lindzen model, and to further highlight that bottom-up mechanisms such as the ITCZ influence are plausible candidates for synchronizing the QBO. Since both the ITCZ migration and the SAO are intimately connected to the march of the annual cycle, it is possible that the observed synchronization of the QBO and SAO could be attributable, at least in part, to a less obvious bottom-up mechanism such as the one considered here.

Chapter 5

Synchronization III: Periodic Wave Forcing and Wave Filtering

5.1 Introduction

Past studies have found evidence of both seasonal and inter-annual variability in the observed energy fluxes of gravity waves (GWs) in the tropical troposphere and stratosphere. These waves provide a significant proportion of the wave momentum flux that drives the QBO (Dunkerton [1997], Baldwin et al. [2001], Ern et al. [2014]). Allen and Vincent [1995] studied high resolution radiosonde measurements over Australia and found a clear seasonal variation in gravity wave activity in the tropical north of the continent, with maximal activity occurring in the monsoon season. Wang and Geller [2003] and later Zhang et al. [2010, 2013] studied radiosonde data from 92 stations located across the contiguous United States as well as Alaska, Hawaii, and the Caribbean and western tropical Pacific islands. They found clear annual cycles in gravity wave kinetic and potential energy fluxes in the low latitudes in both the troposphere and lower stratosphere. Zhang et al. [2013] further found a semiannual oscillation of GW energy density in the Tropical Tropopause Layer (TTL) between

10–16 km. A strong (negative) correlation between GW energy densities and Outgoing Longwave Radiation (OLR) measurements was also found, suggesting a link between the depth of convection and gravity wave activity.

The connection between convective activity and GW fluxes suggests possible interactions between the QBO and the El Niño Southern Oscillation (ENSO). Taguchi [2010] studied the relationship between the QBO and the Oceanic Niño Index (ONI) and found that the period of the QBO was 24.7 months on average during El Niño (EN) phases and 31.9 months during La Niña (LN) phases. Christiansen et al. [2016] found significant phase alignment of the QBO and ENSO after strong EN episodes, most notably in the 1997–1998 EN event. The QBO-ENSO relationship was studied by Schirber [2015] using a comprehensive GCM; he found that the descent rate of the westerly QBO jet was faster during EN than in LN, but that the descent rate of the easterly jet was similar in both EN and LN conditions. Geller et al. [2016] hypothesized that the increase in the area of deep convection during EN years results in greater GW activity and hence greater wave driving of the QBO, but that during LN years the depth of convection is greater, leading to a broader spectrum of waves and hence an increase in the QBO amplitude.

Along with periodic variation in convective activity discussed above, periodic variations in GW fluxes could also be due to periodic variations in the background wind field (Vincent and Alexander [2000]). Since wave dissipation is greater when the Doppler shifted wind speed is small, periodic variations in winds at the tropopause would modulate the strength of wave fluxes propagating through to the stratosphere. Such considerations are relevant, for example, when setting the launch heights of parameterized GWs in GCMs (Manzini and McFarlane [1998], Ern et al. [2006]).

The effect of a time-varying wave forcing on the QBO was studied by Geller et al. [1997] using a one-dimensional model of the QBO. The authors were primarily interested in the possible modulation of the QBO by ENSO events, and as such focused on relatively long-period time variations. For a simple sinusoidal time variation they found evidence of phase locking of the QBO, with the strongest locking occurring when the QBO period under mean forcing conditions was close to the period of the time-varying wave forcing. When more complicated time variations were considered, the relationship between the time-varying QBO period and the time varying wave forcing was not obvious as a result of the nonlinear relationship between the variables.

In this chapter we revisit and extend the results of Geller et al. [1997] to focus on seasonal variations of wave forcing strength. We investigate a broad region of the wave forcing parameter space, and show how imposed sinusoidal variations in the wave momentum flux affect the period of the QBO. We also consider the effects of the filtering of waves by the background winds in the upper tropical troposphere, by imposing a background wind profile in the upper troposphere. Experiment descriptions and results are presented in Sections 5.2 and 5.3 for the wave forcing and wave filtering studies respectively. In both sets of experiments we find that synchronization of the QBO is possible, and furthermore that the behaviour of the QBO period outside of the synchronization regions is very similar to results found in preceding chapters. We summarise and discuss our findings in Section 5.4.

5.2 Periodic wave forcing

As before we consider the Holton-Lindzen model of the QBO, where the acceleration of zonal wind in the stratosphere is driven by the dissipation of two identical gravity waves travelling in opposite directions. The equation in full is:

$$
\begin{aligned}
\frac{\partial \bar{u}(z,t)}{\partial t} &= F_W(t) e^{z/H_\rho} \frac{N\mu(z)}{k(\bar{u}(z,t)-c)^2} \exp\left\{ -\int_{z_0}^{z} \frac{N\mu(z')}{k(\bar{u}(z',t)-c)^2} dz' \right\} \\
&+ F_E(t) e^{z/H_\rho} \frac{N\mu(z)}{k(\bar{u}(z,t)+c)^2} \exp\left\{ -\int_{z_0}^{z} \frac{N\mu(z')}{k(\bar{u}(z',t)+c)^2} dz' \right\} \\
&+ \Lambda(z) \frac{\partial^2 \bar{u}(z,t)}{\partial z^2}.
\end{aligned} \tag{5.2.1}
$$

Here the parameter values for N, μ, H_ρ, k, c and $\Lambda(z)$ are set as in previous chapters. We introduce time-varying wave forcing by separating the wave forcing amplitudes for the westerly and easterly propagating waves - $F_W(t)$ and $F_E(t)$ respectively - into mean and sinusoidally varying components:

$$
F_W(t) = F_0 + F_1 \sin\left(\frac{2\pi t}{\tau}\right) \tag{5.2.2}
$$

$$
F_E(t) = -F_0 + F_1 \sin\left(\frac{2\pi t}{\tau}\right). \tag{5.2.3}
$$

Here the absolute magnitude of the mean forcing, F_0, is the same for both waves, and the waves have been set to vary in phase with each other. The period of the forcing variations τ is set as either 180, 360, or 1,440 days, representing semi-annual, annual, and inter-annual variations respectively.

5.2.1 Semi-annual forcing

We investigate the response of the QBO to systematic changes in the values of F_0 and F_1 when $\tau = 180$ days, reflecting the semi-annual variation in wave-forcing strength described by Zhang et al. [2013]. We pick 100 different values of F_0, and for each F_0 value we let F_1 vary uniformly over 10 values between 0% and 90% of F_0 - giving a total of 1000 different simulations. The Holton-Lindzen model (5.2.1) is solved for each set of parameters for 22,000 days. Each simulation converges onto a limit cycle representing the QBO oscillation, the period of which is then characterised by

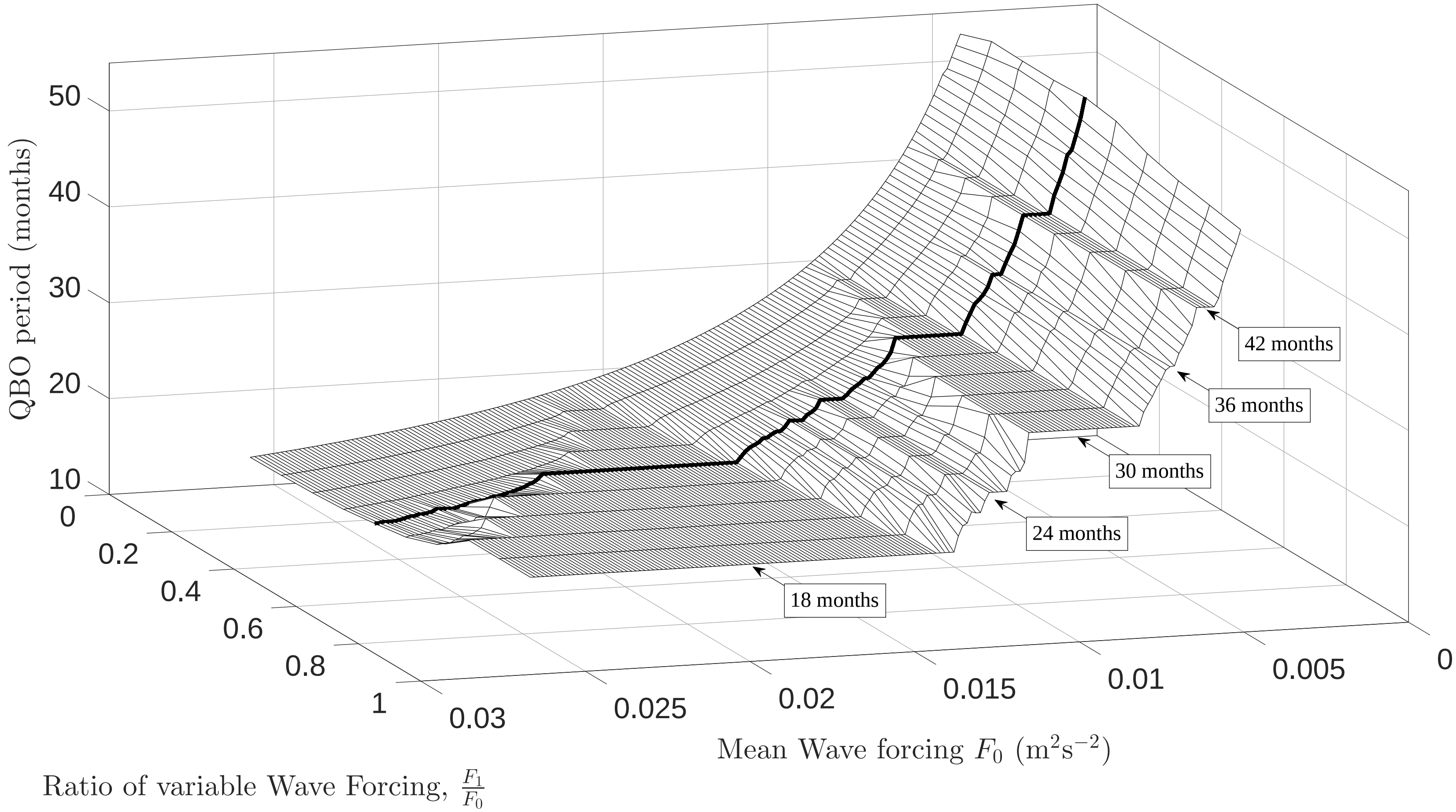

Figure 5.1: Variation of mean QBO period with changes to mean wave forcing F_0, as well as to changes in the ratio of the time-varying forcing to mean forcing, F_1/F_0, when the period of the time-varying component of wave forcing is set at $\tau = 180$ days. Prominent synchronization regions have been labelled. The dark line is explored from a cycle to cycle perspective in Figure 5.2.

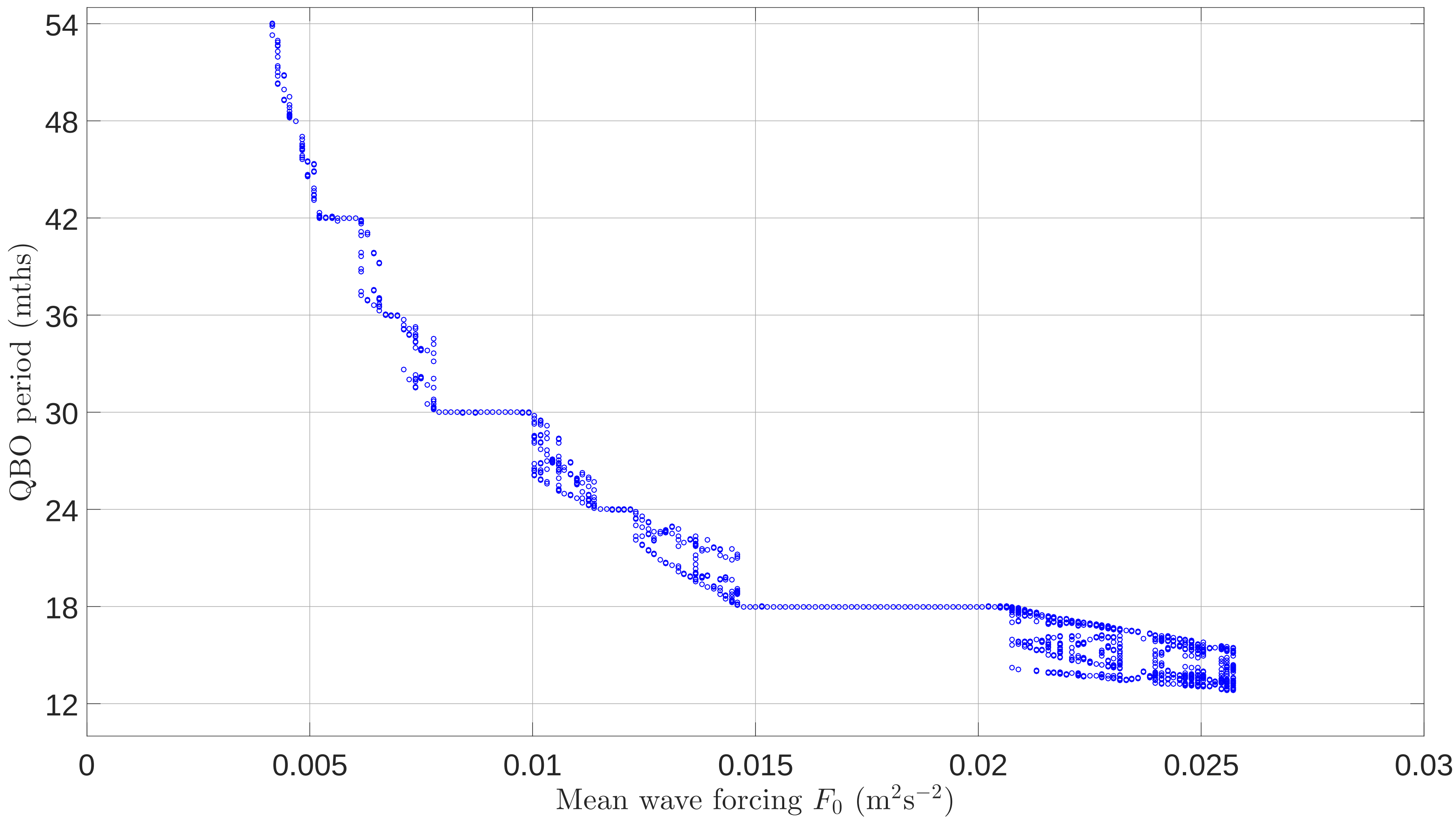

Figure 5.2: Cycle by cycle variation of the QBO period for the set of simulations with ${}^{F_1}/{}_{F_0} = 0.4$ and $\tau = 180$ days. Individual QBO periods are plotted against the corresponding mean wave forcing value F_0.

measuring the times between the onset of westerly zonal winds at $z = 24\,\text{km}$.

Figure 5.1 presents the mean period of the QBO as F_0 and F_1 are varied. As usual, the QBO period surfaces slopes downward as F_0 increases. As the ratio of the time-varying forcing increases - as measured by the ratio ${}^{F_1}/_{F_0}$ - the surface develops plateaus which are the same regions of synchronization described in Chapters 3 and 4. The synchronization regions are especially prominent at 18, 30 and 42 months - odd multiples of the 6 month period of the time-varying forcing. There are also synchronization regions at even-integer multiples of the forcing period, as well as at other rational multiples. These are comparatively narrow, however. As the ratio ${}^{F_1}/_{F_0}$ increases the synchronization regions become increasingly wide, such that almost all simulations are locked by the forcing cycle when ${}^{F_1}/_{F_0} = 0.9$ (the largest ratio considered).

To investigate the cycle by cycle variation of the QBO period within each simulation run, we took the set of runs where ${}^{F_1}/_{F_0} = 0.4$ - represented by the dark line in Figure 5.1 - and plotted each individual QBO period against the mean wave forcing F_0 in Figure 5.2. Thus each point in Figure 5.2 represents the length of a particular QBO cycle that occurred over the course of the simulation run with the corresponding F_0 value. As in previous chapters, we see there is significant cycle to cycle variability of the QBO period. The QBO cycles through sets of periods which can be either discrete or continuous. As in previous chapters we see evidence of bifurcations and fine structure in the set of QBO periods as F_0 varies.

5.2.2 Annual forcing

Figures 5.3 and 5.4 present results of a set of experiments identical to those described in the previous section, but now with the period of the time-varying forcing fixed as $\tau = 360$ days to simulate the effect of a simple annual cycle. As before, the mean QBO period surface in Figure 5.3 has plateaus corresponding to synchronized QBO

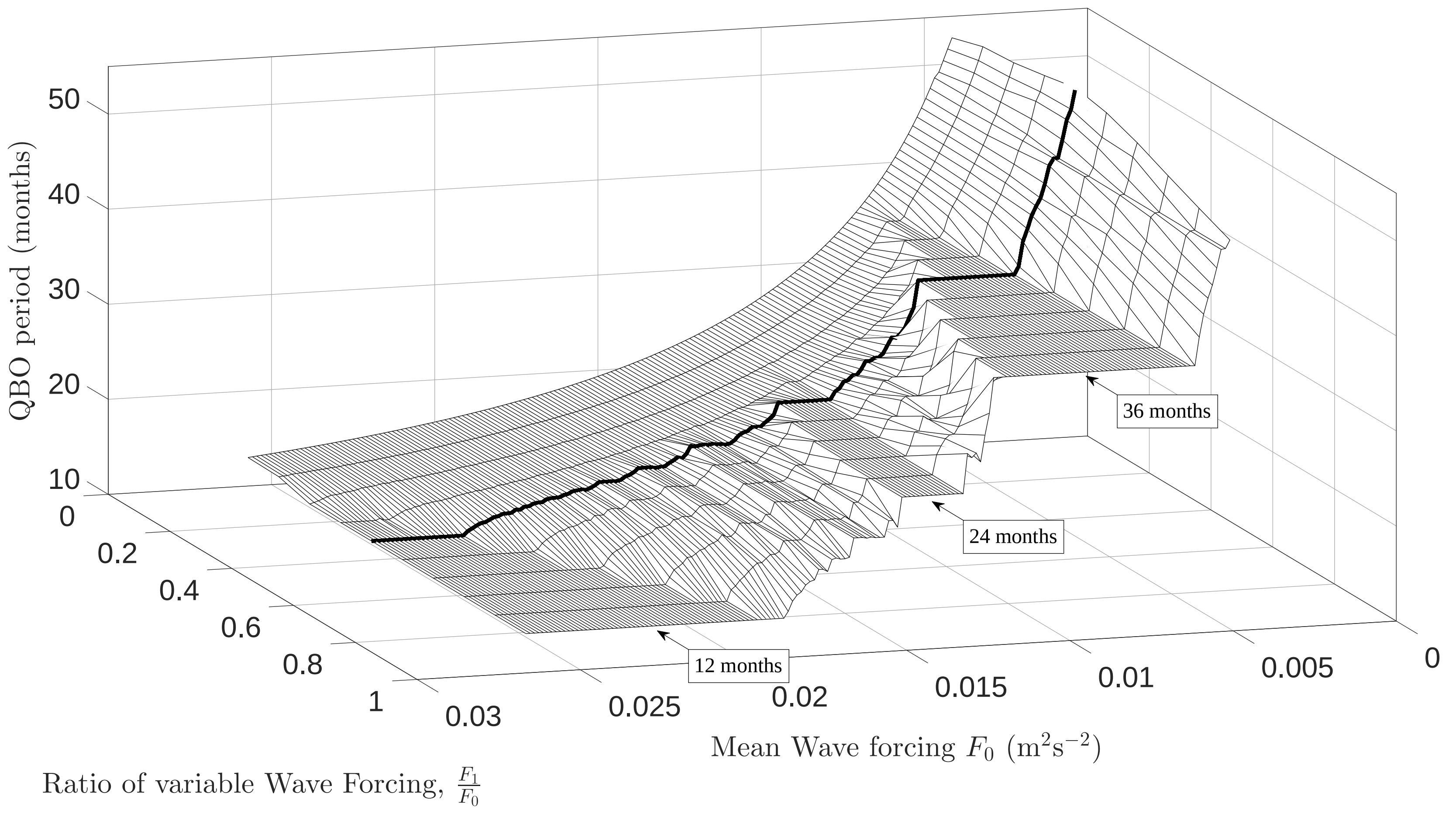

Figure 5.3: As in Figure 5.1, but for the period of time-varying forcing set to $\tau = 360$ days. The dark line is explored from a cycle to cycle perspective in Figure 5.4.

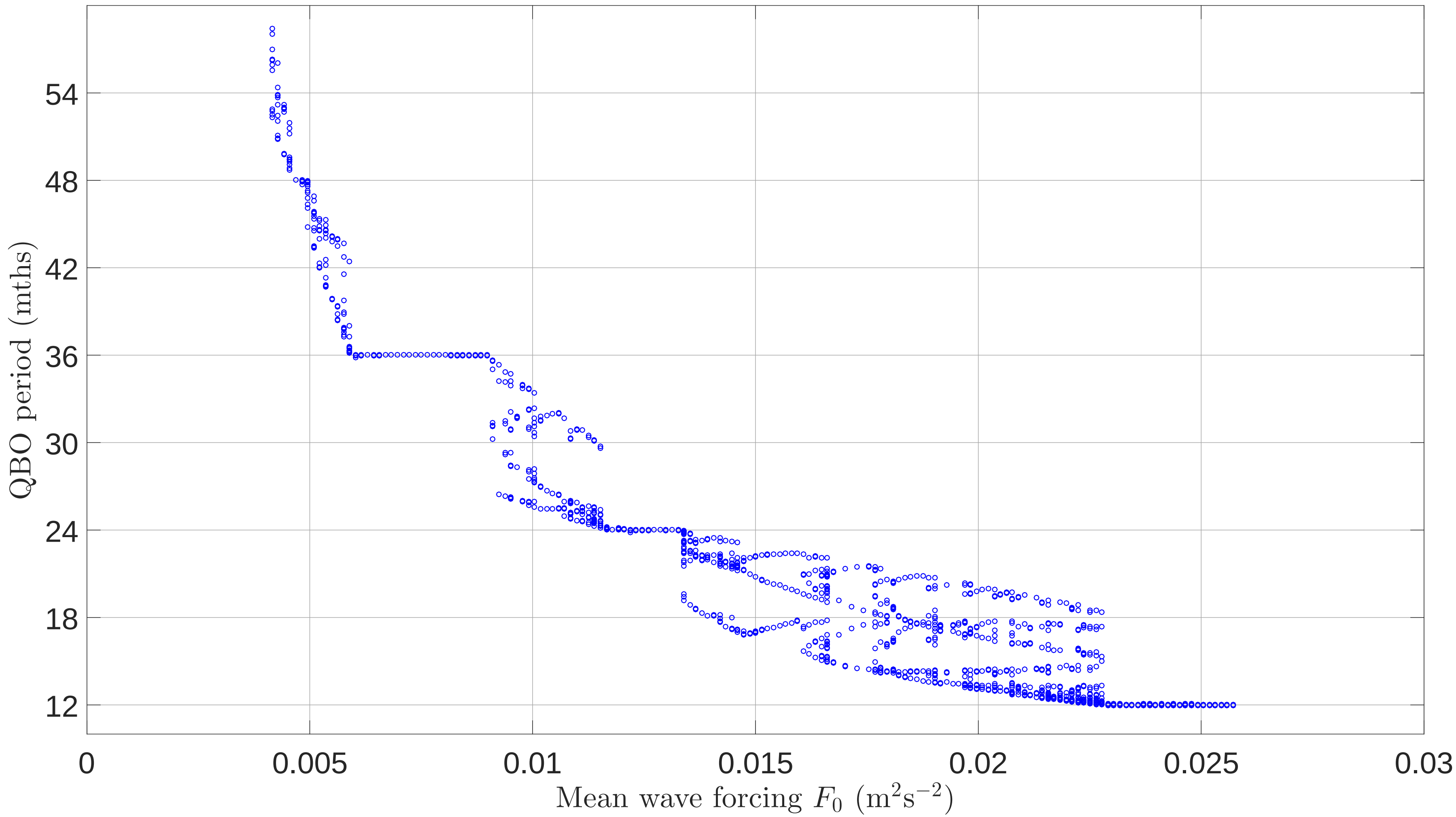

Figure 5.4: Cycle by cycle variation of the QBO period for the set of simulations with $F_1/F_0 = 0.4$ and $\tau = 360$ days. Individual QBO periods are plotted against the corresponding mean wave forcing value F_0.

states. The most prominent regions occur at integer multiples of the forcing period, with odd multiple synchronization regions wider than even multiple synchronization regions.

Figure 5.4 displays the length of individual QBO cycles for different values of F_0 and with $F_1/F_0 = 0.4$. The most striking feature of the plot is the complex set of QBO periods that occur for mean QBO periods between 24 and 12 months. There is clear evidence of systematic bifurcations of the QBO period set as F_0 increases. We also note that the range of variation in the QBO periods can be quite large. For example, in the case when $F_0 = 11.4 \times 10^{-3}\,\mathrm{m}^2\,\mathrm{s}^{-2}$ (just before the 24 month locking region), the QBO period varies between 24.3 and 30.2 months, with a mean period of 25.1 months. We note the relatively large 6 month range of variability in the QBO period.

5.2.3 Inter-annual forcing

As a final case we study the QBO period evolution when $\tau = 1,440$ days, or 4 years. This period was chosen to simulate the effects of low-frequency variability on the QBO period, and is a rough measure of the possible effects of ENSO on the QBO. We note that this is the first occasion in the thesis where we consider an external forcing with a period that is greater than the range of the intrinsic QBO period.

Figures 5.5 and 5.6 display the results of QBO period variation with changes in the strengths of mean and time-varying wave forcing, in analogy to the results in the previous two subsections. In Figure 5.5 the plot of the mean QBO period surface reveals the strong influence of the long period variation. The QBO is locked into a 48 month period over a wide range of F_0 values, creating a very large synchronization plateau. As F_1/F_0 increases, values of F_0 with mean QBO period above and below the locking frequency are equally absorbed into this locking region. Indeed, for larger values of F_1/F_0, the synchronization region spans the entire range of F_0 values considered.

Cycle to cycle QBO period variability is presented in Figure 5.6 for the ratio

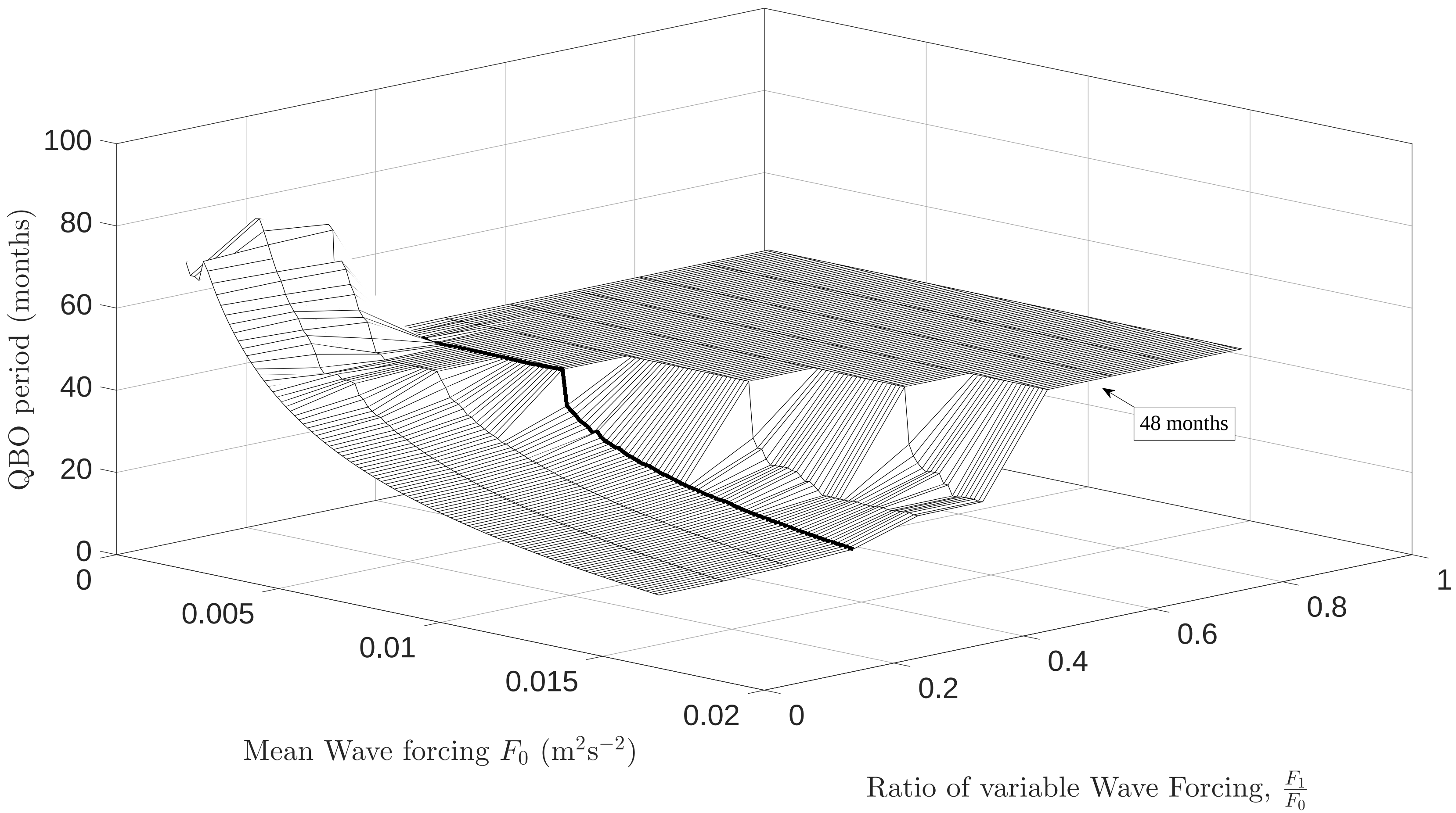

Figure 5.5: As in Figure 5.1, but for the period of time-varying forcing set to $\tau = 1,440$ days. The dark line is explored from a cycle to cycle perspective in Figure 5.6.

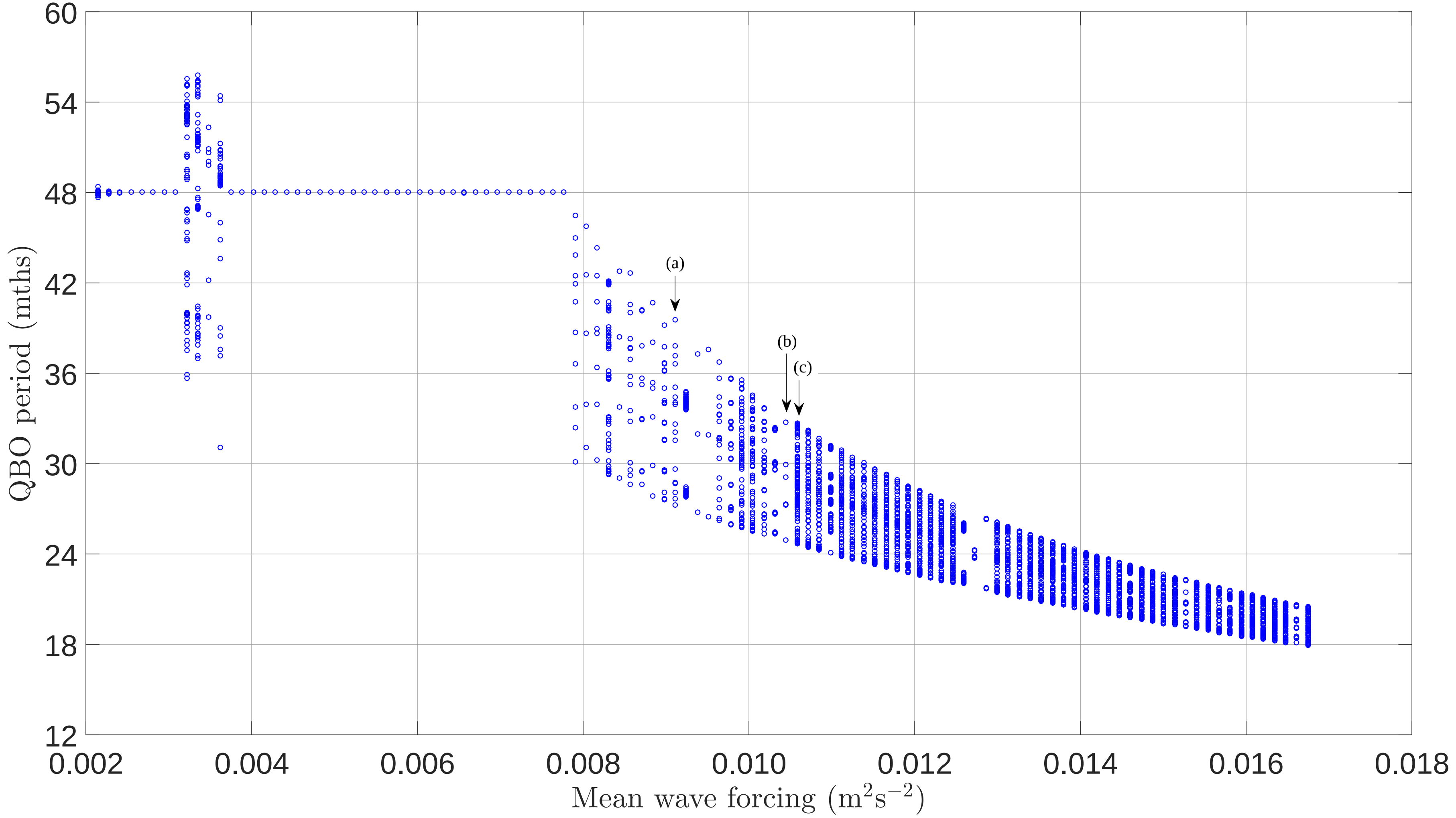

Figure 5.6: Cycle by cycle variation of the QBO period for the set of simulations with $^{F_1}/_{F_0} = 0.3$ and $\tau = 1,440$ days. Individual QBO periods are plotted against the corresponding mean wave forcing value F_0.

${}^{F_1}/_{F_0} = 0.3$. For low values of F_0 the QBO period is dominated by the 48 month locking region. The locking region is disjoint: there is an interval of F_0 values, between $F_0 = 3.2 - 3.6 \times 10^{-3}\,\mathrm{m^2\,s^{-2}}$,within which the QBO period is variable and not locked to 48 months, even though the QBO period is locked to 48 months for F_0 values on either side of this interval. We ran the simulations for a further 100,000 days to ensure that the QBO variation was not a finite time effect due to slow convergence onto a limit cycle, but the QBO periods in this interval did not converge even in the extended runs. This suggests that the relationship between the QBO period and the mean wave forcing is not necessarily monotonic when wave forcing is periodic; in this case the QBO enters, exits and re-enters the 48 month locking region as the mean wave forcing changes.

The QBO eventually breaks out of the 48 month locking region for larger values of F_0. In this non-locked region the QBO period is variable and both discrete and continuous QBO sets can be discerned. The 4-year time variation allows for very large variability in the QBO period. For example, just as the QBO leaves the 48 month locking region it cycles through a discrete set of periods that vary between 30 and 46 months - giving a range of 16 months.

We further exemplify the QBO variation with three sample simulations, with mean wave forcing values set at $F_0 = 9.1 \times 10^{-3}\,\mathrm{m^2\,s^{-2}}$, $10.4 \times 10^{-3}\,\mathrm{m^2\,s^{-2}}$ and $10.6 \times 10^{-3}\,\mathrm{m^2\,s^{-2}}$ respectively. These have been labelled (a)–(c) in Figure 5.6. The evolution of the QBO period for these three cases is presented in Figures 5.7(a1–c1), together with histograms of the onset month of westerly QBO winds at 24 km (Figures 5.7(a2–c2)).

In example (a), the QBO cycles through a discrete set of periods that range between 27 and 40 months (Figure 5.7(a1)). The discrete set is made up of 19 unique QBO periods, with an average length of 32.8 months. The time taken to run through the complete set of 19 periods is exactly 624 months, or 52 years. We note that

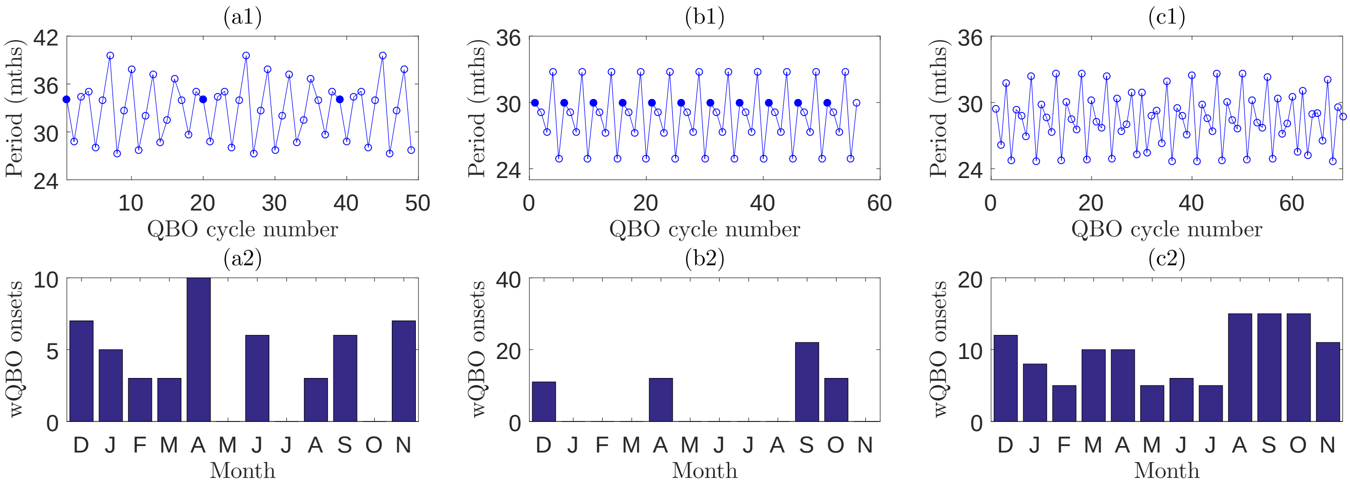

Figure 5.7: Cycle to cycle variability and QBO onset months for three sample QBO runs with mean wave forcing corresponding to: (a1–a2) $F_0 = 9.1 \times 10^{-3}\,\mathrm{m^2\,s^{-2}}$, (b1–b2) $F_0 = 10.4 \times 10^{-3}\,\mathrm{m^2\,s^{-2}}$ and (c1–c2) $F_0 = 10.6 \times 10^{-3}\,\mathrm{m^2\,s^{-2}}$ respectively. The filled dots in (a1) and (b1) mark the starting points of new discrete QBO cycle sets.

$52 = 13 \times 4$ is a multiple of the 4 year forcing period. The long duration of the multi-cycle QBO in this instance - close to the length of the entire observed QBO record - highlights the long-term impact of low-frequency variability as it interacts with the natural frequency of the QBO. Seasonal variations due to the inter-annual variation are not so clear (Fig. 5.7(a2)), although there seems to be a weak tendency to prefer QBO onsets in the first half of the year.

Examples (b) and (c) represent the evolution of QBO periods close to the observed mean QBO period of 28 months. The two simulations have very similar mean wave forcings of $10.4\times10^{-3}\,\mathrm{m^2\,s^{-2}}$ and $10.6\times10^{-3}\,\mathrm{m^2\,s^{-2}}$ respectively. Figure 5.7(b1) shows that the QBO in (b) cycles through a set of five periods of length 30, 29, 27, 33, and 25 months respectively. The range of periods fits well with the range of periods of the observed QBO (compare with Figure 7.13), and the mean period is 28.8 months. The QBO onset months display a seasonal regularity as well (Fig. 5.7(b2)). This proves to be sensitive to small changes in F_0, however, as Figure 5.7(c2) demonstrates for QBO example (c). Although the variation in F_0 is small between Fig.5.7(b2) and Fig.5.7(c2), in the latter case the seasonality has largely disappeared. The small

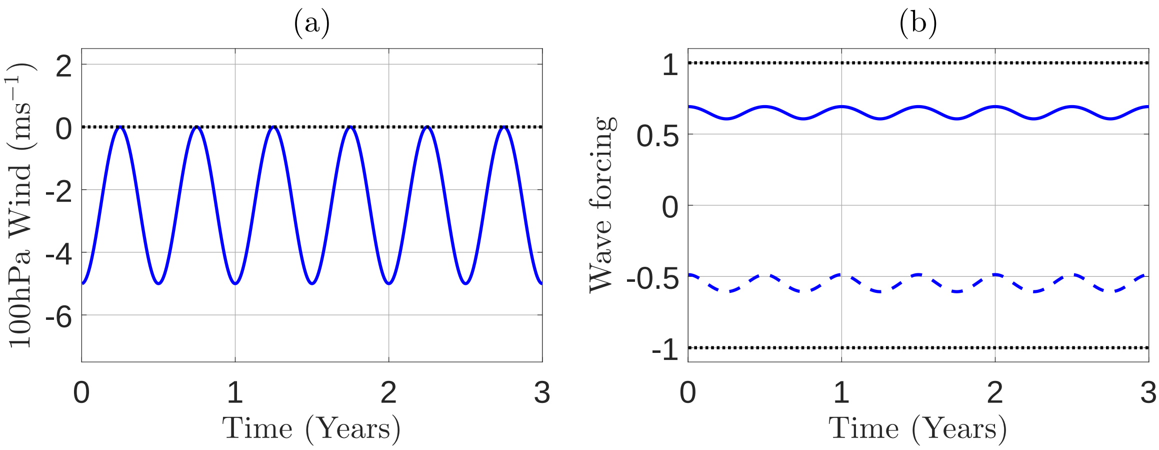

Figure 5.8: (a) Sample time series of prescribed winds just below the tropopause, given by $\bar{u}_{TTL} = \bar{u}_0 \cos^2\left({}^{2\pi t}/_{360}\right)$. Here we have set $\bar{u}_0 = -5\,\mathrm{m\,s^{-1}}$; the zero wind line is marked as the dotted line. (b) Wave momentum flux at the tropopause as a result of filtering by the wind layer described in (a), assuming a layer thickness of 3 km. The solid and dashed lines represent the normalised wave momentum fluxes of westerly and easterly waves after passing through the wind layer. The dotted lines represent the unfiltered wave momentum fluxes that would pertain if the filtering wind layer was absent.

change in F_0 has changed the relationship between the intrinsic QBO period and the forcing period, such that the QBO can no longer complete multiple of 4 years every 5 cycles, even though it comes quite close (Figure 5.7(c1)). As a result, the QBO period keeps adjusting slightly in response to the forcing, resulting in a continuous set of QBO periods that are reminiscent of the 5-cycle observed in example (b), but are unable to close the loop to create a discrete cycle.

5.3 Periodic wave filtering

We consider the effect of the periodic filtering of the waves that drive the QBO. To do this we prescribe a layer of time-varying wind, $\bar{u}_{TTL}(t)$, in the upper troposphere - just below the lower boundary of the model. The depth of the prescribed wind layer is set as $h = 3\,\mathrm{km}$; for simplicity, we assume that the wind strength at a given time is uniform throughout the layer. Further, we assume that the wind strength is not significantly modified by wave dissipation.

As a vertically propagating wave passes through the prescribed wind layer, it loses momentum due to dissipation. The wave momentum flux, $F(t)$, of the wave after passing through the prescribed wind layer is thus given by

$$F(t) = F_0 \exp\left\{-h\frac{N\mu(z_0)}{k\left(\bar{u}_{TTL}(t) - c\right)^2}\right\}. \tag{5.3.1}$$

Here we have evaluated the wave momentum flux integral (2.4.37) based on dissipation due to a uniform layer of wind $\bar{u}_{TTL}$ of depth h. F_0 is the momentum flux of the wave prior to passing through the wind layer and N, μ, k and c take the usual requisite values for westerly and easterly travelling waves. Due to the time-varying nature of the prescribed wind, the momentum flux is now also time-dependent.

We model the wind layer as having a semi-annual variation with an easterly bias, due to the migration of the ITCZ (refer to Figure 4.2). Hence we define

$$\bar{u}_{TTL} = \bar{u}_0 \cos^2\left(\frac{2\pi t}{360}\right). \tag{5.3.2}$$

A sample time series of $\bar{u}_{TTL}$ is plotted in Figure 5.8(a), for $\bar{u}_0 = -5\,\mathrm{m\,s^{-1}}$. We assume that the prescribed wind is forced externally and we ignore the acceleration of $\bar{u}_{TTL}$ due to the momentum deposition of the dissipating waves.

Figure 5.8(b) plots the normalized wave momentum fluxes of two waves at the tropopause after passing through the wind layer depicted in Figure 5.8(a). The solid and dashed lines are the wave momentum fluxes of westerly and easterly waves at the tropopause; the dotted horizontal lines represent the unfiltered wave momentum fluxes, that would pertain in the absence of the wind layer. We see that dissipation of the waves through the background wind has imprinted a sinusoidal variation in the wave momentum flux of both waves. Given the easterly bias in the prescribed wind layer, the absolute flux of the easterly wave is less than that of the westerly wave.

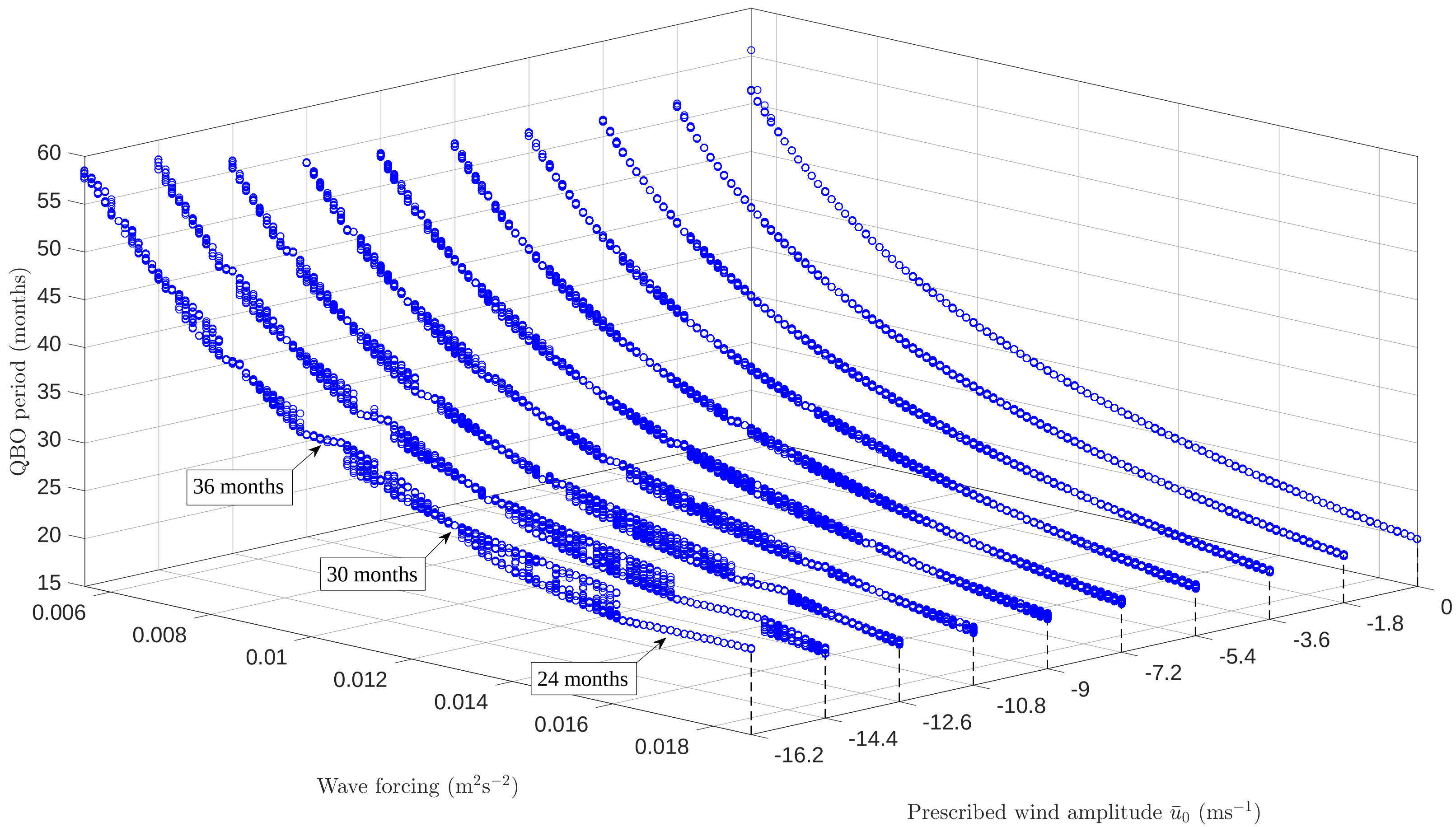

Figure 5.9: Cycle to cycle variability of the QBO period as the wave forcing F_0 and amplitude of filtering winds $\bar{u}_0$ vary. Synchronization regions at 24, 30 and 36 months have been labelled.

We investigate the response of the QBO to the amplitude of the prescribed wind layer, $\bar{u}_0$. This is done by prescribing a time-varying wave forcing at the base of the usual Holton-Lindzen model (2.4.39), using values of $F(t)$ for each wave as given by equation (2.4.39).

Figure 5.9 plots the cycle to cycle variation of the QBO period across 10 values of $\bar{u}_0$ and 100 values of the unfiltered wave forcing F_0, which is the strength of the waves before passing through the prescribed wind layer. As before, increases in F_0 result in a decrease in the average QBO period. As $\bar{u}_0$ increases, the variability of the QBO period increases, and locking regions at 24, 30 and 36 months form and widen.

Figure 5.10 depicts the cycle to cycle variability of the QBO when $\bar{u}_0 = -16.2\,\mathrm{m\,s^{-1}}$, the case of most significant synchronization depicted in Figure 5.9. The general structure of the QBO variability is strongly reminiscent of variability seen in earlier chapters. There is evidence of both discrete and continuous sets of QBO periods, with prominent locking regions at integer multiples of the filtering period. The 24 month and 36 month locking regions are much more prominent than the 30 month and 42 month locking regions, suggesting that even ratio locking regions are favoured in this mechanism of synchronization over odd ratio locking regions. The range of variability of the QBO period outside of the locking regions is largest near the boundaries of the even-multiple locking regions, and in general does not exceed 3 months. In contrast, the range of variability of the QBO period shrinks to zero when approaching odd-multiple locking regions. We note also that the distribution of QBO periods between the 30 month and 24 month locking regions is approximately bimodal.

5.4 Discussion

In this chapter we considered the impacts of time-varying wave forcing on the period of the QBO, as well as the effect of the periodic filtering of waves by background

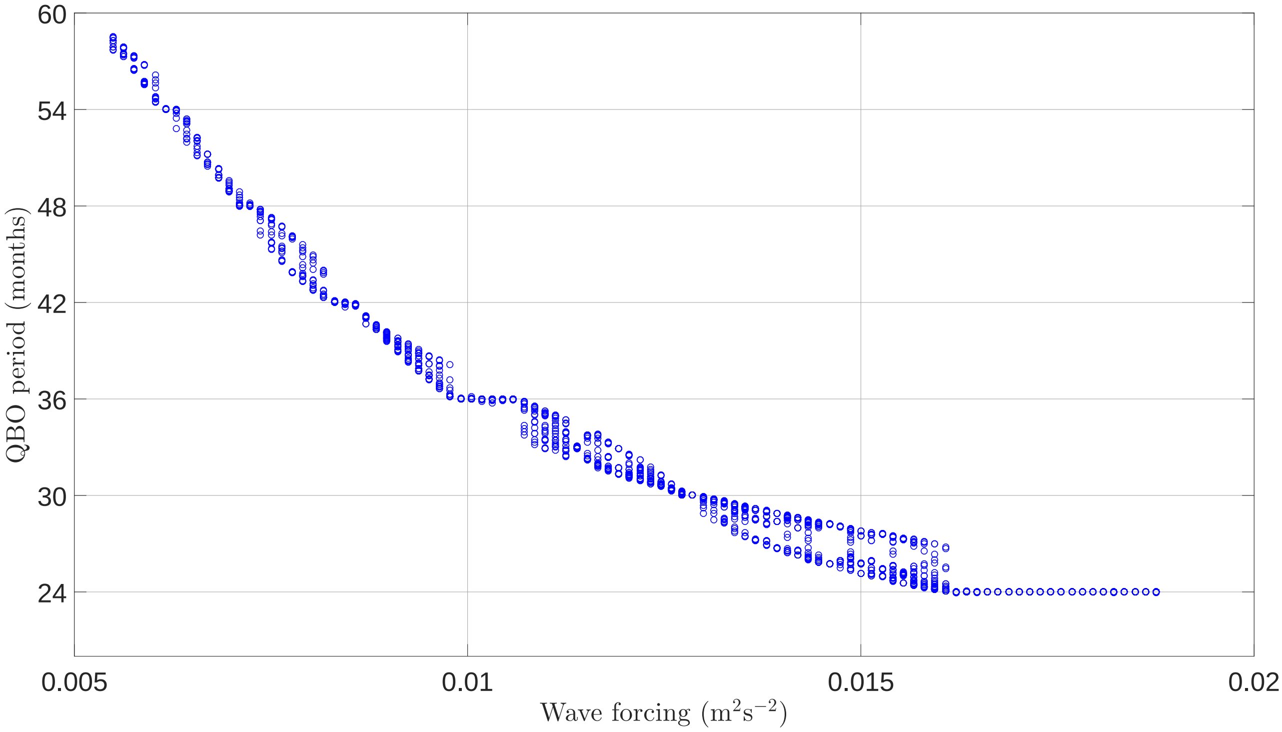

Figure 5.10: Cycle to cycle variability of the QBO when $\bar{u}_0 = -16.2\,\mathrm{m\,s^{-1}}$.

tropospheric winds. We found that both phenomena are possible mechanisms for synchronizing the QBO, at least in principle.

Periodicity in wave forcing resulted in robust synchronization of the QBO, and created wide synchronization regions at integer multiples of the forcing period across semi-annual, annual, and inter-annual time scales. We also found a large range of variability of the QBO period. This was most prominent in the inter-annual case, where the range of QBO variability was in line with the variability of the observed QBO. The interaction between the 4-year cycle in wave forcing and the intrinsic period of the QBO yielded multi-decadal oscillations in the period of the resultant QBO, some stretching for over 50 years. This result highlights the importance of long observational records to truly understand the variability of the QBO in the Earth's atmosphere. It also underlines the utility of studying the QBO using simple idealised models, where it is possible to run extensive studies of parameter space and to understand long-term variations in the QBO period.

We have shown that wave filtering by tropospheric winds can in principle engender synchronization of the QBO. However, the required amplitude of tropospheric winds at which synchronization becomes significant is quite large compared to observations (see Figure 4.2). The modelling of wave filtering suffers from the defect that there is no wave-induced feedback on the mean flow - although a related situation was studied in Chapter 4 when we considered direct accelerations of the tropopause and lower stratospheric winds. In that case it was found that the widest synchronization regions occurred at odd multiples of the forcing period (see Figure 4.9), whereas here the widest intervals occur at even multiples of the forcing period (see Figure 5.10). We also note that the depth of tropospheric winds may also vary seasonally, although we did not explore the effects of this and kept a fixed depth of 3 km.

The generic features of synchronization have proven to be remarkably similar across the different mechanisms of synchronization we have studied. All feature a mixture of discrete and continuous QBO cycles and show evidence of period bifurcations as wave forcing (or some other relevant forcing parameter) is varied. In the next chapter we make some initial steps towards an understanding of these synchronization structures.

Chapter 6

Descent rate models of the QBO

6.1 Introduction

In the previous chapters we have seen several examples of QBO interactions with an external periodic influence, that result in the oscillation period of the QBO exhibiting complex variations. These variations have a particular structure, wherein the QBO periods are either:

- locked to an integer multiple of the forcing period;
- arranged as n-cycles, such that the sum of every n periods is an integer multiple of the forcing period; or
- continuous, with the average QBO period being an irrational multiple of the forcing period (or at least a rational multiple with large denominator).

(Note that the first property is in fact a subset of the second property, with $n = 1$).

Thus far, we have not been able to explain the underlying dynamics driving the above behaviour. To make steps in that direction, in this chapter we will consider a further simplification of the Holton-Lindzen model, by studying a class of equations for the rate of descent of the QBO shear zones which we shall call *descent rate models*.

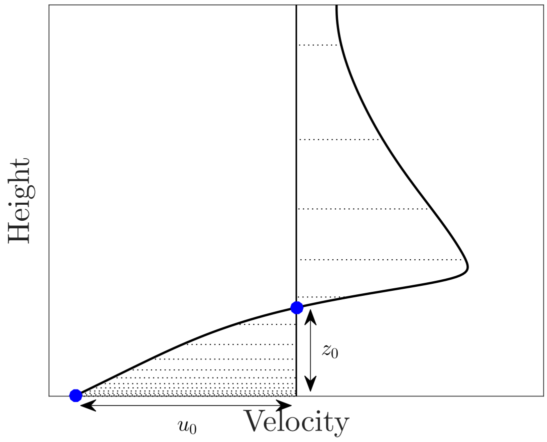

Figure 6.1: Definitions of z_0 and u_0 as the height of the zero wind line and the tropopause velocity respectively. The dynamics of these two variables are the main components of the descent rate models introduced in this chapter.

These models are based on the assumption that the QBO period variations can be approximately described by modelling the dynamics of just two points: the height of the zero-wind line z_0, and the velocity at the tropopause u_0 (Figure 6.1). In this way, the dynamics of the QBO period are reduced from an infinite-dimensional PDE (the Holton-Lindzen equation (6.3.1)) to a small set of ordinary differential equations for z_0 and u_0.

The remainder of this chapter proceeds as follows. In section 6.2 we investigate a heuristic model for the descent rate, and consider the relevant factors required to model the wave forces adequately at different heights of z_0. We then solve the descent rate model for two candidate wave forcing profiles. We find that the behaviour of the QBO in the models is very similar to that of the full HL equation. In section 6.3 we show that the HL equation itself can be put into descent rate form via a simple change of coordinates and a quadratic approximation of the velocity profile. Thus, it would seem that most of the complex behaviour of the QBO in the HL equation can be captured by a single ordinary differential equation - achieving a large reduction in complexity with no significant loss in dynamical detail. We discuss the implications of our results in section 6.4.

6.2 A heuristic descent rate model

6.2.1 Formulation

The idea behind a descent rate equation is to model the temporal rate of change of the zero wind line, dz_0/dt, rather than the velocity profile itself. We consider the case where the QBO is forced by two identical waves, as well as upwelling and the usual diffusion. The balance of wave forces at the height of the zero wind line z_0 is such that the net contribution of wave forcing is always downward; this will be discussed in more detail later. Diffusion also exerts a downward force on z_0, because absolute zonal wind velocities just above z_0 are always larger than absolute wind velocities just below z_0 (a consequence of the nature of wave forcing). In contrast, the tendency of upwelling is to impede the descent of z_0. Thus we posit the following model for z_0 dynamics:

$$\frac{dz_0^*}{dt^*} = -D^* + \left[w_c^* + w_a^* \cos\left(\frac{2\pi t^*}{360}\right)\right] - F^* \exp\left(\frac{z_0^*}{H_\rho^*}\right) G\left(z_0^*\right), \tag{6.2.1}$$

where asterisks denote dimensional quantities. Here we have modelled diffusion as a constant downward tendency of strength D^*, and upwelling has been separated into constant and annual components w_c^* and w_a^*, as in Chapter 3. The wave forcing is expressed as the product of the wave amplitude F^* with an exponential term (representing density stratification with a scale height H_ρ^*) and a wave profile $G(z_0^*)$ that will be defined below. Since we have chosen the waves to be identical, the wave forcing structure for descending westerlies and descending easterlies is the same, and so we can use the single evolution equation (6.2.1) for both cases. The height domain is chosen to be between $z^* = 17\,\mathrm{km}$ and $z^* = 43\,\mathrm{km}$. For simplicity we assume a periodic domain, so that when z_0 passes below the tropopause at 17 km it maps automatically to the mid-stratosphere at 43 km, where it is assumed that new QBO shear zones form. This behaviour approximates the destruction of the underlying shear zone as z_0 descends to the lower boundary, and the immediate formation of a new shear zone aloft. Although this assumption divorces the model dynamics from the physical mechanisms driving QBO shear zone formation, it does not substantially affect the dynamics driving the QBO period, which is the main quantity of interest in our study. The approximation is reasonable if there is a negligible time difference between the destruction of a shear zone at the lower boundary and its re-formation in the mid-stratosphere as a new shear layer, which is a fair description of the dynamics of the QBO in the Holton-Lindzen model.

In section 6.1 we defined a tropopause velocity, u_0, together with z_0. For the heuristic models discussed in this section, we simply define

$$u_0 = \begin{cases} +1, & \text{westerly winds at lower boundary,} \\ -1, & \text{easterly winds at lower boundary.} \end{cases} \tag{6.2.2}$$

Thus u_0 contains no dynamical content in the heuristic models, and serves purely as a placeholder for the direction of winds at the tropopause. As the zero wind line z_0 passes through $z_0 = 0$, the descending shear layer above z_0 settles at the bottom boundary and so u_0 reverses sign.

Before proceeding further we non-dimensionalise (6.2.1) by introducing a height scale $H^* = 6.5\,\text{km}$ and a time scale $T^* = 1\,\text{day}$. We can then define non-dimensional time and zero wind height variables via $t^* = T^* t$ and $z_0^* = 17 + H^* z_0$. Substituting into (6.2.1) and rearranging gives

$$\frac{dz_0}{dt} = -D + \left[w_c + w_a \cos\left(\frac{2\pi t}{360}\right)\right] - F \exp\left(\epsilon z_0\right) G\left(z_0\right). \tag{6.2.3}$$

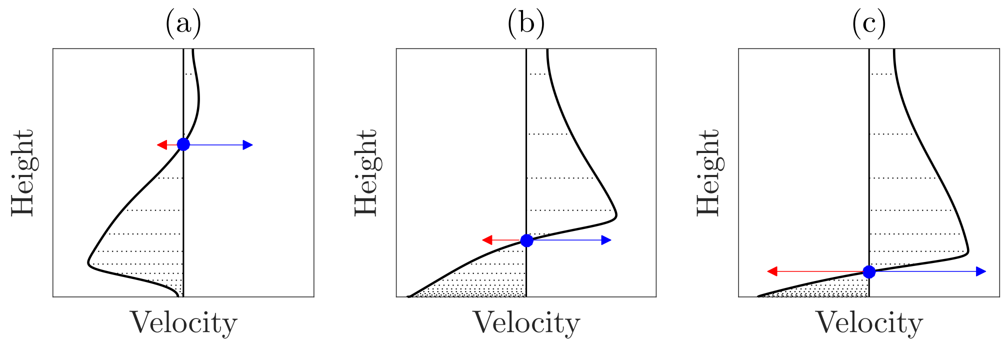

Figure 6.2: Force balance of the waves driving the QBO at the zero wind line at different heights, over the course of the formation and descent of a westerly shear zone. Refer to text for details.

Here the dimensionless parameters D, w_c, w_a and F are given by

$$\{D, w_c, w_a, F\} = \frac{t^*}{H^*}\left\{D^*, w_c^*, w_a^*, F^* \exp(17/H_\rho^*)\right\}, \tag{6.2.4}$$

and $\epsilon = H^*/H_\rho^*$.

To get a feel for an appropriate form of the wave profile G_0 we ignore density stratification for simplicity by letting $H_\rho^* \to \infty$. We then consider the balance of wave forces at the zero wind line as a westerly shear zone descends. This is depicted in Figure 6.2; blue and red arrows denote contributions of the westerly and easterly waves respectively.

When a new westerly shear zone forms in the mid-stratosphere (Figure 6.2(a)), there is a large easterly shear zone separating the zero wind line from the source of the waves at the tropopause. As such, whilst both waves are dissipated as they propagate through the shear zone towards z_0, the easterly wave is absorbed much more than the westerly wave. The easterly wave forcing at z_0 is therefore much weaker than the westerly wave forcing at z_0. This results in a large net westerly/eastward acceleration, which pushes the zero wind line down.

As the zero wind line descends to lower levels (Figure 6.2(b)), the amplitude of both waves increases since the zero wind line is now closer to the source region of

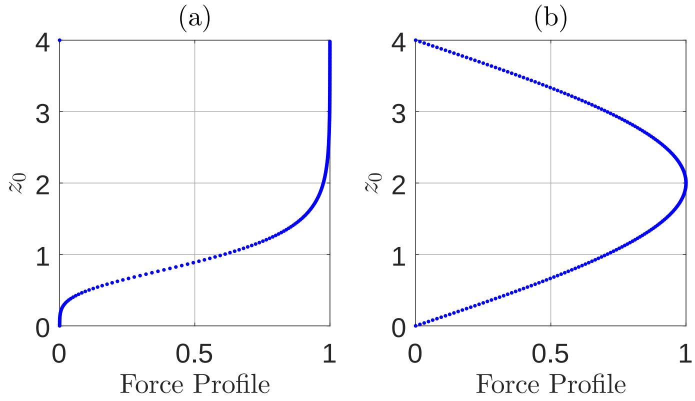

Figure 6.3: Candidate profiles of the variation of the net wave forcing with height, $G_0(z_0)$: (a) Gompertz profile, (b) Sine profile. See text for details.

the waves. As before, there is a discrepancy in wave absorption due to the prevailing easterly winds below the zero wind line. However, the magnitude of this difference is now reduced, since the amplitude of the easterly wave gains disproportionately from the reduced extent of the easterly shear zone as compared to the amplitude of the westerly wave. The net result is that the total wave forcing is still westerly, but the magnitude is reduced as compared to the upper level case discussed earlier. The reduction in strength of the net wave forcing continues all the way down to the tropopause (Figure 6.2(c)), at which point the contributions of both waves are almost equal and so the net eastward acceleration is very weak.

Note that the addition of a density stratification does not change the qualitative picture described above; the amplitudes of both waves will simply gain the same positive exponential factor due to density decreases in height.

Figures 6.3(a) and (b) display two candidate profiles for $G(z_0)$ over the simulation domain $z_0 \in [0, 4]$. We emphasize that the profiles reflect wave forcing *at the zero wind line* z_0, for different heights of z_0. In the first profile (Figure 6.3(a)), the wave forcing is close to zero when z_0 is at the tropopause and increases monotonically with height, eventually becoming almost constant at higher levels. The profile is a sigmoid curve modelled by:

$$G_0(z_0) = \exp\left(-be^{-cz_0}\right), \tag{6.2.5}$$

which is a Gompertz function with shape parameters $b = 10$ and $c = 3$ respectively. The profile was chosen to reflect the fact that one wave is essentially trapped in the lower stratosphere in the HL equation with a no shear lower boundary condition and so, in the upper half of the domain, there is very little counterbalancing of the acceleration and descent induced by the free wave.

The second candidate wave profile (Figure 6.3(b)) is a sine function given by

$$G_0(z_0) = \sin\left(\frac{\pi z}{4}\right). \tag{6.2.6}$$

This profile is continuous across the periodic boundary at $z = 0, 4$, whereas the Gompertz profile (6.2.5) is discontinuous. Given that the wave momentum flux decreases exponentially with height for both waves, this profile might seem to model the decay of net wave forcing at high levels appropriately. It is important to note, however, that the wave forcing at the zero wind line is *never* small at high levels, because the zero wind line is only created after the upper level winds experience significant acceleration and switch signs. Hence, in a sense, z_0 is always created 'fully formed' with a non-zero initial velocity. This means that a discontinuity in dz_0/dt across the boundary is to be expected. Nevertheless, it is useful to consider the case of a continuous G_0 for purposes of comparison.

6.2.2 Results

We solve equations (6.2.2)–(6.2.3) numerically using the forward Euler method, using a time step of $\Delta t = 0.2$ days. The values of $w_c = 0.004$ and $w_a = 0.002$ are chosen, based on physically reasonable values of the corresponding dimensional variables, which are $w_c = 0.3\,\mathrm{mm\,s^{-1}}$ and $w_a = 0.15\,\mathrm{mm\,s^{-1}}$ respectively. D is set equal to

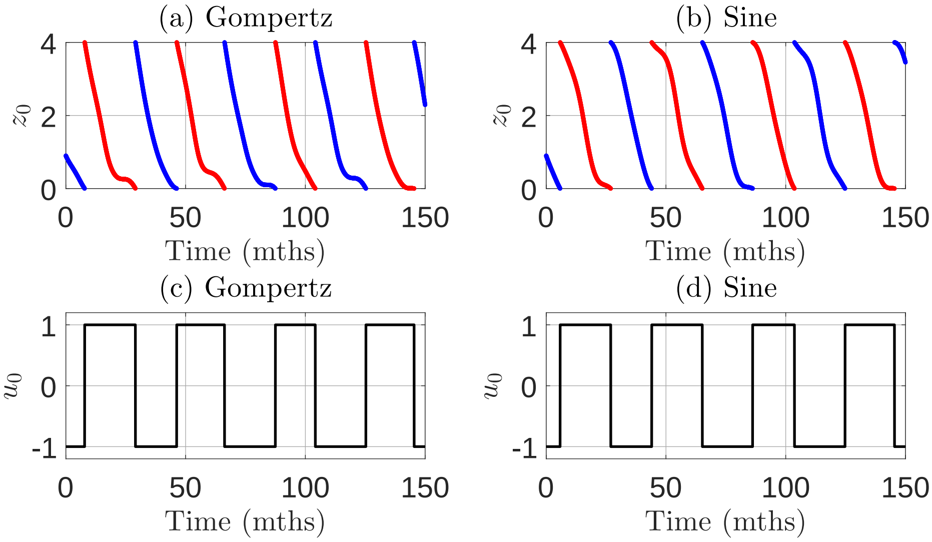

Figure 6.4: Sample solutions of the heuristic descent model, using the Gompertz (a,c) and Sine (b,d) wave profiles. Parameters are set at $F = 0.01$, $D = 0.006$, $w_c = 0.004$ and $w_a = 0.002$. The location of the zero wind line z_0 over time is plotted in (a) and (b) for each profile. Red and blue lines correspond to descending easterly and westerly shear zones respectively. The corresponding changes in the tropopause velocities u_0 are plotted in (c) and (d).

$w_c + w_a = 0.006$ in order to counter-balance the upwelling maximum and prevent the zero wind line from ever ascending. (Ascent past $z = 4$ would undermine the physical meaningfulness of the assumption of circular geometry, and so we remove this possibility from the outset). Initial conditions are set as $z_0(0) = 0.9$ and $u_0(0) = -1$.

Figures 6.4(a)–(d) display sample evolutions of z_0 and u_0 over the course of 150 months, for a wave amplitude set at $F = 0.01$. Results using the Gompertz and Sine wave forcing profiles are given in Figures 6.4(a,c) and 6.4(b,d) respectively. Blue and red lines in Figures 6.4(a,b) represent the descent of westerly and easterly shear zones respectively.

In both cases the descent of the zero wind lines clearly mimic the descent of the QBO; for example, compare with the zero wind contours in Figure 2.2 on page 42. In the Gompertz case (Figure 6.4(a)), descent of z_0 is quite uniform across the upper levels, and then slows near the lower boundary as the net wave acceleration reduces. The effects of varying upwelling strength can be seen in the varying descent rates

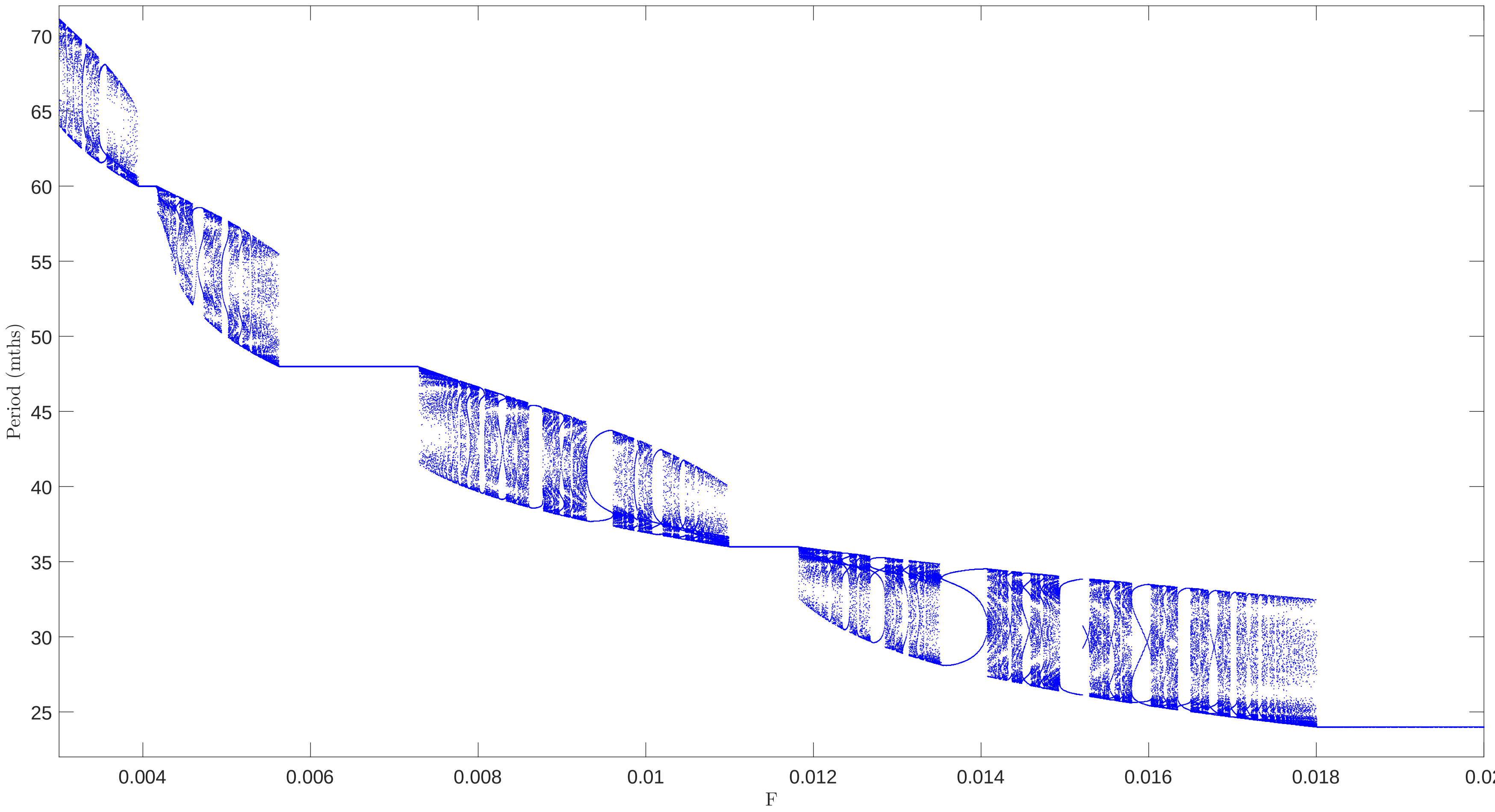

Figure 6.5: Variation of QBO period with wave amplitude F, for the Gompertz wave forcing profile. At each value of F, the set of measured QBO periods has been plotted.

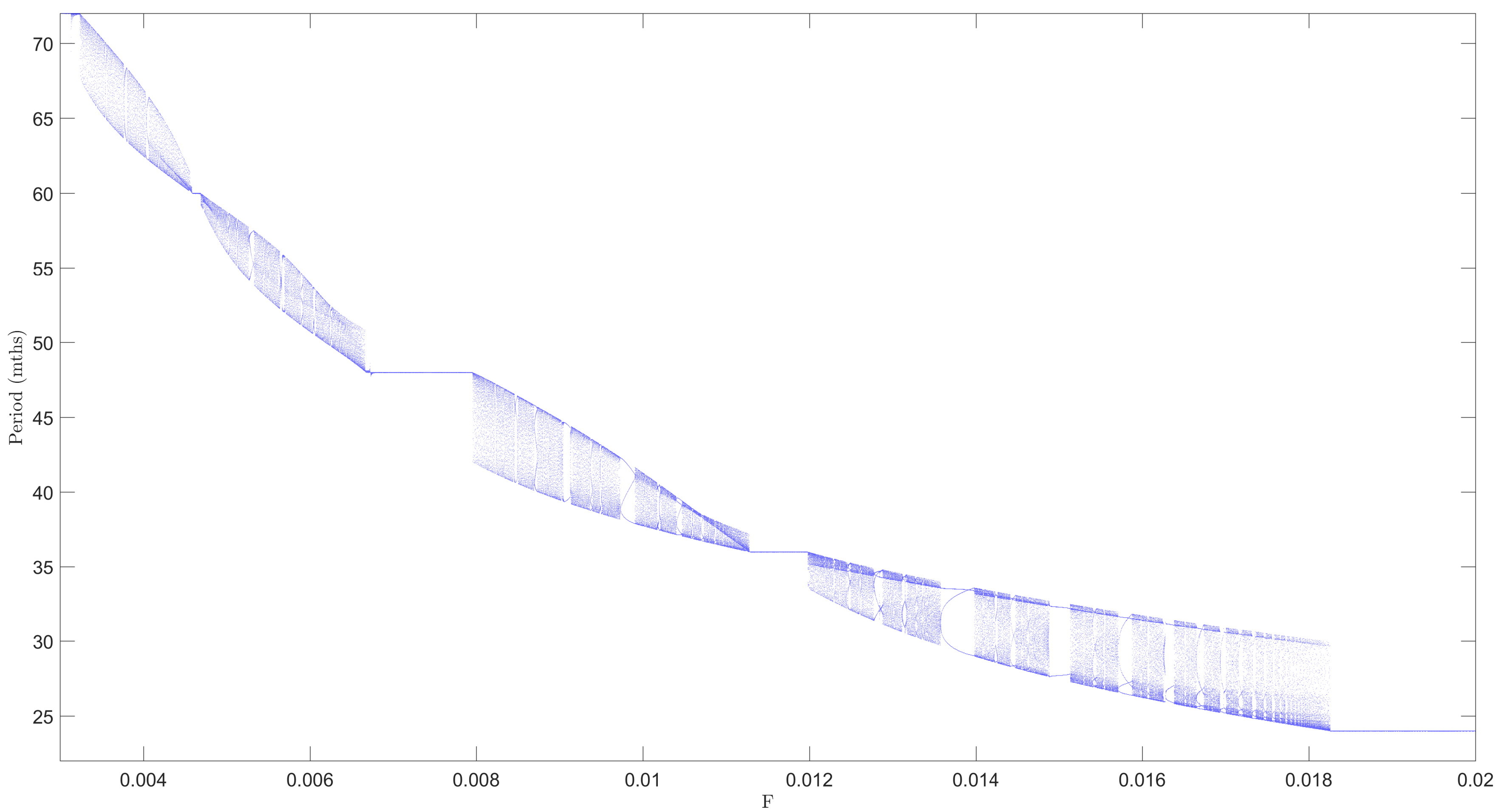

Figure 6.6: Variation of QBO period with wave amplitude F, for the Sine wave forcing profile. At each value of F, the set of measured QBO periods has been plotted.

near the bottom boundary, where the wave forcing is weak and upwelling effects are significant.

Similar behaviour is seen in the Sine case (Figure 6.4(b)), except that there is significant variation near the upper boundary as well, due to the reduction of wave forcing there. The average oscillation periods are quite similar, however, at 38.7 and 39.6 months for the Gompertz and Sine cases respectively.

The corresponding variations of u_0 are plotted in Figures 6.4(c,d). As noted before, these simply mark the times where new shear zones are formed aloft.

Having elucidated the basic model behaviour, we performed a parameter sweep by varying the value of F in small increments between $F = 0.003$ and $F = 0.02$. A total of 10,000 different values of F were studied for each of the two wave profiles. Each simulation was run for 50,000 model days - including a startup runtime of 20,000 days to allow time for transients to disappear - and the set of QBO periods was derived by measuring the time between westerly onsets at $z_0 = 0.5$.

Figures 6.5 and 6.6 plot the set of QBO periods obtained as described above against their corresponding values of F, in the Gompertz and Sine wave forcing cases respectively. The plots reveal intricate patterns in the detailed QBO period structure. There are prominent locking regions at multiples of the upwelling period (24, 36, 48 and 60 months for the F range considered here). Outside of these regions the QBO is either in a multi-cycle state - identifiable as the white bands within which the QBO period takes on a small set of finite values - or in a quasi-periodic state wherein the QBO 'fills-out' a band of periods. The variation of the QBO period within these regions can be quite large. For example, in the Gompertz case (Figure 6.5) the range of QBO periods just before the 24 month locking region is 8 months.

These results show that the heuristic descent rate model successfully recreates many of the QBO synchronization phenomena documented in previous chapters.

6.3 Descent rate model of the HL equation

6.3.1 Formulation

We now show how the Holton-Lindzen equation (2.4.39) can be transformed into a descent rate equation. Denoting dimensional quantities with asterisks, the Holton-Lindzen equation is

$$\begin{aligned}\frac{\partial \bar{u}^*}{\partial t^*} + w^* \frac{\partial \bar{u}^*}{\partial z^*} = {} & \frac{F^* N^* \mu_0^*}{k_0^* (\bar{u}^* - c^*)^2} \exp\left\{ - \int_{17}^{z^*} \frac{N^* \mu_0^*}{k_0^* (\bar{u}^* - c^*)^2} dz^* \right\} \\ & - \frac{F^* N^* \mu_0^*}{k_0^* (\bar{u}^* + c^*)^2} \exp\left\{ - \int_{17}^{z^*} \frac{N^* \mu_0^*}{k_0^* (\bar{u}^* + c^*)^2} dz^* \right\} + \Lambda_0^* \frac{\partial^2 \bar{u}^*}{\partial z^{*2}}.\end{aligned} \tag{6.3.1}$$

Values of N^*, μ_0^*, k_0^*, c^* and Λ_0^* are fixed at the values stated in Table 2.1. For simplicity of presentation we have assumed that the dissipation and diffusion terms are constant in height, and we ignore density stratification; the derivation extends immediately to these cases as required. We non-dimensionalise (6.3.1) by introducing a height scale $H^* = 6.5\,\mathrm{km}$, a time scale $T^* = 1\,\mathrm{day}$, and a horizontal velocity scale $U^* = c^* = 30\,\mathrm{m\,s^{-1}}$. Thus we can define non-dimensional time, velocity and height scales via

$$t^* = T^* t, \qquad \bar{u}^* = c^* \bar{u}, \qquad z^* = 17 + H^* z. \tag{6.3.2}$$

Substituting into (6.3.1) and rearranging gives the non-dimensional HL equation

$$\begin{aligned}\frac{\partial \bar{u}}{\partial t} + w \frac{\partial \bar{u}}{\partial z} = {} & \frac{F}{(\bar{u} - 1)^2} \exp\left\{ - \int_0^z \frac{\gamma}{(\bar{u} - 1)^2} dz \right\} \\ & - \frac{F}{(\bar{u} + 1)^2} \exp\left\{ - \int_0^z \frac{\gamma}{(\bar{u} + 1)^2} dz \right\} + \Lambda \frac{\partial^2 \bar{u}}{\partial z^2},\end{aligned} \tag{6.3.3}$$

where the non-dimensional parameters w, F, γ and Λ are defined as

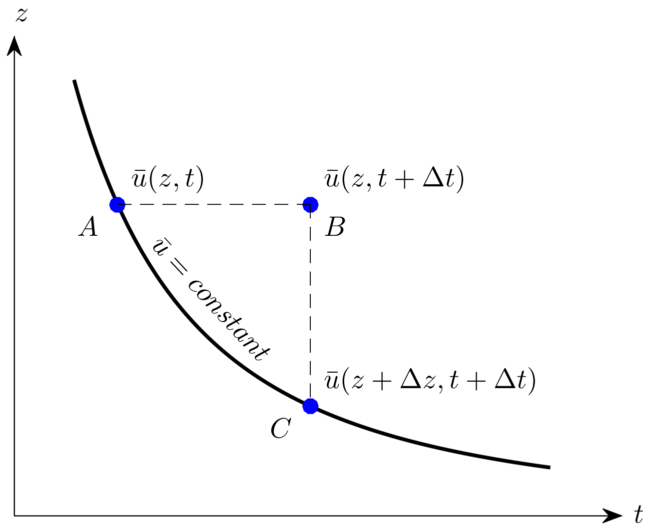

Figure 6.7: Schematic for derivation of the relationship between horizontal acceleration and vertical descent. See text for details.

$$w = \frac{w^* T^*}{H^*}, \qquad F = \frac{F^* N^* \mu^* T^*}{k^* c^{*3}}, \qquad \gamma = \frac{N^* \mu^*}{k^* c^{*2}}, \qquad \Lambda = \frac{\Lambda_0^* T^*}{H^{*2}}. \tag{6.3.4}$$

We note for the chosen parameters that $\gamma \approx 1$, and so for simplicity we will fix $\gamma = 1$ in (6.3.3).

In order to convert the HL equation (6.3.3) into descent rate form we proceed as follows. Figure 6.7 shows a schematic diagram of the geometry of a surface of constant $\bar{u}$ across height z and time t. We have marked the three points A, B, and C on the diagram; these have coordinates (z,t), $(z,t-\Delta t)$, and $(z+\Delta z, t+\Delta t)$ respectively, where Δz and Δt are small positive increments. Points A and C sit on the constant $\bar{u}$ surface, and B is a neighbouring point. The wind field at point C can be related to the wind field at point A by going via point B as follows:

$$\begin{aligned} \bar{u}(z+\Delta z, t+\Delta t) = \bar{u}(z,t) & \\ & + \bar{u}(z,t+\Delta t) - \bar{u}(z,t) \\ & + \bar{u}(z+\Delta z, t+\Delta t) - \bar{u}(z, t+\Delta t). \end{aligned} \tag{6.3.5}$$

However, since both points A and C are on a surface of constant $\bar{u}$, we must have that $\bar{u}(z+\Delta z, t+\Delta t) = \bar{u}(z,t)$. Substituting this into (6.3.5) and rearranging gives:

$$\frac{\bar{u}(z,t+\Delta t) - \bar{u}(z,t)}{\Delta t} = -\frac{\bar{u}(z,t+\Delta t) - \bar{u}(z+\Delta z,t+\Delta t)}{(-\Delta z)}\frac{\Delta z}{\Delta t}. \tag{6.3.6}$$

Taking the limit as $\Delta t \to 0$ then yields

$$\left.\frac{\partial \bar{u}}{\partial t}\right|_z = -\left.\frac{\partial \bar{u}}{\partial z}\right|_t \left.\frac{\partial z}{\partial t}\right|_{\bar{u}}. \tag{6.3.7}$$

The equation reveals that horizontal acceleration and vertical descent can be related via vertical shear. We substitute (6.3.7) into the HL equation (6.3.3), rearrange for $\partial z/\partial t|_{\bar{u}}$, and set the surface of constant $\bar{u}$ to be the zero wind surface $\bar{u} = 0$. This gives the following descent rate model for the HL equation:

$$\begin{aligned}\frac{dz_0}{dt} &= w_c + w_a \cos\left(\frac{2\pi t}{360}\right) - \Lambda\frac{\partial^2 \bar{u}}{\partial z^2}\Big/\frac{\partial \bar{u}}{\partial z} \\ &\quad - F\exp\left\{-\int_0^z \frac{1}{(\bar{u}-1)^2}dz\right\}\Big/\frac{\partial \bar{u}}{\partial z} + F\exp\left\{-\int_0^z \frac{1}{(\bar{u}+1)^2}dz\right\}\Big/\frac{\partial \bar{u}}{\partial z}.\end{aligned} \tag{6.3.8}$$

Here we have re-expressed upwelling w as the sum of a mean and annually-varying part, as usual. The upwelling terms are of the exact same form as was posited in the heuristic model (6.2.1); however, the forms of diffusion and wave forcing still depend on the velocity profile $\bar{u}$ at and below the height of the zero wind line.

In order to make further progress, we must consider a specific form for the velocity profile $\bar{u}$. We assume that the wind profile is given by a quadratic function of height:

$$\bar{u}(z) = \alpha_2 z^2 + \alpha_1 z + \alpha_0, \tag{6.3.9}$$

subject to the following constraints:

$$\bar{u}(0) = u_0, \qquad \bar{u}(z_0) = 0, \qquad \frac{d\bar{u}}{dz}(0) = 0. \tag{6.3.10}$$

The first two conditions simply state the values of the velocity profile at the heights of the lower boundary ($z = 0$) and zero wind line ($z = z_0$) respectively. The third condition is the no shear boundary condition which is applied at the lower boundary.

The above conditions are used to to fix the values of the three parameters $\alpha_{1,2,3}$, giving the following form for the velocity profile:

$$\bar{u}(z) = u_0 \left[1 - \left(\frac{z}{z_0}\right)^2\right]. \tag{6.3.11}$$

We can now use (6.3.11) to compute the derivatives of the zonal wind with height for substitution into (6.3.8), giving

$$\frac{\partial \bar{u}}{\partial z} = -\frac{2u_0}{z_0^2} z, \qquad \frac{\partial^2 \bar{u}}{\partial z^2} = -\frac{2u_0}{z_0^2}, \qquad \frac{\partial^2 \bar{u}}{\partial z^2} \bigg/ \frac{\partial \bar{u}}{\partial z} = \frac{1}{z_0}. \tag{6.3.12}$$

For the quadratic velocity profile (6.3.11) the integrals in (6.3.8) can also be evaluated analytically to give closed form expressions for the wave forcing; these are stated below.

The final equation for the descent rate is

$$\frac{dz_0}{dt} = w_c + w_a \cos\left(\frac{2\pi t}{360}\right) - \frac{\Lambda}{z_0} - FG(z_0, u_0), \tag{6.3.13}$$

where the wave forcing $G(z_0, u_0)$ now depends on both z_0 and u_0 and is given by

$$G(z_0, u_0) = \frac{z_0}{2u_0} \left[e^{-N_w(z_0, -u_0)} - e^{-N_w(z_0, u_0)}\right], \tag{6.3.14}$$

with

$$N_w(z_0, u_0) = \begin{cases} \frac{z_0}{2(1-u_0)} \left[1 - \frac{1}{2\sqrt{u_0(u_0-1)}} \ln\left(\frac{\sqrt{u_0(u_0-1)}+u_0}{\sqrt{u_0(u_0-1)}-u_0}\right)\right], & u_0 < 0, \\ z_0, & u_0 = 0, \\ \frac{z_0}{2(1-u_0)} \left[1 - \frac{1}{\sqrt{-u_0(u_0-1)}} \arctan\left(\frac{-u_0}{\sqrt{-u_0(u_0-1)}}\right)\right], & u_0 > 0. \end{cases} \tag{6.3.15}$$

We note that $G(z_0, u_0)$ is even in u_0; that is, $G(z_0, -u_0) = G(z_0, u_0)$. This reflects the symmetry in the characteristics of the waves we have chosen.

6.3.2 Dynamics of u_0

To complete the description of the descent rate model we need an equation for the tropopause velocity u_0, which is a crucial ingredient in the quadratic approximation used in the previous section. The evolution of u_0 can be deduced by discretizing the non-dimensional Holton-Lindzen equation (6.3.3) into n uniformly spaced vertical levels $Z_{-1}, Z_0, Z_1, \ldots, Z_{n-2}$, with the separation between adjacent levels given by $h = (z_t - z_b)/n$. Here z_t and z_b are defined as in Table 2.1. The corresponding zonal velocities at each height level are given by $u_{-1}, u_0, u_1, \ldots, u_{n-2}$. We then assume that the dynamics of the lower boundary are well-captured by considering the evolution of the the velocity field u_0 at the second grid point, Z_0.

If we approximate the spatial derivatives of (6.3.1) using their discrete counterparts, we can write the evolution equation of u_0 as follows:

$$\begin{aligned} \frac{du_0}{dt} &= -w\frac{u_1 - u_0}{h} + \Lambda\frac{u_1 - 2u_0 + u_{-1}}{h^2} \\ &+ \frac{F}{(u_0 - 1)^2} \exp\left\{-\frac{1}{2}\left(\frac{h}{(u_0 - 1)^2} + \frac{h}{(u_{-1} - 1)^2}\right)\right\} \\ &- \frac{F}{(u_0 + 1)^2} \exp\left\{-\frac{1}{2}\left(\frac{h}{(u_0 + 1)^2} + \frac{h}{(u_{-1} + 1)^2}\right)\right\}. \end{aligned} \tag{6.3.16}$$

Here we have have approximated the integral using the trapezium rule.

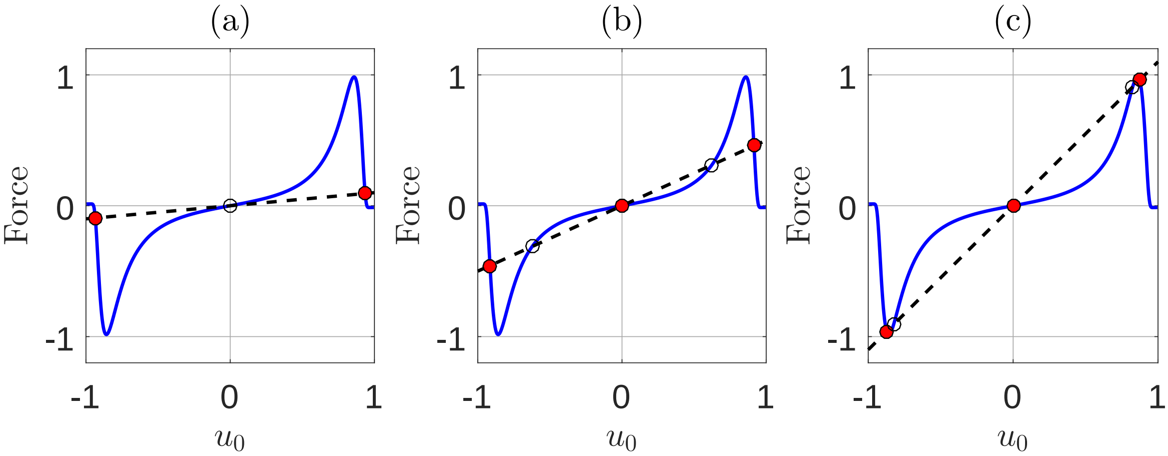

Figure 6.8: Changes in the stable and unstable equilibria at the lower boundary over the course of descent of a shear zone. The solid blue line is the net wave forcing at the lower boundary, and the dashed black line is the negative of the sum of diffusive and upwelling forces at the lower boundary; see the first term on the RHS of equation (6.3.17). Filled and open circles denote stable and unstable equilibria respectively.

We recall that the no shear boundary condition implies that $u_{-1} = u_0$. Further, we identify u_1 with $\bar{u}(h) = u_0(1 - h^2/z_0^2)$, where $\bar{u}$ refers to the quadratic approximation of the zonal wind (6.3.11) and recall that z_0 is the height of the zero wind line. Substituting these values into (6.3.16) and simplifying yields the following evolution equation for the dynamics of u_0:

$$\frac{du_0}{dt} = -\frac{\Lambda'}{z_0^2}u_0 + \frac{F}{(u_0-1)^2}\exp\left\{-\frac{h}{(u_0-1)^2}\right\} - \frac{F}{(u_0+1)^2}\exp\left\{-\frac{h}{(u_0+1)^2}\right\}, \tag{6.3.17}$$

where

$$\Lambda' = \Lambda - wh \tag{6.3.18}$$

represents the combined effects of diffusion and upwelling.

The essential dynamics of equation (6.3.17) are summarised in Figures 6.8(a)–(c) for $h = 4/200 = 0.02$ and $F = he$ (picked to normalise the wave forcing profile). Each plot displays graphs of the total wave forcing (solid blue line) and the negative of the total resistance $-\Lambda' u_0/z_0^2$ (dashed black line), plotted against the possible values of

u_0. The points where the lines intersect give the equilibrium values of u_0; stable and unstable equilibria are denoted by filled and open circles respectively.

The three plots represent the changing force balance between the waves and diffusion/upwelling over the course of the descent of the zero wind line. Whilst the value of the wave forcing is independent of the position of the zero wind line z_0, the total resistance is not, and in fact increases as the zero wind line descends. Figure 6.8(a) depicts the situation when a new shear layer forms in the upper levels of the model. The large value of z_0 is associated with a correspondingly weak resistance term, as reflected in the shallow gradient of the dashed black line. There are three equilibria; an unstable origin and 2 stable points close to the extremal values of $u_0 = \pm 1$. The value of u_0 is quickly attracted to one of the extremal equilibria; which one is determined by the initial sign of u_0.

As the shear zone descends, the resistance term $-\Lambda' u_0/z_0^2$ increases in strength, and the gradient of the dashed line steepens. Two new unstable equilibria are created in a subcritical pitchfork bifurcation, which also stabilises the origin. Since the value of u_0 would have been closer to the extremal stable equilibria at the onset of the bifurcation, however, u_0 will continue to track the location of one of the extremal stable equilibria.

Finally, when the zero wind line is close to the bottom boundary (Figure 6.8(c)), the resistance increases to the point that the stable extremal equilibria collide with the previous unstable equilibria and are annihilated in a saddle-node bifurcation. This is the point in the QBO evolution when the zonal winds at the lower boundary are attracted toward the origin and so begin to switch direction. Our quadratic approximation to the zonal wind field no longer holds through the transition.

In order to step the model forward at this point, we make the assumption that a new shear zone forms aloft as soon as z_0 descends to the height where the saddle-node bifurcation occurs. Thus, the bifurcation point becomes a trigger at which we impose

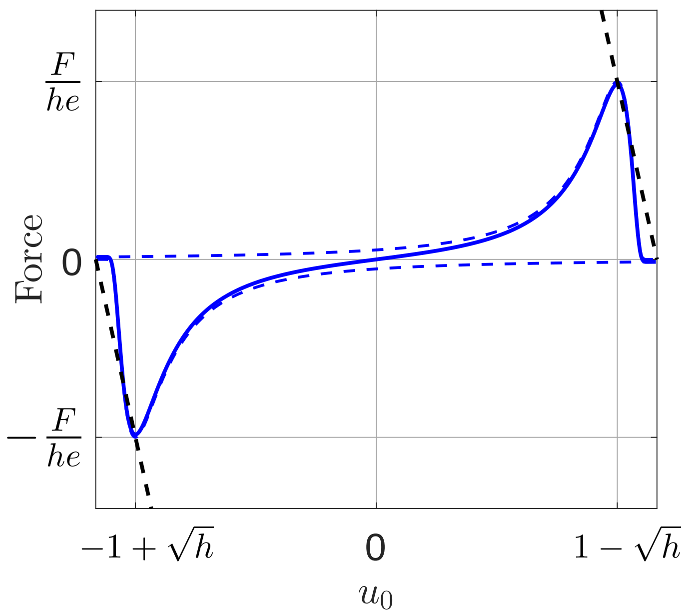

Figure 6.9: Linear approximations to the wave forcing near the peak values of wave forcing. The two blue dashed lines represent the wave forcing contributed by each wave for different values of u_0; the solid blue line is the sum of the two wave forcings. The black dashed lines are linear approximations to the wave forcing near the peak forcing values.

$z_0 = 4$ (the upper boundary of the model). This change in height of z_0 immediately reduces the strength of the resistance force at the lower boundary, returning us to the situation described in Figure 6.8(a) but now with u_0 attracted to the *opposite* stable equilibrium than it was at before.

We can derive an expression for the bifurcation height - call it z_c - by approximating the wave forcing terms by simple linear functions for values of u_0 near to ± 1; see Figure 6.9. Each peak in the wave forcing profile corresponds to the point of maximal forcing driven by either the westerly (positive peak) or easterly (negative peak) wave - these are depicted by the dashed blue lines in Figure 6.9. For small values of h the contribution to the peak forcing is given almost entirely by a single wave, and so we can calculate the peak locations by setting

$$\frac{d}{dz}\left[\frac{F}{(u_0^- - 1)^2}\exp\left\{-\frac{h}{(u_0^- - 1)^2}\right\}\right] = \frac{d}{dz}\left[\frac{F}{(u_0^+ + 1)^2}\exp\left\{-\frac{h}{(u_0^+ + 1)^2}\right\}\right] = 0, \tag{6.3.19}$$

where $u_0^\pm$ are the values of u_0 for which the corresponding wave forcings are largest. Solving (6.3.19) yields $\mathrm{u}_0^- = -1 + \sqrt{h}$ and $u_0^+ = 1 - \sqrt{h}$, with corresponding peak wave forcings of $\mp F/he$ respectively.

We can fit straight lines through the peak wave forcing values, that also pass through $u_0 = \pm 1$ as appropriate (these are the dashed black lines in Figure 6.9). In this approximation we get the following expressions for u_0 dynamics near the turning points:

$$\frac{du_0}{dt} = -\frac{F}{h^{3/2}e}(1 + u_0) - \frac{\Lambda'}{z_0}u_0, \qquad u_0 < 0, \tag{6.3.20}$$

$$\frac{du_0}{dt} = \frac{F}{h^{3/2}e}(1 - u_0) - \frac{\Lambda'}{z_0}u_0, \qquad u_0 > 0. \tag{6.3.21}$$

At the equilibrium points we can set $du_0/dt = 0$, which allows us to rearrange (6.3.20) and (6.3.21) to yield an expression for the equilibrium values of u_0:

$$u_0 = \pm\frac{z_0^2}{z_0^2 + \chi^2} = \pm\frac{1}{1 + \frac{\chi^2}{z_0^2}}, \tag{6.3.22}$$

where

$$\chi^2 = \frac{\Lambda' h^{3/2} e}{F}. \tag{6.3.23}$$

As described earlier, for large values of z_0, the equilibrium value of u_0 is very close to either $+1$ or -1, depending on the initial condition. As the shear layer descends, z_0 decreases and so the magnitude of the u_0 also decreases.

At the bifurcation height z_c, we have approximately that $u_0 = -1 + \sqrt{h}$ or $u_0 = 1 - \sqrt{h}$. Substituting these values into (6.3.20),(6.3.21) and rearranging then yields

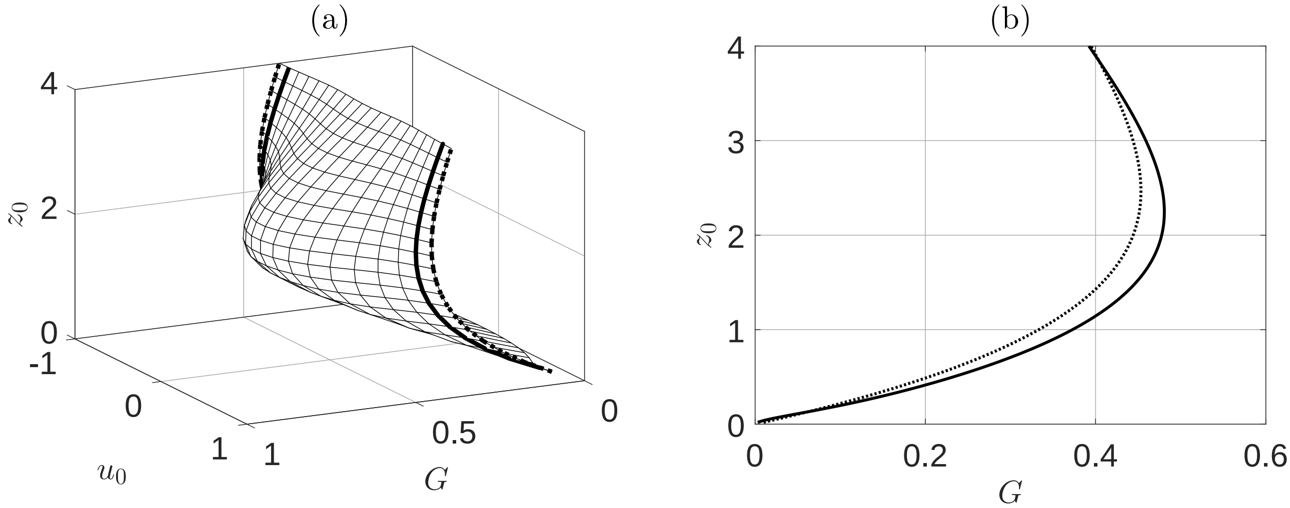

Figure 6.10: (a) Profile of the wave forcing $G(z_0, u_0)$ as defined in (6.3.14)–(6.3.15) for the full HL descent rate model (6.3.13). The darkened solid and dotted lines give the values of G within the bounds of the realisable values of u_0 in the model. These lines are re-plotted in the vertical in (b), for positive values of u_0.

the bifurcation height:

$$z_c = \sqrt{\frac{(\Lambda - wh)(1 - \sqrt{h})he}{F}}. \tag{6.3.24}$$

6.3.3 Results

Figures 6.10(a)–(b) show the value of the wave forcing profile $G(z_0, u_0)$ as defined in (6.3.14), for different values of z_0 and u_0. The wave forcing has the shape of a paraboloid (Figure 6.10(a)). Recalling our discussion in the previous section, however, we note that u_0 values are largely confined to stay within two quite narrow ranges of values of width $\sqrt{h}$ on the extreme ends of the u_0 range. The corresponding range of G values within these bounds have been highlighted on Figure 6.10(a) as the narrow strips bounded by the bold solid and dotted lines.

Figure 6.10(b) plots the vertical slices through the solid and dotted lines corresponding to $u_0 = 1 - \sqrt{h}$ and $u_0 = 1$ respectively in Figure 6.10(a). The two curves give the range of variation of the wave profile G in the HL descent equation as the shear zone descends. The profiles can be compared to the heuristic Gompertz and

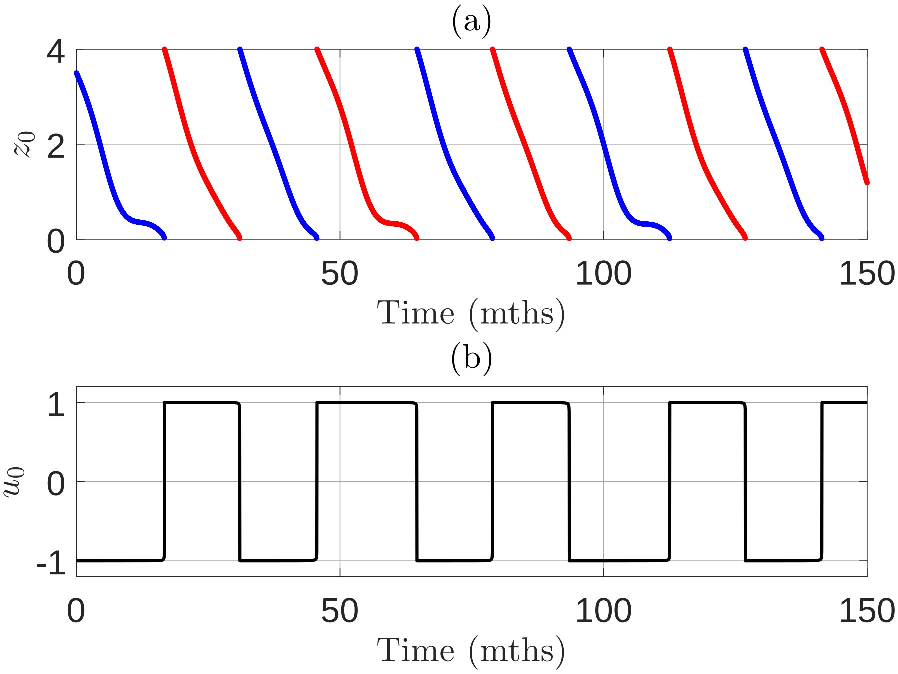

Figure 6.11: (a) Sample solution of the HL descent rate model (6.3.13). Red and blue lines correspond to descending easterly and westerly shear zones respectively. In (b) the corresponding change in the tropopause velocity u_0, given by (6.3.22), is plotted.

Sine wave profiles described in (6.2.5) and (6.2.6) (see also Figure 6.3). The wave profile in the full model is more similar to that of the Sine profile, than to the Gompertz profile. The main difference is the asymmetry of the HL wave profile; rather than weakening symmetrically from $z_0 = 2$ as in the sine profile, the wave forcing remains fairly significant up to the top of the model.

We solve the full descent model of the HL equation (6.3.13) numerically, using approximate values for u_0 given by (6.3.22). The non-dimensional parameters w_c, w_a and Λ are fixed by setting the corresponding dimensional quantities $w_c^* = 0.3\,\mathrm{mm\,s^{-1}}$, $w_a^* = 0.2\,\mathrm{mm\,s^{-1}}$ and $\Lambda_0^* = 0.3\,\mathrm{m}^2\,s^{-1}$ respectively. The vertical spacing h between levels in the lower boundary discretization (6.3.16) is set as $h = 0.02$, based on an assumption of 200 vertical levels. The initial condition is given by $z_0(0) = 3.5$. When the value of z_0 reaches the critical bifurcation height given by (6.3.24), the value of z_0 is immediately reset to $z_0 = 4$, simulating the destruction of the shear zone at the

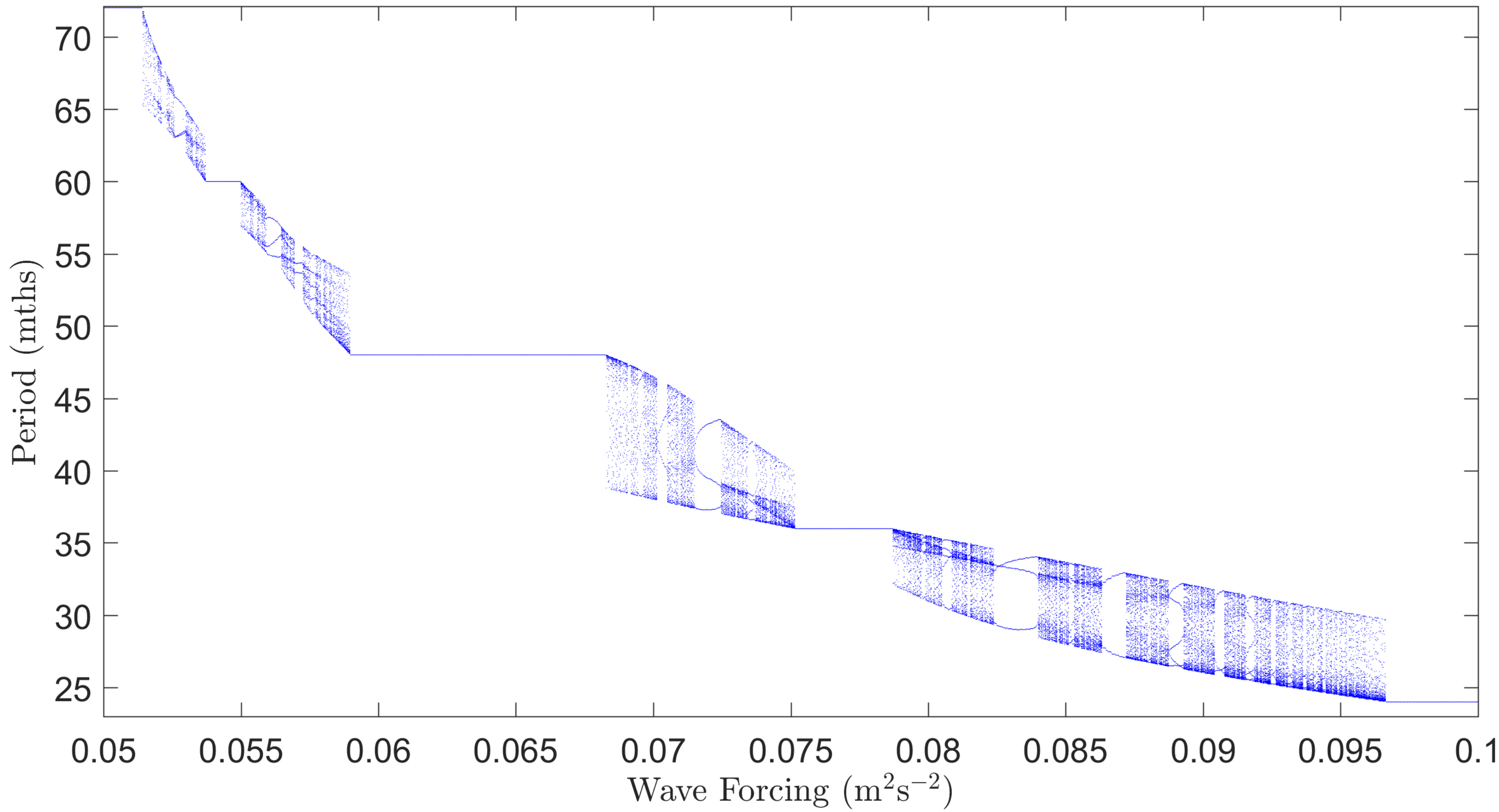

Figure 6.12: Variation of QBO period with wave amplitude F, for the full HL descent rate model. At each value of F, the set of measured QBO periods has been plotted.

lower boundary and the creation of a new shear zone at the upper boundary.

Figure 6.11 displays results for a sample simulation with forcing wave amplitude set at $F^{*} = 8.3 \times 10^{-2} \mathrm{m}^2\,\mathrm{s}^{-2}$, which corresponds to a non-dimensional value given by $F = 0.0036$. The zero wind line descends as expected, and is a good approximation to the dynamics of the zero wind line of the QBO. The average period of the QBO was found to be 32.3 months. We note that the wave amplitude F required to produce this period is very large; around four times the maximum value of F utilised in previous chapters.

Finally, we vary F systematically across 5000 values between $F^{*} = 5.0 - 10.0 \times 10^{-2} \mathrm{m}^2\,\mathrm{s}^{-2}$ and measure the set of QBO periods that result for each value of F, as described previously at the end of section 6.2. Results are plotted in Figure 6.12. The resulting variations in the QBO period are very similar to the heuristic model results, especially that of the Sine wave profile case (Figure 6.6). We see all the hallmarks of synchronization, including locking regions, multi-period cycles, and quasiperiodicity.

6.4 Discussion

In this chapter we have shown how the complex dynamics of the QBO periods - seen in previous chapters, for example, Figures 3.2 (pg. 62), 3.3 (pg. 63), 4.10 (pg. 99) and 5.2 (pg. 114) - are reproduced in simple heuristic models of the descent rate of the QBO. Furthermore, by converting the HL equation into descent rate form via a simple transformation, and making a quadratic approximation for the zonal wind velocities, we have derived an approximate descent rate model for the HL equation itself.

The descent rate models provide a powerful framework within which to interpret synchronization of the QBO. The essential dynamics are captured in a simple one-dimensional ODE, which is a huge reduction in complexity from the one-dimensional

PDE used in previous chapters. The fact that the descent rate models are one-dimensional ODEs also immediately rules out the possibility of chaos in the response of the QBO period to external forcings.

Although the models derived here contain various simplifications such as a discrete set of identical waves, no density stratification, and a relatively simple wave forcing parameterisation, there is no obvious reason why the results of the simple descent models would not naturally carry forward to more complex/realistic situations. Indeed, we have seen that variations in the wave forcing profile do not engender significant qualitative changes to the structure of synchronization (compare Figures 6.5, 6.6 and 6.12). The key ingredient for the synchronization behaviour seems to be the reduction in the strength of the net wave forcing as the zero wind line approaches the tropopause. This reduction allows for significant interactions between the descending shear zone and the periodic variation in the upwelling, which is the driver of the synchronization behaviour in this instance. As long as this requirement is met - which is certainly justifiable physically - the results of the simple models should carry through to more complex cases.

A clear drawback in the modelling approach described here is in the restriction of consideration to the zero wind line. In reality new QBO shear zones originate at different heights, depending on background wind conditions. Our model is not able to represent any of that variation and is restricted to generating shear zones at the same height. The model also cannot cope with the possibility of there being no zero wind line at all in the stratosphere - or indeed, multiple zero wind lines. As a result, some of the more complex variability of the QBO will not be reflected in the model.

In the full HL descent model we note that the values of wave forcing amplitude required to drive the QBO at physically observed periods was much larger than in the case of the full HL PDE solutions discussed in previous chapters. This is because our quadratic parameterisation of the zonal velocity implies relatively weak shear in the descent rate model as compared to the full HL model, hence requiring stronger wave amplitudes to maintain the QBO period. More generally, the explicit dependence of the QBO period on diffusion in the descent rate models underscores the crucial role of diffusion in determining the period of the QBO. It is well-known that the QBO generated in GCM's is very sensitive to the choices of model setup, with the QBO period varying in response to changes in grid spacing, method of discretization, choice of dynamical core, etc (Yao and Jablonowski [2015], Schenzinger et al. [2016]). The descent rate models show why this might be the case by highlighting the influence of diffusion - or any of its proxies in a numerical model - in driving the downward propagation of the QBO.

The set of behaviours described by the descent rate models are reminiscent of a class of mathematical models known as *circle maps*, which are well known in the literature of dynamical systems theory (e.g. Jensen et al. [1983, 1984], Bak et al. [1985], Katok and Hasselblatt [1997], Ott [2002]). The classical 'sine' circle map was defined by Arnold [1965] as a map on the circle

$$\theta_{n+1} = f(\theta_n) = \theta_n + \Omega - \frac{K}{2\pi}\sin(2\pi\theta_n)\,, \tag{6.4.1}$$

where we have set the periodicity equal to 1 rather than 2π and so $\theta \in [0, 1]$. In general, f could be any periodic function in θ. In the case of the sine circle map, the dynamics of the map, for given nonlinearity parameter K and period Ω, are captured by defining a winding number W as

$$W = \lim_{n\to\infty} \frac{f^n_{\Omega,K}(\theta) - \theta}{n}. \tag{6.4.2}$$

The plot of winding number W against Ω yields a complex geometrical object known as the *devil's staircase*, plotted in Figure 6.13(a). At each Ω the value of the winding number reflects either rational or irrational/quasiperiodic motion. For small values of

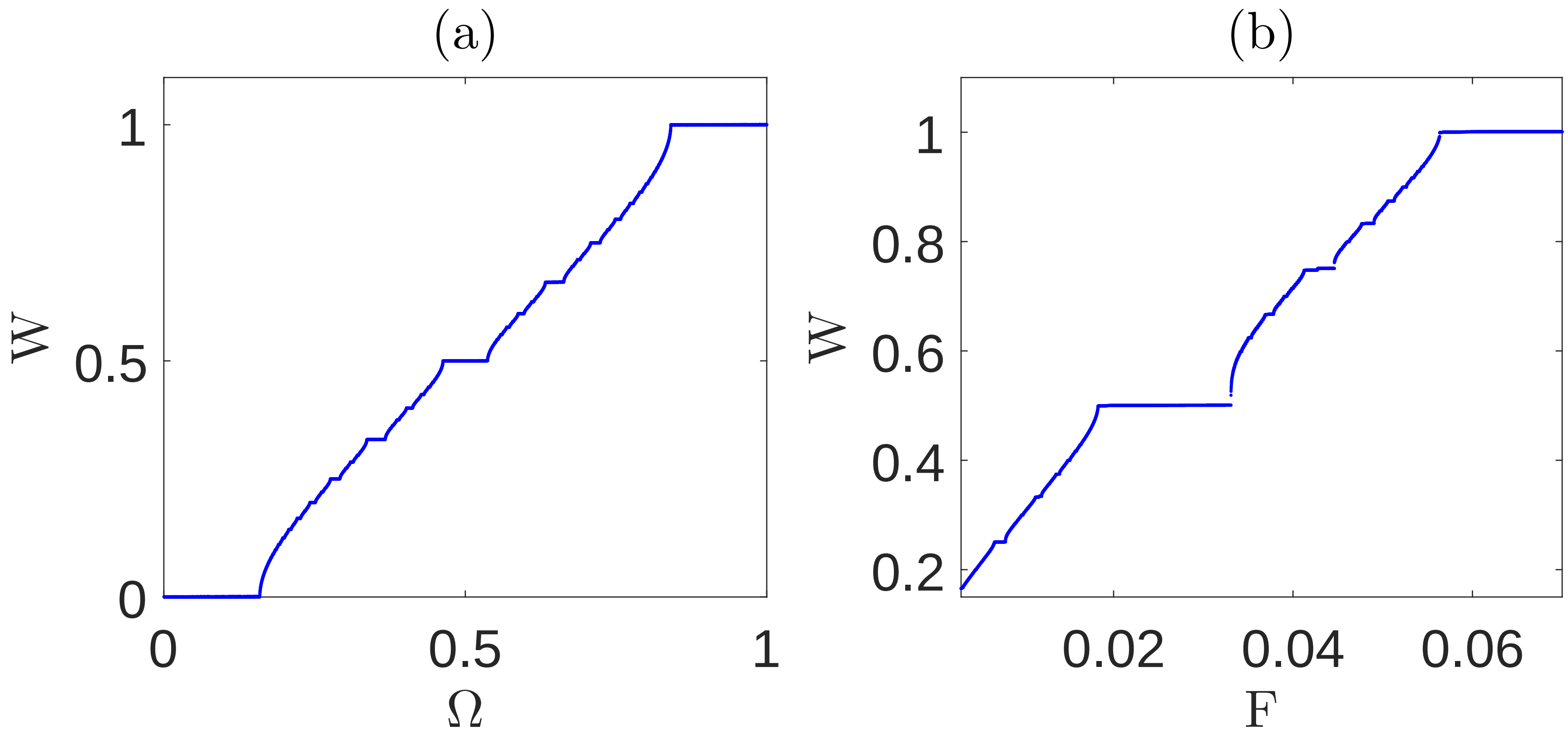

Figure 6.13: Winding number variations in the case of the circle map (a), and the QBO with Sine wave profile (b).

K the Lebesgue measure of the set of Ω values yielding quasiperiodicity is close to 1 (Arnold [1965]); however, the distribution of these values is non-trivial because there are *intervals* of rational winding number values arbitrarily close to *every* quasiperiodic value of Ω. As the strength of K increases the size of the rational intervals also increases, eventually confining the set of quasiperiodic values to a set of Lebesgue measure zero - giving the devil's staircase (Figure 6.13(a)).

The winding number concept described above can be easily extended to the descent rate models by defining a related map via the forward integration of the descent rate model over a length of time equal to the period of the external force (360 days in the case of tropical upwelling). Figure 6.13(b) shows the equivalent variation of winding number with wave forcing in the case of the heuristic model using the Sine wave profile (6.2.6); qualitatively similar plots are produced using both the Gompertz profile and the full descent model (not shown). The similarities between the results of iterating the Sine profile map and the circle map are striking; it is clear that the basic fractal structure of the staircase is present in the QBO models as well. Thus, it would seem safe to claim that that the mathematical structure of QBO descent in the presence of external periodic influences is essentially described by a circle map.

Chapter 7

QBO synchronization in Reanalysis and Climate Model data

7.1 Introduction

In the preceding chapters our focus has been primarily in the domain of low-dimensional models of the QBO. The relative simplicity and low computational cost of solving these sets of equations allowed us to test various synchronization hypotheses in fine detail. We found that the descent rate of the simulated QBO is sensitive to variations in the strength of upwelling of tropical air, as well as to variations in tropical wave activity. As such, periodic variations in the strength of these quantities - the annual cycle in tropical upwelling induced by the Brewer-Dobson circulation, for example - can have a strong synchronizing effect on the period of the simulated QBO.

The drawback of the one-dimensional modelling framework, of course, is that there are many other dynamically important processes and pathways that are not accounted for. The value of the simple model derives primarily from the physical insights gleaned from the simplified picture; these inform us of the types of behaviour to look for in more advanced climate models and in the real atmosphere. A positive identification of similar features in these vastly more complex situations can then be interpreted and given meaning within the physical framework provided by the basic model.

In this chapter we investigate the seasonal synchronization of the QBO by the SAO and the tropical branch of the Brewer-Dobson circulation, using reanalysis and climate model data. Three sets of wind data are used: one reanalysis data set (ERA-40/Interim) and two General Circulation Model (GCM) data sets (HadGEM2-CC and MIROC-ESM-CHEM). For brevity, we will refer to each data set as ERA, MOHC, and MIROC respectively. In Section 7.2 we describe the data used in the study in more detail and highlight the basic characteristics of the wind systems. We begin our analysis in Section 7.3 with a characterisation of the descent rate of the QBO by tracking the location of zero-wind lines in the data. We investigate seasonal variations in the QBO descent rate, and diagnose the relationship between the descent rate of the QBO and the strength of the residual circulation. We also consider, in line with our findings in Chapter 3, the seasonal tendency in the evolution of the QBO period.

In Section 7.3.2 we use Extended Empirical Orthogonal Function Analysis (Fraedrich et al. [1993], Read and Castrejón-Pita [2012]) to isolate coherent structures in the data that are associated with the QBO, SAO, and Brewer-Dobson (BD) circulation. Using analytic phase techniques, we investigate synchronisation between these wind structures. We summarise and discuss our findings in Section 7.4.

7.2 Data

7.2.1 Reanalysis

We used global atmospheric reanalysis data from the European Centre for Medium-Range Weather Forecasting (ECMWF), consisting of the 40-year ERA-40 data set from 1957–2002 (Uppala et al. [2005]) and its subsequent extension in ERA-Interim

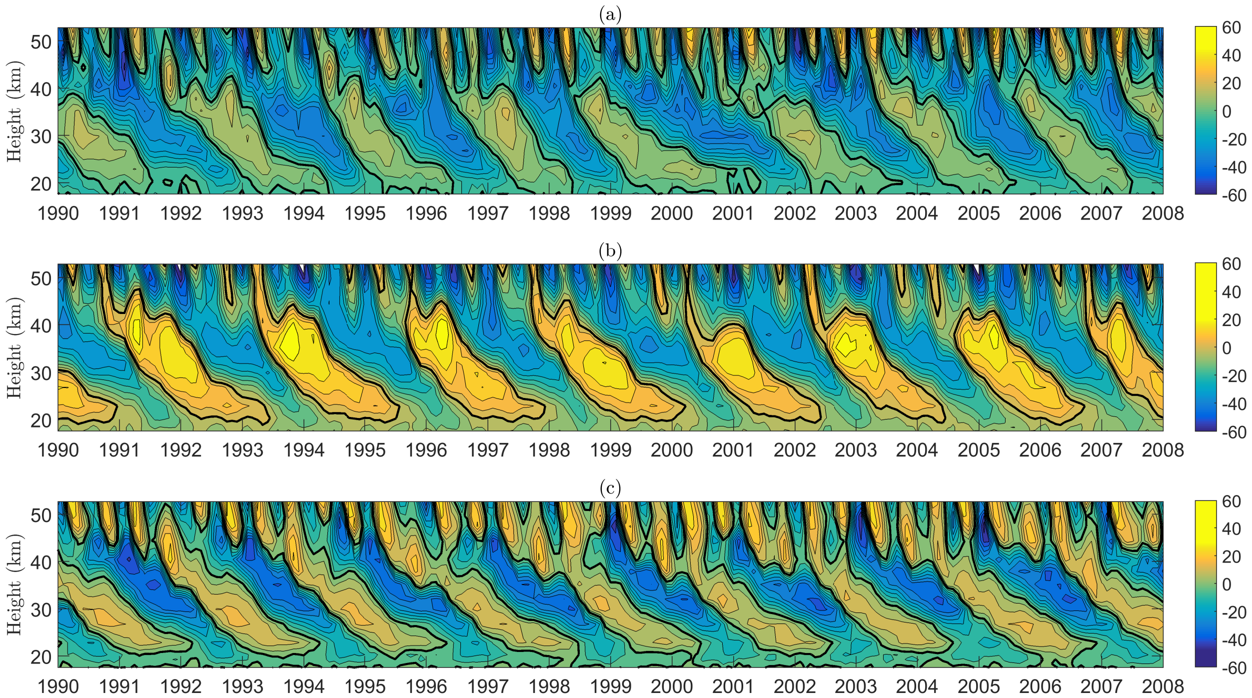

Figure 7.1: Sample height-time contour plots of the the zonal mean zonal wind at the equator (averaged over 5°S–5°N) in (a) ERA-Interim, (b) MOHC, and (c) MIROC data. The contour interval is $5\,\mathrm{m\,s^{-1}}$, and the zero wind line is highlighted by a bold contour.

from 1979–2016 (Dee et al. [2011]). ERA-Interim data was preferred for the time periods over which the data sets overlapped. Monthly zonal-mean zonal wind was extracted and averaged over the latitudes of 5°S–5°N. A representative contour plot of the height-time zonal wind evolution is presented in Figure 7.1(a). We converted the model pressure levels p to log-pressure height levels z using

$$z(p) = H \ln\left(\frac{1000\,\mathrm{hPa}}{p}\right), \tag{7.2.1}$$

where an atmospheric scale height of $H = 7.64\,\mathrm{km}$ was assumed. The alternating pattern of descending zones of QBO winds is clearly evident in the lower and middle stratosphere, as are the SAO winds in the upper stratosphere.

7.2.2 GCMs

The two GCM data sets used in this study are from the Met Office HadGEM2 (Martin et al. [2011]) and MIROC-ESM (Watanabe et al. [2011]) families of climate models respectively. The model runs are contributions to the fifth phase of the Coupled Model Inter-Comparison Project (CMIP5: see Taylor et al. [2012]), and consist of mean monthly data. Both runs are of the Pre-industrial Control ('piControl') type, wherein external forcings (solar irradiance, CO_2) are fixed at 1850 levels.

7.2.2.1 HadGEM2-CCS

HadGEM2-CCS (Martin et al. [2011], Hardiman et al. [2012], Osprey et al. [2013]) is a 'high-top' configuration of the UK Met Office HadGEM2 model. It consists of atmosphere, ocean, and sea-ice components, coupled with carbon cycle processes including dynamic vegetation and ocean biogeochemistry. The atmospheric horizontal resolution is $1.875° \times 1.25°$ (approximately 140 km in mid-latitudes). The –CCS configuration uses 60 vertical levels going up to 84km, allowing for a well-resolved stratosphere; however, atmospheric chemistry is not included. A non-orographic gravity wave drag scheme is used to simulate the effects of sub-gridscale buoyancy waves (Scaife et al. [2000]). The model was run for 240 years (1860–2099) in the piControl setting, and produced a realistic QBO (Figure 7.1(b)).

7.2.2.2 MIROC-ESM-CHEM

MIROC-ESM-CHEM (Watanabe et al. [2011]) is an Earth System Model cooperatively developed by the University of Tokyo, the National Institute for Environmental Studies (NIES), and the Japan Agency for Marine-Earth Science and Technology (JAMSTEC). MIROC contains components for the atmosphere, oceans, aerosols, sea-ice, and land surface, as well as terrestrial and ocean biogeochemistry and atmospheric chemistry. The atmospheric component utilises a spectral dynamical core run at T42

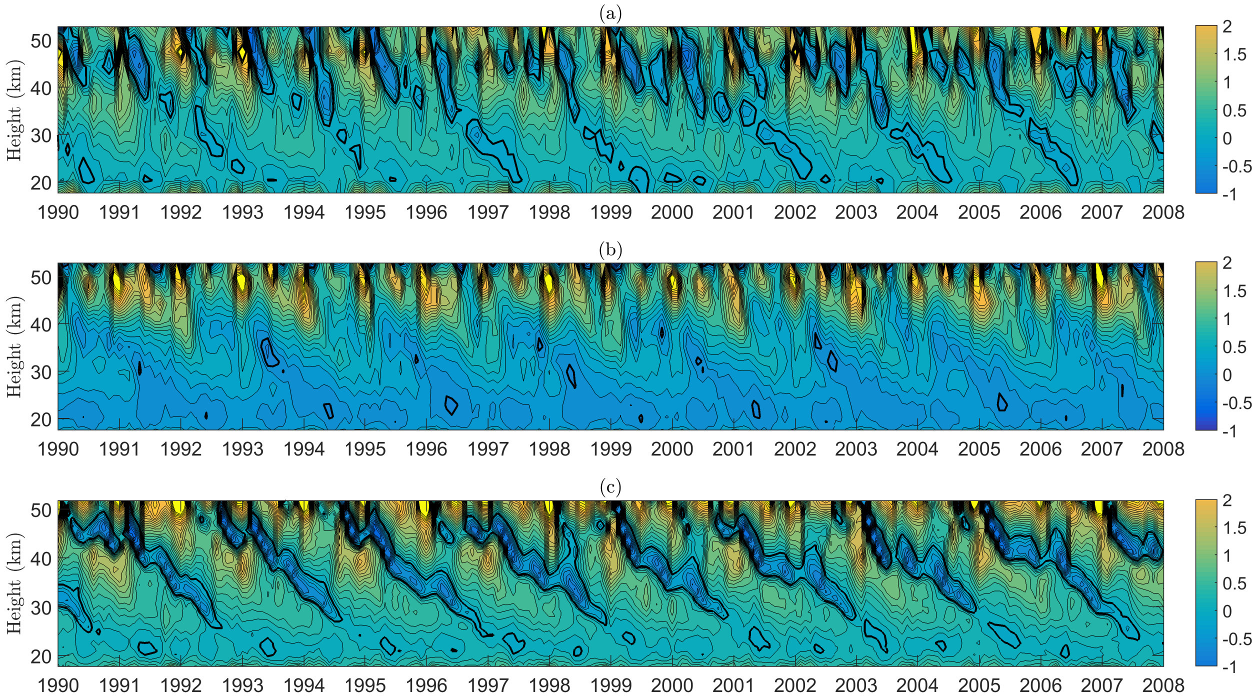

Figure 7.2: Contour plots of the residual vertical velocity $\overline{w}^*$ as defined in the Transformed Eulerian Mean (TEM) framework (refer to text for details). (a) ERA-Interim, (b) MOHC, (c) MIROC. The contour interval is $0.15\,\mathrm{mm\,s^{-1}}$, and the zero wind line is highlighted by a bold contour.

horizontal resolution (approximately 2.8 degrees in latitude and longitude), with 80 vertical levels from the surface to 80km including a fine resolution of 680m in the lower stratosphere. The piControl run was simulated for 250 years (1850–2099) and produced a realistic QBO (Figure. 7.1(c)). The oscillation was forced via a combination of explicitly resolved waves and parameterised non-orographic gravity wave drag, the latter of which was tuned empirically to accurately reflect the observed QBO (Watanabe et al. [2008]).

7.2.3 Residual circulation

The strength of tropical upwelling was diagnosed in each model using the Transformed Eulerian Mean (TEM) formulation (Andrews and McIntyre [1976a]), which approxi-

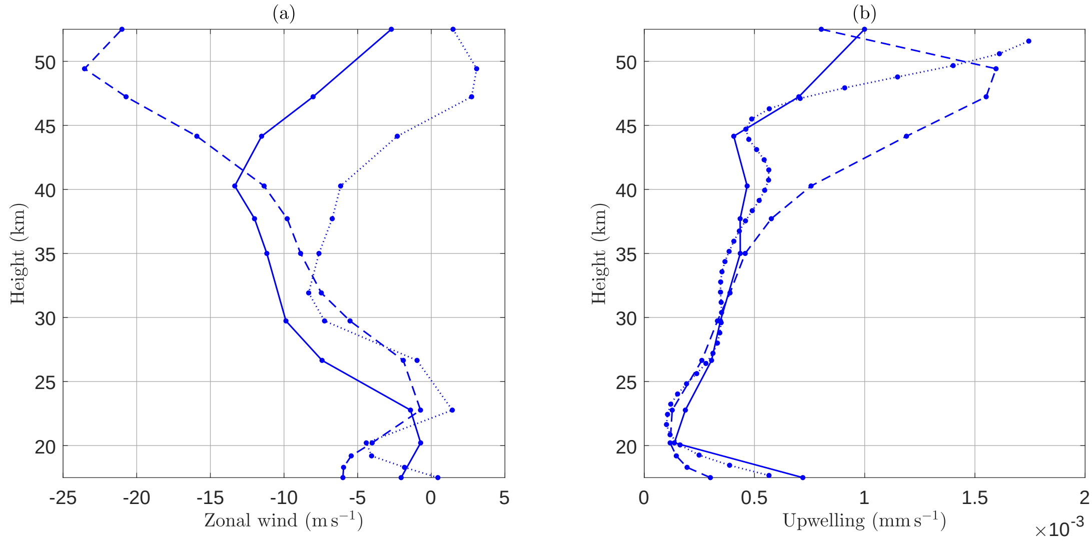

Figure 7.3: Profiles of (a) mean zonal winds and (b) mean residual upwelling in the stratosphere. Straight, dashed, and dotted lines are from ERA, MOHC, and MIROC respectively.

mates the Lagrangian-mean circulation under time-averaged conditions. Within this framework the mean residual vertical velocity $\overline{w}^*$ can be calculated as:

$$\overline{w}^* = \overline{w} + \frac{1}{a\cos\phi}\frac{\partial}{\partial\phi}\left[\cos\phi\frac{\overline{v'\theta'}}{\overline{\theta}_z}\right] \tag{7.2.2}$$

(Andrews et al. [1987]; see also Seviour et al. [2012], Osprey et al. [2013], Kawatani et al. [2011]). Here over-bars represent zonal averages, primes represent deviations from the zonal average, and a, z, ϕ, v, w, θ represent the radius of the Earth, height in log-pressure coordinates, latitude, meridional wind velocity, vertical wind velocity, and potential temperature respectively.

For the ERA data set, values of $\overline{w}^*$ were available only over the range 1979–2010. Hence, whenever comparisons are made between $\bar{u}$ and $\overline{w}^*$ data the range of the $\bar{u}$ data was restricted to this subset as well. When only zonal wind data was required in the analysis, the full range of the ERA zonal wind data set was used (September 1957– August 2016). For the MOHC and MIROC models, however, values of $\overline{w}^*$ were available over the entire span of the zonal wind data sets.

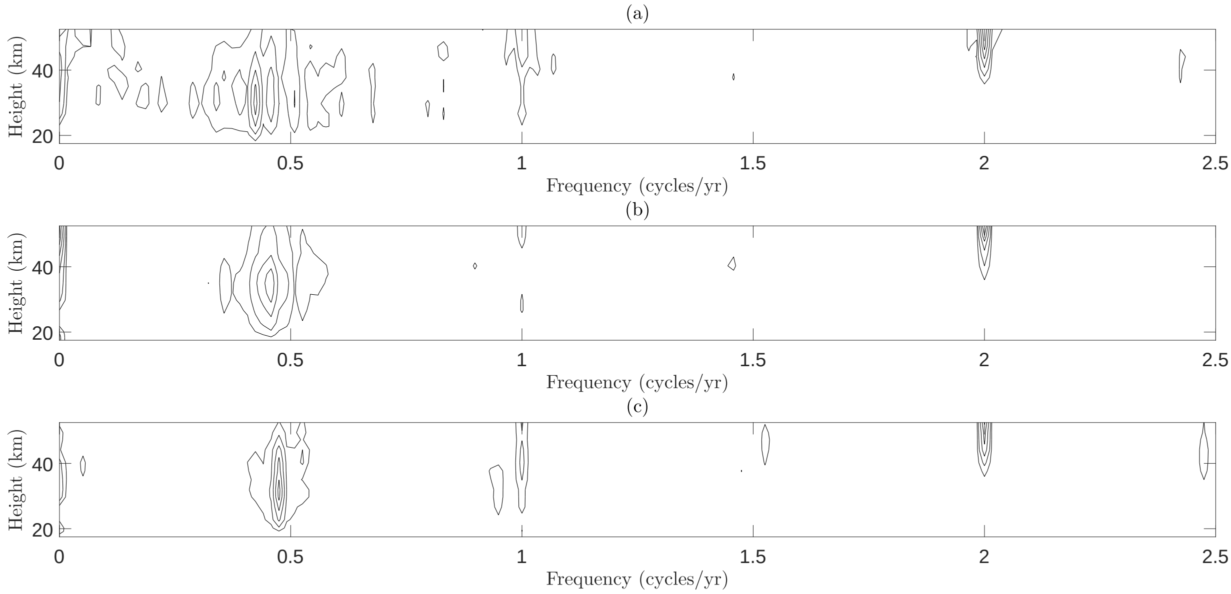

Figure 7.4: Contour maps of the Fourier spectra of zonal-mean zonal winds $\bar{u}$ across the whole stratosphere: (a) ERA, (b) MOHC, (c) MIROC. Contours are drawn at Fourier amplitudes of 2, 5, 10, 15, 20, and 30 $\mathrm{m\,s^{-1}}$ respectively.

Sample height-time contours of $\overline{w}^*$ are displayed in Figure 7.2. Bold contours represent zero vertical wind lines. In all three data sets we see that there is a general upwelling of air in the equatorial stratosphere. Areas of downwelling are associated with enhanced westerly wind shear, due to the onset of quasi-biennial or semi-annual westerly winds in the lower-mid and upper stratosphere respectively. There is a clear annual cycle in the strength of upwelling in the lowermost stratosphere in the ERA data; this is present but much weaker in the GCM data sets.

Figure 7.3 shows climatological mean height profiles of zonal wind and upwelling for the three data sets. Around the tropopause the MOHC and MIROC zonal winds have easterly and westerly biases with respect to ERA winds (Figure 7.3(a)). Throughout the QBO range (roughly 20–40 km) both models display a westerly bias relative to ERA. In the upper stratosphere the MIROC winds retain their westerly bias, while MOHC winds decelerate strongly above 40 km resulting in a strong easterly bias at the stratopause. For example, mean zonal winds at 52 km (1 hPa) are -21.3 $\mathrm{m\,s^{-1}}$ and 1.5 $\mathrm{m\,s^{-1}}$ in MOHC and MIROC respectively, compared to -4.0 $\mathrm{m\,s^{-1}}$

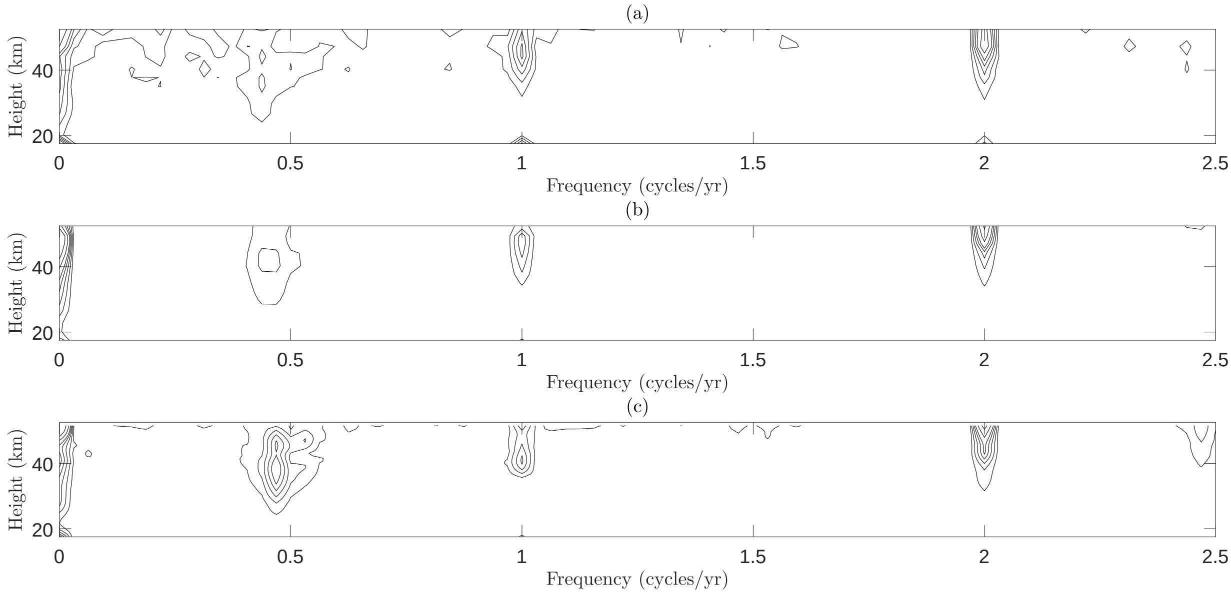

Figure 7.5: Contour maps of the Fourier spectra of residual vertical upwelling $\overline{w}^*$ across the whole stratosphere: (a) ERA, (b) MOHC, (c) MIROC. Contours are drawn at Fourier amplitudes of 0.1, 0.2, 0.3, 0.4, 0.5, 0.7 and 1.0 mm s^{-1} respectively.

in the ERA data.

In contrast, the mean residual circulation in both models (Figure 7.3(b)) approximate the mean upwelling in ERA very well from the tropopause up to 35 km. Above this level, the MOHC upwelling develops a significant positive bias up to the stratopause. The MIROC winds track the ERA mean up to 45 km, before developing a similar positive bias.

Spectral properties of the zonal wind are revealed in Figure 7.4, which portrays contour maps of the Fourier spectra calculated at each vertical level of the $\bar{u}$ data. The plots are similar to ones found in Pascoe et al. [2005]. There are clear peaks at quasi-biennial, annual, and semi-annual frequencies in all three data sets. Quasi-biennial peaks are quite broad, reflecting the non-stationary nature of the QBO due to its cycle to cycle variation. The peaks in the $\bar{u}$ spectra give QBO periods of 28.3, 26.2 and 25.3 months in the ERA, MOHC and MIROC cases respectively. Corresponding QBO amplitude maxima are 17.8, 19.1 and 22.2 m s^{-1}. The annual cycle at the stratopause is relatively weak in both models, with spectral amplitudes of 3.9 and 5.6 m s^{-1} in

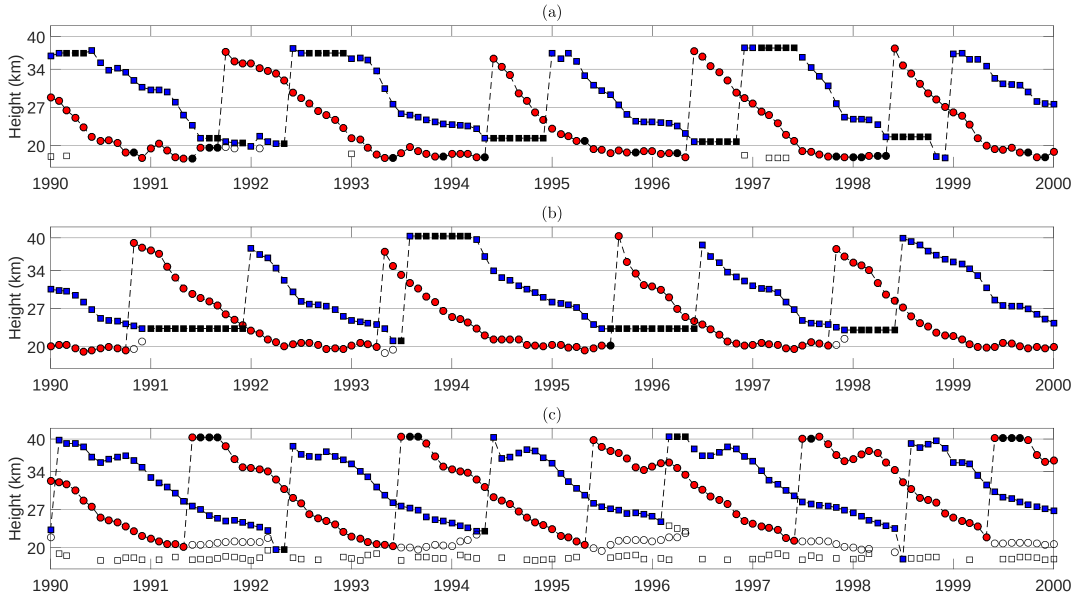

Figure 7.6: Zero wind heights in the stratosphere in (a) ERA, (b) MOHC, and (c) MIROC. Circles represent westerly onset heights, i.e. $\bar{u} > 0$ and $\bar{u} < 0$ just above and below the height point respectively. Similarly, squares represent easterly onset heights. The dotted lines joining up sets of red circles and blue squares characterise the descent of QBO westerly and easterly shear zones respectively. The black circles and squares are heights that have been artificially added as necessary in order to maintain continuity of the lines.

MOHC and MIROC respectively, compared to $9.6\,\mathrm{m\,s^{-1}}$ in ERA. The semi-annual signal at the stratopause is also relatively weak in MIROC, with a peak amplitude of $20.7\,\mathrm{m\,s^{-1}}$ compared to 25.3 and $26.8\,\mathrm{m\,s^{-1}}$ in ERA and MOHC.

Figure 7.5 plots the corresponding spectral properties of the residual circulation. Again, there are clear peaks corresponding to quasi-biennial, annual and semi-annual cycles. The quasi-biennial signal in $\overline{w}^*$ is too strong in MIROC (7.5(c)), with a peak amplitude of $0.6\,\mathrm{mm\,s^{-1}}$ compared to $0.2\,\mathrm{mm\,s^{-1}}$ in both ERA and MOHC. The annual and semi-annual signals in ERA have peaks in both the upper and lowermost stratosphere, with the latter peaks having amplitudes of 0.4 and $0.2\,\mathrm{mm\,s^{-1}}$ respectively. In contrast, both GCM data sets display annual and semi-annual peaks in the upper stratosphere only.

7.3 Results

7.3.1 Seasonal synchronisation of the QBO

7.3.1.1 Zero-wind line tracking

As discussed in Chapter 6, the evolution of the QBO phase can be characterised by tracking the locations of the zero wind lines in the stratospheric zonal winds. Figure 7.6 shows the location of zero wind points over the height range of 16–42 km. Points marked as circles and squares represent heights of westerly and easterly zero winds respectively. We used a simple algorithm to trace the location of the QBO westerly and easterly zero wind lines $z_w(t)$ and $z_e(t)$. These have been drawn in as dashed lines in the figure, and the corresponding markers have been shaded red and blue for the westerly and easterly zero wind lines respectively. The lines clearly track the descent of the QBO shear zones.

If no zero line was found at a given time point, the location of the zero line was set to that of the previous time point; this requirement was imposed in order to maintain the continuity of the zero wind line over time. These artificially added points are colored black in Figure 7.6 and are ignored in subsequent analysis; note that they do *not* represent QBO stalling events.

7.3.1.2 QBO descent rate and the annual cycle

By measuring the slope of the westerly and easterly QBO zero wind lines at each time point, we get estimates of the descent rates of the westerly and easterly QBO shear zones. To get a sense of the relationship between QBO descent rate and the annual cycle, we partition the descent rates by month; these are presented in Figures 7.7, 7.8, and 7.9 for ERA, MOHC, and MIROC data respectively. The zero wind lines are segmented by height, to compare descent rates in the upper, middle, and lower ranges of the QBO. In all three data sets, we see that there is a clear seasonal

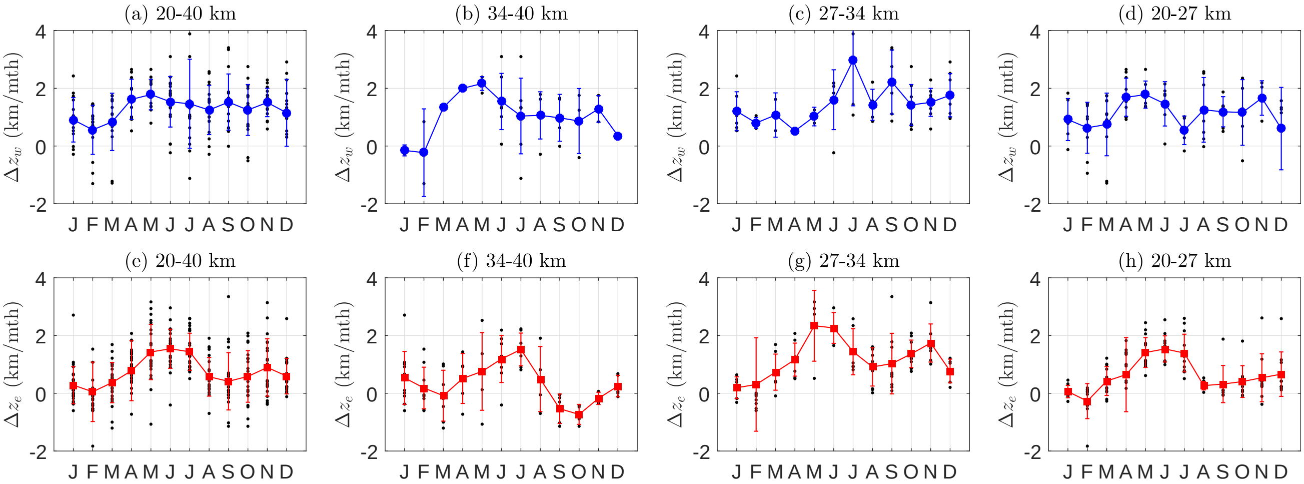

Figure 7.7: Scatter plots of QBO descent rate by month in the ERA data set between 1979–2010. The data is segmented into height ranges that represent, from left to right, the whole, upper, middle, and lower ranges of the QBO respectively. The top row [Figs.(a)-(d)] and bottom row [Figs.(e)-(h)] show descent rates of the westerly and easterly zero wind lines respectively. The mean descent rate in each month is marked as a blue circle or a red square (in respective westerly and easterly cases); these are then connected by straight lines. Corresponding error bars measure the standard deviation of the descent rate in each month.

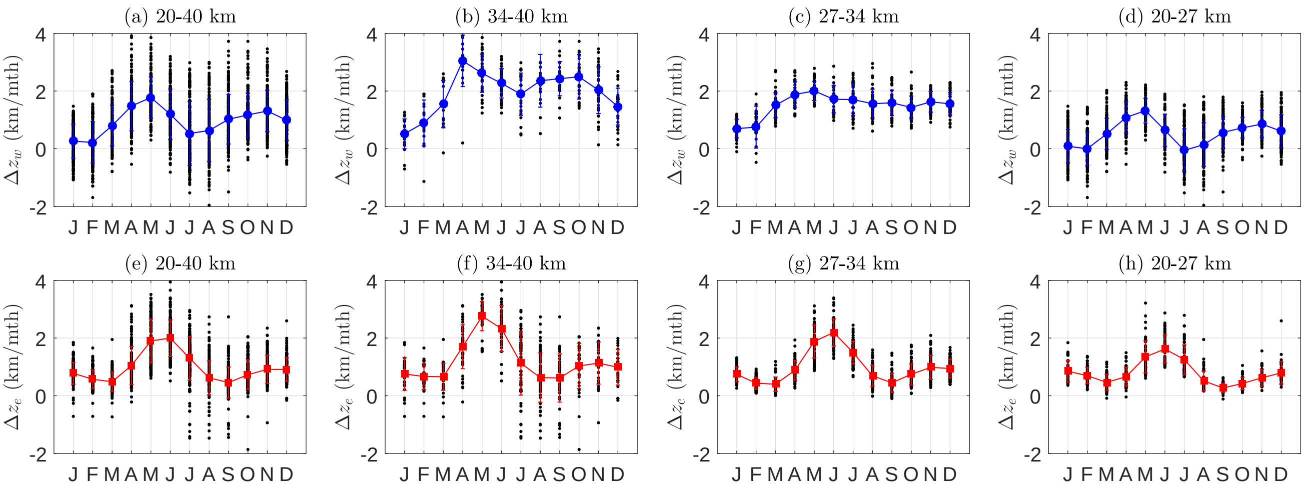

Figure 7.8: Scatter plots of QBO descent rate by month, in the MOHC data set between 1860–2099. Refer to Figure 7.7 for details.

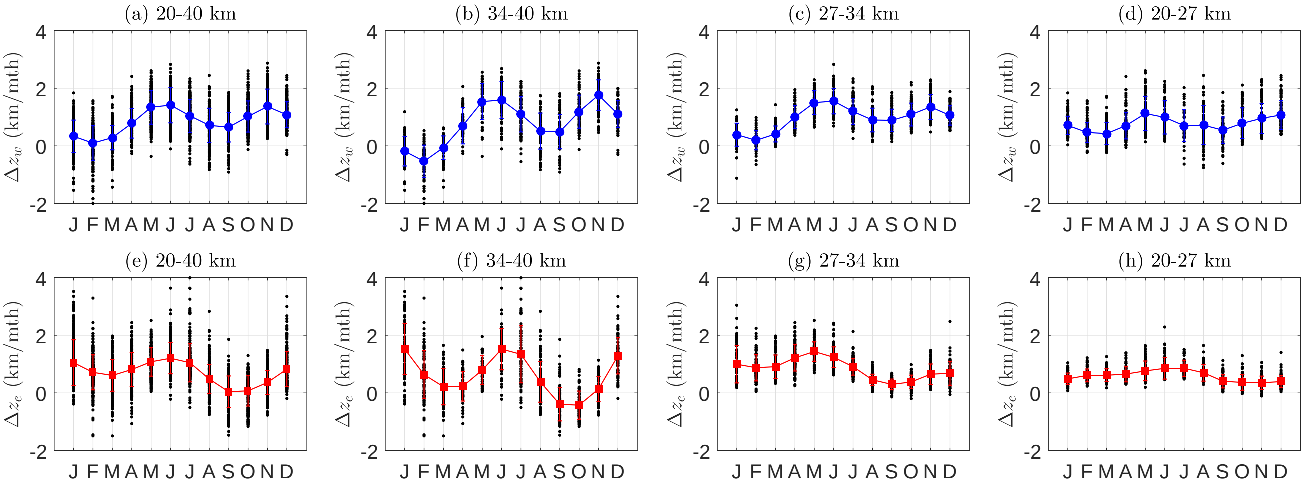

Figure 7.9: Scatter plots of QBO descent rate by month, in the MIROC data set between 1850–2099. Refer to Figure 7.7 for details.

tendency in the QBO descent rates, which consists of a combination of annual and semi-annual variability at all levels. In general, the descent rate seems to be highest in the solstice months, and weakest during the equinoxes.

7.3.1.3 QBO descent rate and upwelling strength

We now correlate the descent rate of the QBO with the strength of the residual circulation by moving along a zero wind line and measuring both quantities at each corresponding height. Results are displayed in Figures 7.10, 7.11 and 7.12. In all three figures we see that there is generally a negative correlation between vertical upwelling and the descent rate. To quantify this relationship, we calculate the Spearman rank correlation coefficient r_S (Zar [1972]) between the upwelling and the descent rate in each case. The Spearman coefficient is a measure of the monotonic relationship between variables; values of $r_S = 1, -1$, and 0 correspond to perfect positive monotonic, perfect negative monotonic, and no monotonic relationships respectively. Table 7.1 lists the values of the Spearman r_S in the different height ranges considered in the three data sets. A corresponding p-value for each correlation coefficient has been calculated, based on a null hypothesis of there being no monotonic relationship between

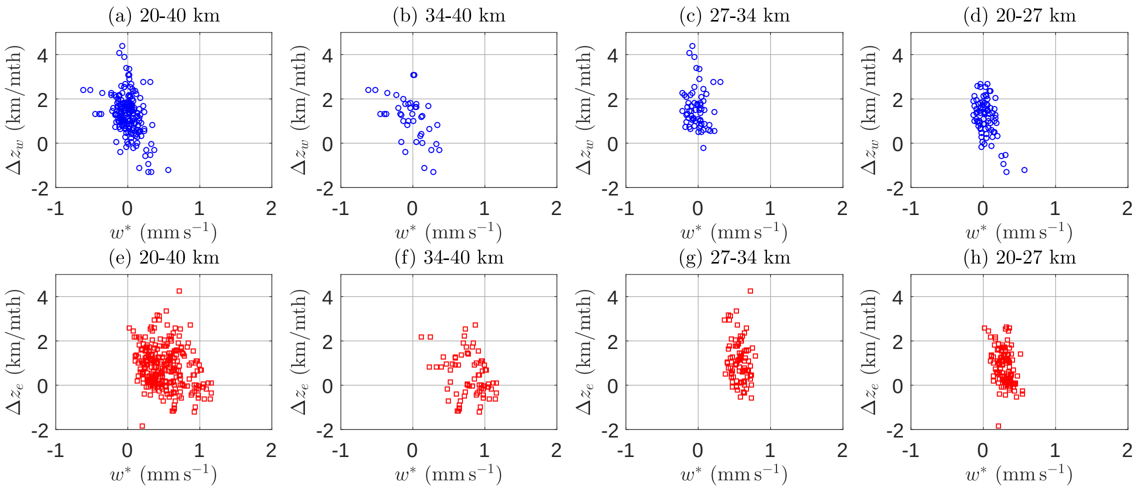

Figure 7.10: Scatter plots of QBO descent rate in the ERA data set between 1979–2010. The data is segmented into height ranges that represent, from left to right, the whole, upper, middle, and lower ranges of the QBO respectively. Figs.(a)-(d) (blue circles) and Figs.(e)-(f) (red squares) are results for westerly and easterly zero wind lines respectively.

upwelling and the QBO descent rate in the given height range (i.e. $\rho = 0$, where ρ is the population rank correlation coefficient). The p-value calculates the probability of occurrence of a sample correlation as or more extreme than the measured sample, under the null hypothesis. Small values of p, therefore, imply a greater probability that the null hypothesis is false.

From Table 7.1 we see that in all three data sets there is a negative correlation between descent rate and upwelling strength, with the exception of the easterly zero line in MOHC between 27–34 km. The corresponding p-values are generally less than 5%; indeed, most are so small as to be approximately 0%. Exceptions are the ERA data between 27–34 km (shaded in Table 7.1). The overall picture, then, gives us strong confidence that the null hypothesis is false, and that there is a monotonic and generally negative correlation between the QBO descent rate and upwelling.

Comparing westerly and easterly descent in the ERA data, we see that the strength of the negative correlation is large in the upper and lower QBO range, and weak in the middle range. In the upper QBO range the westerly correlation is stronger than

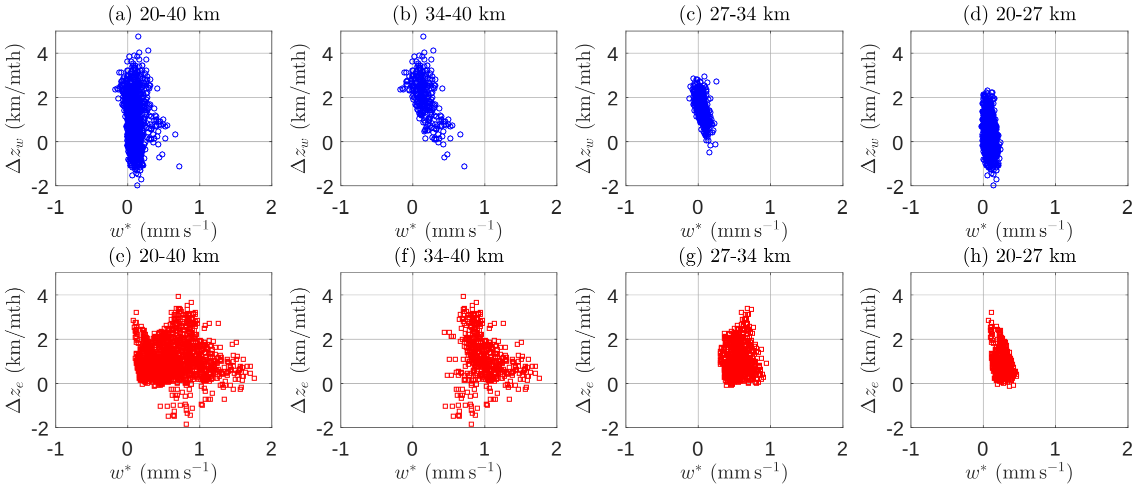

Figure 7.11: Scatter plots of QBO descent rate in the MOHC data set between 1860–2099. The notation is the same as in Fig.7.10.

		ERA		MOHC		MIROC	
Height (km)	Onset	r_S	p value	r_S	p value	r_S	p value
20-40	Westerly	-0.329	0.0%	-0.311	0.0%	-0.217	0.00%
20-40	Easterly	-0.200	0.1%	0.135	0.0%	-0.438	0.00%
34-40	Westerly	-0.537	0.0%	-0.540	0.0%	-0.204	0.00%
34-40	Easterly	-0.237	4.3%	-0.304	0.0%	-0.269	0.00%
27-34	Westerly	-0.153	23.3%	-0.604	0.0%	-0.316	0.00%
27-34	Easterly	-0.158	15.0%	0.171	0.0%	-0.540	0.00%
20-27	Westerly	-0.332	0.2%	-0.308	0.0%	-0.162	0.00%
20-27	Easterly	-0.408	0.0%	-0.122	0.3%	-0.494	0.00%

Table 7.1: Statistics of the correlation of $\bar{w}^*$ and the descent rate Δz following the westerly and easterly zero wind lines of the QBO in ERA, MOHC and MIROC. The Spearman rank correlation coefficient r_S measures the strength of the monotonic relationship between $\bar{w}^*$ and Δz. The significance of correlation is measured by the p value, based on a null hypothesis of no monotonic relationship between the variables. Smaller values of p indicate an increasing likelihood of a monotonic relationship between the variables. p values greater than 5% - indicating insufficient evidence to reject the null hypothesis at 5% level - have been shaded in gray.

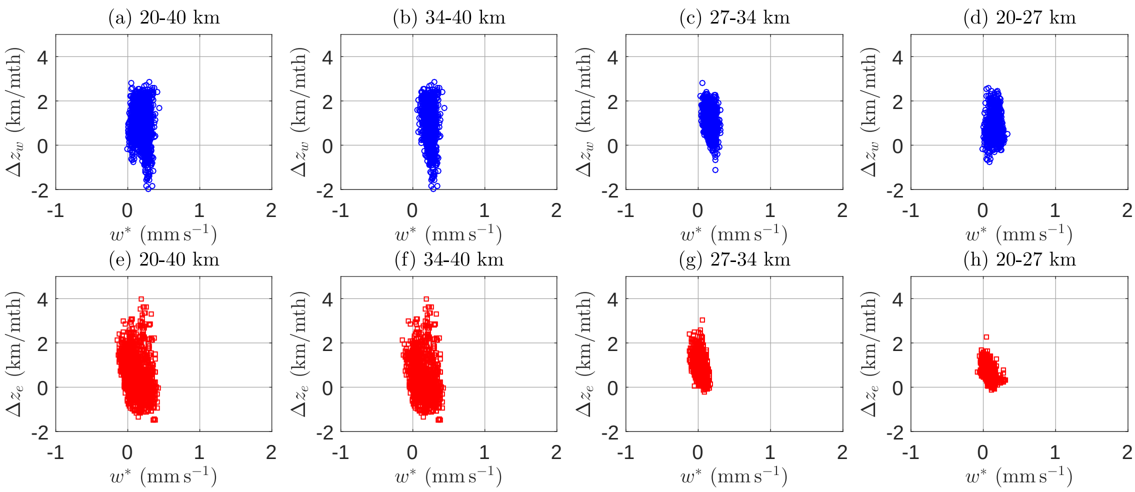

Figure 7.12: Scatter plots of QBO descent rate in the MIROC data set between 1850–2099. The notation is the same as in Fig.7.10.

the easterly correlation, and vice versa in the lower range.

The behaviour of westerlies in both climate models are quite similar. In MOHC the correlation between westerly descent and upwelling is strong in the upper range, peaks in the middle range, and weakens in the lower range. A similar pattern of westerly descent is seen in MIROC, although the strength of the correlations is weaker.

The strength of the negative correlation for easterly descent in MIROC is similar to ERA in the upper and lower ranges, but is too strong in the mid-range. In the MOHC data, however, the easterly correlation in the middle stratosphere is weakly *positive*, which is inconsistent with the other two data sets and does not fit our intuition of the relationship between QBO descent and upwelling. The easterly upper and lower range correlations are consistent with the ERA values, although the easterly correlation in the lower range is relatively weak.

7.3.1.4 Evolution of the QBO period

We estimate the period of each QBO cycle by measuring the time between successive crossings of the westerly zero wind line at 28 km. The choice of height level is somewhat arbitrary, but we have found the following results to be consistent at any height

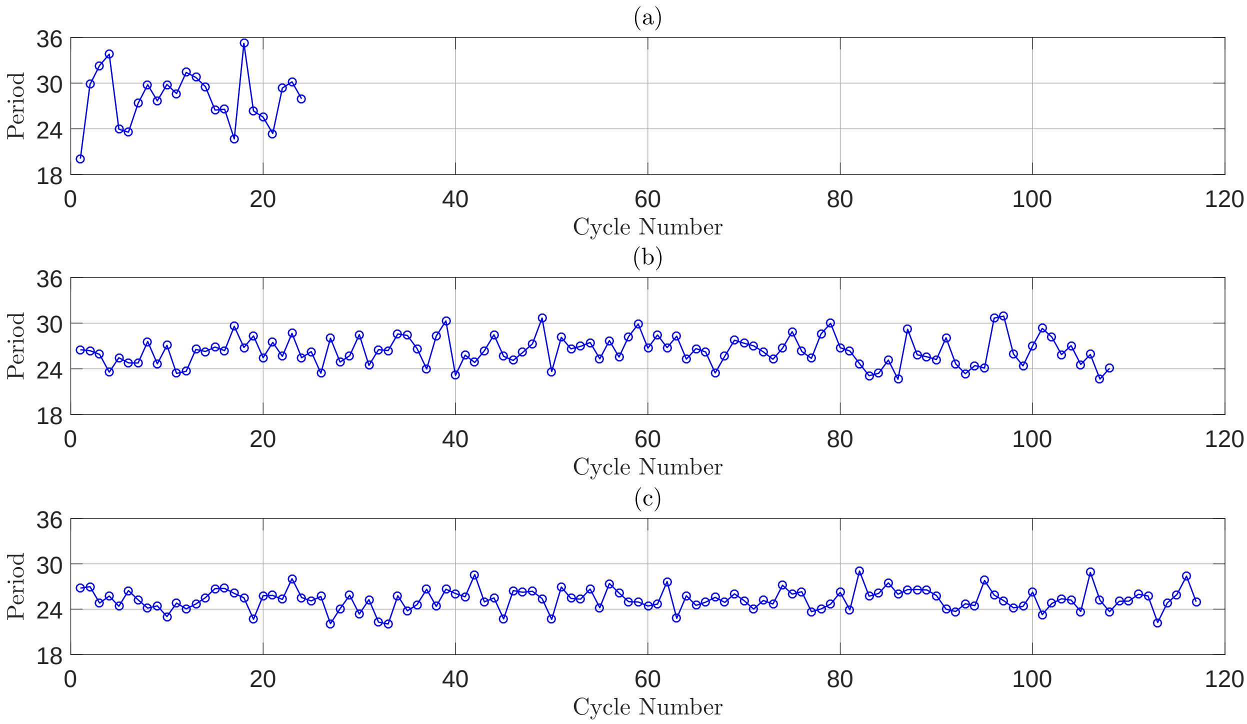

Figure 7.13: Evolution of QBO periods in (a) ERA, (b) MOHC, and (c) MIROC data. Periods are measured in months, and are defined as the time between successive crossings of the westerly zero wind line at 28 km.

level between 24–29 km. The evolution of the QBO periods derived in this manner is presented in Figure 7.13. We have kept the abscissa the same in each of the subplots, in order to highlight the relative paucity of complete QBO cycles we have observed in the atmosphere (24 cycles in approximately 60 years; see Figure 7.13(a)). The climate models, having been run for over 200 years each, give a better impression of the dynamics of the QBO period over a longer timescale. However, the periods tend to cluster within a band between 23 and 30 months, and hence fail to reflect the full range of variability of QBO periods observed in the reanalysis data.

Histograms of the QBO period are presented in Figure 7.14. The QBO in ERA has a mean period of 28 months, with a standard deviation of 3.6 months. There is a prominent modal peak at 30 months, with a weaker peak at 26 months. The distribution has a fairly large variance, with cycle lengths as low as 20 months and as high as 35 months. In contrast, the set of MOHC QBOs have a mean period of 26.3

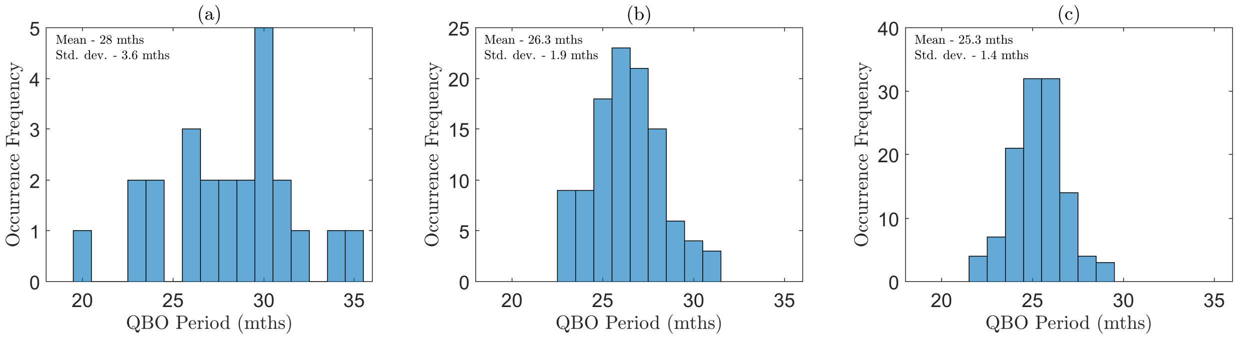

Figure 7.14: Histograms of QBO period in (a) ERA, (b) MOHC, and (c) MIROC data. The bins used have a uniform width of one month.

months and a standard deviation of 1.9 months; corresponding values in MIROC are 25.3 and 1.4 months respectively. The mean period in both models is a little short compared to observations, and does not display the same range of variability as seen in the reanalysis data, even over a longer period.

It was noticed in Chapter 3 that the QBO in the Holton-Lindzen model tended to have periods that added to multiples of 12 as a result of the interaction with the annual cycle in upwelling. In order to test whether this is the case in the reanalysis and climate model data, we computed the vector of cumulative sums **C** of the QBO periods, for which the n^{th} entry is defined as $C_n = \sum_{j=1}^{n} p_j$. Here p_j is the period of the j^{th} QBO cycle, and n ranges from 1 to the total number of QBO periods in the data set.

We then calculate the vector of remainders $R_n \equiv C_n \pmod{12}$, which is the set of remainders when each cumulative sum C_n is divided by 12. If successive sets of QBO periods tend to add to multiples of 12, we would expect a peak to form in the histogram of R_n as calculated over the whole data set. For example, consider the set of periods $p_n = \{17, 22, 26, 29, 32, 23\}$, which is made up a single period of length 17, followed by a 2-cycle of length 48 and a 3-cycle of length 84. The corresponding set of remainders is $R_n = \{5, 3, 5, 10, 6, 5\}$; the histogram of R_n has a peak at $R_n = 5$ due to the 2-cycle and the 3-cycle, thus reflecting the influence of the annual cycle on

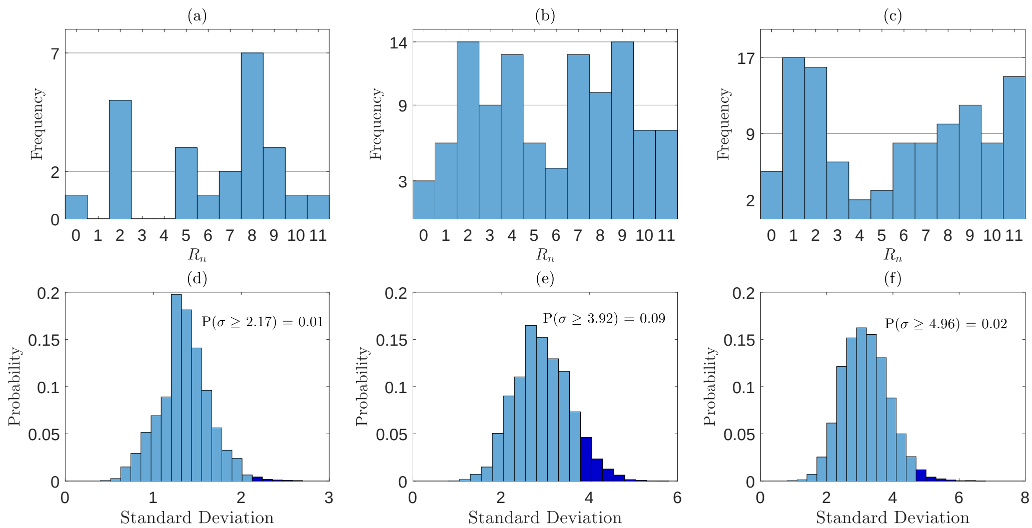

Figure 7.15: (a)-(c): Histograms of $R_n \equiv C_n \pmod{12}$, where $C_n = \sum_{i=1}^{n} p_i$ is the cumulative sum of QBO periods, as measured in ERA, MOHC, and MIROC data respectively. Horizontal ordinate lines are drawn at the minimum, mean and maximum bin heights of each histogram. (d)-(f): Corresponding derived probability distributions, based on a null hypothesis that the QBO period is normally distributed. The darkened bins correspond to the probability under the null hypothesis of producing a sample with a bin height and standard deviation that is as or more extreme as the measured value. Refer to text for details.

the QBO periods.

We note that the histograms of R_n, so constructed, are simply translations of the usual 'QBO onset month' histograms commonly used to depict seasonal synchronization of the QBO (e.g. Figure 1.4, or Figure 2 of Baldwin et al. [2001]), if we associate bin 0 with the onset month of the first QBO cycle and map the other months accordingly.

Figure 7.15(a)–(c) show the histograms of R_n for ERA, MOHC and MIROC. There are strong peaks and troughs in the bin heights of all three histograms, consistent with the expectation that the QBO evolution is synchronised to the 12-month annual cycle. To get a measure of spread, we calculate the standard deviations of the bin heights in the three cases; these are $\sigma = 2.17$, 3.92, and 4.96 respectively. Note that these are standard deviations of bin heights, which are not the same as the standard deviations of the QBO periods calculated earlier.

In order to test the statistical significance of the spread in bin heights in each of the histograms 7.15(a)–(c), we generated 10,000 sets of sample QBO periods. Each sample set was generated by repeatedly drawing from a normal distribution with mean and standard deviation given by the mean and standard deviation of the observed QBO periods in the reanalysis/model data. For example, $(\mu_{ERA}, \sigma_{ERA}) = (28, 3.6)$, as noted in the second paragraph of this section. The number of periods drawn for each sample was the same as the number of full QBO cycles observed in the data. For each of the 10,000 sets, corresponding histograms of the remainders R_n were produced, and the standard deviation of the bin heights measured. This yielded sets of 10,000 standard deviation values for each of the three data sets.

Figures 7.15(d)–(f) show probability-normalised histograms of the bin height standard deviations generated as described above. These were used to calculate the probability of occurrence of any given spread of bin heights as predicted by the null hypothesis; in particular, we measured the probability of observing the bin height standard deviations found in the data sets. As noted in the figures, the probabilities of observing a bin height standard deviation equal to or greater than observed are 1%, 9% and 2% for ERA, MOHC, and MIROC QBO periods respectively . This provides strong evidence, at least in the ERA and MIROC cases, for rejecting the hypothesis that the observed cycle-to-cycle variation in the QBO periods is simply due to random fluctuations.

7.3.2 Phase synchronization of the QBO

In this section we diagnose phase synchronization between the QBO, SAO, and the annual cycle in tropical upwelling due to the Brewer-Dobson circulation (or BD for brevity). This is achieved via a combination of Extended Empirical Orthogonal Function (EEOF) analysis and analytic phase techniques, and closely follows earlier work by Read and Castrejón-Pita [2012].

7.3.2.1 EEOF analysis

EEOF analysis is a form of Principal Component Analysis, and is very similar to the Empirical Orthogonal Function (EOF) method that is commonly used to study spatial structures in climate data. For a review of both techniques, see, e.g. Hannachi et al. [2007].

In traditional EOF analysis, sets of time series, usually deriving from measurements of a scalar field at a set of m spatial points, are concatenated together to form an $(n \times m)$ data matrix $\mathbf{X}$, where n is the length of each time series. Thus, the i^{th} column of $\mathbf{X}$ is the time series corresponding to measurements at the i^{th} spatial point. The data matrix is centered by subtracting the mean of each column of the data matrix, and spatial correlations in the data are then measured by calculating the covariance matrix,

$$\mathbf{S} = \frac{1}{n-1}\mathbf{X}^{\top}\mathbf{X}. \tag{7.3.1}$$

The eigen-decomposition of $\mathbf{S}$ yields m real eigenvalues λ_i and a set of orthogonal eigenvectors $\boldsymbol{\psi}_i$, $(1 \leq i \leq m)$. The eigenvectors $\boldsymbol{\psi}_i$ have the same spatial dimensions as the data and are known as *Empirical Orthogonal Functions* (EOFs). They can be interpreted as spatial structures representing the principal modes of variability in the data. The corresponding eigenvalues give a measure of the amount of variance in the data that is explained by each EOF. The projection of the data matrix onto the k^{th} EOF yields the corresponding *Principal Component* (PC) time series, $\mathbf{p}_k$. This measures the contribution of the EOF to the total variance at each time point. Using the set of EOFs and PCs, we can then reconstruct the data matrix as $\mathbf{X} = [\mathbf{p}_1\,\mathbf{p}_2 \ldots \mathbf{p}_m][\boldsymbol{\psi}_1\,\boldsymbol{\psi}_2 \ldots \boldsymbol{\psi}_m]^{\top}$ (where we have expressed all $\mathbf{p}$'s and $\boldsymbol{\psi}$'s as column vectors).

By construction, EOF analysis deals only with spatial correlations in a data set. Extended EOF (EEOF) analysis expands upon the EOF technique by also considering *temporal* correlations in the data. This is very useful when analysing climate data that is strongly correlated across time and space, and allows for the characterisation of oscillatory phenomena such as the QBO (Fraedrich et al. [1993]). The technique works by extending each atmospheric state vector $\mathbf{x}_i = [X_{i,1}, X_{i,2}, \ldots, X_{i,m}]$, $1 \leq i \leq n$, to create an extended state vector $\mathbf{y}_i$ that adds *time-delayed* information at each spatial point, viz.

$$\mathbf{y}_i = [\underbrace{X_{i,1}, X_{i,2}, \ldots, X_{i,m}}_{Set\,1}, \underbrace{X_{i+1,1}, X_{i+1,2}, \ldots, X_{i+1,m}}_{Set\,2}, \ldots, \underbrace{X_{i+M-1,1}, X_{i+M-1,2}, \ldots, X_{i+M-1,m}}_{Set\,M}]. \tag{7.3.2}$$

Here we have concatenated M sets of adjacent-in-time state vectors from the original data matrix; M is known as the window length. As a result of this concatenation, the length of each extended vector $\mathbf{y}$ is $m \times M$, compared to the original state vectors $\mathbf{x}$ which were of length m. Further, in light of the time lag the total number of extended state vectors is correspondingly reduced by the window length: $1 \leq i \leq n - M + 1$. The extended data matrix $\mathbf{Y}$ is constructed out of the extended atmospheric state vectors, and has dimensions $(n - M + 1) \times (M \times m)$:

$$\mathbf{Y} = \begin{bmatrix} \mathbf{y}_1 \\ \mathbf{y}_2 \\ \vdots \\ \mathbf{y}_{n-M+1} \end{bmatrix}. \tag{7.3.3}$$

Using the extended data matrix we calculate the covariance matrix as usual:

$$\mathbf{S} = \frac{1}{n - M + 1} \mathbf{Y}^\top \mathbf{Y}, \tag{7.3.4}$$

and calculate the corresponding EEOFs and Principal Components as before. Due to the time-delay, each EEOF is now a spatio-temporal pattern rather than just a spatial one, as it contains correlations across both space and time. By carefully

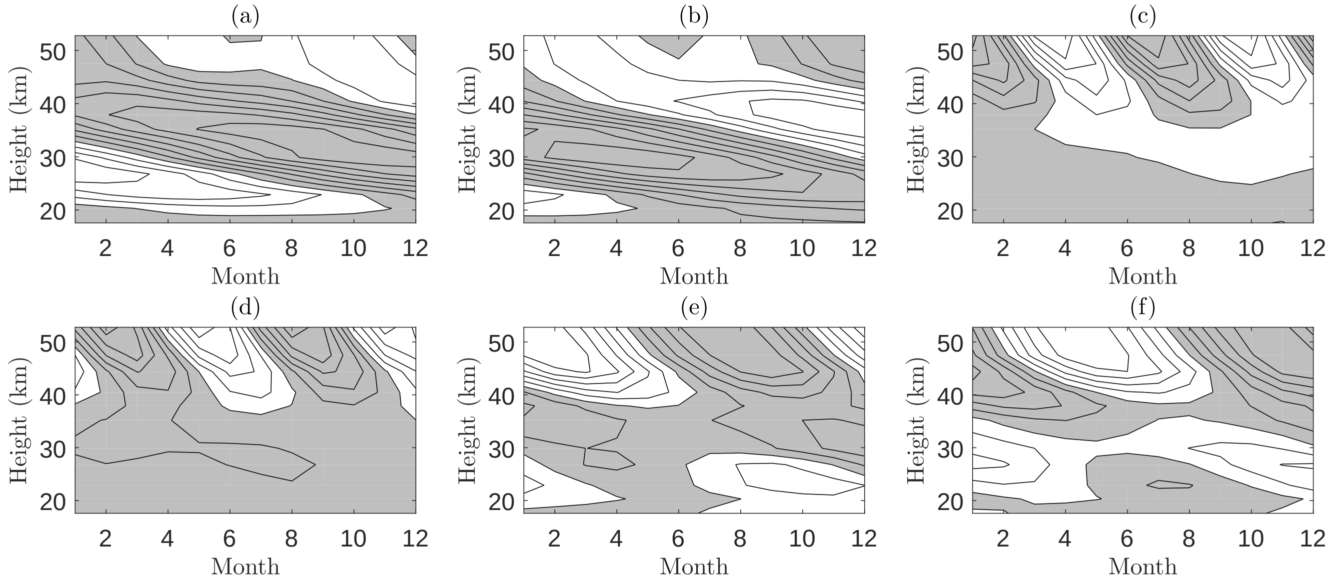

Figure 7.16: Spatio-temporal structure of the first 6 EEOFs of zonal wind data from the ERA data set. Shaded regions represent easterly winds. The percentage contribution of each EEOF to the total variance in the data is (a) 22.6%, (b) 22.5%, (c) 14.8%, (d) 14.8 %, (e) 4.5 %, and (f) 4.6% respectively.

choosing relevant sets of EEOFs, we can isolate coherent space-time structures in the data that represent different oscillatory wind systems.

Figures 7.16 and 7.17 illustrate the application of the EEOF technique to zonal wind and vertical upwelling data from the ERA data set. From the figures, the space-time structure of each EEOF becomes clear, and we can assign dynamical associations to the patterns. For example, in Figure 7.16 it is clear that EEOFs 1–2 and EEOFs 3–4 are quadrature pairs representing quasi-biennial and semi-annual oscillations in the zonal wind respectively. Similarly, in Figure 7.17 EEOFs 1–2 and 3–4 are dominated by the QBO and the BD respectively, while EEOFs 5–6 represent the SAO. The first 6 EEOFs contribute 86.8% and 75% of the total variability in the $\bar{u}$ and $\overline{w}^*$ ERA data sets respectively, as measured by the proportional contribution of the corresponding eigenvalues to the total variance.

Principal component time series for the EEOF pairs representing the zonal mean QBO, the zonal mean SAO, and the upwelling BD are presented in Figure 7.18. As

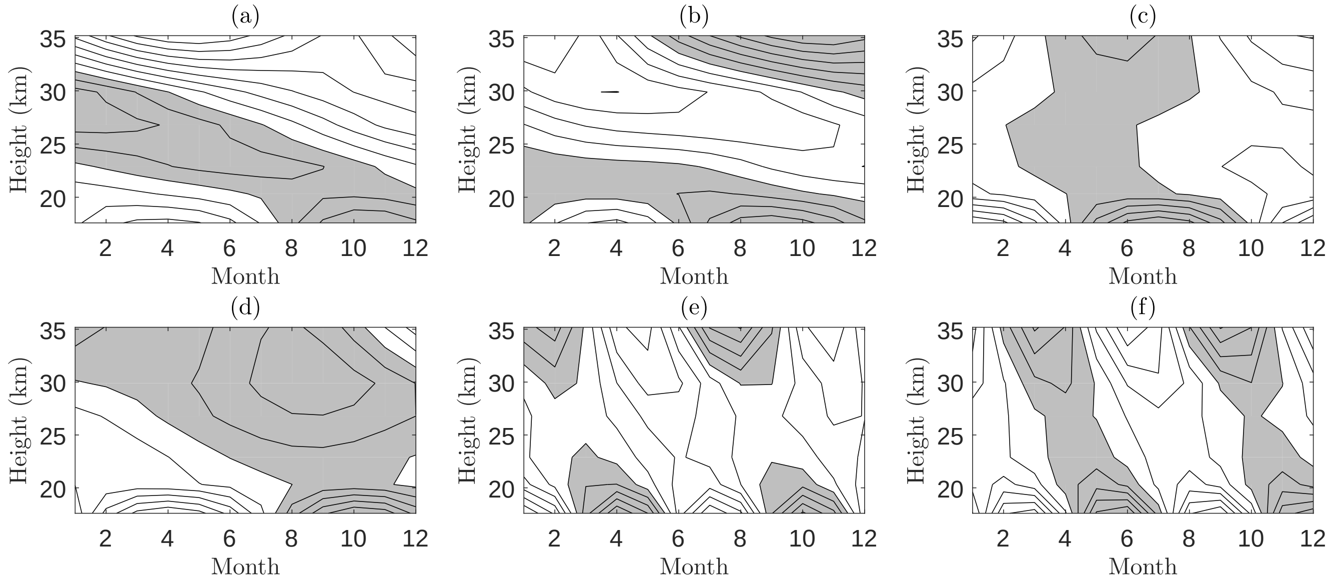

Figure 7.17: Spatio-temporal structure of the first 6 EEOFs of $\overline{w}^*$ data from the ERA data set. Vertical velocities are positive in the shaded regions. The percentage contribution of each EEOF to the total variance in the data is (a) 18.2%, (b) 17.4%, (c) 13.7%, (d) 12.8 %, (e) 6.4 %, and (f) 6.5% respectively.

noted earlier, the PC pairs are close to being in quadrature with each other, reflecting the fact that they represent coherent oscillations.

The EEOF and PC subsets identified in the preceding paragraphs can be combined to reconstruct the modes of variability in the data set. Results are shown in Figure 7.19, where the reconstructions are displayed together with Fourier spectra of the leading PC for each oscillation pair. There is very little cross-mixing of frequencies in the Fourier spectra; the EEOF technique has cleanly extracted the QBO, SAO, and BD structures from the data set.

Applying the EEOF technique to the MOHC and MIROC data sets revealed very similar patterns as described above. The corresponding figures for these data sets are included, for reference, in Appendices B and C respectively.

We note that the EEOF technique does not necessarily guarantee a good separation of the wind structures; it simply identifies space-time structures that maximise the variance of the data set. In some cases, therefore, it proved necessary to utilise

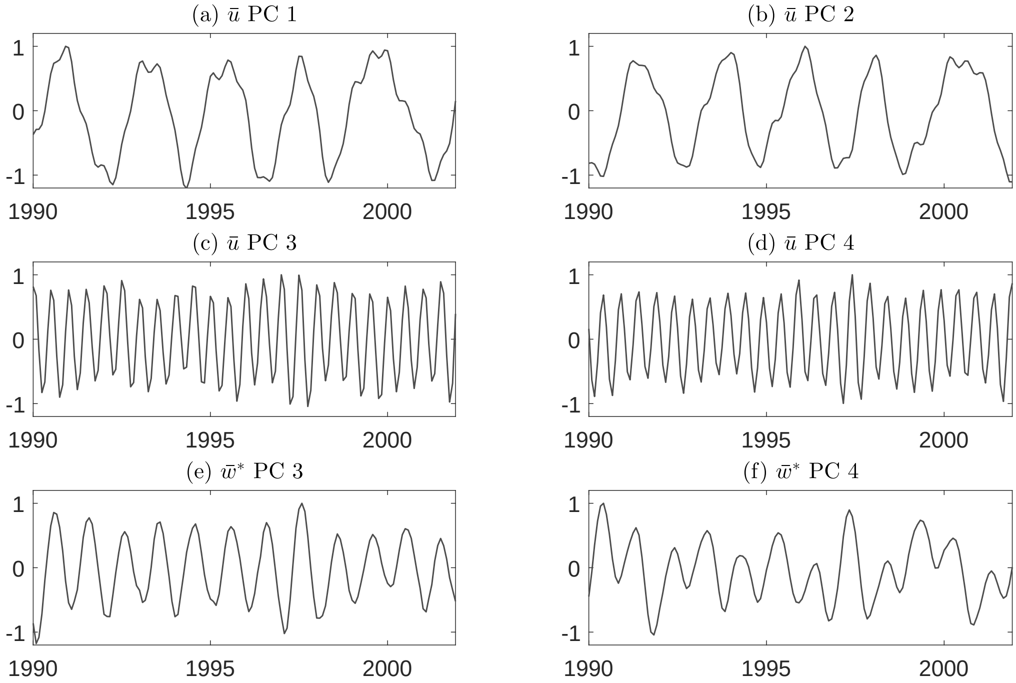

Figure 7.18: Principal Component times series representing the QBO in zonal winds [(a)-(b)], the SAO in zonal winds [(c)-(d)] and the BD (annual cycle) in vertical residual winds [(e)-(f)]. Refer to Figs. 7.16 and 7.17 for the corresponding EEOF patterns.

the known height structure of stratospheric winds to help to tease out the relevant patterns. For example, the EEOFs presented for the annual cycle in the BD were extracted by limiting the height span of the data set to the lower and mid-stratosphere (as can be seen in the height axes in Figures 7.17 and 7.19), in order to reduce the mixing of the BD signal with the QBO and SAO signals.

7.3.2.2 Phase relationships

The Principal Component time series of the QBO, SAO, and BD oscillations derived in the preceding section effectively represent the entire height-time variability of their respective oscillations in a single time series. In order to derive a phase for each oscillation, we apply a Hilbert transform to each PC, following Read and Castrejón-

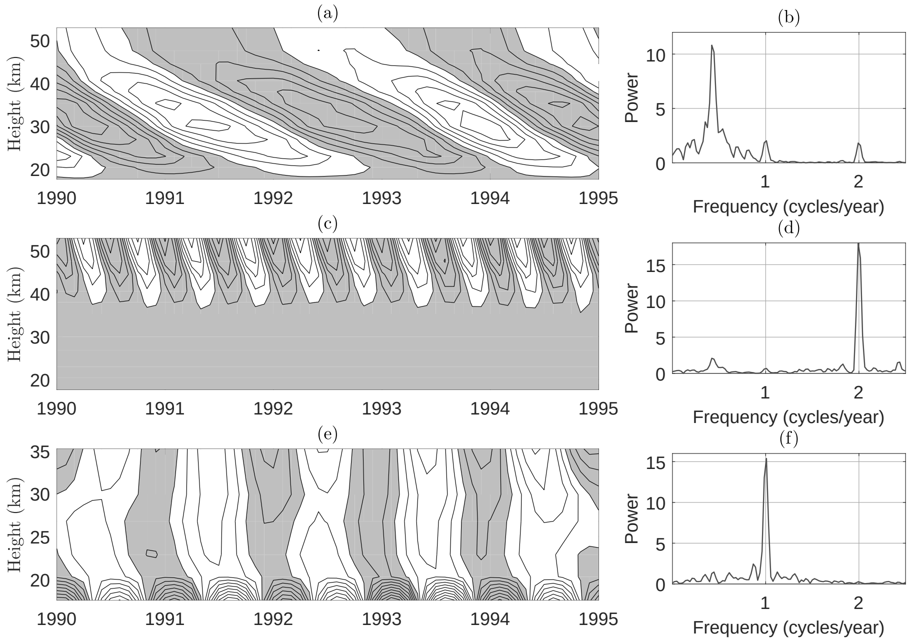

Figure 7.19: Sample reconstruction of various height-time structures in ERA: (a) QBO (EEOFs 1–2 of $\bar{u}$), (c) SAO (EEOFs 3–4 of $\bar{u}$), and (e) BD (EEOFs 3–4 of $\overline{w}^*$). Corresponding Fourier spectra are shown for: (b) PC 1 of $\bar{u}$, (d) PC 3 of $\bar{u}$, and (f) PC 3 of $\overline{w}^*$ respectively. Shaded regions represent easterly zonal winds in (a) and (c), and positive upwelling in (e).

Pita [2012]. For a given time series $p(t)$, the Hilbert transform is defined as

$$p_H(t) = \pi^{-1}\,\mathcal{P}\int_{-\infty}^{\infty} \frac{p(\tau)}{t-\tau} d\tau, \tag{7.3.5}$$

where the $\mathcal{P}$ indicates the principal value of the integral. Using the Hilbert transform we construct a complex time series $\xi(t)$ as

$$\xi(t) = p(t) + ip_H(t) = A(t)e^{i\phi(t)}; \tag{7.3.6}$$

the corresponding analytic phase $\phi(t)$ of $p(t)$ can then be recovered via

$$\phi(t) = \tan^{-1}\left[\frac{p_H(t)}{p(t)}\right]; \tag{7.3.7}$$

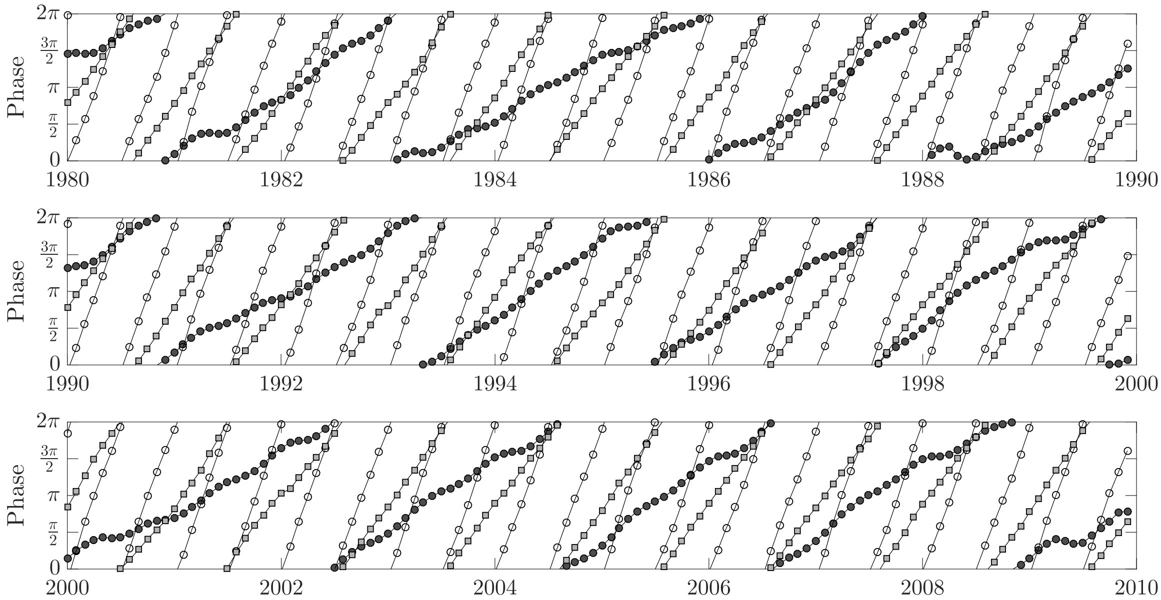

Figure 7.20: Evolution of phases in the ERA data set over the time period 1980–2010. Here dark gray circles, light gray squares, and plain circles represent phase evolution of the QBO, BD, and SAO respectively. The phases have been presented modulo 2π, so that the upper boundary of the figure effectively wraps round to the bottom boundary (akin to a flat sheet of paper that has been rolled into the shape of a spherical cylinder, with the two edges just touching).

and this characterises the phase dynamics of each EEOF. Note that the phase here is defined such that $\phi \in [0, 2\pi]$. It can be made continuous ('unwrapped') if desired, by simply accumulating the phase by 2π each time it crosses the discontinuity separating $\phi = 2\pi$ and $\phi = 0$).

Figure 7.20 displays the evolution of the phases of the QBO, SAO, and BD winds in the ERA data set from 1980–2010 as dark gray circles, light gray squares, and plain circles respectively. We note the non-uniform nature of the QBO phase propagation relative to the other two wind systems.

We would like to investigate whether the evolution of the QBO phase is in any way related to or dependent on the phases of the SAO or BD. One simple way to visualise these relationships is to create scatter plots of the phases (modulo 2π) of the different wind systems with each other. This is done for the QBO, SAO, and BD in all three data sets, and presented in Figure 7.21. We can interpret each scatter plot as a kind of 'joint probability distribution' of the two phase variables in question: we are more likely to find the two phases in areas where the points in the scatter plot are densely concentrated.

The first column of plots [(a), (d), (g)] in Figure 7.21 are scatter plots of the phase of the QBO, ϕ_{QBO}, against the phase of the SAO, ϕ_{SAO}, in ERA, MOHC, and MIROC respectively. Each plot in the column is stratified into 6 horizontal layers, reflecting the fact that the monthly sampling rate in the data is not very high compared to the frequency of the semiannual oscillation, as well as the relatively uniform propagation of the SAO phase. Along the bands there is little visual evidence of preferential concentrations of points; perhaps weakly in the MIROC data set (Figure 7.21(g)). However, the lack of high frequency sampled data may be confounding the picture, and therefore it is difficult to draw any conclusive statement about any possible QBO-SAO phase relationship from the plots other than to say that it would possibly be fairly weak.

The scatter plots of the second column, which plot the QBO and BD phases against each other, show much more structure. In all three plots there is clear evidence of diagonal bands along which a fair proportion of the points are clustered. Equally significant are the gaps between the bands, which suggest that particular phase pairings between the QBO and BD are much less likely than others. We note that in all three plots there are two distinct diagonal bands that cut the ϕ_{QBO} axis (keeping in mind the periodic boundary conditions), whereas there is only one band that cuts the ϕ_{BD} axis. This suggests that along the bands, the BD completes two phase cycles for every one phase cycle completed by the QBO. In other words, the QBO:BD frequency ratio is approximately 1:2 (or equivalently, the periods are in the ratio 2:1).

The banded structure is even clearer in the third column, which contains scatter plots of the BD vs. SAO phases. The lines are unmistakeable despite the low sampling

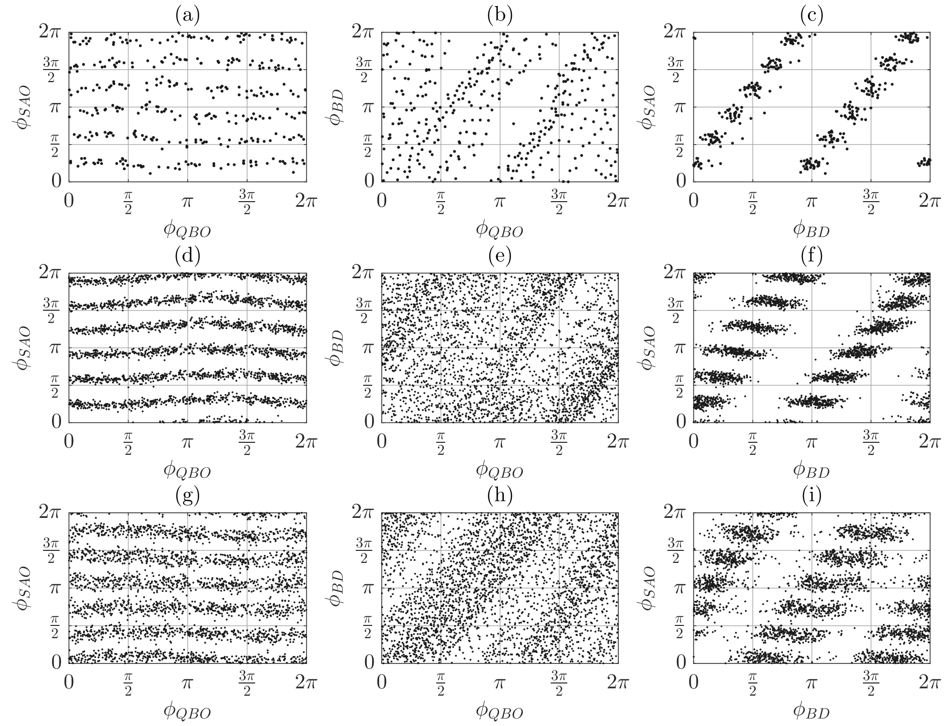

Figure 7.21: Scatter plots of the QBO, SAO, and BD phases in ERA [(a)-(c)], MOHC [(d)-(f)] and MIROC [(g)-(i)]. All phases are modulo 2π. The first column of figures [(a),(d)(g)] are scatter plots ϕ_{QBO} vs. ϕ_{SAO}; similarly, the second and third columns are scatter plots of ϕ_{QBO} vs. ϕ_{BD} and ϕ_{BD} vs. ϕ_{SAO} respectively.

frequency of the SAO, which in this case simply breaks each band into six discrete 'chunks' that all lie along the same diagonal. It is thus quite clearly the case that the BD and SAO phases are synchronized, as would be expected given the direct coupling of each to the annual cycle. As before, the frequency ratio of the BD and SAO can be gleaned from the plots by counting the number of diagonals that cut each axis; we find, unsurprisingly, that the BD:SAO period ratio is 2:1.

7.3.2.3 Phase synchronization of the QBO and BD in ERA

We now investigate a particular class of synchronization relationship known as *phase synchronization* in the context of the QBO, the SAO and the BD. This is classically considered to occur when two oscillators adjust their rhythms as a result of interaction (Pikovsky et al. [2003]). In general, two oscillators are said to be $(m : n)$ phase synchronized if their corresponding phases, ϕ_1 and ϕ_2, obey the following temporal relation:

$$\Delta\phi(t) = |m\phi_1(t) - n\phi_2(t)| < const, \tag{7.3.8}$$

where m and n are integers (e.g. Tass et al. [1998], Read and Castrejón-Pita [2012]), and the phases ϕ_1, ϕ_2 are defined on the real line. This metric allows us to measure how often the two oscillators are in a phase coherent state, and therefore how strongly coupled they are.

On average, $m : n$ synchronization between oscillators with phases ϕ_1 and ϕ_2 implies that their periods are approximately in the ratio $P_1 : P_2 = m : n$. In contrast, their frequencies are in the ratio $f_1 : f_2 = n : m$. In what follows, when we refer to $m : n$ phase locking it is helpful to remember that this refers to the ratio of the *periods*, and not the frequencies.

In Figure 7.22 the phase differences $\Delta\phi = |m\phi_{QBO} - n\phi_{BD}|$ between the QBO and BD phases in ERA data are plotted for three choices of locking ratio: $(m : n)$ = $(2 : 1)$, $(5 : 2)$, and $(3 : 1)$. These ratios were chosen to reflect QBO periods of

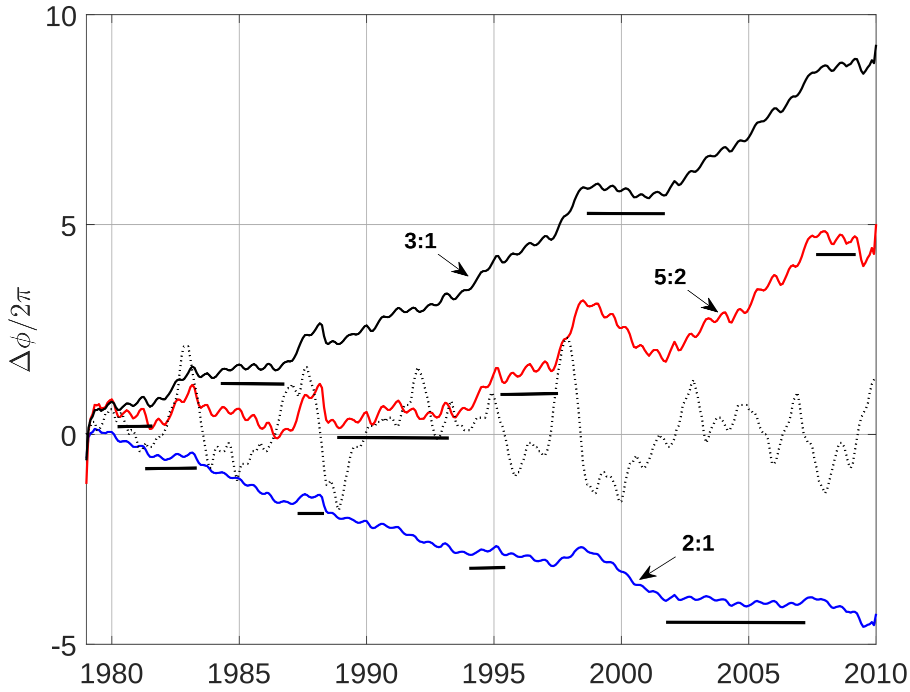

Figure 7.22: Evolution of the normalized phase difference $\Delta\phi/2\pi$ between the QBO and BD in the ERA data set. The blue, red and black lines represent tests of $m : n$ phase synchronization between the QBO and BD corresponding to $2 : 1$, $5 : 2$, and $3 : 1$ respectively (corresponding to QBO periods of approximately 24, 30 and 36 months). The bold horizontal lines highlight sections along the phase difference lines where $\Delta\phi/2\pi$ is relatively constant, indicating synchronization. The dotted line plots the Oceanic Niño Index over the same period.

around 24, 30 and 36 months respectively (assuming that the BD period is always approximately 12 months). The phase difference generally increases in the (5 : 2) and (3 : 1) cases, and decreases in the (2 : 1) case, indicating that the average QBO period is somewhere between 24 and 30 months. There are numerous plateaus in the lines, highlighted by bold lines on the plot. This is consistent with phase synchronization of the QBO and BD frequencies at particular synchronization ratios over the given time periods. Over the entire length of the observation period, the QBO phase relationship with the BD jumps erratically between different synchronization regimes, spending most time between the (2 : 1) and (5 : 2) ratios and occasionally drifting to (3 : 1). Significantly, there is never a time that the QBO is not synchronized to the BD cycle at one of these 3 ratios.

7.3.2.4 An ENSO connection?

The dotted line in Figure 7.22 plots the Oceanic Niño Index (ONI), which is one measure of intensity of the El Niño / Southern Oscillation (ENSO). The data was obtained from the website of the Climate Prediction Center of the National Oceanic and Atmospheric Administration[1]. Comparing the ONI and the QBO phase descent, we see that large ENSO events - most notably in 1982-83, 1987-88, and 1997-98 - tend to correlate with large phase slips in the phase difference $\Delta\phi$. From the phase evolution of each wind system (Figure 7.20) we note that the phase slips are due to accelerated phase propagation in the QBO; there are no obvious changes in the BD phase. This observed correlation between ENSO and the QBO phase evolution supports the theory (Geller et al. [1997], Taguchi [2010]) that strong ENSO events accelerate the descent of the QBO by increasing wave activity in the Tropics.

We note the presence in Figure 7.22 of a fairly large ENSO event in 1991-1992 that does not cohere to this pattern. The lack of a QBO phase acceleration in this instance,

[1] `http://www.cpc.ncep.noaa.gov/products/analysis_monitoring/ensostuff/ensoyears.shtml`. Accessed 03/12/2016.

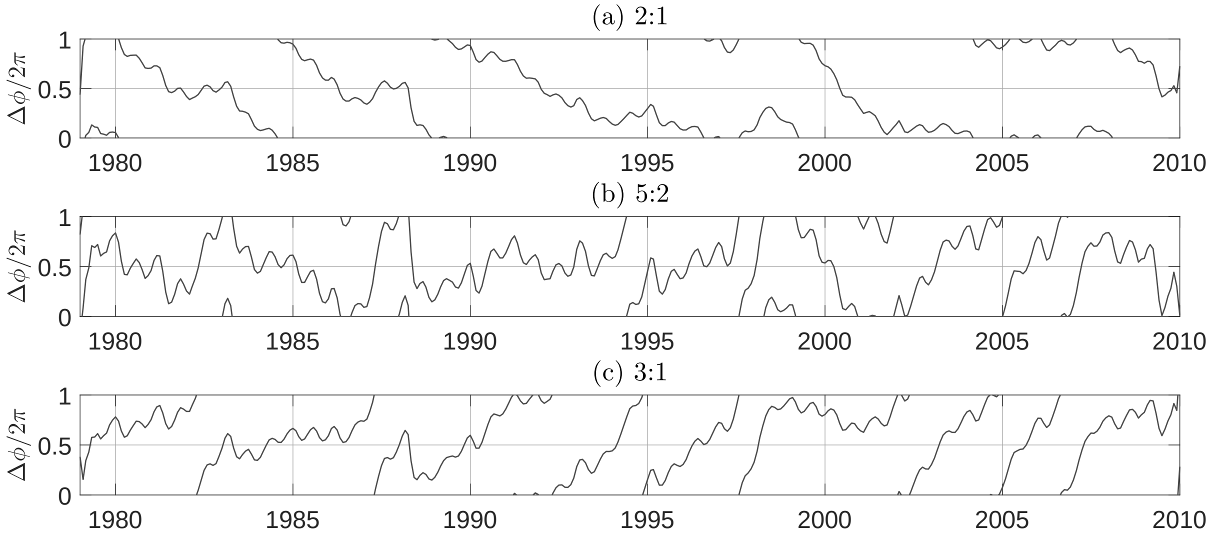

Figure 7.23: Normalized phase difference plots of the QBO and BD in ERA data, corresponding to synchronization ratios of (a) 2 : 1, (b) 5 : 2, and (c) 3 : 1 respectively. Refer to text for details.

however, maybe related to the eruption of Mount Pinatubo in June 1991. Volcanic aerosols have been shown to delay the descent of QBO shear zones (Dunkerton [1983]); thus, the effect of the increased wave activity may well have been negated by the countervailing increase in upwelling induced by volcanic aerosol heating.

7.3.2.5 Statistical significance of phase synchronization

We can visualise the phase difference curves in a different way by plotting the graphs of $[\Delta\phi \pmod{2\pi}]/2\pi$ and ignoring jumps from 1 to 0; see Figure 7.23(a)-(c). This is equivalent to wrapping each curve in Figure 7.22 around a cylinder of circumference 1, and then reshaping the cylinder into a rectangular plane by making a cut along the straight side (time axis) of the cylinder at the point corresponding to $\Delta\phi \pmod{2\pi} = 0$. A key advantage of this representation over Figure 7.22 is that it enables a consistent visualisation of the fine structure of the phase differences, which would no longer be visible in an accumulating phase plot for long data sets such as MOHC and MIROC. The flattening of the $(m : n)$ phase difference lines, a key indicator of synchronization, is preserved by the transformation.

Figure 7.24 presents histograms of the phase differences between the QBO and BD in ERA for the three synchronization ratios. Each histogram is produced by dividing the relevant phase difference $\Delta\phi \pmod{2\pi}/2\pi$ - the ordinates in Figure 7.23 - into a set of $N = 20$ intervals. The phase differences across time are then binned into the relevant intervals as appropriate.

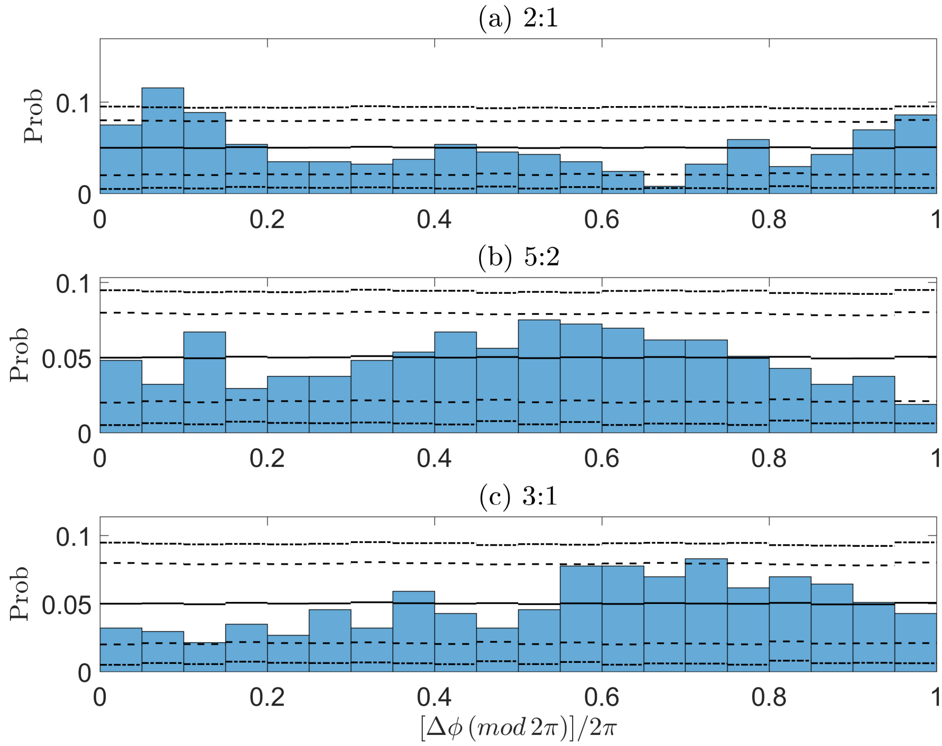

Figure 7.24: Histograms of the normalized phase difference $[\Delta\phi \pmod{2\pi}]/2\pi]$ between the QBO and the BD in ERA, for the three synchronization ratios: (a) $(2:1)$, (b) $(5:2)$, and (c) $(3:1)$. Horizontal lines are statistics for the probability distribution of the height of each bin, as generated by surrogate time series. Solid, dashed and dash-dotted lines mark the locations of the mean and the 2σ and 3σ significance levels respectively.

The histogram height structure allows us to quantify the strength of $(m:n)$ synchronization between the signals. In the absence of synchronization, we expect that the histogram of phase differences would be flat, with a height close to $1/N$. However, in the presence of synchronization there would be a preference for a particular phase difference, which would result in a peak in the histogram (Tass et al. [1998]).

To calculate the statistical significance of the histogram peaks we generated a set of 10^3 surrogate time series for each of the three analytic phase signals of the QBO, SAO, and BD. Each surrogate time series was designed to have an identical Fourier spectrum as its parent phase signal, but with a randomized phase; see Theiler et al. [1992] for details. By calculating equivalent phase differences and histograms of numerous pairs of surrogate signals, we can derive the probability distribution for the height of each bin in the phase difference histogram. These are found to be approximately normal.

Locations of the mean, 2σ and 3σ levels for each bin are plotted in Figure 7.24 as solid, dashed, and dash-dotted lines respectively. (2σ and 3σ levels correspond to significance levels of approximately 5% and 0.3% respectively). We find a very strong peak in the histogram corresponding to $(2 : 1)$ synchronization (Figure 7.24(a)), confirming that the QBO and BD are $(2 : 1)$ synchronized at least to the 3σ level. There are peaks and troughs in both the $(5 : 2)$ and $(3 : 1)$ histograms as well (Figure 7.24(b) and (c)). There is a trough in the $(5 : 2)$ case and a peak in the $(3 : 1)$ case that are significant at the 2σ level; however in general the locking is not as strong at these ratios as it was in the $(2 : 1)$ case.

7.3.2.6 Phase synchronization of the QBO and SAO in ERA

We apply the same analysis to study phase synchronization between the zonal wind QBO and SAO phases in the ERA data set. In this case the appropriate synchronization ratios are $(4 : 1)$, $(5 : 1)$, and $(6 : 1)$, which approximately correspond to QBO periods of 24, 30, and 36 months respectively. We note that there is also a semiannual oscillation in upwelling, represented by EEOFs 5 and 6 in the analysis of $\overline{w}^*$ (Figure 7.17(e)–(f)), in addition to the SAO in the zonal winds. Synchronization tests of the zonal wind and upwelling SAO phase signals, not presented here, showed that they are in exact $(1 : 1)$ synchronization. In what follows we focus on the zonal wind SAO,

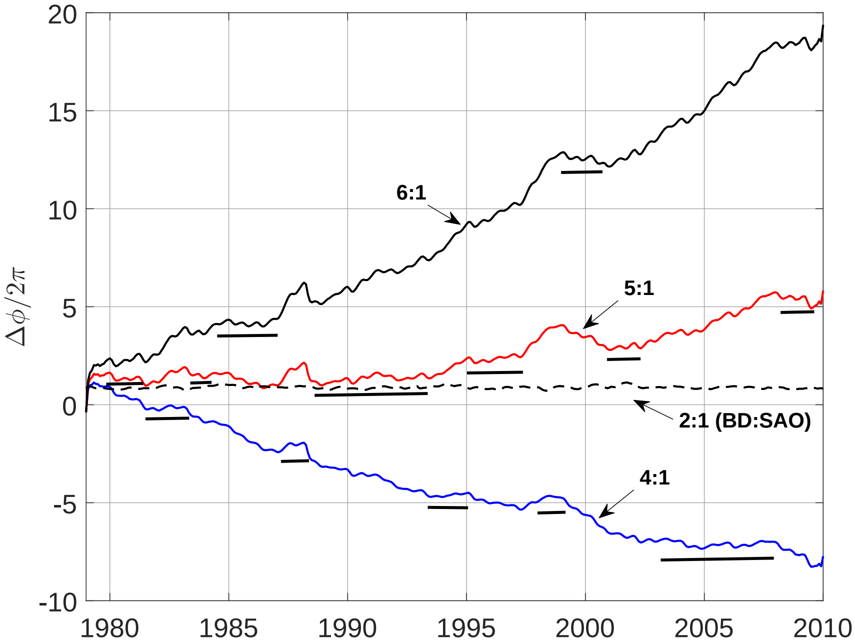

Figure 7.25: Evolution of the normalized phase difference $\Delta\phi/2\pi$ between the QBO and SAO in the ERA data set. The blue, read and black lines represent $m : n$ synchronization ratios of $4 : 1$, $5 : 1$, and $6 : 1$ respectively. Dark bold lines highlight sections along the phase difference lines where $\Delta\phi/2\pi$ is relatively constant. The dashed line represents the $(2 : 1)$ synchronization ratio between the BD and the SAO.

following Read and Castrejón-Pita [2012], keeping in mind that the synchronization results hold equally between the QBO and the SAO in $\overline{w}^*$ as well.

Figure 7.25 plots the evolution of the phase differences between the zonal wind QBO and SAO over the duration of the reanalysis. As before, we note the presence of sporadic periods of synchronization (highlighted by the bold underlining) where the phase difference remains relatively constant. The phase evolution tracks that of the QBO and BD phase differences discussed earlier (Figure 7.22).

The phase difference line corresponding to the $(2 : 1)$ synchronization ratio between the BD and the SAO is also plotted (dotted line in Figure 7.25). The line is remarkably flat, indicating a very strong $(2 : 1)$ synchronization between the BD and SAO signals at all times. Such strong synchronization can be attributed to the common annual cycle that is the fundamental driver of both signals.

Figures 7.26 and 7.27 plot the phase difference evolution and corresponding his-

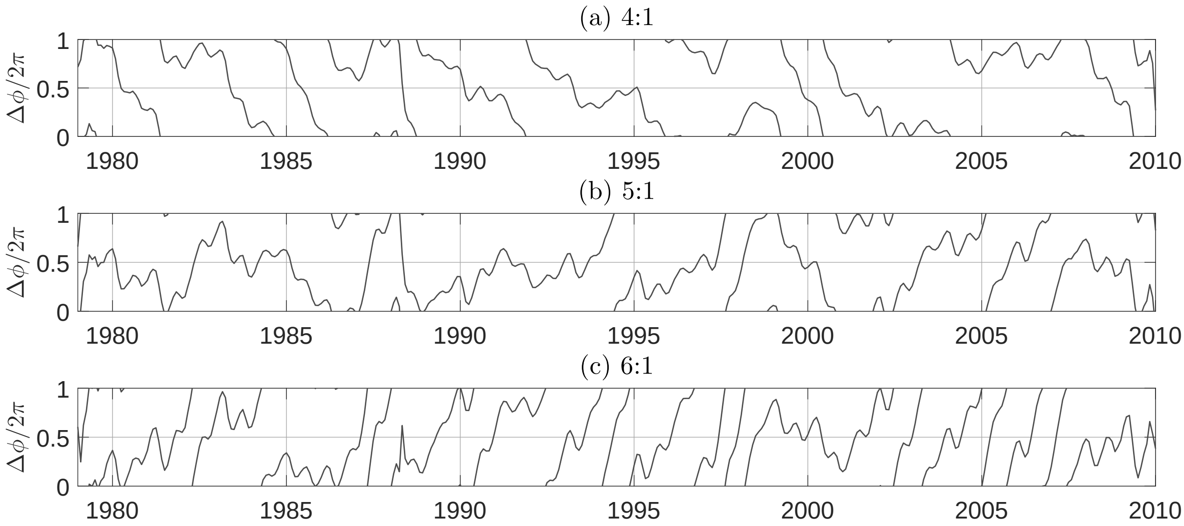

Figure 7.26: Normalized phase difference plots of the zonal wind QBO and SAO in ERA data, corresponding to synchronization ratios of (a) $4:1$, (b) $5:1$, and (c) $6:1$ respectively.

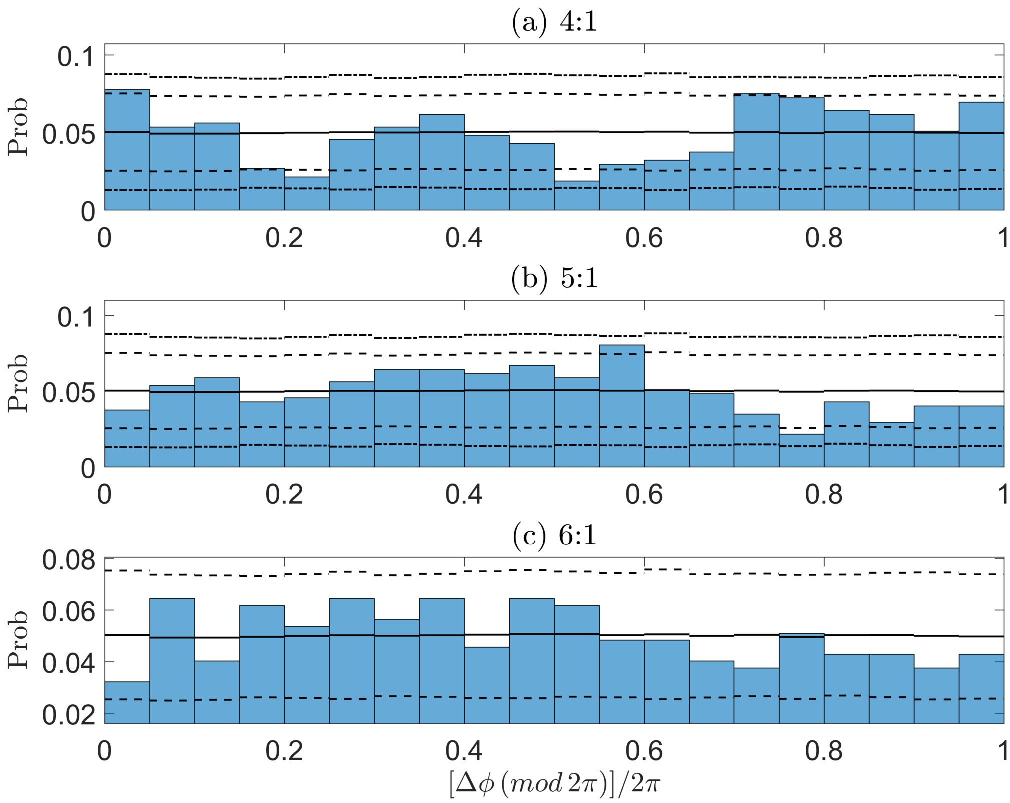

Figure 7.27: Histograms of the normalized phase difference $[\Delta\phi \pmod{2\pi}]/2\pi]$ between the QBO and the SAO in ERA, for the three synchronization ratios: (a) $(4:1)$, (b) $(5:1)$, and (c) $(6:1)$.

tograms of phase differences between the QBO and SAO. From the histograms in Figure 7.27 we see that the QBO and SAO are synchronized, at 5% significance, for the (4 : 1) and (5 : 1) ratios. In contrast, there is no significant synchronization for the (6 : 1) ratio.

Table 7.2 provides a detailed breakdown of the statistical significance of phase synchronization found in each of the six phase difference histograms we have computed using the ERA data (three cases for QBO and BD synchronization as in Figures 7.23–7.24, and three cases for QBO and SAO synchronization as in Figures 7.26–7.27). Each column in the table lists, for each bin in a particular histogram, the probability of measuring a bin height as or more extreme than the bin height observed from the data. Statistically significant bin heights at 10%, 5% and 1% levels have been given light, medium, and heavy shading respectively. There is ample evidence for the synchronization of the QBO with both the BD and the SAO. Synchronization with the BD is significant at all the ratios considered, and is as strong as 0.02% in the case of (2 : 1) synchronization. Synchronization between the QBO and SAO is not as strong, but still significant except for the (6 : 1) case.

7.3.2.7 Synchronization of the QBO in GCMs

We repeat the entire analysis presented above on the MOHC and MIROC data sets. EEOFs, PCs, and appropriate phase signals were extracted from zonal wind data (for the QBO and SAO) and the upwelling data (for the BD). These signals were subjected to the same battery of synchronization tests. To keep the presentation compact we have relegated most of the figures to the Appendices (Appendix B,C for MOHC and MIROC respectively), where the interested reader will find plots of the EEOFs, PCs, and QBO, SAO, BD reconstructions (Figs B.1–B.4 and C.1–C.4), as well as plots and histograms of the phase differences (B.5–B.8 and C.5–C.8) for QBO-BD and QBO-SAO synchronization.

ERA						
	QBO : BD			QBO : SAO		
Bin	2 : 1	5 : 2	3 : 1	4 : 1	5 : 1	6 : 1
1	8.84	47.03	11.9	3.2	19.66	7.35
2	0.02	11.28	7.96	40.63	41.29	10.72
3	1.69	12.82	2.82	33.64	27.5	22.71
4	41.1	8.63	13.91	5.23	31.5	15.03
5	21.89	19.72	5.57	1.83	36.51	37.65
6	21.43	19.73	38	36.15	33.69	12.36
7	17.55	46.09	10.21	40.32	16.45	29.37
8	25.48	39.94	27.54	21.12	17.1	11.53
9	42.62	12.33	31.89	47.1	20.3	34.85
10	39.45	35.53	10.18	32.29	12.46	13.3
11	33.99	4.55	39.38	1.54	25.84	17.99
12	22.33	6.64	2.72	7.86	2.52	43.64
13	9.36	8.99	2.96	11.76	45.98	42.97
14	1.33	23.18	9.44	19.89	43.98	20.89
15	17.34	21.41	1.2	4.43	16.37	14.16
16	30.75	47.48	21.28	6.27	2.85	45.28
17	13.26	31.78	8.69	14.22	32.86	26.6
18	34.19	11.98	14.87	20.85	8.26	27.06
19	16.92	21.53	45.6	47.26	25.38	15.77
20	3.21	1.77	30.38	8.58	25.4	28.69

Table 7.2: Table of significance levels for the height of each bin in each of the 6 phase synchronization histograms derived from ERA data. Each column lists the probabilities of obtaining bin heights as or more extreme than the observed bin heights as derived from phase differences of the QBO and BD (columns 2–4) or the QBO and SAO (columns 5–7). The light, medium, and heavy shadings highlight significance levels of 10%, 5%, and 1% respectively.

MOHC						
	QBO : BD			QBO : SAO		
Bin	2 : 1	5 : 2	3 : 1	4 : 1	5 : 1	6 : 1
1	37.61	1.5	6.83	33.24	2.06	24.77
2	19.42	46.82	26.47	24.64	6.46	42.16
3	0.7	36.35	36.97	36.35	4.46	47.68
4	2.27	27.37	32.9	0.83	46.53	35.92
5	12.2	28.68	4.05	1.12	14.97	37.41
6	27	7.63	0	0.28	17.83	49.77
7	29.86	15.78	2.13	8.72	38.23	36.84
8	43.61	11.99	3.55	32.58	8.77	27.99
9	4.78	40.9	0.2	4.19	14.78	4.45
10	2.74	22.9	18.28	33.24	5.63	16.33
11	0	35.55	10.7	25.27	19.45	10.96
12	0	16.21	39.94	3.31	7.88	47.33
13	0	31.41	18.02	4.67	15.01	49.09
14	16.31	18.46	10.34	0.65	22.09	28.16
15	49.69	19.96	1.01	1.31	11.31	29.6
16	3.69	28.42	1.52	6.96	31.38	26.5
17	0.29	28.36	32.18	37.36	25.89	22.8
18	4.94	41.86	0.96	9.07	42.29	38.74
19	4.07	3.35	0.3	3.35	24.82	30.95
20	7.51	2.89	0.09	0.15	48.51	45.75

Table 7.3: Table of significance levels for the height of each bin in each of the 6 phase synchronization histograms derived from MOHC data. Each column lists the probabilities of obtaining bin heights as or more extreme than the observed bin heights as derived from phase differences of the QBO and BD (columns 2–4) or the QBO and SAO (columns 5–7). The light, medium, and heavy shadings highlight significance levels of 10%, 5%, and 1% respectively.

MIROC						
	QBO : BD			QBO : SAO		
Bin	2 : 1	5 : 2	3 : 1	4 : 1	5 : 1	6 : 1
1	34.17	7.08	4.01	0.91	38.17	38.41
2	1.5	6.32	4.09	7.82	31	32.61
3	0.2	39.11	18.17	31.4	42.88	47.94
4	0	2.95	31.5	24.1	18.14	47.43
5	0.85	6.68	15.8	5.03	31.04	20.21
6	1.13	1.22	43.89	0.74	12.87	40.87
7	2.64	1.11	36.23	3.8	10.63	41.19
8	19.42	28.07	21.75	24.85	16.8	24.5
9	24.81	38.42	36	33.44	23	31.55
10	13.99	8.96	12.13	0.39	10.57	43.69
11	1.35	4.51	18.84	13.45	28.72	47.46
12	0.33	41.49	10.31	28.92	45.29	5.96
13	0.04	11.13	0.29	22.48	49.32	44.12
14	0.07	49.37	4.06	5.29	13	15.3
15	1.17	40.72	40	0.43	18.56	38.56
16	4.06	24.15	21.94	1.79	1.25	46.74
17	18.33	10.56	21.94	23.77	2.32	6.46
18	15.24	21.29	13.38	27.1	26.63	41.24
19	19.95	0.42	36.51	37.38	1	24.54
20	28.73	12.47	19.97	10.04	36.72	2.96

Table 7.4: Table of significance levels for the height of each bin in each of the 6 phase synchronization histograms derived from MIROC data. Each column lists the probabilities of obtaining bin heights as or more extreme than the observed bin heights as derived from phase differences of the QBO and BD (columns 2–4) or the QBO and SAO (columns 5–7). The light, medium, and heavy shadings highlight significance levels of 10%, 5%, and 1% respectively.

The key results are summarised in the synchronization tables 7.3 and 7.4. These were produced from the MOHC and MIROC data sets in the same way that Table 7.2 was produced from the ERA data set. The tables indicate that the QBO is very strongly synchronized in both climate models. In the MOHC case, QBO synchronization is strongest with the BD and occurs for all three synchronization ratios with very high significance of effectively 0% for both (2 : 1) and (3 : 1), and 1.5% for (5 : 2). Synchronization with the SAO is also very strong for the (4 : 1) and (5 : 1) ratios, with significance of 0.15% and 2.06% respectively. The (6 : 1) case is marginally weaker, but still significant at 4.45%.

Synchronization of the QBO in MIROC is similarly strong, with QBO-BD significance levels at 0%, 0.42% and 0.29% respectively. For QBO-SAO synchronisation, peak significance levels are 0.39%, 1% and 2.96% respectively.

7.4 Discussion

In this chapter we have investigated several aspects of the synchronization of the QBO in the reanalysis and GCM data. By analysing the evolution of the QBO period we have shown that the QBO is synchronized to the seasonal cycle with high statistical significance. We found a general negative correlation between the descent rate of the QBO winds and the strength of upwelling, which we interpret as a causal relationship in the natural way. We expect, therefore, that any consistent periodic variation in the upwelling strength is likely to push the QBO towards synchronization.

Periodicity in upwelling is primarily due to the semi-annual oscillation in the upper stratosphere (which also has a significant annual modulation), and the annual cycle due to the Brewer-Dobson circulation. There is also a semi-annual oscillation in upwelling in the lower stratosphere, presumably due to the semiannual migration of the Inter-Tropical Convergence Zone across the Equator. We also found tantalising hints of an ENSO connection to the QBO phase, wherein phase slips in the QBO tend to correspond to strong ENSO events. The influence of ENSO on the QBO phase is possibly due to greater disruption of the polar night jet due to increased wave driving during ENSO episodes. The deceleration of the night jet westerlies leads to anomalous downwelling at the poles, with corresponding upwelling at low latitudes. The net QBO response to ENSO, however, is further complicated by the fact that increased wave driving during ENSO episodes would also act to accelerate the descent of the QBO winds (cf. Chapter 5). Further work will be needed to clearly establish the sensitivity of the QBO to the balance between these two mechanisms.

Using a combination of EEOF analysis and analytic phase construction we managed to isolate the principal modes of variability in the different data sets corresponding to the evolution of the QBO, the SAO, and the BD. We then assigned a phase evolution to each signal, which allowed us to test the strength of synchronization between particular wind systems in detail. We found that the QBO is strongly synchronized to both the BD and the SAO in both the reanalysis and model data. Synchronization with the BD is strongest, suggesting that the annual cycle plays the largest role in affecting the QBO phase. However, synchronization with the SAO is also significant. In general, synchronization in models is actually stronger than seen in the reanalysis. This suggests that some of the low-frequency variability observed in the ERA data - which seems responsible for the phase slips that weaken the strength of the synchronization - is not filtering through to the stratosphere in the models. This is also reflected in the spread of the QBO period in the models, which is much narrower than in in the reanalysis even though the model data sets are much larger and therefore, would be expected to express a greater range of variability over time.

In truth it is quite difficult to truly separate out the influences of annual and semi-annual signals on the QBO in a way that verifies causality. The EEOF for the BD, for example, has a contribution from variability in the upper stratosphere which could easily be due to the annual modulation of the SAO winds. Given that the SAO itself is not a pure semiannual signal but rather consists of a mixture of annual and semiannual frequencies, one might argue that the distinction between annual/semiannual rapidly becomes meaningless. In fact, it is probably most accurate to conclude that the QBO phase evolution is strongly synchronized to the seasonal cycle, in both its annual and semi-annual incarnations.

Chapter 8

Conclusion

As discussed in Chapter 1, the QBO is the dominant mode of variability in the tropical stratosphere, and it has numerous interactions with - and influences upon - other parts of the climate system. In this thesis, we have successfully contributed to the understanding of the cycle to cycle variability of the QBO by identifying various candidate forcings that might affect the period of the QBO, and by demonstrating how they can have a synchronizing influence that constrains and structures the evolution of the QBO period. In this final chapter we give a summary of our findings, and point out directions for future work.

In Chapter 2 we gave a theoretical introduction to the Holton-Lindzen model, the basic equation used in later chapters to study synchronization of the QBO. We studied the effect that changes to various model parameters - such as wave forcing amplitude, wave number, wave speed, and diffusion strength - had on the amplitude and period of the QBO. In the process, we discovered an amplitude bifurcation of the QBO that occurred at large values of wave forcing. This bifurcation is distinct from the QBO amplitude bifurcation studied by Yoden and Holton [1988]. We gave a qualitative explanation of the source of the new amplitude variability in terms of the decreasing timescales of wave-induced accelerations at lower levels in the model relative to the diffusive timescale. It is possible that the bifurcation could be relevant to actual atmospheric dynamics if it would occur at smaller values of wave forcing; we believe that this might be possible if the value of diffusion in the model were to be smaller. This hypothesis could be tested - and the analytical properties of the bifurcation studied in detail - in further work.

In the middle chapters of the thesis - Chapters 3, 4 and 5 - we considered different types of periodic forcings on the QBO, and evaluated them as candidate synchronization mechanisms. In Chapter 3, we studied the interaction of the QBO with the annual cycle in tropical upwelling due to the Brewer-Dobson circulation. We found that the interaction affected the period of the QBO, resulting in the creation of finite-length intervals in the wave forcing parameter space within which the average QBO period was a rational multiple of the annual forcing period. Analysis of the cycle by cycle evolution of the QBO period then revealed that the QBO cycled through a finite set of periods within these regions, the sum of each set being a multiple of the annual forcing period. In other cases, the QBO adopted a broad set of individual periods that suggested quasi-periodic behaviour. We tested the robustness of these results to stochastic perturbations of the wave forcing, and found that the synchronization structure was broadly maintained even in the presence of noise. In the final section of the chapter, we considered how the QBO might evolve in a warming climate, as the strength of the Brewer-Dobson circulation increases gradually. We found that the QBO period generally increased, but in a non-monotonic fashion that reflected the change in its relationship to the annual cycle.

A natural extension of the study in Chapter 3 would be to consider two-dimensional effects, such as the effect of the QBO meridional circulation on the interaction between the QBO and tropical upwelling. The idealised model utilised here also uses a discrete spectrum of waves - generalisations to a continuous spectrum would help to confirm the robustness of the results. It would also be interesting to investigate, in line with the Holton-Tan effect, the possibility of a two-way feedback loop between the QBO and the polar vortex, wherein the phase of the QBO affects the strength of the polar vortex, which in turn affects the strength of tropical upwelling and hence the evolution of the QBO.

In Chapter 4, we considered the synchronization of the QBO by direct forcing due to the SAO and ITCZ winds at 1 hPa and 100 hPa respectively. We also considered QBO synchronization due to upwelling associated with the two forcing wind systems. We found that the SAO was unable to induce synchronization of the QBO in the Holton-Lindzen equation, although it did modulate the frequency of individual QBO cycles. Our study conclusively shows that the QBO and SAO are not synchronized in the Holton-Lindzen model. In contrast, we found that the ITCZ winds at the bottom of the model induced significant synchronization of the QBO. These results highlight the fact that synchronization of the QBO is only attained by forcing the QBO near the lower boundary of the model domain, in line with the principle of no downward influence elucidated by Plumb [1977]. Our parameterisation of the ITCZ influence is quite ad hoc, and based on the exertion of a direct force on the zonal wind; it would be useful to investigate the actual mechanism in a full 3-D model of the atmosphere.

In Chapter 5, the final modelling chapter, we took up the question of the effect of periodic wave forcing on the QBO. Our study was essentially an extension of the investigation conducted by Geller et al. [1997]. We considered the synchronization of the QBO in response to semi-annual, annual, and inter-annual variations in wave forcing strength. In all three cases we found robust synchronization of the QBO, with similar frequency modulation to that found in Chapter 3. The QBO exhibited a large range of variability in the inter-annual case, with a range of periods that was comparable to observations. The time taken for the QBO to cycle through a set of discrete periods was also quite long - over 50 years in some cases. This result emphasizes how short the length of QBO observations are, relative to the range of variability of its period. It would seem that a much longer observational record would be required to tease out the influence of long-period variability on the QBO.

We consolidated our modelling results with a theoretical study of QBO period variation in Chapter 6. We introduced the idea of a descent rate model, which models the dynamics of the zero wind line of the QBO in order to better express the key dynamical relationships that affect the period of the QBO. The study of two heuristically motivated profiles of the zero wind wave forcing led us to find in both cases that the descent rate models captured the key dynamical behaviours of the QBO period in the full Holton-Lindzen PDE studied in previous chapters. We then showed that the Holton-Lindzen equation itself could be recast in the form of a descent rate model, by making a simple transformation and assuming a quadratic profile for the zonal wind velocities. This full descent rate model provided us with a quantitative link between the heuristic model and full Holton-Lindzen model results. We found that the QBO in this model displayed all of the same behaviours as the heuristic models, including frequency locking, multi-cycle QBO periods, and quasiperiodicity. We showed that in this formulation the behaviour and dynamics of the QBO fall under the class of circle maps, which are well-known models of synchronization in the mathematics literature. In this way, we established a theoretical basis to understand synchronization of the QBO. Our study focused on the interaction between the QBO and periodicities in tropical upwelling. A natural and simple extension would be to consider the behaviour of the descent rate model in the case of periodic wave forcing.

Finally, in Chapter 7, we investigated the presence of synchronization in the QBO found in the real atmosphere - as captured in the ERA reanalysis dataset - as well as in two climate models. By tracking the location of zero wind lines, we showed that the descent rate of the QBO varied with the annual cycle, and furthermore that the descent rate was (anti)correlated with the strength of tropical upwelling at the zero wind line. We designed a metric to capture multi-cycle behaviour of the QBO, and applied it to the datasets to show that the observed and modelled QBO periods behave in a way that is consistent with synchronization to an annual forcing. Using a combination of Extended Empirical Orthogonal Function analysis and analytic phase techniques, we then derived phase signals for the QBO, SAO and Brewer-Dobson (BD) circulation. In all three datasets we found evidence of statistically significant synchronization of the QBO and the BD circulation at synchronization ratios of $2:1$, $5:2$, and $3:1$ respectively. Synchronization in the GCMs was particularly strong compared to the reanalysis data. The phase relationship between the QBO and the BD circulation was observed to jump in an irregular fashion between the three ratios, and the timing of the jumps was found to show some relationship to strong El Niño events. We also found significant synchronization between the QBO and the SAO phases, although a causal mechanism that unambiguously links the two wind systems is yet to be established. It seems likely that the observed synchronization between the QBO and SAO is at least partly due to the independent synchronization of each wind system to the BD circulation. In this thesis, we were limited to the study of synchronization in only two GCM datasets, due to a lack of availability of residual circulation data in other models. Future work could apply the above synchronization metrics to a broader set of QBO-generating GCMs, to help to diagnose the strength of the connection between the QBO and the annual cycle in the models.

In conclusion, we believe that the results contained in this thesis make a novel and interesting contribution to the literature of the QBO. We have shown that synchronization is a robust aspect of QBO dynamics in both an idealised modelling study as well as in data from GCMs and atmospheric reanalyses. Furthermore, we have provided a general framework within which to understand and interpret the variability of the QBO period. This theoretical basis - framed within the context of descent rate models - will be a valuable addition to the hierarchy of mathematical models used to understand the QBO.

Appendix A

Equatorial waves in shear: derivation of the equation for $\hat{\Phi}$

We start by restating equations (2.2.32), (2.2.33), (2.2.34), and (2.2.35):

$$
\begin{aligned}
i\hat{\omega}\hat{u} + \hat{w}\bar{u}_z - \beta y\hat{v} &= -ik\hat{\Phi}, && \text{(A.0.1)}\\
i\hat{\omega}\hat{v} + \beta y\hat{u} &= -\hat{\Phi}_y, && \text{(A.0.2)}\\
\hat{w} &= \frac{1}{N^2}\left[-i\hat{\omega}\hat{\Phi}_z + \beta y\bar{u}_z\hat{v}\right], && \text{(A.0.3)}\\
ik\hat{u} + \hat{v}_y + \hat{w}_z &= 0. && \text{(A.0.4)}
\end{aligned}
$$

Using (A.0.3) to eliminate $\hat{w}$ from (A.0.1), and dropping terms $\mathcal{O}(\mathrm{Ri}^{-1})$ yields

$$
i\hat{\omega}\hat{u} - \beta y\hat{v} = -ik\hat{\Phi} + i\hat{\omega}\frac{\bar{u}_z}{N^2}\hat{\Phi}_z, \tag{A.0.5}
$$

where we recall that

$$
\mathrm{Ri}^{-1} = \frac{\bar{u}_z^2}{N^2}. \tag{A.0.6}
$$

Next we eliminate $\hat{u}$ between (A.0.5) and (A.0.2) by calculating $(i\hat{\omega})$(A.0.2)$-(\beta y)$(A.0.5), which gives

$$(\beta^2 y^2 - \hat{\omega}^2)\hat{v} = ik\beta y\hat{\Phi} - i\hat{\omega}\beta y\frac{\bar{u}_z}{N^2}\hat{\Phi}_z - i\hat{\omega}\hat{\Phi}_y. \tag{A.0.7}$$

Similarly $\hat{u}$ can be eliminated from (A.0.4) by substituting from (A.0.5) to give

$$ik\beta y\hat{v} + k^2\hat{\Phi} - k\hat{\omega}\frac{\bar{u}_z}{N^2}\hat{\Phi}_z + i\hat{\omega}\hat{v}_y + i\hat{\omega}\hat{w}_z = 0. \tag{A.0.8}$$

Calculating the z derivative of (A.0.3) yields

$$\hat{w}_z = \frac{1}{N^2}\left[-ik\hat{\Phi}_z\bar{u}_z - i\hat{\omega}\hat{\Phi}_{zz} + \beta y\bar{u}_{zz}\hat{v} + \beta y\hat{u}_z\hat{v}_z\right] \tag{A.0.9}$$

which, when substituted into (A.0.8) and neglecting $\bar{u}_{zz}\hat{\omega}/N^2$ as small, gives:

$$\beta yik\hat{v} + i\hat{\omega}\hat{v}_y + i\hat{\omega}\beta y\frac{\bar{u}_z}{N^2}\hat{v}_z = -k^2\hat{\Phi} - \hat{\omega}^2\frac{\hat{\Phi}_{zz}}{N^2}. \tag{A.0.10}$$

Note that (A.0.7) and (A.0.10) relate quantities involving $\hat{v}$ and $\hat{\Phi}$ only. Multiply (A.0.10) by $(\beta^2y^2 - \hat{\omega}^2)^2$ to get

$$\begin{aligned}\underbrace{\beta yik(\beta^2y^2 - \hat{\omega}^2)^2\hat{v}}_{A_0} + \underbrace{i\hat{\omega}(\beta^2y^2 - \hat{\omega}^2)^2\hat{v}_y}_{B_0} \quad + \quad & \underbrace{i\hat{\omega}\beta y\frac{\bar{u}_z}{N^2}(\beta^2y^2 - \hat{\omega}^2)^2\hat{v}_z}_{C_0} \\ + \quad & \underbrace{(\beta^2y^2 - \hat{\omega}^2)^2\left(k^2\hat{\Phi} + \hat{\omega}^2\frac{\hat{\Phi}_{zz}}{N^2}\right)}_{D_0} = 0.\end{aligned} \tag{A.0.11}$$

We express each of $A_0 - C_0$ as functions of $\hat{\Phi}$ and its derivatives (D_0 already being in this form). Multiplying (A.0.7) by $\beta yik(\beta^2y^2 - \hat{\omega}^2)$ gives an expression for A_0:

$$A_0 = (\beta^2y^2 - \hat{\omega}^2)\left[-\beta^2y^2k^2\hat{\Phi} + \beta^2y^2\hat{\omega}k\frac{\bar{u}_z}{N^2}\hat{\Phi}_z + \beta y\hat{\omega}k\hat{\Phi}_y\right]. \tag{A.0.12}$$

For B_0 we differentiate (A.0.7) with respect to y, multiply the resulting equation by $i\hat{\omega}(\beta^2 y^2 - \hat{\omega}^2)$, and substitute for $\hat{v}$ using (A.0.7) to get

$$\begin{aligned} B_0 \;&= (\beta^2 y^2 - \hat{\omega}^2)\left[-\hat{\omega}k\beta\hat{\Phi} - k\hat{\omega}\beta y\hat{\Phi}_y + \hat{\omega}^2\beta\tfrac{\bar{u}_z}{N^2}\hat{\Phi}_z + \hat{\omega}^2\beta y\tfrac{\bar{u}_z}{N^2}\hat{\Phi}_{zy} + \hat{\omega}^2\hat{\Phi}_{yy}\right] \\ &\quad -2\beta^2 y\left[-\beta y k\hat{\omega}\hat{\Phi} + \hat{\omega}^2\beta y\tfrac{\bar{u}_z}{N^2}\hat{\Phi}_y + \hat{\omega}^2\hat{\Phi}_y\right]. \end{aligned} \tag{A.0.13}$$

To get C_0, first differentiate (A.0.7) with respect to z, then multiply by $(\beta^2 y^2 - \hat{\omega}^2)$, substitute for $\hat{v}$ using (A.0.7), and drop terms that are $\mathcal{O}(\mathrm{Ri}^{-1})$. This gives

$$\begin{aligned} (\beta^2 y^2 - \hat{\omega}^2)^2\hat{v}_z \;&=\; (\beta^2 y^2 - \hat{\omega}^2)\left[ik\beta y\hat{\Phi}_z - i\hat{\omega}\beta y\frac{\bar{u}_z}{N^2}\hat{\Phi}_{zz} - i\hat{\omega}\beta y\frac{\bar{u}_{zz}}{N^2}\hat{\Phi}_z - ik\bar{u}_z\hat{\Phi}_y - i\hat{\omega}\hat{\Phi}_{yz}\right] \\ &\quad - \; 2\hat{\omega}k\bar{u}_z\left[ik\beta y\hat{\Phi} - i\hat{\omega}\beta y\frac{\bar{u}_z}{N^2}\hat{\Phi}_z - i\hat{\omega}\hat{\Phi}_y\right]. \end{aligned} \tag{A.0.14}$$

Now, multiply $(A.0.14)$ by $(i\hat{\omega}\beta y\bar{u}_z N^{-2})$ and neglect terms $\mathcal{O}(\mathrm{Ri}^{-1})$ to get

$$C_0 = (\beta^2 y^2 - \hat{\omega}^2)\left[-\beta^2 y^2 k\hat{\omega}\frac{\bar{u}_z}{N^2}\hat{\Phi}_z + \beta^2 y^2\hat{\omega}^2\frac{\bar{u}_z}{N^2}\frac{\bar{u}_{zz}}{N^2}\hat{\Phi}_z + \beta y\hat{\omega}^2\frac{\bar{u}_z}{N^2}\hat{\Phi}_{yz}\right]. \tag{A.0.15}$$

By substituting (A.0.12), (A.0.13), and (A.0.15) into (A.0.11), collecting terms, and dividing by $\hat{\omega}/N^2(\beta^2 y^2 - \hat{\omega}^2)$, we are obtain the requisite equation for $\hat{\Phi}$:

$$\begin{aligned} (\beta^2 y^2 - \hat{\omega}^2)\hat{\Phi}_{zz} \;&+\; 2\beta y\bar{u}_z\hat{\Phi}_{zy} + N^2\hat{\Phi}_{yy} + \beta\bar{u}_z\left[\frac{\beta y^2}{N^2}\bar{u}_{zz} - \frac{\beta^2 y^2 + \hat{\omega}^2}{\beta^2 y^2 - \hat{\omega}^2}\right]\hat{\Phi}_z \\ &-\; \frac{2N^2\beta^2 y}{\beta^2 y^2 - \hat{\omega}^2}\hat{\Phi}_y + \frac{N^2 k}{\hat{\omega}}\left[\beta\frac{\beta^2 y^2 + \hat{\omega}^2}{\beta^2 y^2 - \hat{\omega}^2} - k\hat{\omega}\right]\hat{\Phi} = 0. \end{aligned} \tag{A.0.16}$$

Appendix B

Synchronization in GCMs: MOHC figures

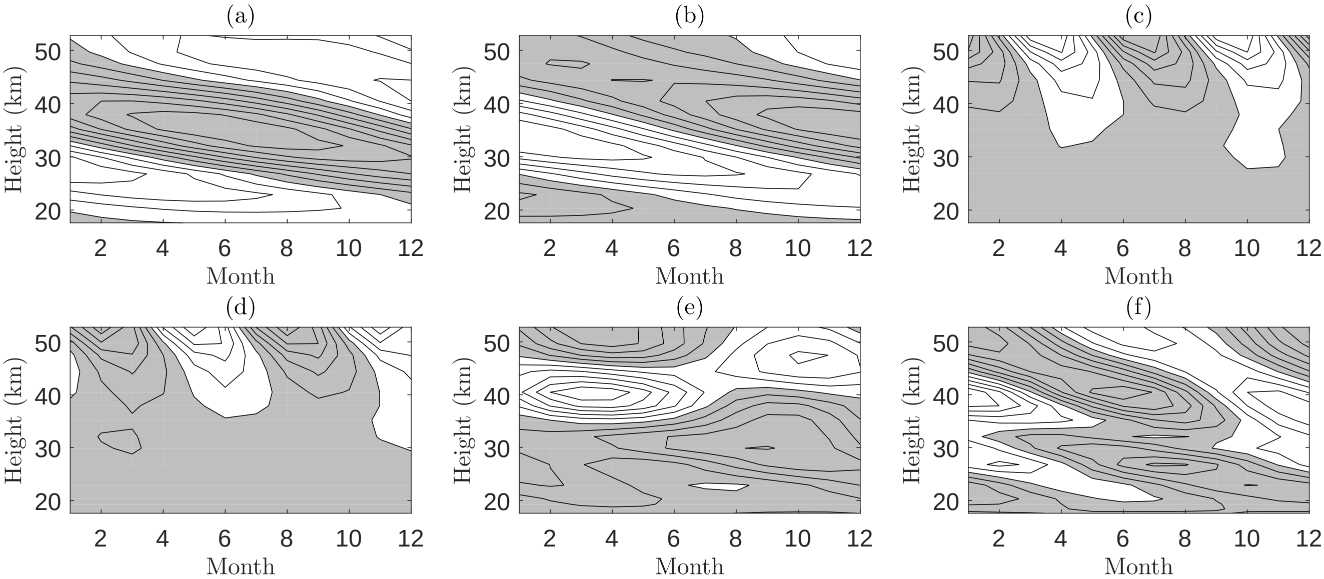

Figure B.1: Spatio-temporal structure of the first 6 EEOFs of zonal wind data from the MOHC dataset. Shaded regions represent easterly winds. The percentage contributions of each EEOF to the total variance in the data are (a) 35.3%, (b) 33.6%, (c) 10.3%, (d) 10.3 %, (e) 1.3 %, and (f) 1.2% respectively. The first 4 EEOFs account for 89.5% of the total variance in the dataset.

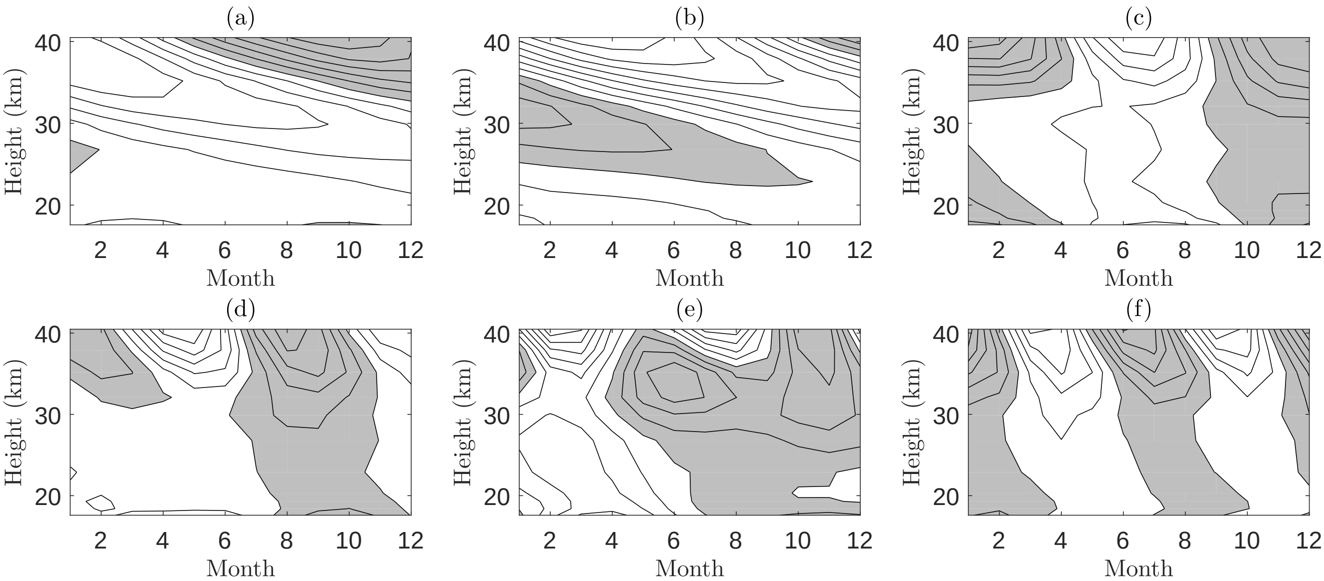

Figure B.2: Spatio-temporal structure of the first 6 EEOFs of $\overline{w}^*$ data from the MOHC dataset. Vertical velocities are positive in the shaded regions. The percentage contribution of each EEOF to the total variance in the data is (a) 30.9%, (b) 29.8%, (c) 8.4%, (d) 7 %, (e) 4.7 %, and (f) 6% respectively. The first 6 EEOFs account for 86.8% of the total variance in the dataset.

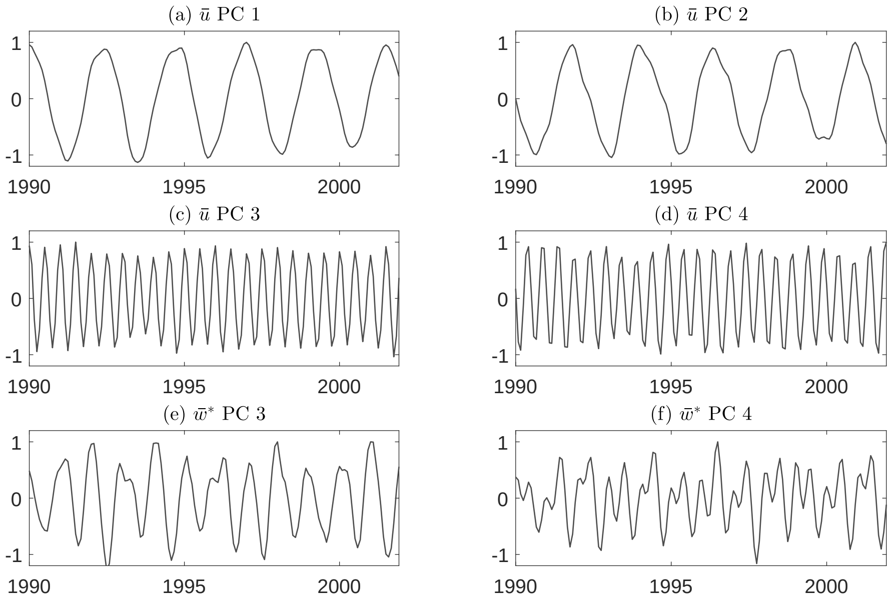

Figure B.3: Principal Component times series representing the QBO in zonal winds [(a)-(b)], the SAO in zonal winds [(c)-(d)] and the BD (annual cycle) in vertical residual winds [(e)-(f)] for the MOHC dataset.

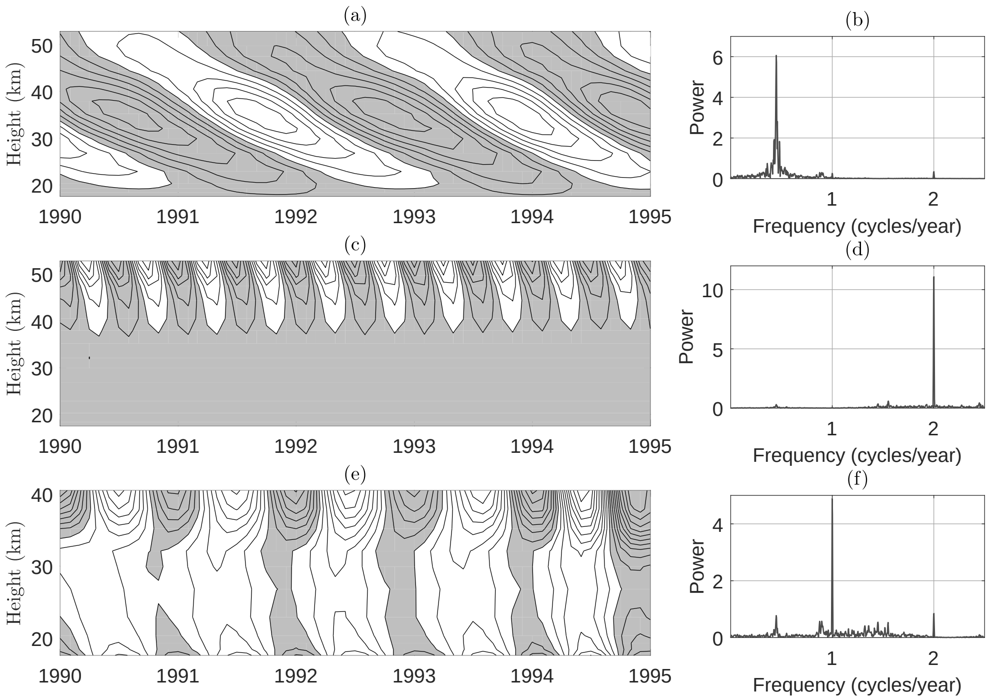

Figure B.4: Sample reconstruction of various height-time structures in MOHC data: (a) QBO (EEOFs 1–2 of $\bar{u}$), (c) SAO (EEOFs 3–4 of $\bar{u}$), and (e) BD (EEOFs 3 of $\overline{w}^*$). Corresponding Fourier spectra are shown for: (b) PC 1 of $\bar{u}$, (d) PC 3 of $\bar{u}$, and (f) PC 3 of $\overline{w}^*$ respectively. Shaded regions represent easterly zonal winds in (a) and (c), and positive upwelling in (e).

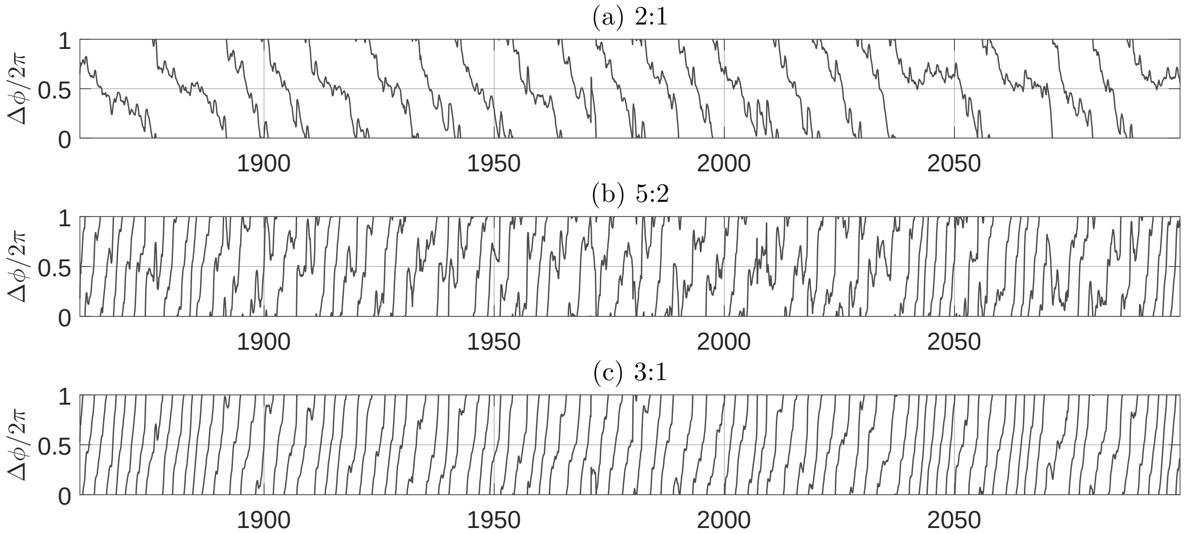

Figure B.5: Normalized phase difference plots of the QBO and BD in MOHC data, corresponding to synchronization ratios of (a) $2:1$, (b) $5:2$, and (c) $3:1$ respectively.

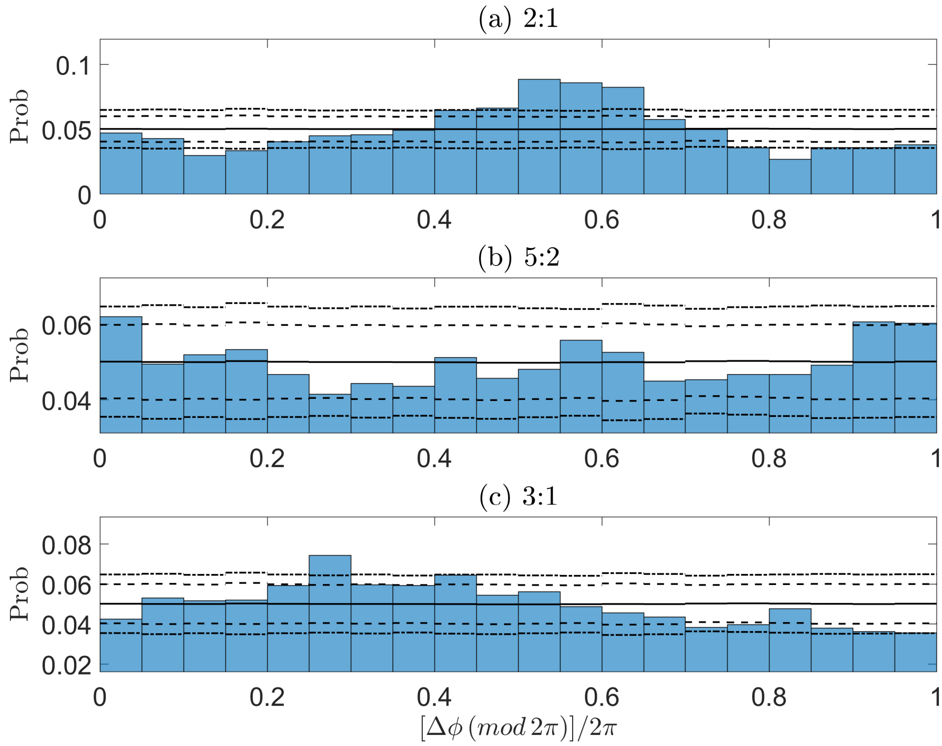

Figure B.6: Histograms of the normalized phase difference $[\Delta\phi \pmod{2\pi}]/2\pi$ between the QBO and the BD in MOHC, for the three synchronization ratios: (a) $(2:1)$, (b) $(5:2)$, and (c) $(3:1)$. Horizontal lines are statistics for the probability distribution of the height of each bin, as generated by surrogate time series. Solid, dashed and dash-dotted lines mark the locations of the mean and the 2σ and 3σ significance levels respectively.

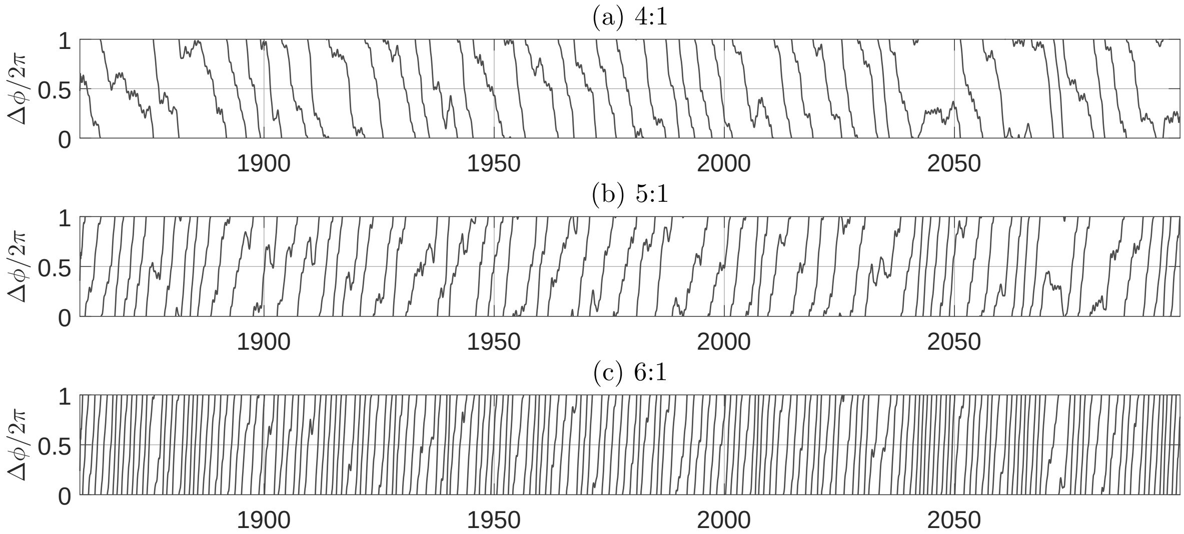

Figure B.7: Normalized phase difference plots of the QBO and SAO in MOHC data, corresponding to synchronization ratios of (a) $4:1$, (b) $5:1$, and (c) $6:1$ respectively.

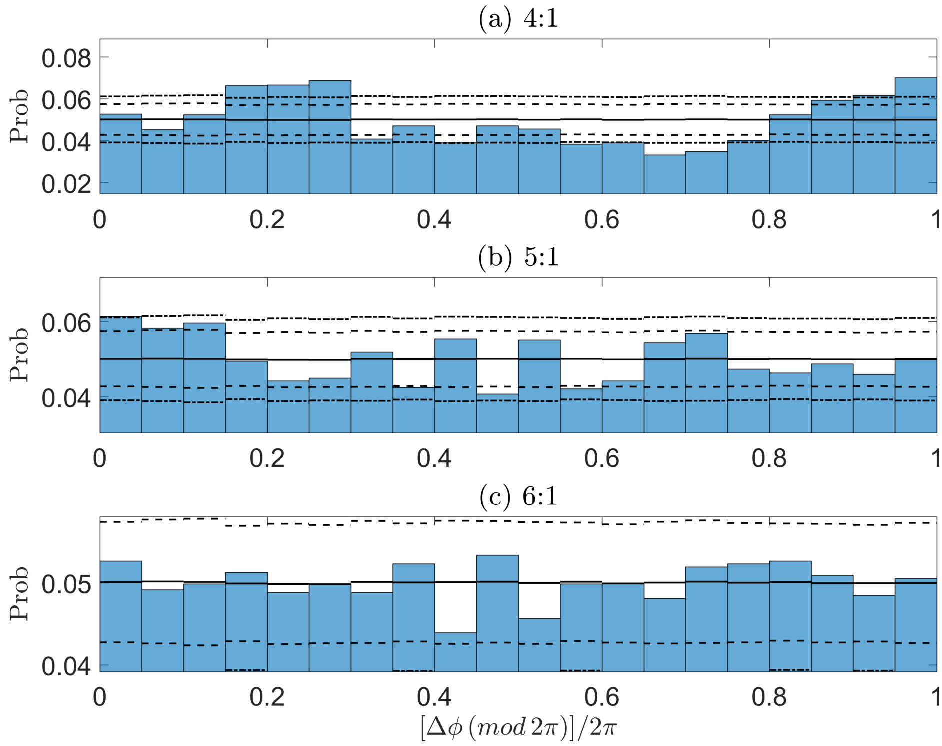

Figure B.8: Histograms of the normalized phase difference $[\Delta\phi\ (\mathrm{mod}\ 2\pi)]/2\pi]$ between the zonal wind QBO and SAO in MOHC, for the three synchronization ratios: (a) $(4:1)$, (b) $(5:1)$, and (c) $(6:1)$. Horizontal lines are statistics for the probability distribution of the height of each bin, as generated by surrogate time series. Solid, dashed and dash-dotted lines mark the locations of the mean and the 2σ and 3σ significance levels respectively.

Appendix C

Synchronization in GCMs: MIROC figures

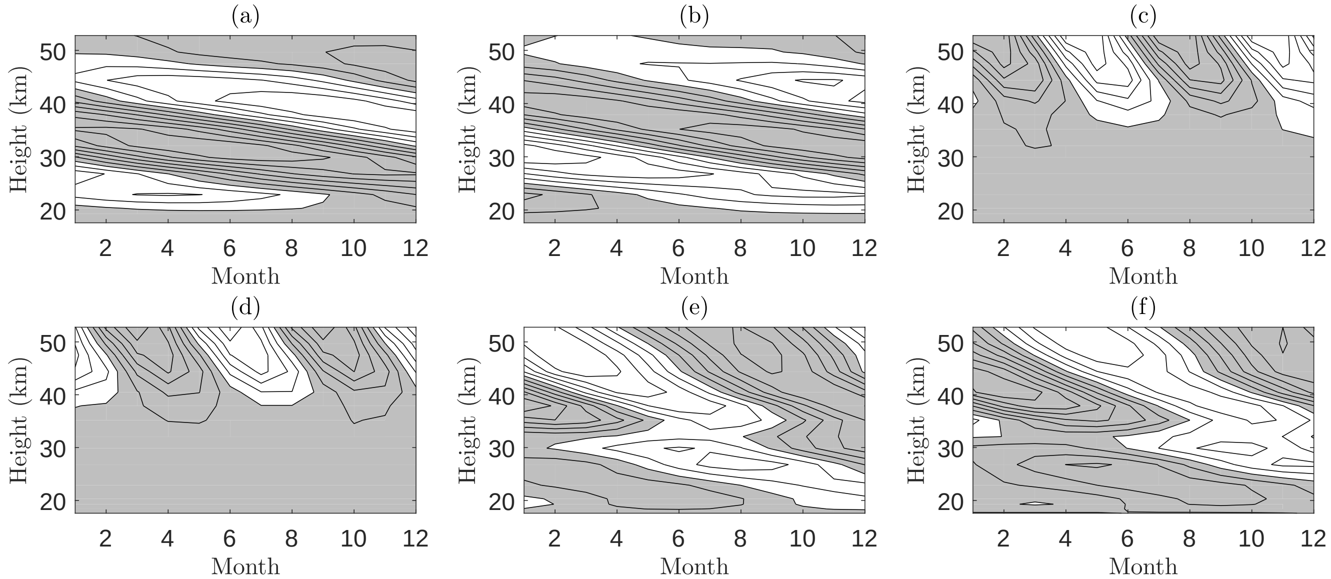

Figure C.1: Spatio-temporal structure of the first 6 EEOFs of zonal wind data from the MIROC dataset. Shaded regions represent easterly winds. The percentage contributions of each EEOF to the total variance in the data are (a) 29.0%, (b) 28.5%, (c) 11.3%, (d) 11.1 %, (e) 3.0 %, and (f) 3.1% respectively. The first 6 EEOFs account for 86% of the total variance in the dataset.

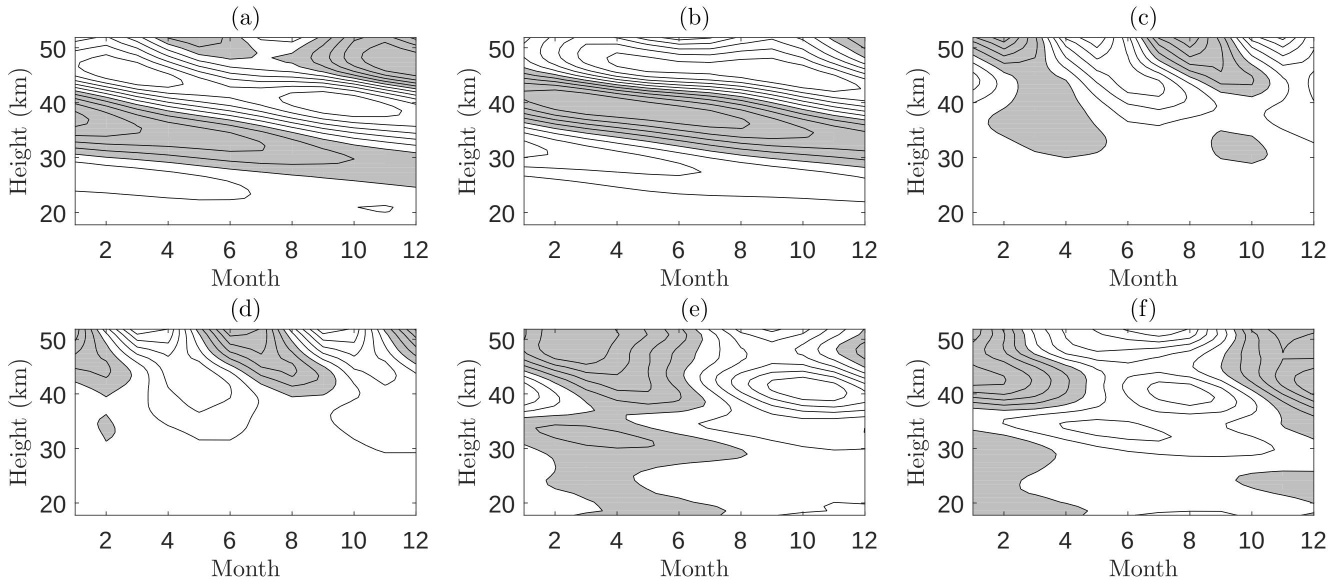

Figure C.2: Spatio-temporal structure of the first 6 EEOFs of $\overline{w}^*$ data from the MIROC dataset. Vertical velocities are positive in the shaded regions. The percentage contribution of each EEOF to the total variance in the data is (a) 19.9%, (b) 20%, (c) 12.8%, (d) 13.1 %, (e) 4.2 %, and (f) 2% respectively. The first 6 EEOFs account for 86.8% of the total variance in the dataset.

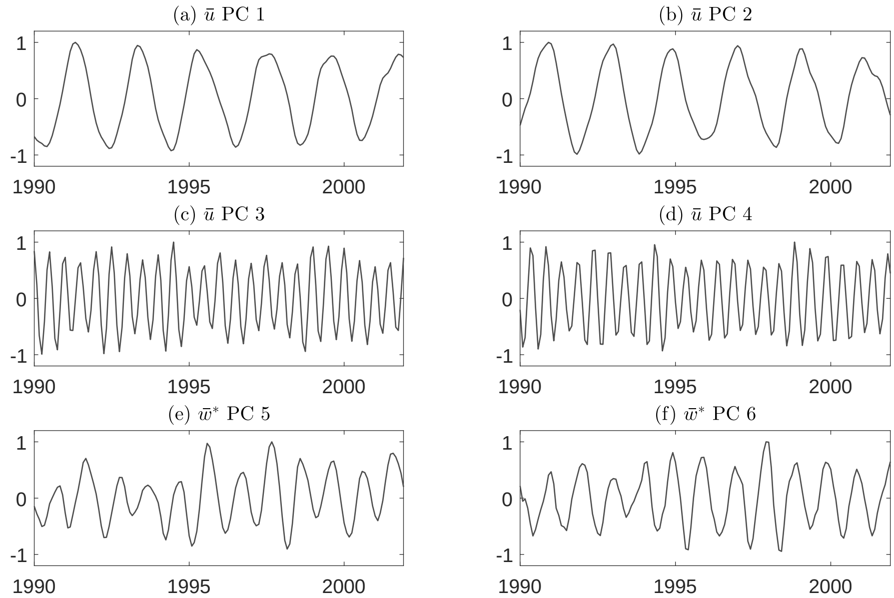

Figure C.3: Principal Component times series representing the QBO in zonal winds [(a)-(b)], the SAO in zonal winds [(c)-(d)] and the BD (annual cycle) in vertical residual winds [(e)-(f)] for the MIROC dataset.

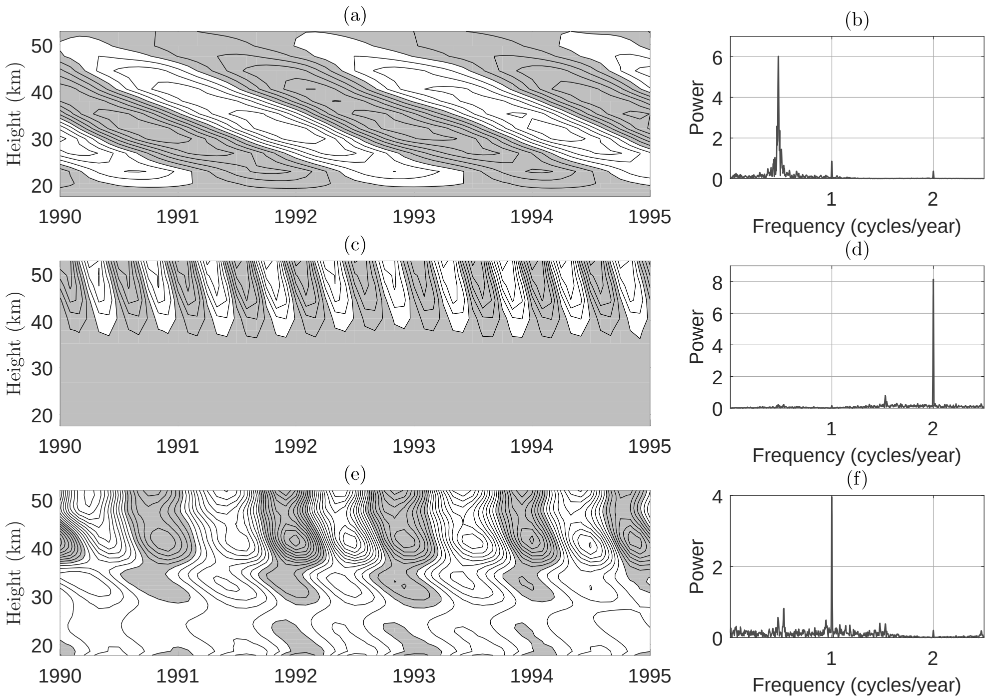

Figure C.4: Sample reconstruction of various height-time structures in MIROC data: (a) QBO (EEOFs 1–2 of $\bar{u}$), (c) SAO (EEOFs 3–4 of $\bar{u}$), and (e) BD (EEOFs 3 of $\overline{w}^*$). Corresponding Fourier spectra are shown for: (b) PC 1 of $\bar{u}$, (d) PC 3 of $\bar{u}$, and (f) PC 3 of $\overline{w}^*$ respectively. Shaded regions represent easterly zonal winds in (a) and (c), and positive upwelling in (e).

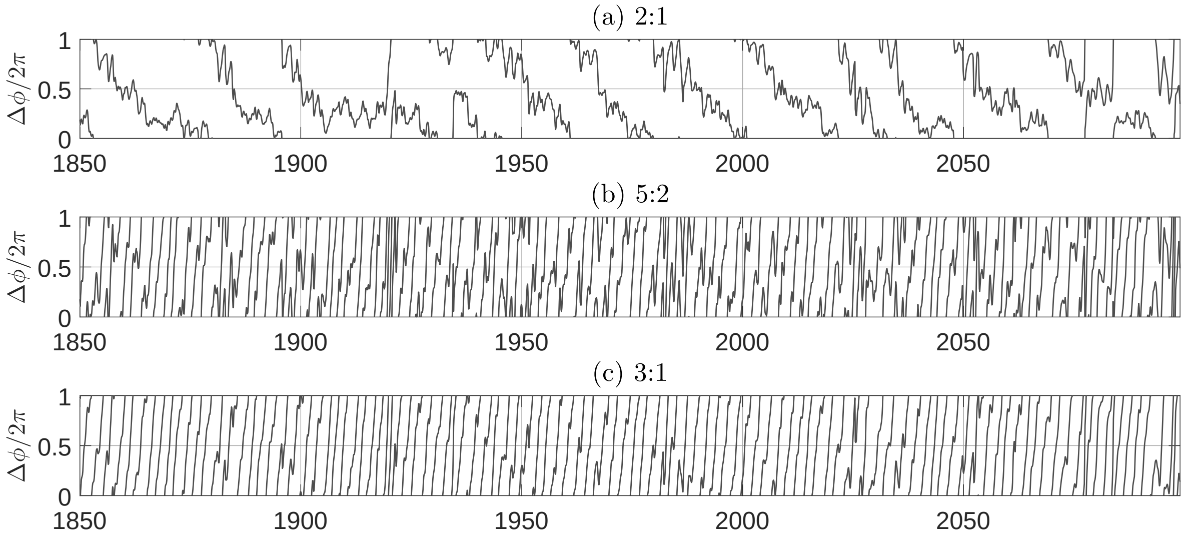

Figure C.5: Normalized phase difference plots of the QBO and BD in MIROC data, corresponding to synchronization ratios of (a) $2:1$, (b) $5:2$, and (c) $3:1$ respectively.

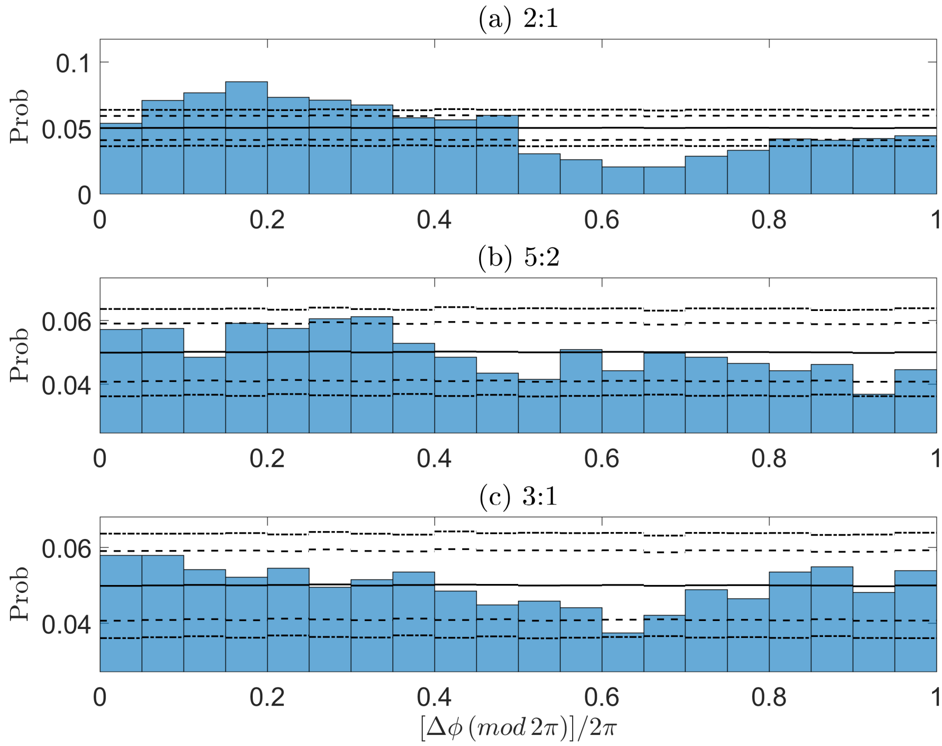

Figure C.6: Histograms of the normalized phase difference $[\Delta\phi \pmod{2\pi}]/2\pi$ between the QBO and the BD in MIROC, for the three synchronization ratios: (a) $(2:1)$, (b) $(5:2)$, and (c) $(3:1)$. Horizontal lines are statistics for the probability distribution of the height of each bin, as generated by surrogate time series. Solid, dashed and dash-dotted lines mark the locations of the mean and the 2σ and 3σ significance levels respectively.

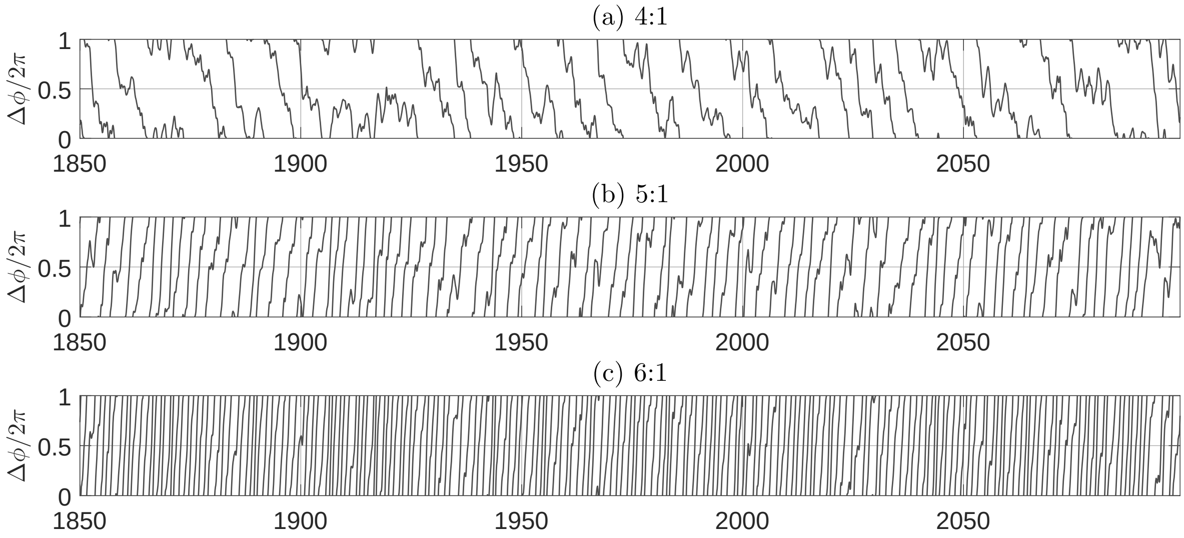

Figure C.7: Normalized phase difference plots of the QBO and SAO in MIROC data, corresponding to synchronization ratios of (a) $4:1$, (b) $5:1$, and (c) $6:1$ respectively.

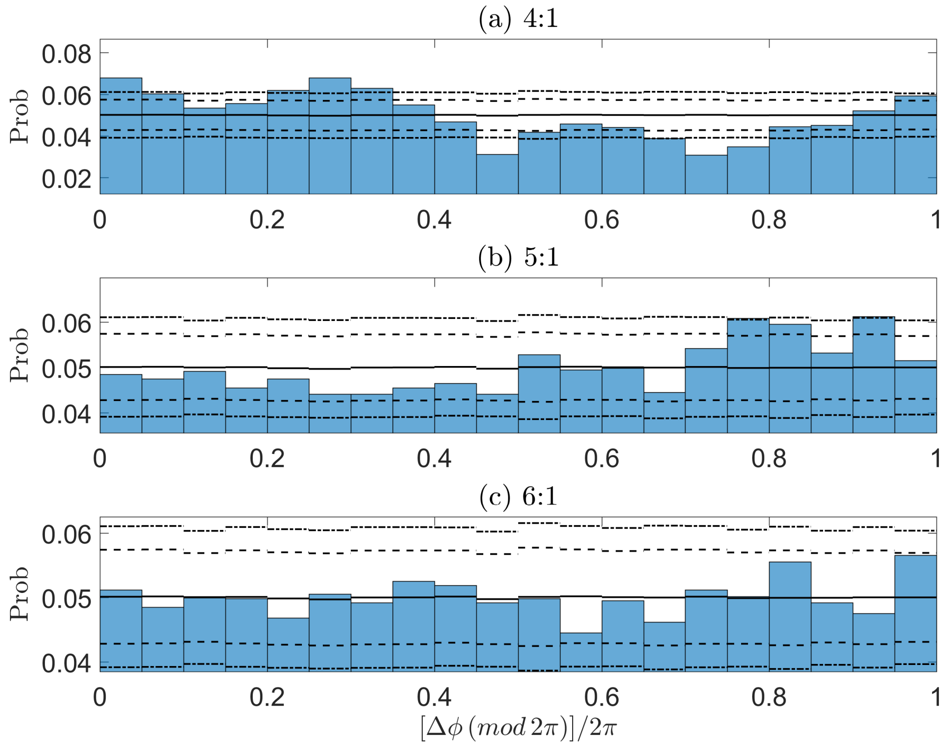

Figure C.8: Histograms of the normalized phase difference $[\Delta\phi \pmod{2\pi})]/2\pi]$ between the zonal wind QBO and SAO in MIROC, for the three synchronization ratios: (a) $(4:1)$, (b) $(5:1)$, and (c) $(6:1)$. Horizontal lines are statistics for the probability distribution of the height of each bin, as generated by surrogate time series. Solid, dashed and dash-dotted lines mark the locations of the mean and the 2σ and 3σ significance levels respectively.

References

S.J. Allen and R.A. Vincent. Gravity wave activity in the lower atmosphere: Seasonal and latitudinal variations. *J. Geophys. Res.-Atmos.*, 100(D1):1327–1350, 1995.

D.G. Andrews and M.E. McIntyre. Planetary waves in horizontal and vertical shear: The generalized Eliassen-Palm relation and the mean zonal acceleration. *J. Atmos. Sci.*, 33(11):2031–2048, 1976a.

D.G. Andrews and M.E. McIntyre. Planetary waves in horizontal and vertical shear: Asymptotic theory for equatorial waves in weak shear. *J. Atmos. Sci.*, 33(11): 2049–2053, 1976b.

D.G. Andrews and M.E. McIntyre. An exact theory of nonlinear waves on a Lagrangian-mean flow. *J. Fluid Mech.*, 89(04):609–646, 1978.

D.G. Andrews, J.R. Holton, and C.B. Leovy. *Middle Atmosphere Dynamics*, volume 40. Academic Press, 1987.

J.A. Anstey and T.G. Shepherd. High-latitude influence of the quasi-biennial oscillation. *Quart. J. Roy. Meteor. Soc.*, 140(678):1–21, 2013.

V.I. Arnold. Small denominators I. Mappings of the Circumference onto Itself. *AMS Translations, Series 2*, 46:213–284, 1965.

P. Bak, T. Bohr, and M.H. Jensen. Mode-locking and the transition to chaos in dissipative systems. *Phys. Scripta*, 1985(T9):50, 1985.

M.P. Baldwin, L.J. Gray, T.J. Dunkerton, K. Hamilton, P.H. Haynes, W.J. Randel, J.R. Holton, M.J. Alexander, I. Hirota, T. Horinouchi, et al. The quasi-biennial oscillation. *Rev. Geophys.*, 39(2):179–229, 2001.

A.D. Belmont and D.G. Dartt. Variation with longitude of the quasi-bienial oscillation. *Mon. Wea. Rev.*, 96(11):767–777, 1968.

J.W. Bergman and M.L. Salby. Equatorial wave activity derived from fluctuations in observed convection. *J. Atmos. Sci.*, 51(24):3791–3806, 1994.

J.R. Booker and F.P. Bretherton. The critical layer for internal gravity waves in a shear flow. *J. Fluid Mech.*, 27(51):517–539, 1967.

A.W. Brewer. Evidence for a world circulation provided by the measurements of helium and water vapour distribution in the stratosphere. *Quart. J. Roy. Met. Soc.*, 75(326):351–363, 1949.

N. Butchart. The Brewer-Dobson circulation. *Rev. Geophys.*, 52(2):157–184, 2014.

A.J. Charlton and L.M. Polvani. A new look at stratospheric sudden warmings. Part I: Climatology and modeling benchmarks. *J. Climate*, 20(3):449–469, 2007.

J.G. Charney and P.G. Drazin. Propagation of planetary-scale disturbances from the lower into the upper atmosphere. *J. Geophys. Res.*, 66(1):83–109, 1961.

B. Christiansen, S. Yang, and M.S. Madsen. Do strong warm ENSO events control the phase of the stratospheric QBO? *Geophys. Res. Lett.*, 43(19):10,489–10,495, 2016.

C.C. Collimore, D.W. Martin, M.H. Hitchman, A. Huesmann, and D.E. Waliser. On the relationship between the QBO and tropical deep convection. *J. Climate*, 16 (15):2552–2568, 2003.

J. Crank and P. Nicolson. A practical method for numerical evaluation of solutions of partial differential equations of the heat-conduction type. In *Mathematical Proceedings of the Cambridge Philosophical Society*, volume 43, pages 50–67, 1947.

D.P. Dee, S.M. Uppala, A.J. Simmons, P. Berrisford, P. Poli, S. Kobayashi, U. Andrae, M.A. Balmaseda, G. Balsamo, P. Bauer, et al. The ERA-Interim reanalysis: Configuration and performance of the data assimilation system. *Quart. J. Roy. Met. Soc.*, 137(656):553–597, 2011.

G.M.B. Dobson. Origin and distribution of the polyatomic molecules in the atmosphere. *P. Roy. Soc. A-Math. Phy.*, 236(1205):187–193, 1956.

T. Dunkerton. On the role of the Kelvin wave in the westerly phase of the semiannual zonal wind oscillation. *J. Atmos. Sci.*, 36(1):32–41, 1979.

T.J. Dunkerton. Laterally-propagating Rossby waves in the easterly acceleration phase of the quasi-biennial oscillation. *Atmos. Ocean*, 21(1):55–68, 1983.

T.J. Dunkerton. Annual variation of deseasonalized mean flow acceleration in the equatorial lower stratosphere. *J. Meteor. Soc. Japan*, 68(4):499–508, 1990.

T.J. Dunkerton. Nonlinear propagation of zonal winds in an atmosphere with Newtonian cooling and equatorial wavedriving. *J. Atmos. Sci.*, 48(2):236–263, 1991.

T.J. Dunkerton. The role of gravity waves in the quasi-biennial oscillation. *J. Geophys. Res.-Atmos.*, 102(D22):26053–26076, 1997.

T.J. Dunkerton and D.P. Delisi. Climatology of the equatorial lower stratosphere. *J. Atmos. Sci.*, 42(4):376–396, 1985.

T.J. Dunkerton and D.P. Delisi. Interaction of the quasi-biennial oscillation and stratopause semiannual oscillation. *J. Geophys. Res.-Atmos.*, 102(D22):26107–26116, 1997.

R.A. Ebdon. Notes on the wind flow at 50 mb in tropical and sub-tropical regions in January 1957 and January 1958. *Quart. J. Roy. Meteor. Soc.*, 86(370):540–542, 1960.

M. Ern, P. Preusse, and C.D. Warner. Some experimental constraints for spectral parameters used in the Warner and McIntyre gravity wave parameterization scheme. *Atmos. Chem. Phys.*, 6(12):4361–4381, 2006.

M. Ern, F. Ploeger, P. Preusse, J.C. Gille, L.J. Gray, S. Kalisch, M.G. Mlynczak, J.M. Russell, and M. Riese. Interaction of gravity waves with the QBO: A satellite perspective. *J. Geophys. Res.-Atmos.*, 119(5):2329–2355, 2014.

K. Fraedrich, S. Pawson, and R. Wang. An EOF analysis of the vertical-time delay structure of the quasi-biennial oscillation. *J. Atmos. Sci.*, 50(20):3357–3365, 1993.

I.P. Gabis. The validity of long-term prediction of quasi-biennial oscillation (QBO) as a proof of the exact seasonal synchronization of the equatorial stratospheric QBO cycle. *J. Atmos. Sol.-Terr. Phy.*, 124:44–58, 2015.

R.R. Garcia, T.J. Dunkerton, R.S. Lieberman, and R.A. Vincent. Climatology of the semiannual oscillation of the tropical middle atmosphere. *J. Geophys. Res.-Atmos.*, 102(D22):26019–26032, 1997.

M.A. Geller, W. Shen, M. Zhang, and W.W. Tan. Calculations of the stratospheric quasi-biennial oscillation for time-varying wave forcing. *J. Atmos. Sci.*, 54(7):883–894, 1997.

M.A. Geller, T. Zhou, and W. Yuan. The QBO, gravity waves forced by tropical convection, and ENSO. *J. Geophys. Res.-Atmos.*, 121(15):8886–8895, 2016.

M.A. Giorgetta, L. Bengtsson, and K. Arpe. An investigation of QBO signals in the east Asian and Indian monsoon in GCM experiments. *Climate Dyn.*, 15(6): 435–450, 1999.

M.A. Giorgetta, E. Manzini, and E. Roeckner. Forcing of the quasi-biennial oscillation from a broad spectrum of atmospheric waves. *Geophys. Res. Lett.*, 29(8):86–1–86–4, 2002.

L. Glass and M.C. Mackey. *From clocks to chaos: the rhythms of life.* Princeton University Press, 1988.

L.J. Gray and J.A. Pyle. A two-dimensional model of the quasi-biennial oscillation of ozone. *J. Atmos. Sci.*, 46(2):203–220, 1989.

W.M. Gray. Atlantic seasonal hurricane frequency. part i: El niño and 30 mb quasi-biennial oscillation influences. *Mon. Wea. Rev.*, 112(9):1649–1668, 1984.

K. Hamilton. Rocketsonde observations of the mesospheric semiannual oscillation at Kwajalein. *Atmos. Ocean*, 20(4):281–286, 1982.

K. Hamilton. On the quasi-decadal modulation of the stratospheric QBO period. *J. Climate*, 15(17):2562–2565, 2002.

J. Hampson and P. Haynes. Phase alignment of the tropical stratospheric QBO in the annual cycle. *J. Atmos. Sci.*, 61(21):2627–2637, 2004.

A. Hannachi, I.T. Jolliffe, and D.B. Stephenson. Empirical orthogonal functions and related techniques in atmospheric science: A review. *Int. J. Climatol.*, 27(9):1119–1152, 2007.

S.C. Hardiman, N. Butchart, T.J. Hinton, S.M. Osprey, and L.J. Gray. The effect of a well-resolved stratosphere on surface climate: Differences between CMIP5 simulations with high and low top versions of the Met Office climate model. *J. Climate*, 25(20):7083–7099, 2012.

P.H. Haynes, M.E. McIntyre, T.G. Shepherd, C.J. Marks, and K.P. Shine. On the 'downward control' of extratropical diabatic circulations by eddy-induced mean zonal forces. *J. Atmos. Sci.*, 48(4):651–678, 1991.

I. Hirota. Equatorial waves in the upper stratosphere and mesosphere in relation to the semiannual oscillation of the zonal wind. *J. Atmos. Sci.*, 35(4):714–722, 1978.

C.H. Ho, H.S. Kim, J.H Jeong, and S.W. Son. Influence of stratospheric quasi-biennial oscillation on tropical cyclone tracks in the western North Pacific. *Geophys. Res. Lett.*, 36(6), 2009.

J.R. Holton. *The Dynamic Meteorology of the Stratosphere and Mesosphere*, volume 15. Springer, 1975.

J.R. Holton and G.J. Hakim. *An Introduction to Dynamic Meteorology*, volume 88. Academic Press, 2012.

J.R. Holton and R.S. Lindzen. An updated theory for the quasi-biennial cycle of the tropical stratosphere. *J. Atmos. Sci.*, 29(6):1076–1080, 1972.

J.R. Holton and H.C. Tan. The influence of the equatorial quasi-biennial oscillation on the global circulation at 50 mb. *J. Atmos. Sci.*, 37(10):2200–2208, 1980.

J.R. Holton, P.H. Haynes, M.E. McIntyre, A.R. Douglass, R.B. Rood, and L. Pfister. Stratosphere-troposphere exchange. *Rev. Geophys.*, 33(4):403–439, 1995.

M.H. Jensen, P. Bak, and T. Bohr. Complete devil's staircase, fractal dimension, and universality of mode-locking structure in the circle map. *Phys. Rev. Lett.*, 50(21): 1637–1639, 1983.

M.H. Jensen, P. Bak, and T. Bohr. Transition to chaos by interaction of resonances in dissipative systems. I. Circle maps. *Phys. Rev. A*, 30(4):1960–1969, 1984.

R.P. Kane. Quasi-biennial and quasi-triennial oscillations in the summer monsoon rainfall of the meteorological subdivisions of India. *Mon. Weather Rev.*, 123(4): 1178–1184, 1995.

A. Katok and B. Hasselblatt. *Introduction to the Modern Theory of Dynamical Systems*, volume 54. Cambridge University Press, 1997.

Y. Kawatani and K. Hamilton. Weakened stratospheric quasibiennial oscillation driven by increased tropical mean upwelling. *Nature*, 497(7450):478–481, 2013.

Y. Kawatani, K. Hamilton, and S. Watanabe. The quasi-biennial oscillation in a double CO2 climate. *J. Atmos. Sci.*, 68(2):265–283, 2011.

J.S. Kinnersley and S. Pawson. The descent rates of the shear zones of the equatorial QBO. *J. Atmos. Sci.*, 53(14):1937–1949, 1996.

T.R. Krismer, M.A. Giorgetta, and M. Esch. Seasonal aspects of the quasi-biennial oscillation in the Max Planck Institute Earth System Model and ERA-40. *Journal of Advances in Modeling Earth Systems*, 5(2):406–421, 2013.

L. Kuai, R.L. Shia, X. Jiang, K.K. Tung, and Y.L. Yung. Nonstationary synchronization of equatorial QBO with SAO in observations and a model. *J. Atmos. Sci.*, 66 (6):1654–1664, 2009.

K. Labitzke and H.V. Loon. Associations between the 11-year solar cycle, the QBO and the atmosphere. Part I: the troposphere and stratosphere in the northern hemisphere in winter. *J. Atmos. Terr. Phys.*, 50(3):197–206, 1988.

S. Liess and M.A. Geller. On the relationship between QBO and distribution of tropical deep convection. *J. Geophys. Res.-Atmos.*, 117(D3), 2012.

R.S. Lindzen. Internal equatorial planetary-scale waves in shear flow. *J. Atmos. Sci.*, 27:394–405, 1970.

R.S. Lindzen. Equatorial planetary waves in shear: Part I. *J. Atmos. Sci.*, 28(4): 609–622, 1971.

R.S. Lindzen and J.R. Holton. A theory of the quasi-biennial oscillation. *J. Atmos. Sci.*, 25(6):1095–1107, 1968.

E. Manzini and N.A. McFarlane. The effect of varying the source spectrum of a gravity wave parameterization in a middle atmosphere general circulation model. *J. Geophys. Res.-Atmos.*, 103(D24):31523–31539, 1998.

A.G. Marshall and A.A. Scaife. Impact of the QBO on surface winter climate. *J. Geophys. Res.-Atmos.*, 114(D18), 2009.

G.M. Martin, N. Bellouin, W. J. Collins, I. D. Culverwell, P. R. Halloran, S. C. Hardiman, T. J. Hinton, C. D. Jones, R. E. McDonald, A. J. McLaren, et al. The HadGEM2 family of Met Office Unified Model climate configurations. *Geoscientific Model Development*, 4(3):723–757, 2011.

T. Matsuno. A dynamical model of the stratospheric sudden warming. *J. Atmos. Sci.*, 28(8):1479–1494, 1971.

R.E. Mirollo and S.H. Strogatz. Synchronization of pulse-coupled biological oscillators. *SIAM Journal on Applied Mathematics*, 50(6):1645–1662, 1990.

B. Naujokat. An Update of the Observed Quasi-Biennial Oscillation of the Stratospheric Winds over the Tropics. *J. Atmos. Sci.*, 43(16):1873–1877, 1986.

P.A. Newman, L. Coy, S. Pawson, and L.R. Lait. The anomalous change in the QBO in 2015–2016. *Geophys. Res. Lett.*, 43(16):8791–8797, 2016.

J. Nie and A.H. Sobel. Responses of tropical deep convection to the QBO: Cloud-resolving simulations. *J. Atmos. Sci.*, 72(9):3625–3638, 2015.

S.M. Osprey, L.J. Gray, S.C. Hardiman, N. Butchart, and T.J. Hinton. Stratospheric variability in twentieth-century CMIP5 simulations of the Met Office climate model: High top versus low top. *J. Climate*, 26(5):1595–1606, 2013.

S.M. Osprey, N. Butchart, J.R. Knight, A.A. Scaife, K. Hamilton, J.A. Anstey, V. Schenzinger, and C. Zhang. An unexpected disruption of the atmospheric quasi-biennial oscillation. *Science*, 353(6306):1424–1427, 2016.

D. O'Sullivan and T.J. Dunkerton. The influence of the quasi-biennial oscillation on global constituent distributions. *J. Geophys. Res.*, 102(D18):21731–21743, 1997.

Edward Ott. *Chaos in Dynamical Systems.* Cambridge University Press, 2002.

C.L. Pascoe, L.J. Gray, S.A. Crooks, M.N. Juckes, and M.P. Baldwin. The quasi-biennial oscillation: Analysis using ERA-40 data. *J. Geophys. Res.*, 110(D8), 2005.

A. Pikovsky, M. Rosenblum, and J. Kurths. *Synchronization: a universal concept in nonlinear sciences*, volume 12. Cambridge University Press, 2003.

R.A. Plumb. The interaction of two internal waves with the mean flow: Implications for the theory of the quasi-biennial oscillation. *J. Atmos. Sci.*, 34(12):1847–1858, 1977.

R.A. Plumb. The quasi-biennial oscillation. In J.R. Holton and T. Matsuno, editors, *Dynamics of the Middle Atmosphere*, pages 217–251. Terra Sci., 1984.

R.A. Plumb. Stratospheric transport. *J. Meteor. Soc. Japan. Ser. II*, 80(4B):793–809, 2002.

R.A. Plumb and R.C. Bell. A model of the quasi-biennial oscillation on an equatorial beta-plane. *Quart. J. Roy. Meteor. Soc.*, 108(456):335–352, 1982.

K. Rajendran, I.M. Moroz, P.L. Read, and S.M. Osprey. Synchronisation of the equatorial QBO by the annual cycle in tropical upwelling in a warming climate. *Quart. J. Roy. Meteor. Soc.*, 142(695):1111–1120, 2016.

P.L. Read and A.A. Castrejón-Pita. Phase synchronization between stratospheric and tropospheric quasi-biennial and semi-annual oscillations. *Quart. J. Roy. Meteor. Soc.*, 138(666):1338–1349, 2012.

R.J. Reed. Some features of the annual temperature regime in the tropical stratosphere. *Mon. Wea. Rev.*, 90(6):211–215, 1962.

R.J. Reed. Zonal wind behavior in the equatorial stratosphere and lower mesosphere. *J. Geophys. Res.*, 71(18):4223–4233, 1966.

R.J. Reed, W.J. Campbell, L.A. Rasmussen, and D.G. Rogers. Evidence of a downward-propagating, annual wind reversal in the equatorial stratosphere. *J. Geophys. Res.*, 66(3):813–818, 1961.

K.H. Rosenlof. Seasonal cycle of the residual mean meridional circulation in the stratosphere. *J. Geophys. Res.-Atmos.*, 100(D3):5173–5173, 1995.

M. Salby and P. Callaghan. Connection between the solar cycle and the QBO: The missing link. *J. Climate*, 13(14):2652–2662, 2000.

M.L. Salby and P.F. Callaghan. Relationship of the quasi-biennial oscillation to the stratospheric signature of the solar cycle. *J. Geophys. Res.*, 111(D6), 2006.

R. Saravanan. A multiwave model of the quasi-biennial oscillation. *J. Atmos. Sci.*, 47(21):2465–2474, 1990.

A.A. Scaife, N. Butchart, C.D. Warner, D. Stainforth, W. Norton, and J. Austin. Realistic quasi-biennial oscillations in a simulation of the global climate. *Geophys. Res. Lett.*, 27(21):3481–3484, 2000.

A.A. Scaife, M. Athanassiadou, M. Andrews, A. Arribas, M. Baldwin, N. Dunstone, J. Knight, C. MacLachlan, E. Manzini, W.A. Müller, et al. Predictability of the quasi-biennial oscillation and its northern winter teleconnection on seasonal to decadal timescales. *Geophys. Res. Lett.*, 41(5):1752–1758, 2014.

V. Schenzinger, S. Osprey, L. Gray, and N. Butchart. Defining metrics of the Quasi-Biennial Oscillation in global climate models. *Geoscientific Model Development Discussions*, 2016:1–21, 2016.

S. Schirber. Influence of ENSO on the QBO: Results from an ensemble of idealized simulations. *J. Geophys. Res.-Atmos.*, 120(3):1109–1122, 2015.

S. Schirber, E. Manzini, T. Krismer, and M. Giorgetta. The quasi-biennial oscillation in a warmer climate: sensitivity to different gravity wave parameterizations. *Climate Dyn.*, 45(3):825–836, 2014.

W.J.M. Seviour, N. Butchart, and S.C. Hardiman. The Brewer–Dobson circulation inferred from ERA-Interim. *Quart. J. Roy. Meteor. Soc.*, 138(665):878–888, 2012.

J. Simonet, M. Warden, and E. Brun. Locking and arnold tongues in an infinite-dimensional system: the nuclear magnetic resonance laser with delayed feedback. *Phys. Rev. E*, 50(5):3383–3391, 1994.

M. Taguchi. Observed connection of the stratospheric quasi-biennial oscillation with El Niño–Southern Oscillation in radiosonde data. *J. Geophys. Res.*, 115(D18), 2010.

M. Takahashi. Simulation of the quasi-biennial oscillation in a general circulation model. *Geophys. Res. Lett.*, 26(9):1307–1310, 1999.

F. Takens. Detecting strange attractors in turbulence. In *Dynamical systems and turbulence, Warwick 1980*, pages 366–381. Springer, 1981.

P. Tass, M.G. Rosenblum, J. Weule, J. Kurths, A. Pikovsky, J. Volkmann, A. Schnitzler, and H.J. Freund. Detection of n: m phase locking from noisy data: application to magnetoencephalography. *Phys. Rev. Lett.*, 81(15):3291–3294, 1998.

K.E. Taylor, R.J. Stouffer, and G.A. Meehl. An overview of CMIP5 and the experiment design. *B. Am. Meterol. Soc.*, 93(4):485–498, 2012.

J. Theiler, S. Eubank, A. Longtin, B. Galdrikian, and J.D. Farmer. Testing for nonlinearity in time series: the method of surrogate data. *Physica D*, 58(1-4): 77–94, 1992.

D.W.J. Thompson, M.P. Baldwin, and J.M. Wallace. Stratospheric connection to Northern Hemisphere wintertime weather: Implications for prediction. *J. Climate*, 15(12):1421–1428, 2002.

S.M. Uppala, P.W. Kållberg, A.J. Simmons, U. Andrae, V.D. Bechtold, M. Fiorino, J.K. Gibson, J. Haseler, A. Hernandez, G.A. Kelly, et al. The ERA-40 re-analysis. *Quart. J. Roy. Met. Soc.*, 131(612):2961–3012, 2005.

H. Van Loon and R.L. Jenne. On the half-yearly oscillations in the tropics. *Tellus A*, 22(4):391–398, 1970.

R.A. Vincent and J.M. Alexander. Gravity waves in the tropical lower stratosphere: An observational study of seasonal and interannual variability. *J. Geophys. Res.-Atmos.*, 105(D14):17971–17982, 2000.

L. Wang and M.A. Geller. Morphology of gravity-wave energy as observed from 4 years (1998–2001) of high vertical resolution US radiosonde data. *J. Geophys. Res.-Atmos.*, 108(D16), 2003.

S. Watanabe, H. Miura, M. Sekiguchi, T. Nagashima, K. Sudo, S. Emori, and M. Kawamiya. Development of an atmospheric general circulation model for integrated Earth system modeling on the Earth Simulator. *J. Earth Simulator*, 9: 27–35, 2008.

S. Watanabe, T. Hajima, K. Sudo, T. Nagashima, T. Takcmura, H. Okajima, T. Nozawa, H. Kawase, M. Abe, T. Yokohata, et al. MIROC-ESM 2010: model description and basic results of CMIP5-20c3m experiments. *Geoscientific Model Development*, 4(4):845–872, 2011.

W. Yao and C. Jablonowski. Idealized Quasi-Biennial Oscillations in an Ensemble of Dry GCM Dynamical Cores. *J. Atmos. Sci.*, 72(6):2201–2226, 2015.

S. Yoden and J. Holton. A new look at equatorial quasi-biennial oscillation models. *J. Atmos. Sci.*, 45(19):2703–2717, 1988.

C. Yoo and S.W. Son. Modulation of the boreal wintertime Madden-Julian oscillation by the stratospheric quasi-biennial oscillation. *Geophys. Res. Lett.*, 43(3):1392–1398, 2016.

E. Yulaeva, J.R. Holton, and J.M. Wallace. On the cause of the annual cycle in tropical lower-stratospheric temperatures. *J. Atmos. Sci.*, 51(2):169–174, 1994.

J.H. Zar. Significance testing of the Spearman rank correlation coefficient. *J. Am. Stat. Soc.*, 67(339):578–580, 1972.

S.D. Zhang, F. Yi, C.M. Huang, and Q. Zhou. Latitudinal and seasonal variations of lower atmospheric inertial gravity wave energy revealed by US radiosonde data. *Annales Geophysicae*, 28(5):1065–1074, 2010.

S.D. Zhang, F. Yi, C.M. Huang, K.M. Huang, Q. Gan, Y.H. Zhang, and Y. Gong. Latitudinal and altitudinal variability of lower atmospheric inertial gravity waves revealed by US radiosonde data. *J. Geophys. Res.-Atmos.*, 118(14):7750–7764, 2013.